

# GRAPH THEORY TO STUDY COMPLEX NETWORKS IN THE BRAIN

A DISSERTATION SUBMITTED TO  
THE GRADUATE SCHOOL OF ENGINEERING AND SCIENCE  
OF BILKENT UNIVERSITY  
IN PARTIAL FULFILLMENT OF THE REQUIREMENTS FOR  
THE DEGREE OF  
DOCTOR OF PHILOSOPHY  
IN  
MATERIALS SCIENCE AND NANOTECHNOLOGY

By  
Mite Mijalkov  
April 2018

Graph theory to study complex networks in the brain

By Mite Mijalkov

April 2018

We certify that we have read this dissertation and that in our opinion it is fully adequate, in scope and in quality, as a dissertation for the degree of Doctor of Philosophy.

---

Giovanni Volpe(Advisor)

---

Hasan Tayfun Özçelik

---

Alpan Bek

---

Hande Toffoli

---

Seymur Jahangirov

Approved for the Graduate School of Engineering and Science:

---

Ezhan Kardeşan  
Director of the Graduate School

# ABSTRACT

## GRAPH THEORY TO STUDY COMPLEX NETWORKS IN THE BRAIN

Mite Mijalkov

Ph.D. in Materials Science and Nanotechnology

Advisor: Giovanni Volpe

April 2018

The brain is a large-scale, intricate web of neurons, known as the *connectome*. By representing the brain as a network i.e. a set of nodes connected by edges, one can study its organization by using concepts from graph theory to evaluate various measures. We have developed *BRAPH - BRain Analysis using graPH* theory, a MatLab, object-oriented freeware that facilitates the connectivity analysis of brain networks. BRAPH provides user-friendly interfaces that guide the user through the various steps of the connectivity analysis, such as, calculating adjacency matrices, evaluating global and local measures, performing group comparisons by non-parametric permutations and assessing the communities in a network. To demonstrate its capabilities, we performed connectivity analyses of structural and functional data in two separate studies. Furthermore, using graph theory, we showed that structural magnetic resonance imaging (MRI) undirected networks of stable mild cognitive impairment (sMCI) subjects, late MCI converters (lMCIc), early MCI converters (eMCIc), and Alzheimer's Disease (AD) patients show abnormal organization. This is indicated, at global level, by decreases in clustering and transitivity accompanied by increases in path length and modularity and, at nodal level, by changes in nodal clustering and closeness centrality in patient groups when compared to controls. In samples that do not exhibit differences in the undirected analysis, we propose the usage of directed networks to assess any topological changes due to a neurodegenerative disease. We demonstrate that such changes can be identified in Alzheimer's and Parkinson's patients by using directed networks built by delayed correlation coefficients. Finally, we put forward a method that improves the reconstruction of the brain connectome by utilizing the delays in the dynamic behavior of the neurons. We show that this *delayed correlation* method correctly identifies 70% to 80% of the real connections in simulated networks and performs well in the identification of their global and nodal properties.

*Keywords:* Graph theory, BRAPH, directed networks, connectome reconstruction.

## ÖZET

# BEYİNDEKİ KOMPLEKS AĞLARI ANALİZ ETMEK İÇİN GRAF TEORİSİ

Mite Mijalkov

Malzeme Bilimi ve Nanoteknoloji, Doktora

Tez Danışmanı: Giovanni Volpe

Nisan 2018

Beyin, karmaşık ve geniş kapsamlı nöral ağlardan oluşmakta ve bu yapılara da “konektom” adı verilmektedir. Bu sebeple, beyin, düğüm ve kenarlardan oluşan bir ağ olarak düşünüldüğünde, graf teori konseptleri ile beynin organizasyonu ile alakalı çeşitli analizler yapılabilir. Bu çalışmada, beynin bağlantı analizini yapmak için MatLab temelli, nesne odaklı, ücretsiz bir yazılım olan BRAPH (Graf teori ile beyin alanizi) geliştirilmiştir. BRAPH, kullanımı kolay bir arayüze sahiptir ve bağlantı analizi yapan kullanıcıyı çeşitli şekillerde yönlendirmektedir (komşuluk matrisi hesaplama, genel ve bölgesel ölçü analizi, non-parametrik permütasyon yöntemi ile gruplar arası karşılaştırma ve ağ içerisindeki alt grupları analiz etme gibi). BRAPH ile yapılabilecekleri göstermek amacıyla, iki farklı çalışmada yapısal ve fonksiyonel bağlantı analizi yapılmıştır. Graf teori kullanılarak, sMCI, lMCIc, eMCIc ve AD hastalarından elde edilen yapısal MRI datası yönlendirilmemiş ağlarda analiz edildiğinde anormal organizasyon gözlenmiştir. Kontrol gruplarıyla kıyaslandığında, bu hastalarda, genel seviyede gruplaşma ve geçişliliğin azalması, aynı zamanda yol uzunluğunun ve modüleritenin artması, düğüm seviyesinde ise düğüm gruplaşmasında ve merkeze yakınlıkta değişimler gösterilmiştir. Burada, yönlendirilmemiş analizlerde farklılık göstermeyen örneklerin nörodejeneratif hastalıklardan kaynaklı topolojik değişimlerinin incelenmesi için yönlendirilmiş ağlarla analiz edilmesi önerilmektedir. Alzheimer ve Parkinson hastaları için gecikmiş korelasyon katsayıları ile yapılan yönlendirilmiş ağlar analizi sonucunda, bahsedilen değişikliklerin tespit edilebildiği gösterilmiştir. Son olarak, nöronların dinamik yapısındaki gecikmeleri kullanarak beyin konektomunun rekonstrüksiyonunu geliştiren bir yöntem ileri sürülmektedir. İleri sürülen “gecikmiş korelasyon” metodunun, simüle edilen ağlardaki gerçek bağlantıları %70-80 oranında doğru tespit ettiği, aynı zamanda genel ve boğum özelliklerinin tespitinde de oldukça iyi olduğu gösterilmiştir.

*Anahtar sözcükler:* Graf teori, BRAPH, yönlendirilmiş ağ, konektom rekonstrüksiyonu.

## Acknowledgement

I would like to express my endless gratitude to Dr. Giovanni Volpe, for his support, guidance and fruitful discussions during my graduate studies. He has been instrumental in my development from an undergraduate student to holding a PhD degree, giving me the confidence that I am prepared for the challenges ahead. It has been a great opportunity and experience working with him and I sincerely hope that our collaboration will extend beyond my PhD years.

I would also like to thank Dr. Tayfun Özçelik and Dr. Alpan Bek for being part of my thesis monitoring committee. They were closely following my work during the past couple of years and offered very useful comments and suggestions that led to vast improvements in this work. In addition, thanks to Dr. Hande Toffoli and Dr. Seymur Jahangirov for accepting to be part of the jury committee. It really takes a lot of time and effort to read a thesis and I would like to thank all jury members for making this effort and offer their views on how to improve this thesis.

I wish to extend a huge thank you to our collaborations in the Karolinska Institute, Dr. Joana Pereira and Dr. Eric Westman. They have been closely involved in all the research I conducted during my PhD and offered invaluable inputs. I learned a lot from my frequent discussion with Dr. Pereira and her counsel was essential to make my transition to neuroscience as smooth as possible.

Thanks to all my friends and, in particular, members of the Soft Matter Lab, for just being with me for better or worse. We shared a lot of discussions (although I do not remember us solving any of the socio-economic problems we so passionately talked about), painful courses, jokes and outings (quite a few beer and raki parties); all of these made these past years very enjoyable and so much fun. Although most of you are currently scattered around the world pursuing various degrees and jobs, I write this in hope that everyone has found their calling, with the wish to meet again and reminiscence about some of the fun moments we experienced.

To my uncle and parents, thank you. No words can really describe how grateful I feel for everything you did for me during my life. The support and motivation that you selflessly provided during these times was helpful in many occasions and

made the hard things and choices I had to make very easy.

Finally, pursuing a PhD degree was a bumpy road, with many good and bad moments that served as a source for so many frustrations. However, with all done and dusted, I can honestly say, I do not remember any of those moments. What will forever be etched in my memory though, is the person who lived these moments with me, optimistic and supportive when times got bad, happy with me when everything was going as planned. To Behide, my more beautiful half, thank you for getting me over the line. I cherish every moment we spent together. If every opportunity is a star in the sky, I hope that when you finally land on your star, I will be there with you, and maybe start to repay for your generousness and the incredible things you did for me. I would do it all over again if it means I will get to have you next to me.

I would like to acknowledge the scholarship from TÜBİTAK (The Scientific and Research Council of Turkey) BİDEB 2215 - Graduate Scholarship Programme for International Students that I received during my PhD. Additionally, my PhD studies were partially supported by TÜBİTAK project 116F111.



# Contents

<b>1</b>	<b>Introduction</b>	<b>1</b>
<b>2</b>	<b>Graph Theory Concepts</b>	<b>18</b>
2.1	Graphs . . . . .	19
2.2	Types of graphs . . . . .	21
2.3	Graph measures . . . . .	23
2.3.1	Degree . . . . .	24
2.3.2	Strength . . . . .	25
2.3.3	Eccentricity . . . . .	26
2.3.4	Path length . . . . .	28
2.3.5	Triangles . . . . .	29
2.3.6	Clustering coefficient . . . . .	30
2.3.7	Transitivity . . . . .	31
2.3.8	Closeness centrality . . . . .	31
2.3.9	Betweenness centrality . . . . .	31
2.3.10	Global efficiency . . . . .	32
2.3.11	Local efficiency . . . . .	33
2.3.12	Modularity . . . . .	34
2.3.13	Within-module z-score . . . . .	35
2.3.14	Participation coefficient . . . . .	36
2.3.15	Assortativity coefficient . . . . .	37
2.3.16	Small-worldness . . . . .	38
<b>3</b>	<b>Building the Networks of the Brain</b>	<b>39</b>
3.1	Imaging methods . . . . .	40

3.1.1	MRI . . . . .	41
3.1.2	Functional MRI . . . . .	43
3.2	General workflow to analyze brain connectivity . . . . .	44
3.2.1	Definition of nodes . . . . .	45
3.2.2	Definition of edges . . . . .	46
3.2.3	Building the adjacency matrix . . . . .	48
3.2.4	Calculation of graph measures . . . . .	50
3.3	Between-group comparison . . . . .	51
3.3.1	Permutation test . . . . .	51
3.3.2	Comparison with random graphs . . . . .	53
3.3.3	False discovery rate (FDR) . . . . .	53
<b>4</b>	<b>BRAPH – BRain Analysis using graph theory</b>	<b>56</b>
4.1	Introduction . . . . .	56
4.2	Materials and methods . . . . .	59
4.2.1	Overview and analysis workflow . . . . .	59
4.2.2	Graphical user interfaces in BRAPH . . . . .	65
4.2.3	The underlying BRAPH architecture . . . . .	77
4.2.4	Subjects . . . . .	84
4.2.5	Network construction and analysis . . . . .	87
4.3	Results . . . . .	89
4.3.1	Structural network topology in amnesic MCI and AD . . . . .	89
4.3.2	Functional network topology in PD-MCI . . . . .	93
4.4	Discussion . . . . .	98
4.4.1	Large-scale structural networks in amnesic MCI and AD . . . . .	99
4.4.2	Large-scale functional networks in PD . . . . .	100
4.4.3	BRAPH features . . . . .	102
<b>5</b>	<b>Disrupted Network Topology in Patients with Stable and Progressive MCI and Alzheimer’s Disease</b>	<b>104</b>
5.1	Introduction . . . . .	104
5.2	Materials and methods . . . . .	107
5.2.1	Subjects . . . . .	107
5.2.2	MRI acquisition . . . . .	109

5.2.3	Image preprocessing . . . . .	110
5.2.4	Network construction and analysis . . . . .	111
5.2.5	Comparison of network measures between groups . . . . .	114
5.3	Results . . . . .	114
5.3.1	Global network analysis . . . . .	114
5.3.2	Nodal network analysis . . . . .	119
5.3.3	Brain communities . . . . .	127
5.4	Discussion . . . . .	134
<b>6</b>	<b>Directed Networks in Parkinson’s and Alzheimer’s Patients</b>	<b>141</b>
6.1	Introduction . . . . .	141
6.2	Materials and methods . . . . .	143
6.2.1	Analysis overflow . . . . .	143
6.2.2	Network measures . . . . .	145
6.2.3	Subjects . . . . .	146
6.3	Results and discussion . . . . .	147
6.3.1	Parkinson’s Disease patients . . . . .	148
6.3.2	Alzheimer’s Disease patients . . . . .	154
6.4	Future perspectives . . . . .	160
<b>7</b>	<b>Delayed Correlations Improve Reconstruction of the Brain Con-</b>	<b>161</b>
	<b>nectome</b>	
7.1	Introduction . . . . .	161
7.2	Materials and methods . . . . .	163
7.2.1	Model of neuronal activity . . . . .	163
7.2.2	Analysis overview . . . . .	164
7.3	Results and discussion . . . . .	167
7.3.1	Network reconstruction accuracy . . . . .	167
7.3.2	Features of the delayed correlation model . . . . .	169
7.3.3	Global network properties . . . . .	171
7.3.4	Nodal network properties . . . . .	176
7.3.5	Community structure . . . . .	178
7.3.6	Diffusion tensor imaging networks . . . . .	184
7.4	Future perspectives . . . . .	184

<b>8 Conclusion</b>	<b>187</b>
<b>A Data</b>	<b>217</b>
A.1 Chapter 5 . . . . .	217
A.1.1 Differences in global measures after controlling for scanning centers . . . . .	217
A.2 Chapter 6 . . . . .	226
A.2.1 Directed network analysis in Parkinson’s Disease patients: High resolution networks . . . . .	226
A.2.2 Correlation of global measures with UPDRS: Delay 7 . . .	229
A.2.3 Longitudinal analysis of Parkinson’s Disease patients . . .	232
A.2.4 Directed network analysis in Alzheimer’s Disease patients: Delays 4-6 . . . . .	234
<b>B Publications</b>	<b>240</b>

# List of Figures

1.1	Watts–Strogatz model of small-world networks. . . . .	7
1.2	Barabási–Albert model of growing networks. . . . .	8
1.3	From a single neuron to brain. . . . .	9
2.1	Königsberg’s bridges and the corresponding graph. . . . .	19
2.2	A simple graph and connectivity matrix. . . . .	20
2.3	Graph types. . . . .	22
2.4	Degree of a node. . . . .	24
2.5	Strength of a node. . . . .	26
2.6	Distance between nodes. . . . .	27
2.7	Triangles around a node. . . . .	29
2.8	Betweenness centrality of a node. . . . .	32
2.9	High modularity. . . . .	33
2.10	Low modularity. . . . .	34
2.11	Within-module z-score of a node. . . . .	36
2.12	Participation coefficient of a node. . . . .	37
3.1	Workflow of MRI imaging procedure. . . . .	42
3.2	Construction of the adjacency matrix. . . . .	45
3.3	Permutation test and p-value. . . . .	52
3.4	False discovery rate (FDR). . . . .	54
4.1	Overview of BRAPH software architecture . . . . .	58
4.2	BRAPH workflow . . . . .	61
4.3	Connectivity analysis using the GUIs in BRAPH . . . . .	67
4.4	Initial GUI that becomes visible after launching BRAPH. . . . .	68

4.5	Screenshot of GUI Brain Atlas . . . . .	70
4.6	Screenshot of GUI MRI Cohort. . . . .	71
4.7	Screenshot of GUI MRI Graph Analysis. . . . .	73
4.8	GUI Community structure. . . . .	74
4.9	Snapshot of GUI MRI Graph Analysis BUD. . . . .	75
4.10	Interface used to compare the measures of two groups . . . . .	77
4.11	Structural brain networks in controls, MCI patients, and AD patients. . . . .	90
4.12	Differences between groups in global structural topology. . . . .	91
4.13	Differences between groups in nodal structural measures. . . . .	92
4.14	Functional brain networks and modules in controls and PD-MCI patients. . . . .	95
4.15	Differences between groups in the nodal functional degree. . . . .	96
5.1	Brain regions that were used in network construction and analysis. . . . .	111
5.2	Structural adjacency matrices. . . . .	113
5.3	Changes in global network measures as a function of network density. . . . .	115
5.4	Differences between controls and sMCI, lMCIC, eMCIC, and AD patients in global network measures. . . . .	116
5.5	Differences between sMCI and lMCIC, eMCIC, and AD patients in global network measures. . . . .	117
5.6	3. Changes in global network measures as a function of network density. . . . .	118
5.7	Significant decreases in the nodal clustering coefficient between groups. . . . .	120
5.8	Significant differences in the nodal closeness centrality between groups. . . . .	125
5.9	Brain communities in all subject groups. . . . .	128
6.1	Directed network analysis overview. . . . .	144
6.2	Changes in global network measures as a function of network density: delays 6-8. . . . .	151
6.3	Changes in global network measures as a function of network density: delays 9-10. . . . .	152

6.4	Changes in global network measures as a function of network density for longitudinal data. . . . .	153
6.5	Changes in global efficiency as a function of network density: delays 1-3. . . . .	155
6.6	Changes in local efficiency as a function of network density: delays 1-3. . . . .	156
6.7	Changes in clustering coefficient as a function of network density: delays 1-3. . . . .	157
6.8	Changes in transitivity as a function of network density: delays 1-3.	158
6.9	Changes in modularity as a function of network density: delays 1-3.	159
7.1	Overview of the network reconstruction procedure. . . . .	166
7.2	Accuracy of network reconstruction. . . . .	168
7.3	Network reconstruction efficiency of the delayed correlation method.	170
7.4	Global network measures as a function of network density . . . . .	172
7.5	Nodal network measures as a function of density. . . . .	177
7.6	Community structure in a modular graph. . . . .	181
7.7	Reconstruction of structural networks derived from DTI data. . . . .	186
A.1	Changes in global network measures as a function of network density: delays 6-8. . . . .	227
A.2	Changes in global network measures as a function of network density: delays 9-10. . . . .	228
A.3	Changes in global network measures as a function of network density for longitudinal data. . . . .	233
A.4	Changes in global efficiency as a function of network density: delays 4-6. . . . .	235
A.5	Changes in local efficiency as a function of network density: delays 4-6. . . . .	236
A.6	Changes in clustering coefficient as a function of network density: delays 4-6. . . . .	237
A.7	Changes in transitivity as a function of network density: delays 4-6.	238
A.8	Changes in modularity as a function of network density: delays 4-6.	239

# List of Tables

4.1	Characteristics of the structural MRI sample. . . . .	85
4.2	Characteristics of the fMRI sample. . . . .	86
4.3	Nodal degree for regions in Module III in PD-MCI subtypes and controls. . . . .	97
4.4	Nodal degree for regions in Module V in PD-MCI subtypes and controls. . . . .	98
5.1	Characteristics of the sample. . . . .	108
5.2	Significant differences in the nodal clustering coefficient between groups. . . . .	121
5.3	Significant differences in the nodal closeness centrality between groups (FDR - corrected). . . . .	122
5.4	Summary of the global and nodal network results . . . . .	126
5.5	Brain communities in all subject groups. . . . .	129
5.6	Differences in the within-module degree and participation coefficient between groups. . . . .	134
6.1	Characteristics of Parkinson's Disease sample. . . . .	146
6.2	Characteristics of Alzheimer's sample. . . . .	147
7.1	Global network measures as a function of network density. . . . .	174
7.2	Community structure in a modular graph. . . . .	182
A.1	Differences in global network measures between controls and patients after controlling for scanning site. . . . .	218
A.2	Correlation between global measures and UPDRS for low resolution networks. . . . .	229



A.3 Correlation between global measures and UPDRS for high resolution networks. . . . . 231

# Abbreviations

<b>AD</b>	Alzheimer's Disease
<b>ADNI</b>	Alzheimer's Disease Neuroimaging Initiative
<b>BRAPH</b>	BRain Analysis using graPH theory
<b>BUD</b>	Binary Undirected Density
<b>BUT</b>	Binary Undirected Threshold
<b>CDR</b>	Clinical Dementia Rating scale
<b>CDR-SB</b>	Clinical Dementia Rating - Sum of Boxes
<b>CTR</b>	Controls
<b>DTI</b>	Diffusion Tensor Imaging
<b>EEG</b>	Electroencephalography
<b>eMCIc</b>	early Mild Cognitive Impairment converters
<b>FDR</b>	False Discovery Rate
<b>fMRI</b>	functional Magnetic Resonance Imaging
<b>G</b>	Gyrus
<b>GUI</b>	Graphical User Interface
<b>HY stage</b>	Hoehn and Yahr stage
<b>Lh</b>	Left hemisphere
<b>lMCIc</b>	late Mild Cognitive Impairment converters

<b>MCI</b>	Mild Cognitive Impairment
<b>MMSE</b>	Mini-Mental State Examination
<b>MoCA</b>	Montreal Cognitive Assessment scale
<b>MRI</b>	Magnetic Resonance Imaging
<b>PD-CN</b>	Parkinson's Disease Cognitively Normal
<b>PD</b>	Parkinson's Disease
<b>PET</b>	Positron Emission Tomography
<b>PD-MCI</b>	Parkinson's Disease with Mild Cognitive Impairment
<b>PPMI</b>	Parkinson's Progression Markers Initiative
<b>Rh</b>	Right hemisphere
<b>sMCI</b>	stable Mild Cognitive Impairment after 3 years
<b>sMCI-1y</b>	stable Mild Cognitive Impairment after 1 year
<b>UPDRS</b>	Unified Parkinson's Disease Rating Scale
<b>UPDRS-III</b>	Unified Parkinson's disease rating scale - Part III
<b>WU</b>	Weighted Undirected

# Chapter 1

## Introduction

We are surrounded by systems exhibiting complex behaviors that originate from the interactions between few autonomous individuals. Such complex behaviors exist at virtually all scales in nature [1], ranging from the molecular systems [2], the organization of the colonies of bacteria [3, 4], the foraging behavior of ants and bees [5], the organizational patterns of schools of fish [6] or flocks of birds [7] to the collective motion of human crowds [8]. Moreover, many of the man-made systems are also complex, such as the engineered robotic swarms [9], the internet [10, 11], the power grid [12] or the world wide web [13]. The need for the individual agents to organize in such complex systems arises mainly due to the realization that in many cases, the capabilities of a single individual are not enough to perform a particular task, e.g. to escape from a prey or to find food in the case of the schools of fish, or to support a large amount of electrical energy in the power grid. Therefore, it is necessary for individual elements to work together towards a common goal, which then makes the aim more achievable.

During this cooperative activity each agent would typically have a simple task and would only be aware only of its immediate surroundings without possessing any knowledge of the full picture [14]. For example, in a flock of starlings each bird interacts only with six to seven neighbors [15]; this configuration has been shown to optimize the integrity of the group while at the same time requiring

only minimal action from the individuals [16]. This behavior is also present in man-made systems, for example, in the case of the world wide web, one document would typically have links to only a small number of documents which in turn would link to few others. However, although one document have a small amount of links, the progressive action of reaching new documents at each step ensures that the world wide web is a connected system and every document present on the world wide web is reachable.

The above examples show that studying only a single agent in isolation cannot facilitate full understanding of complex systems. Instead, the interactions between agents are crucial to study the emergent behavior in the complex systems and learn how the actions of the individuals shape their behavior as a whole.

One way to accomplish this is to model such systems as networks, a set of nodes, representing the individual agents, and edges, quantifying the interactions between the nodes. Network science has a long history in its application to study complex systems, initially being used in the context of social networks as early as 1940s [17]. Networks continued to be used through the history in order to study the friendship patterns of people [18] or their business relations [19]. Additionally, network studies have been done for citation networks [20] (research papers and citations between them), for world wide web [21] (documents and URLs), for power-grids [12] (generators, transformers and substations, and transmission lines connecting them), airline networks [22] (airports and flights), telephone calls network [23] (phone numbers and telephone calls) or inter-banking networks [24] (banks and claims between banks). In addition to the above mentioned man-made systems, networks are also observed in nature, for example the network of interactions between proteins [25] (proteins and physical contacts between them), the metabolic pathways [26] (biomolecules and chemical reactions) or the food web [27] (species in an ecosystem and their trophic relationships).

Seeing that we have such a diverse set of systems that can be modeled by a single concept, the question arises of whether we are justified to take such approach to the study of complex systems. The answer to this question dates back to 1735 and the Euler's work to solve the Königsberg bridge puzzle; this is thought to

be the beginning of graph theory, the mathematical framework facilitating the analysis of complex networks. At that time, Königsberg was a capital of Eastern Prussia and was split into four different pieces of land by the river Pregel that passed through the city. Seven bridges were built around the city in order to connect the landmasses, prompting the question of whether one could visit all four landmasses by passing each bridge exactly once [28]. The rigorous proof that such path does not exist was presented by Euler [29]. Crucial to his proof was the realization that the landscape can be represented as a graph; each land becomes a node in this graph and an edge is drawn between two lands connected by a bridge. In this way, he showed that the details of the actual landscape do not need to be taken into account, instead it is only the topological properties of the underlying graph that are essential to solve the problem. This work of Euler is considered to be the first one concerning graphs and provided the basis to the field of graph theory that is at the core of the current methods to analyze complex networks.

Therefore, in a network analysis the real nature of the nodes and edges does not convey any crucial information about the network. The nodes can represent people, molecules, proteins or documents and the edges can represent any physical or abstract connection between them; the crucial realization is that all systems share similar patterns of organization. Therefore, many real networks can be represented by their underlying graph in which all relations are captured by the directions and weights of the edges between the nodes [30]. Then, using the tools of the graph theory this fundamental graph can be studied and various information about its topological structure can be obtained.

Complex networks can be characterized by a vast set of measures that serve to assess various properties of the network [31]. The measures can be nodal and convey information about the individual elements of the network, or they can be global, thus reflecting the properties of the complete network. Most of the measures have been derived for binary undirected networks, i.e. networks that have reciprocal relations and no weight assigned to an edge, for example the science collaboration network [32]. However, some measures have their counterparts for the case of weighted networks, e.g. network of mobile phone calls [33], and

directed networks, e.g. citation networks [34] (more detailed description of the network distinction based on the nature of the edges and the measures used to characterize such networks is presented in chapter 2). Moreover, on the basis of the type of information they provide about the functioning of the network, measures can be divided as measures of network segregation, network integration, and influence [31, 35].

Network segregation refers to the localization of the information in a network, indicated by the presence of separate, highly connected sub-networks or patterns of connections [31]. Network segregation can be quantified by the clustering coefficient, defined as the fraction of the neighbors of a given node that are also neighbors to each other; for example, in the context of social networks, clustering reveals how many of one's friends are also friends with each other. In simplest terms, clustering coefficient counts the fraction of triangles that exist around a node, which conveys information about the network robustness [36, 37]. While clustering is a nodal measure, it can be averaged over all nodes in the network to obtain the global clustering coefficient indicating the extent of segregation in the network. Network segregation can be also revealed by the occurrences of motifs, a particular way of connections between a group of nodes that can appear recurrently in a network [38]. Whether some specific sub-network patterns occur in the network more frequently than expected can be studied by comparing the number of motifs of given size in the network of interest to the number of motifs in a random network [39]. In addition to motifs, one can also identify communities in the network. Communities are described as sub-networks that consist of nodes having many more connections with nodes of the same community, when compared to the number of connections with nodes of other communities [40]. Calculating the community structure of a network can reveal an underlying organization or functioning in the network; e.g. in the case of world wide web, different communities might correspond to a set of documents on the same topic [41], or in the context of metabolic networks different communities could be built up from molecules performing similar functions [42].

Measures of network integration evaluate the extent to which nodes in the network can interact and share information between each other. This is most commonly

determined by the concept of shortest distance between two nodes, defined as the lowest number of edges that need to be crossed in order to reach one node from the other. In this context, lower distances between nodes are associated with good integration possibility between the nodes [31]. The shortest path length of a node is calculated as the average of the shortest distances between that node and all other nodes in the graph; lower path length of a node means that the node is well integrated within the network and can easily share information with other network nodes. One can also define the characteristic path length of a network as the average of all nodes' shortest path lengths. Then, the characteristic path length becomes a measure of the possibility of global interaction within that network. One major drawback of these measures is that paths cannot be meaningfully computed on disconnected networks (the shortest path length of a node is infinity if that node is disconnected). As a result, a new measure, the global efficiency [43], can be calculated for disconnected networks. The global efficiency for a node is calculated as the average of the inverses of the shortest distances between that node and all other nodes in the network, and as such, high global efficiency of a node implies higher degree of integration of that node. The global efficiency of the network is defined as the average of the individual global efficiencies and it has been argued that it could be considered as a better measure than the characteristic path length [44]. Both, the path length and the global efficiency, typically are dimensionless measures and they do not correspond to physical distance.

Just how important a node or an edge is to the structure of the network can be shown by various measures of influence. Most commonly, the importance of a node is expressed through its degree, i.e. the number of neighbors that the node has. The higher degree nodes are considered to be more influential in the network. By making a histogram of the degrees of all nodes in a network, one can obtain the degree distribution in that network; it has been shown that since different networks have different node distributions, networks can be distinguished and categorized based on these distributions [36]. Another measure of influence is the betweenness centrality, which counts how many shortest paths pass through a particular node or edge. This measure can be best interpreted in the context



of information flow. Since a node with high betweenness centrality is likely to be involved in many communication pathways, its removal will cause a disruption of the network and cause a decrease in the network's efficiency. The variations in the network efficiency can be captured by the measure of vulnerability. Vulnerability gauges the changes of the global efficiency of a network when a particular node is removed from the network; thus nodes with high vulnerability are considered to be central to the network [45]. The most important nodes in a network are collectively referred to as hubs. Hubs are integral to the integrity of working efficiency of a network, however, since currently there is no separate measure or a clearly defined way to designate certain nodes as hubs, a combination of the above measures are commonly used for their identification [46].

While the networks' properties can be very well characterized by calculating some of the described measures, to completely understand the behavior of the real networks it is crucial to understand the origin of such properties and how they affect each other. To this aim, many network models have been developed, each trying to mimic the behavior of real networks as close as possible [47, 48, 49, 50, 51, 52, 53, 54, 55, 56]. The first and simplest model studied was the random graph model, put forward by Erdős and Rényi in 1959 [47]. According to the random model, a network is built by connecting every pair of nodes in the network with a fixed probability  $p$ , which can take values between zero and one. Many of the properties of random networks have been mathematically demonstrated and it has been shown that they vary with the value of  $p$ . The main result for a random network is that its nodes' degrees follow Poisson distribution which is quite unlike the real networks which tend to have a power law distribution. The Poisson distribution also does not allow for the existence of hubs (most of the nodes in a random network have comparable degrees), which are very often found in the real networks. Moreover, the random networks do not exhibit a particular community structure, they have low path lengths and low clustering coefficient [57, 58]. Consequently, random networks can very well account for the fact that many nodes in the real networks are reachable by only few connections. However, beyond that, they are very poor model for the behavior of real networks. The main application of random networks is to provide a null model for the evaluation

of a given network property. Namely, if a network's property is not present in the random model, one can conclude that it cannot be explained by chance and it is an inherent property of that network, requiring an additional explanation [30].

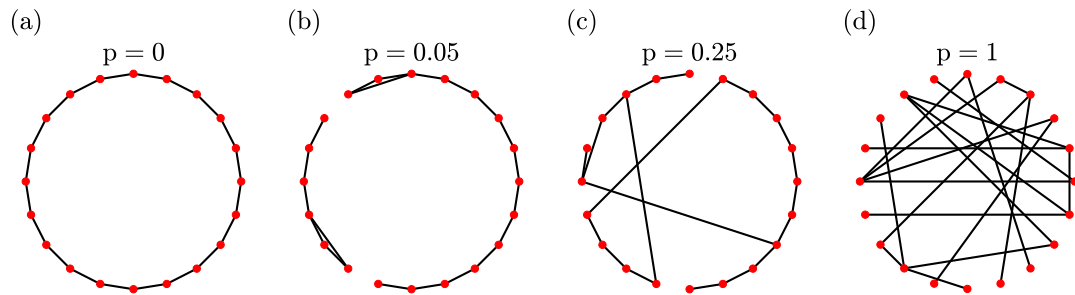


Figure 1.1: Watts–Strogatz model of small-world networks. One starts with a regular network in which all network nodes are placed on a ring lattice. Then, each edge is rewired with fixed probability  $p$ . Depending on this probability, one can interpolate between (a) regular network for  $p = 0$  and (d) random network for  $p = 1$ . For small intermediate values of  $p$  (b, c) one obtains small-world networks.

Watts and Strogatz proposed a model (figure 1.1) that was aimed to explain the high clustering and low path lengths present in the real networks [52]. The starting point of this model is to create a regular network, in which all network nodes are placed on a ring lattice and connected to their nearest  $k$  neighbors. Then, each edge of the network is rewired with a fixed probability  $p$ . This rewiring operation involves going through each edge of the network and then moving only one end of that edge to another node in the network chosen at random with probability  $p$ . Therefore, for  $p = 0$ , the network is a regular network that exhibits high clustering coefficient, but also high path lengths. On the contrary, for  $p = 1$  we obtain a random graph which has short path distances, but also a low clustering coefficient. However, Watts and Strogatz showed that between these two extremes, for small positive values of  $p$ , one can obtain "small-world" networks that have high clustering but low path lengths. The reason for this behavior is that the path length drops to low values even for very small  $p$ . Even if only few edges are rewired, this creates long-range edges between distant nodes that serve as shortcuts. As a result, as more edges are rewired more shortcuts appear in the network, thereby lowering the path length drastically. On the other hand, the rewiring of an edge from highly clustered community does not have a big effect on

the clustering coefficient. As a result, due to the fact that the path length lowers quicker to its value for the random graph when compared to the clustering coefficient, for small non-zero values of  $p$ , a network can have both low path length and high clustering [52]. Consequently, the Watts and Strogatz model is very good into predicting the coexistence of small-world behavior and high clustering present in many real networks. However, similar to the random graph model, networks built from this model also have Poisson degree distribution, therefore this model cannot explain the existence of hubs in real networks.

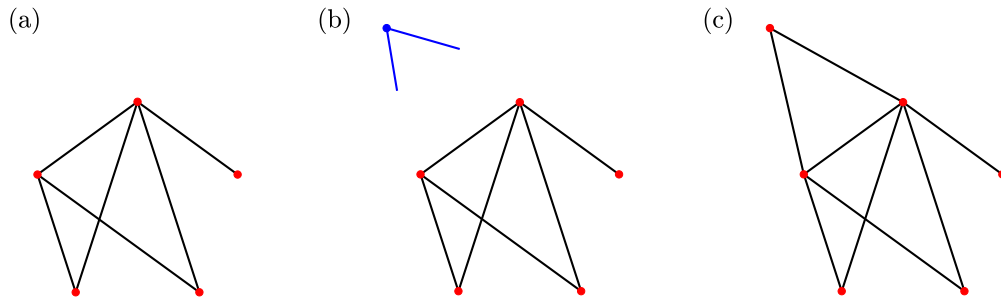


Figure 1.2: Barabási–Albert model of growing networks. The starting point of this model is a small network of few nodes (a). Then, a new node with fixed number of connections is added to the network (b). That node makes connections preferentially with the existing nodes that have high degrees (c) and thus becomes a part of the network. By repeatedly performing the preferential attachment mechanism in (b) and (c) the initial network grows in size and the nodes with high degree acquire new connections at much quicker rate than the ones with low degree.

Trying to explain the hubs and the power law degree distribution observed in real networks, Barabási and Albert [30, 56], inspired from the structure of the world wide web, proposed a model of growing networks (figure 1.2). Their model is based on the growth of a network by adding nodes that attach preferentially to the existing nodes with higher degrees. More specifically, the model starts with a small network. Then, at each step a new node is added to the network by making fixed number of connections with the existing nodes in the network. The probability of making a connection with a node is proportional to that of node’s degree in the network. Therefore, this model results in a network exhibiting the rich gets richer phenomenon, thereby favoring the nodes with high degrees that

have been present in the network early on. The networks resulting from this model are scale-free networks having a degree distribution following a power law with an exponent of three. This model is considered to be an important one when describing the real networks which also follow power law degree distribution, e.g. the internet or world wide web [59]. In an attempt to make this model more realistic, e.g. to obtain a flexible exponent in the power law or to improve the clustering behavior, many alterations to the original model were proposed in the literature, for example nonlinear preferential attachment [60].

The brain is one of the most complex systems, built up from approximately  $10^{11}$  neurons connected by  $10^{14}$  synapses organized in a three dimensional space by optimizing the wiring cost to get maximum flexibility [61]. The neurons are connected by a convoluted net of connections acting as a scaffold supporting the emerging complex dynamic patterns that are considered to shape cognition [62, 63]. While each nerve cell has a particular role to play in this behavior, cognition and other brain functions can only be observed when many neurons are linked together in small networks, subsequently combining to form larger and larger networks eventually building the whole nervous system, as illustrated in figure 1.3. Therefore, to gain insight into the brain functions, we would need to study the brain's complex networks at many levels, from small neuronal circuits to large-scale brain networks, in addition to studying the complex dynamic patterns that emerge from their collective behavior [64].

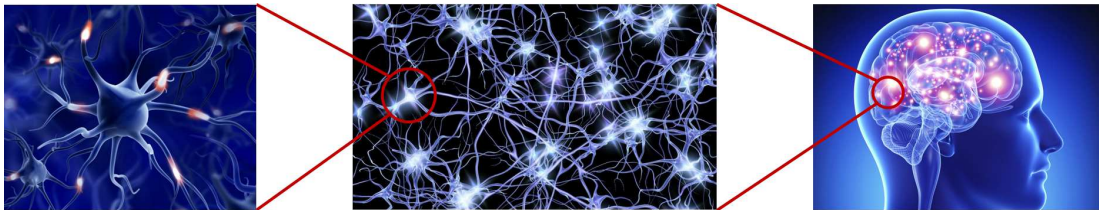


Figure 1.3: From a single neuron to brain. A neuron is the fundamental building block of the brain which can receive and process information. In order to pass information between each other, neurons combine through electrical and chemical synapses to form a network. Many neuronal networks combine into larger ones eventually forming the brain; all brain functions arise due to the collective behavior of this large number of neurons. Adapted from [65, 66, 67]

Representing the brain as a complex network and analyzing its underlying organization could reveal some information about the brain functioning. For example, the brain is made up of spatially distributed areas that have highly specified functions but are still able to communicate efficiently between each other. This illustrates the two basic organizational principles in the brain, functional segregation and functional integration, and they both can be characterized by calculating the appropriate measures on the brain networks as discussed above [68, 31]. Moreover, it has been shown that there is a lot of characteristic activity in the human brain even when the person is at rest [69, 70]. This dynamic activity during rest is supported by the underlying physical network of neurons; therefore investigating how the structural architecture shapes the resulting dynamic behavior could provide great insight into why such networks appear even at rest [64]. Finally, many neurodegenerative diseases or brain traumas can be related to a corresponding damage in the structural connectivity in the brain [71, 72]. Therefore, the quantification of some abnormal topological properties of brain networks present in patients when compared with healthy individuals, could be used as diagnostic markers in some diseases. In addition to the above examples, brain networks could be used to provide insight, for example, into the dynamic patterns that result from an external stimuli to the brain, and into the change of cognition abilities over time [64].

In the early beginnings of the neuroscience, the visual inspection of the anatomy of the brain by using techniques, like staining and sectioning the brain tissue, were the common way to obtain information about the brain's composition [73]. In fact, most of the early knowledge about the working principles of the neurons came by measuring electrophysiological recordings of single intact neurons. While such recordings do allow for direct measurements of the electrical properties of the neuron with high spatial and temporal resolution, the need for the intact brain tissue means that they are highly invasive techniques and could not be applied directly to humans [64]. In order to extract information about the human brain, there was a necessity for a non-invasive imaging technique that could produce large sets of data that could be subsequently analyzed. Electroencephalography (EEG) and magnetoencephalography (MEG) are the first such techniques to be

applied. They measure the fluctuations that occur due to neuronal currents by placing a series of sensors near the scalp. While they have high temporal resolution, they do not have good spatial resolution because they record electromagnetic potentials resulting from the collective currents of large populations of neurons. In addition, the reconstruction process to obtain the real sources responsible for these signals is ambiguous and depends highly on the statistical technique used to process the data [74]. Another frequently used noninvasive technique that helped in the expansion of the neuroscience research is functional magnetic resonance imaging (fMRI). Using the contrast derived from the differences in magnetic susceptibility of oxygenated and deoxygenated blood (shortly termed BOLD contrast where BOLD stands for "Blood Oxygenation Level Dependent") fMRI can measure metabolic activity in the brain. Thus, fMRI does not measure the electric currents (or neuronal activity) directly, rather it measures the changes that this activity causes in the blood flow and oxygenation [75]. The fMRI imaging has high spatial resolution (usually of the order of submillimeters in humans [76]) with temporal resolution of the order of seconds, which is partially due to the delayed response of the BOLD signal from the onset of the neural activity [77].

The main aim of the imaging techniques described above (fMRI and EEG) is to directly measure or infer the neuronal activity ongoing in the brain. In addition, there are few noninvasive techniques that are designed to characterize the structural connections between the neural cells. One of the most widely used technique is the Diffusion Tensor Imaging (DTI), in which the image contrast is obtained by using the anisotropic diffusion of water molecules inside the neural tissue. In particular, the macroscopic axons provide a strong orientational confinement for the water molecules; the easiest direction in which they can diffuse is the direction of the axon. One can reproduce the direction of preferential diffusion of the water molecules in each voxel by using a tensor model [78]. Commonly, a tractography is performed on these images in order to completely reconstruct the white matter paths followed by the diffused molecules of water [79].

Another technique to measure the structural connections is structural MRI, which can generate images that can differentiate between white and gray matter in the brain due to their different compositions. Using certain morphometric techniques

[80], the cortex can be parceled and one can calculate a measure of interest for each region, for example the thickness of the cerebral cortex. Thus, the connectivity between any two regions is estimated indirectly; the strength of their connection is given by the Pearson's correlation coefficient of the cortical thickness values for both regions, across a group of subjects. In contrast to the DTI imaging, by using the structural MRI method one cannot estimate the structural connections for a single subject.

Although there exist various imaging techniques, the building of complex networks from empirical data obtained from these techniques proceeds among few common steps [71]. The first step includes identification of the nodes of the network. The nodes in brain networks represent brain regions and they can be defined by some anatomical atlases in structural and functional MRI or by the position of the electrodes in EEG. This step is followed by the definition of the edges in the network. Each edge describes the degree of interaction between the two nodes it connects. Depending on the neuroimaging technique, edges can be derived in different ways. For example, in structural MRI edges are typically correlations between the cortical thickness values, however in functional MRI the edges are correlations between time series. After calculating the edge strengths for each pair of nodes in the network, these estimates are compiled into an adjacency matrix. Finally, some graph measures are calculated to characterize the network and their statistical significance is reported by comparing them to the measures derived from a set of random networks. It should be noted that each of this steps is essential in the analysis but there is not a unique way to execute them, i.e. some decisions are required at each step, for example one needs to choose a particular parcellation scheme for the brain. Therefore, each decision will influence the results obtained from this analysis; two brain networks can be meaningfully compared only if they have been derived from the same procedure [71].

The existence of many different neuroimaging techniques to capture different aspects of brain connectivity coupled with the plethora of computational methods to analyze the data, results in different ways to describe the networks in the brain. The first method is to build structural networks, defined as the physical web of connections between the different neurons. Then, we could also build

functional networks in the brain which describe the dynamic interactions, or functional correlations, of the neurons. Finally, effective connectivity, or the causal interactions between different neuronal elements, could be also examined.

Structural connectivity refers to the complex web of anatomical connections that link distinctive neuronal elements in the brain, termed as the connectome [81]. These structural connections exist in the brain on multiple scales, from networks of few neurons connected by synapses to brain regions connected by axonal projections. These networks are most frequently derived from DTI and structural MRI and they represent topological association patterns. However, it has been shown that there is a relation between the topological and physical distances in structural networks; the neurons in the proximity of each other have higher probability to be connected [71, 82]. Moreover, the structural networks are thought to be susceptible to change only on longer time scales (e.g. days) while remaining relatively stable on shorter time scales of the order of minutes [35].

Functional connectivity is defined as the statistical correlations between activity patterns produced from spatially distinctive neuronal populations [83, 84]. Functional connectivity data is extracted from functional MRI, EEG and MEG in the form of time series data. The pairwise coupling strengths are estimated by calculating a certain measure between the corresponding time series, such as correlation, coherence or mutual information [85]. As correlation does not necessary imply causation, functional networks do not convey information about the causal relation between its elements. Moreover, differently from structural networks, functional connectivity is very time dependent and also highly dependent on any external sensory input [35].

Effective connectivity aims to describe networks that reflect the influences that one neural system has on another [83, 84]. Effective connectivity is also time dependent and often it is inferred by modulating the neuronal activity by external stimuli or specific tasks. The effective networks are commonly derived by applying a particular model to the time series obtained from different neural elements, therefore the validity of the particular effective network depends highly on the validity of the modeling procedure [83]. One of the most commonly applied model



is the Granger causality [86, 87], which is based on the idea that in the interactions between two events, the cause will always occur earlier in time than the effect. For example, consider the direct causal relation between two regions, from A to B. The Granger causality assumes that in such case, events in A must always precede events in B. Moreover, this method quantifies how much information one has in order to make a prediction about the future values of B, by considering the past values of A. Therefore, Granger causality is fully based on the statistical behavior of the observed time series and does not make any explicit assumption about the structural connections between the neural elements. On the other hand, models such as Dynamic Causal Modeling (DCM) [88] and Structural Equation Modeling (SEM) [89] need *a priori* postulation of structural networks in order to infer the effective connectivity. As a result, they are not able to test many possible network arrangements; moreover DCM is designed only in the framework of task-related experiments since it requires the timings of the external stimuli as input.

What can these different connectivity types reveal about the organization of the brain? Small-world organization in the structural networks of the brain was reported by many studies using various imaging techniques, including correlation of cortical thickness in structural MRI [90] and diffusion weighted MRI [91]. The small-world organization manifests itself in the high clustering coefficients and low path lengths in these networks. These properties support the notion that the brain is organized in order to balance the anatomical and functional segregation (described by the high clustering coefficient as discussed above) with their integration on the global scale (manifested by the low path length). Furthermore, it was realized that the structural brain networks can be very well separated into distinct communities, thus explaining the origin of the high clustering coefficient [35]. The communities were found to consist of elements that have similar physiological responses, have more connections with elements of the same community and, in general, the structural communities form compact functional systems [92, 93]. The existence of separate communities with many densely connected elements is useful for the support of the functional segregation, by providing many connections for efficient communication of the specialized brain regions on

one hand, while restricting the information flow during the whole network by providing boundaries between these specialized regions on the other. Furthermore, it was shown that the communities communicate between them by making use of hubs [46], nodes that have very high degrees and betweenness centrality. Moreover, hubs are densely interconnected with each other [94] forming rich club organization that is mainly used to facilitate the information flow in the network [95, 96, 97].

Small-world properties have also been identified in functional networks with different measures estimating the functional connections [98, 99] and they have reported a power law degree distribution that is exponentially bounded [99]. It has also been shown that the functional networks exhibit significant modularity that can be used to explain their small-worldness [100] analogously to structural network studies. PET has been used to define the default functional network of the human brain at rest [101] and it has been shown the dynamics of a resting brain can be broken down into a small set of “resting-state networks” [35].

By studying complex networks in the brains of individuals with some neurodegenerative diseases and identifying the aberrations in their topological organizations one can obtain many insights about the particular disease [102]. This is possible because it has been postulated that the impairments in cognition that result from the disease occur due to the impact that the disease has on the arrangement of brain connectivity [103]. For example, it has been shown that the structural networks in patients with schizophrenia [104] have abnormal organization manifested by the increased connection distance and the loss of the hierarchical organization. Alterations of the small-world topology of the structural networks, measured as increased clustering and path lengths, were also detected in Alzheimer’s disease (AD) [105]; such findings were also reported for the corresponding functional networks derived from EEG [106]. Similar results were obtained from fMRI and MEG studies for AD [71], autism, epilepsy, multiple sclerosis, Parkinson’s disease [96, 97, 102]. Nonetheless, it should also be noted that while most studies present compelling evidence that neural disorders result in abnormal network organization in patients, a disparity between some results still remains. Therefore, such results need to be considered with caution as the particular findings may depend

on the clinical heterogeneity of the patient and control group as well as on the particular imaging and data analysis methods that were being used [71].

Although networks derived from different imaging modalities can reveal many important properties of the brain organization as outlined above, to get full understanding of the operation of the brain one needs to consider the relation between the structural architecture and the dynamic patterns that it promotes. There are many studies, derived from experimental observation or theoretical models, that strongly support the notion that physical links in the brain can shape neuronal dynamics [107]. In particular, having the information that the structural network has a small-world organization, one could infer that the expected functional connectivity would be manifested by many short-range interactions and smaller number of long-range interactions [63]. The relation between structure and function can be examined on many scales, for example by simulating neural circuits on the microscale or brain regions in the large scale brain networks. The most common method to assess this relation is to use a model that infers the functional connectivity from a structural substrate, and then matches the simulated dynamics with the empirically measured one [107]. Although this procedure will heavily depend on the computation models used to produce simulated functional data as well as the measures used to estimate the connection strengths in the empirical functional data, many studies converge to the conclusion that structure does shape function [107], however the inference of structural connectivity from functional data is less straightforward [108].

In this thesis, I will show that directed networks constructed in the brains of Alzheimer's and Parkinson's patients are more sensitive to the disease when compared to their undirected analogues. Moreover, I establish that the functional networks built by the standard correlation methods do not faithfully represent the underlying structural architecture. Instead, I will demonstrate, by using numerical simulations, that the underlying structure invariably introduces delays in the dynamic behavior of neurons and propose *the delayed correlation* method that utilizes these delays to identify up to 70% of the connections in the corresponding structural network. In order to carry out these analyses, we have

developed BRAPH–BRain Analysis using graPH theory, an object oriented Matlab software that can be used to perform connectivity analysis of brain networks derived by various imaging modalities. My thesis can be divided into two parts, background and application of graph theory to brain connectivity. In the first part, I will introduce the basic concepts of graph theory and the most commonly used measures to characterize the graphs (chapter 2). Then, in chapter 3, I will describe how to build the brain networks from data obtained by some common imaging modalities, before I present BRAPH and its functionalities in chapter 4. The second part of my thesis is concerned with the application of graph theory in brain connectivity studies. In particular, I will discuss the changes in the topological properties of undirected and directed brain networks (chapters 5 and 6 respectively) in Alzheimer’s and Parkinson’s patients, before demonstrating how temporal delays in the neuronal dynamics can help us to reconstruct neurons’ structural connections in chapter 7.

## Chapter 2

# Graph Theory Concepts

In the 1700s Königsberg was a capital of Eastern Prussia and a very important trading center. The city was built on the top of the river Pregel and the two banks of the river separated the city into four different pieces of land. In time, seven bridges were built around the city in order to connect the different landmasses, the resulting landscape had the look as shown in figure 2.1(a). This proved to be the start of a puzzle, with people wondering whether it was possible to visit all four landmasses by crossing every bridge exactly once. There were many attempts to find a solution by drawing all possible ways to cross the seven bridges, however a correct path could not be found [28].

The first rigorous proof that such path does not exist was provided by Euler [29]. He was able to show this by representing the whole landscape as a graph (figure 2.1(b)) in which each landmass is represented by a node and an edge is drawn between two nodes only if the corresponding landmasses are connected by a bridge. By inspecting the resulting graph, he was able to make the observation that if a path connecting all landmasses without passing twice by the same bridge exists, the only nodes with odd number of edges must be the ones corresponding to the starting and ending point of the path. If a node in the middle of the path has an odd number of connections  $2n + 1$ , then  $2n$  connections will be used to arrive to and leave from the node, therefore one connection will always be left

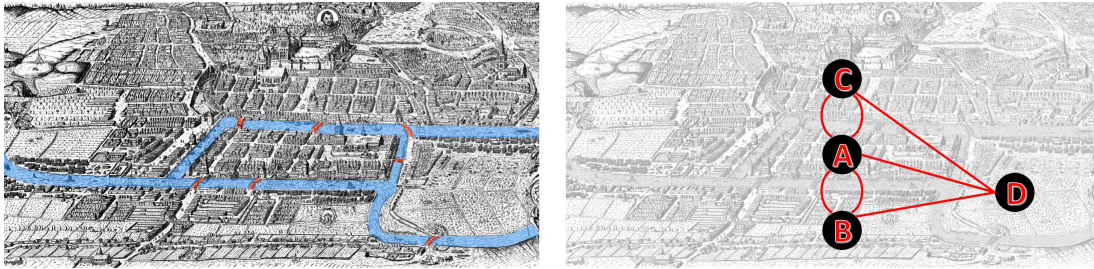


Figure 2.1: Königsberg’s bridges and the corresponding graph. (a) The two banks of the river Pregel (drawn in blue) split Königsberg into four different pieces of land that were connected by seven bridges (shown in red). (b) The corresponding graph of the city in which each landmass is represented by a node and connections between the landmasses are drawn if there is a bridge connecting them. Adapted from [109].

unused [30]. Since in the graph in figure 2.1(b) all four nodes have an odd number of connections, it leads to the conclusion that the required path cannot be found.

Euler’s work was important because he showed that in order to study a complex system, we do not require a complete knowledge of the properties of the system, for example the size of the landmasses or the length and curvature of the bridges. Instead, we could represent the complex system as a graph and we could gain all the relevant information about the system by studying only the topological properties of that graph.

In this chapter, I will give an overview of the measures that are most commonly used to characterize the properties of a graph. I first give a brief introduction to graphs and how they can be represented; then I discuss the different types of graphs that emerge from the different nature of their edges. Finally I present the definitions of some graph measures and explain the various techniques and algorithms that can be used to calculate them.

## 2.1 Graphs

A graph is composed of a collection of *nodes* that are linked by *edges*. An example of a sample graph is shown in figure 2.2(a) where each circle represents a node

and each line represents an edge. This illustration of a graph is very intuitive but it can become very tangled and convoluted as we increase the number of nodes and edges.

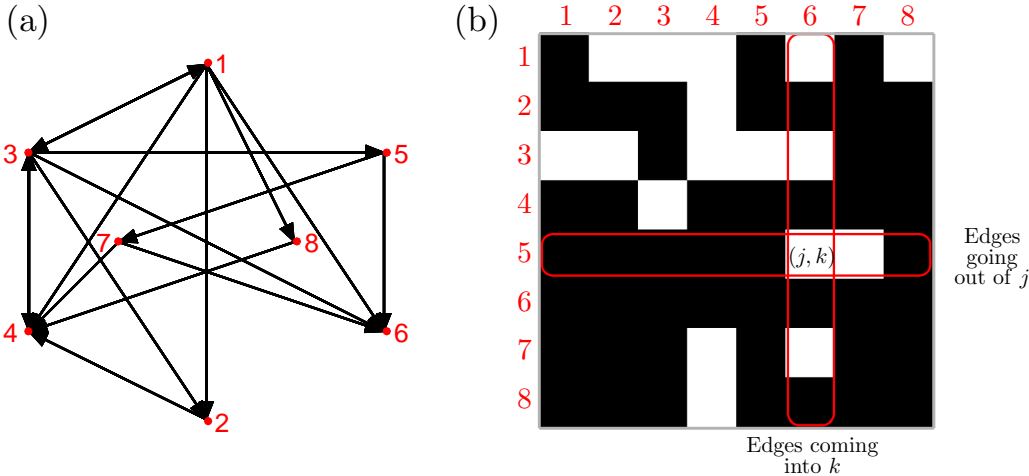


Figure 2.2: A simple graph and connectivity matrix. (a) An example of simple binary graph and (b) the adjacency matrix that corresponds to this graph.

Figure 2.2(b) shows that a graph can be instead described by compiling all nodes and edges in a matrix, called *adjacency matrix*. Each element of the matrix represents an edge between the corresponding nodes; for example, in figure 2.2(b), the element  $(j, k)$  represents the edge that goes from node  $j$  to node  $k$ . The *rows* of the adjacency matrix are regarded as edges that are going outwards from a node; for example, row  $j$  represents the edges that are going out from node  $j$ . On the contrary, each *column* depicts the edges that arrive inwards to a node; for example, all entries in column  $k$  show the edges that are arriving to the node  $k$ . The representation of graphs as adjacency matrices is appealing because this allows one to utilize highly-optimized algorithms that are based on linear algebra [110]. Moreover, it should be noted that the particular way in which nodes are ordered in the adjacency matrix does not affect the evaluation of the graph measures, but it only influences the graphical representation of the adjacency matrix.

## 2.2 Types of graphs

Each edge in a graph can be associated with a weight and direction, based on these characteristics of the edges, four types of graphs can be identified (figure 2.3):

- **Weighted directed (WD) graphs.** A real number that quantifies the *strength* of a connection is associated with each edge. The edges represent *direct* connections, i.e. a given node  $j$  can have a connection to node  $k$  without the need for the node  $k$  to be connected with node  $j$ ).
- **Weighted undirected (WU) graphs.** A real number that quantifies the *strength* of a connection is associated with each edge. The edges represent *undirect* connections, i.e. if a given node  $j$  has a connection to node  $k$ , then node  $k$  is also connected to node  $j$ . For these graphs, the adjacency matrix is symmetric.
- **Binary directed (BD) graphs.** The edges represent *directed* connections and can take values of 0 (in which case they represent the absence of a connection) or 1 (they represent the existence of a connection). In this type of graphs the *strength* of a connection is not quantified.
- **Binary undirected (BU) graphs.** The edges represent *undirected* connections and can take values of 0 (the absence of a connection) or 1 (the existence of a connection). In this type of graphs the *strength* of a connection is not quantified. Moreover, the adjacency matrix is symmetric.

Figure 2.3 shows that these four types of graphs are directly linked to each other, and a transformation between each graph type can be done in the following ways:

- **Weighted to binary.** A weighted graph can be transformed into a binary one by the process of *thresholding*. This process entails the specification of a threshold value and assigning a value of 1 to the edges that have strengths above this threshold and 0 to those edges that have strengths below the



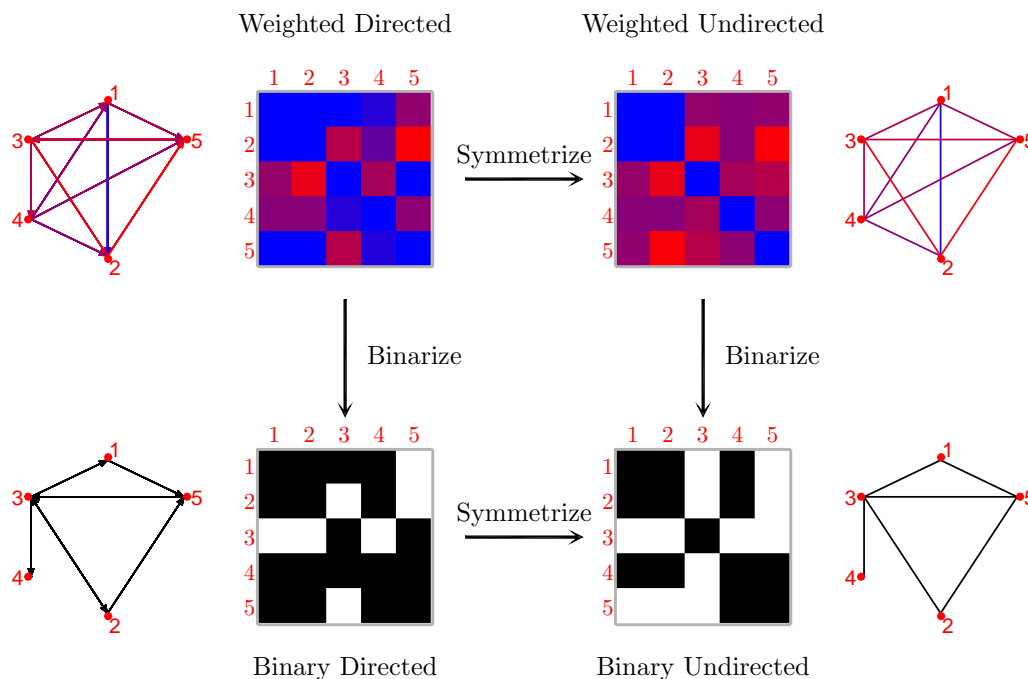


Figure 2.3: Graph types. Based on the nature of their edges, the graph can be classified as weighted or binary (according to the weights of the edges) or as directed or undirected (based of the directionality of the edges). By eliminating the information about the edges' directionality (i.e. symmetrization) one can convert a directed graph into an undirect one. Similarly, by removing the information about the edges' weights (i.e. thresholding) a weighted graph can be converted into a binary graph.

threshold. The threshold value can be identified a priori, or alternatively it can be determined as to ensure that the resulting graph has a certain density, i.e. the fraction of edges that are connected. The choice of the threshold is relevant in the comparison of binarized graphs, because such comparison is only meaningful when the two graphs are compared at fixed threshold or at fixed density.

- **Directed to undirected.** A directed graph can be transformed into an

undirected one by the process of *symmetrization*, which removes the information about the directions of the edges. This is accomplished by symmetrizing the adjacency matrix of the graph. Symmetrization can be performed along several possible directions, e.g.:

1. **Sum.** The adjacency matrix and its transpose are added to each other.
2. **Average.** Average of the adjacency matrix and its transpose.
3. **Minimum.** The adjacency matrix is compared to its transpose; for each element the smaller value of the two is used.
4. **Maximum.** The adjacency matrix is compared to its transpose; for each element the larger value of the two is used.

## 2.3 Graph measures

Two general categories can be used in order to classify the graph measures:

1. **global** measures refer to the properties of a graph as a whole, and therefore, the information they convey is captured by a single number for each graph;
2. **nodal** measures refer to the properties of each node in a graph, and therefore, they consist of a vector of numbers — one for each node of the graph.

In this section I will briefly discuss the most common graph measures. Most of the measures have been derived for binary and undirected graphs, however some of them have extensions or analogues for weighted or directed graphs. Therefore, for each measure, I will indicate to which kind of graph it belongs by denoting **W** (= weighted graphs) or **B** (= binary graphs), and **D** (= directed graphs) or **U** (= undirected graphs). If no particular letter is assigned to the measure, it means that the measure can be used in both cases.

### 2.3.1 Degree

**Degree** (nodal, BU) is defined as the total number of edges that are connected to a node. The **average degree** (global, BU) can be calculated as the average of the degrees of all nodes.

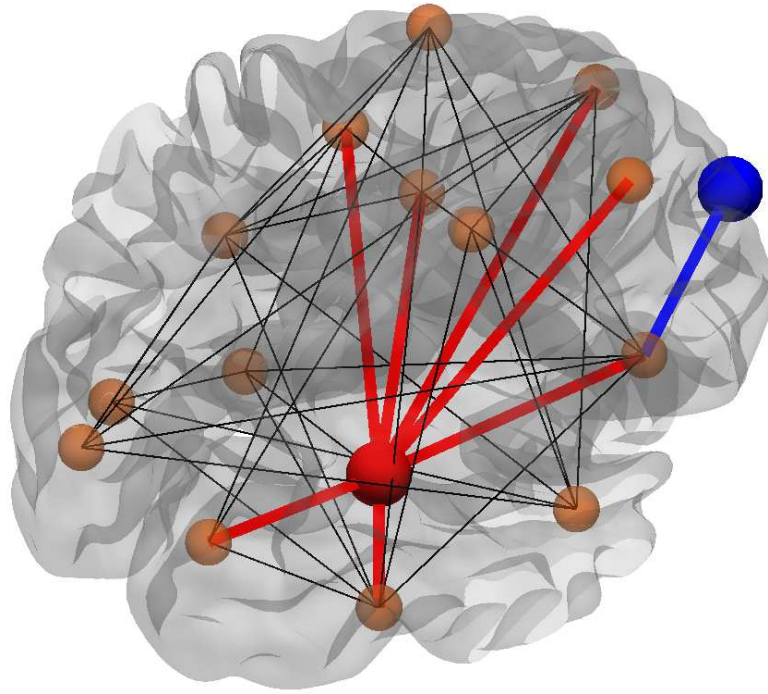


Figure 2.4: Degree of a node. The red is an example of a high degree node (i.e. it has a high number of neighbors), while the blue node possesses a low degree (i.e. it has a small number of neighbors).

**In-degree** (nodal, D) is defined as the total number of edges that are going inwards to a node. Its global extension is the **average in-degree** which is the average of the all nodes' in-degrees.

**Out-degree** (nodal, D) is defined as the total number of outward edges that originate from a node. Its global extension is the **average out-degree** defined as the average of all nodes' out-degrees.

**Methodological notes:** For BU graphs, the degree is given by the sum of the

number of edges across the rows or columns of the adjacency matrix. Since the adjacency matrix is symmetric for BU graphs, both calculations will yield the same result; in other words, for BU graphs, the in-degree and out-degree are equal. For BD graphs, a sum over the columns of the adjacency matrix gives the in-degree, while the out-degree is calculated as sum over the rows. In these graphs, the degree is the sum of in-degree and out-degree. For W graphs, the weights need to be ignored when the degree is calculated. Due to this reason, one needs to first binarize the adjacency matrix so that every edge that corresponds to non-zero weight is set to 1, while the rest remain as 0. Then, the degrees can be calculated on this binarized adjacency matrix analogous to the calculation for B graphs.

A property of a graph closely related to the degree is the **degree distribution**, denoted by  $p_K$ , which represents the probability that a node chosen at random has degree  $K$ . The degree distribution can be calculated as the histogram of the degrees of all nodes in the graph, normalized to 1.

### 2.3.2 Strength

**Strength** (nodal, WU) is defined as the sum of the weights of all edges connected to a node [111]. The **average strength** (global, WU) can be calculated as the average of the strengths of all nodes.

**In-strength** (nodal, WD) is defined as the sum of the weights of all edges that are going inwards to a node. Its global extension is the **average in-strength** which is the average of the all nodes' in-strengths.

**Out-strength** (nodal, WD) is defined as the sum of the weights of all outward edges that originate from a node. Its global extension is the **average out-strength** defined as the average of all nodes' out-strengths.

**Methodological notes:** For WU graphs, the sum over either rows or columns of the weighted adjacency matrix gives the strength of each node. For WD graphs,

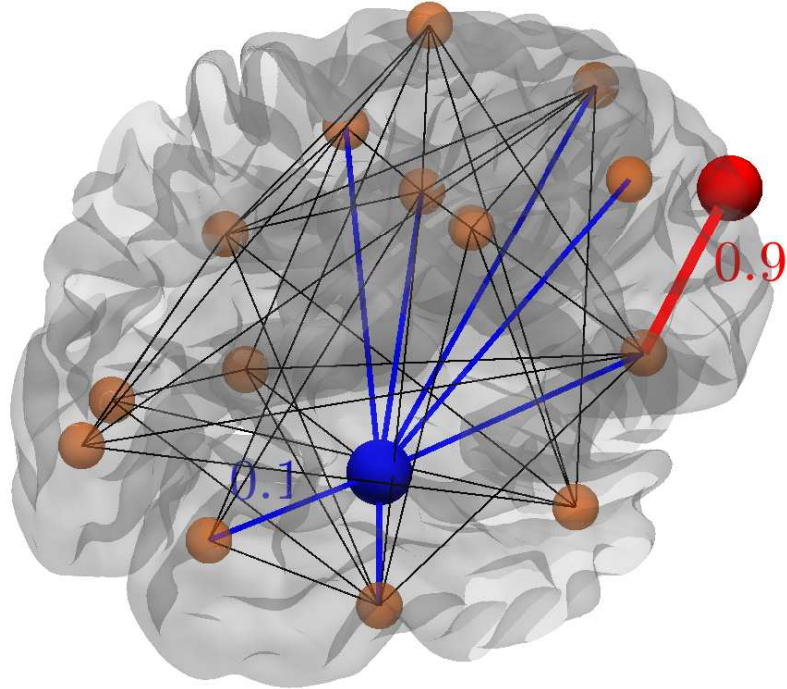


Figure 2.5: Strength of a node. Even though the red node has a low degree, it possesses a higher strength (there is only one connection that has a very high strength of 0.9), while the blue node has a higher degree but smaller strength (although it has 7 connections, each has low strength of only 0.1).

out-strengths are calculated as sums over rows, in-strengths are calculated as sums over columns; the strengths are defined as the sum of the in-strengths and out-strengths.

### 2.3.3 Eccentricity

**Eccentricity** (nodal) is defined as the maximal distance between a given node and any other node in the graph [112]. The global version is the **average eccentricity** that can be calculated as the average of the eccentricities of all nodes.

**In-eccentricity** (nodal,  $D$ ) can be calculated as the maximum of the incoming distances from all other nodes to a given node. Its global extension is the **average**

**in-eccentricity** which is the average of the all nodes' in-eccentricities.

**Out-eccentricity** (nodal,  $D$ ) can be calculated as the maximum of the outgoing distances from a given node to all other nodes. Its global extension is the **average out-eccentricity** which is the average of the all nodes' out-eccentricities.

Two other global measures can be specified once we know all nodes' eccentricities. The first one is the **radius** of the graph which is defined as the minimum eccentricity of all nodes. One can also define the **diameter** of a graph and calculate it as the maximum eccentricity of all nodes.

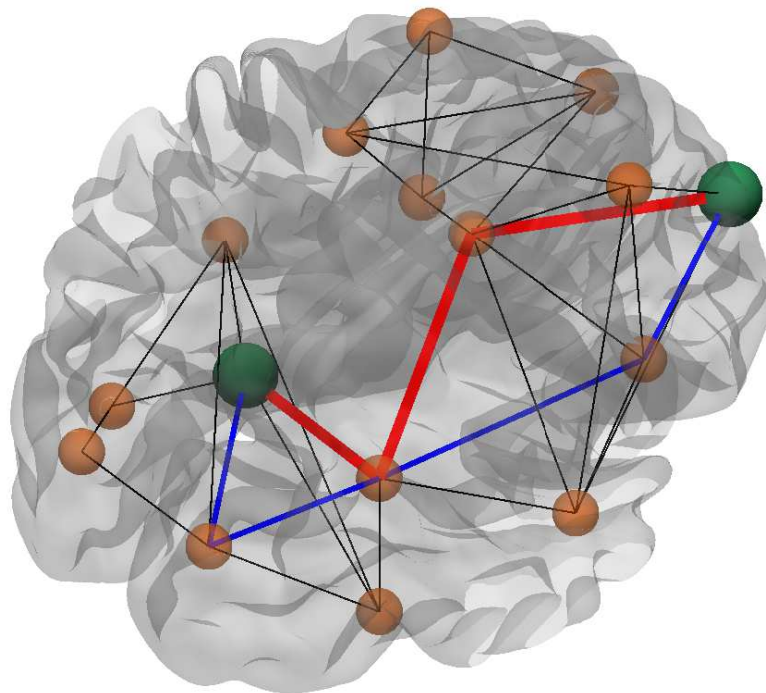


Figure 2.6: Distance between nodes. While there exist many paths between the two green nodes (e.g. the red and blue paths), the distance between the two is defined as the shortest possible path between them (the red path).

**Methodological notes:** For every graph, one can calculate a distance matrix; the elements of this matrix are the distances (the shortest path lengths) between all pairs of nodes in the graph. Then, the eccentricity of a given node is taken to be the maximum of all the distances that are calculated for this node. For  $D$

graphs, the in-eccentricity can be calculated along the columns of the distance matrix, while the rows of the distance matrix specify the out-eccentricity. In this case, the eccentricity of a node is the larger value of its in- and out-eccentricities. The shortest path lengths are not defined for disconnected nodes, therefore in most calculations, the eccentricity for those nodes is commonly taken to be NaN.

### 2.3.4 Path length

**Path length** (nodal) is the average of the distances between a given node and all other nodes in the graph. **Characteristic path length** is its global analog defined as the average of the shortest path lengths of all nodes.

**In-path length** (nodal, D) is calculated as the average of the distances between a given node and all other nodes in the graph calculated over paths that arrive inwards to that node. Its global extension is the **characteristic in-path length** which is the average of the in-path lengths of all nodes.

**Out-path length** (nodal, D) can be calculated as the average of the distances between a given node and all other nodes in the graph calculated over paths that leave outwards from that node. Its global extension is the **characteristic out-path length** which is the average of the out-path lengths of all nodes.

**Methodological notes:** There are many paths that can be used to reach one node from another. The distance between any two nodes is given by the length of the shortest path among all existing paths between those nodes (figure 2.6). For any B graph, the length of a path is defined as the number of edges that need to be crossed so that one node can be reached from the other (due to the fact that each edge has a length of 1). For a W graph, each edge has a length which is a function of its weight; commonly it is assumed that the length of an edge is inversely proportional to its weight. This is due to the fact that a high weight implies a strong connection which in turn can be interpreted as a short length [31]. Therefore, the distance between two nodes in a W graph is defined as the total length of the edges that need to be crossed in order to reach one starting

from the other. For D graphs, the resulting path length of a node is taken as an average of its in- and out-path lengths. On B graphs the shortest path lengths can be found by a *breadth-first search*, while on W graphs the *Dijkstra's algorithm* is used [110].

### 2.3.5 Triangles

**Triangles** (nodal) specify the number of neighbors of a node that are also connected with each other [113, 114].

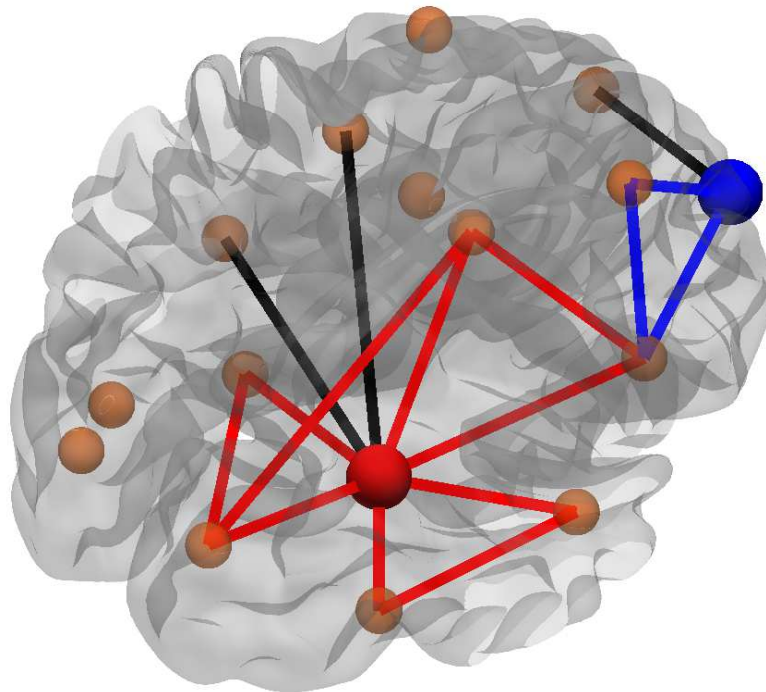


Figure 2.7: Triangles around a node. The red node is an example of a node with high number of triangles around it (because the black edges do not have any connections between themselves, only the red edges contribute to the triangles calculation). On the other hand, the blue node has very low number of triangles (the blue edges form only one triangle).

**Methodological notes:** For BU graphs, the number of triangles around each



node is given by the diagonal entries of  $A^3$  divided by two, where  $A$  is the adjacency matrix of that graph. In the case of WU graph, the contribution of a triangle around a node is defined to be the geometric mean of the weights of the edges that form that triangle. This contribution is calculated by taking each element of  $A$  to the power of  $1/3$ , thus resulting in a new matrix,  $A_{1/3}$ . Then, the collective contribution of all triangles around each node are given by the diagonal entries of  $A_{1/3}^3$  divided by two. For D graphs, a triangle can be defined in eight ways (each convention depends on how restrictive one is with the directions of the edges). The most restrictive way to define a triangle is to impose the constraint that the directed edges between the nodes that are part of the triangle form a closed circle, i.e. each node has one incoming and one outgoing edge.

### 2.3.6 Clustering coefficient

**Clustering coefficient** (nodal) calculates the fraction of triangles that are present around a node [52]. The global **clustering coefficient** is the average of the clustering coefficients of all nodes in the graph.

**Methodological notes:** The clustering coefficient of a node is the ratio of the numbers of triangles (see section 2.3.5) to the maximum number of triangles that could be formed around that node. For the U graphs, considering  $d$  to denote the degree of a node, the maximum number of triangles is given by the equation  $\frac{1}{2}d(d-1)$ . For D graphs, assuming that a triangle is formed only if the directed edges between any three nodes form a complete cycle, the total number of triangles can be calculated as  $d_{in} * d_{out} - d_{ii}$ . In this equation,  $d_{in}$  and  $d_{out}$  denote the in-degree and out-degree of the node,  $d_{ii}$  is the reciprocal connections that cannot result in a triangle (i.e. they denote two nodes that are mutually connected with two edges in both directions).

### 2.3.7 Transitivity

**Transitivity** (global) is considered as an alternative to the *global clustering coefficient*. It is defined as the ratio of the total number of triangles to the number of triplets in the graph.

**Methodological notes:** If  $N_{\text{triangles}}$  represents the total number of triangles in the graph and  $N_{\text{triplets}}$  denotes the total number of triplets, then the transitivity is given by the ratio  $3N_{\text{triangles}}/N_{\text{triplets}}$ .  $N_{\text{triplets}}$  can be calculated as  $N_{\text{triplets}} = \sum_i d_i(d_i - 1) - d_{ii}$ , where  $d_i$  is the degree of each node,  $d_{ii}$  denotes the pairs that do not result in triangles and the sum is done over all nodes in the graph [115].

### 2.3.8 Closeness centrality

**Closeness centrality** (nodal) is evaluated as the inverse of the calculated path length of a node.

**In-closeness centrality** (nodal, D) is defined as the inverse of the the in-path length of a node. **Out-closeness centrality** (nodal, D) is the inverse of the node's out-path length.

**Methodological notes:** See section 2.3.4 for the calculation of the path length.

### 2.3.9 Betweenness centrality

**Betweenness centrality** (nodal) is defined as the fraction of all shortest paths that include a given node. The nodes that have high betweenness centrality take part in many short paths and can be considered essential to the information flow in the graph.

**Methodological notes:** Betweenness centrality can be calculated by an algorithm that was discussed by Kintali [116].

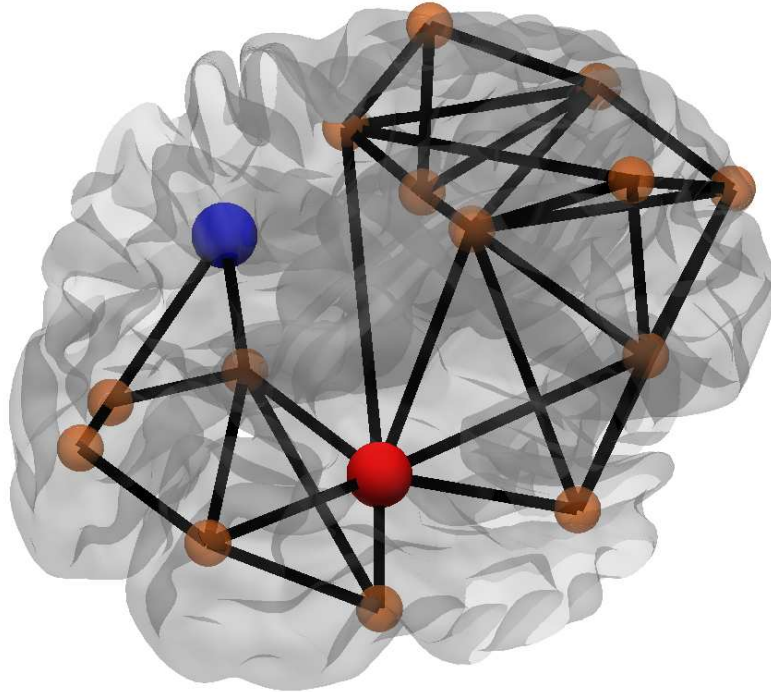


Figure 2.8: Betweenness centrality of a node. Since there exist many shortest paths that pass through the red node (e.g. paths going from left to right), this node has a high betweenness centrality. The blue node is characterized by a low betweenness centrality because there is no shortest path that passes through it.

### 2.3.10 Global efficiency

**Global efficiency** (nodal) is calculated as the average of the inverse of the distances from a node to all other nodes in the graph [43]. Its global analogue is calculated as the average of the global efficiency of all nodes in the graph.

**In-global efficiency** (nodal,  $D$ ) it is defined as the average of the inverse of the in-distances between a given node and all other nodes in the graph. On the other hand, the **out-global efficiency** (nodal,  $D$ ) is calculated as the average of the inverse of the out-distances between a given node and all other nodes in the graph.

**Methodological notes:** See section 2.3.4 for the definition of a distance and

how the path lengths are calculated between any two nodes. After the calculation of the path lengths between a given node and all other nodes in the graph, they are inverted. The average of the resulting values is equal to the global efficiency of the particular node. For D graphs, the global efficiency of a node is the average of its in- and out-global efficiencies.

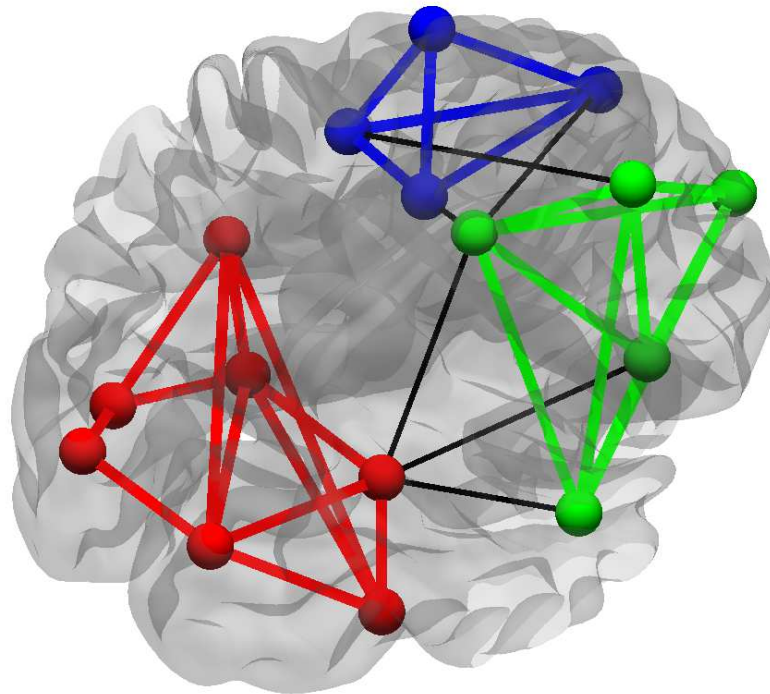


Figure 2.9: High modularity. This graph can be clearly separated into 3 communities each one having a much higher number of within-community connections when compared to the between-community connections.

### 2.3.11 Local efficiency

**Local efficiency** (nodal) is defined as the global efficiency calculated based on the node's local surrounding instead of the whole graph. The local surroundings of a node is the subgraph created by the node and its neighbors. Its global analogue is calculated as the average of the local efficiency of all nodes in the graph.

**Methodological notes:** The calculation of global efficiency is discussed in section 2.3.10. The calculation of the local efficiency proceeds along the same steps, however instead of applying them on the whole graph, they are applied on the subgraph formed by the node and its neighbors. For W graphs, the weighted connections of the neighbors of node  $i$  are defined as  $d_{jk}^{\text{subgraph}} = d_{jk} \sqrt{d_{ij} d_{ik}}$ . The labels  $j$  and  $k$  refer to two nodes that are neighbors of  $i$ , and the weights of each corresponding edge are given by  $d_{ij}$ ,  $d_{ik}$  and  $d_{jk}$ .

### 2.3.12 Modularity

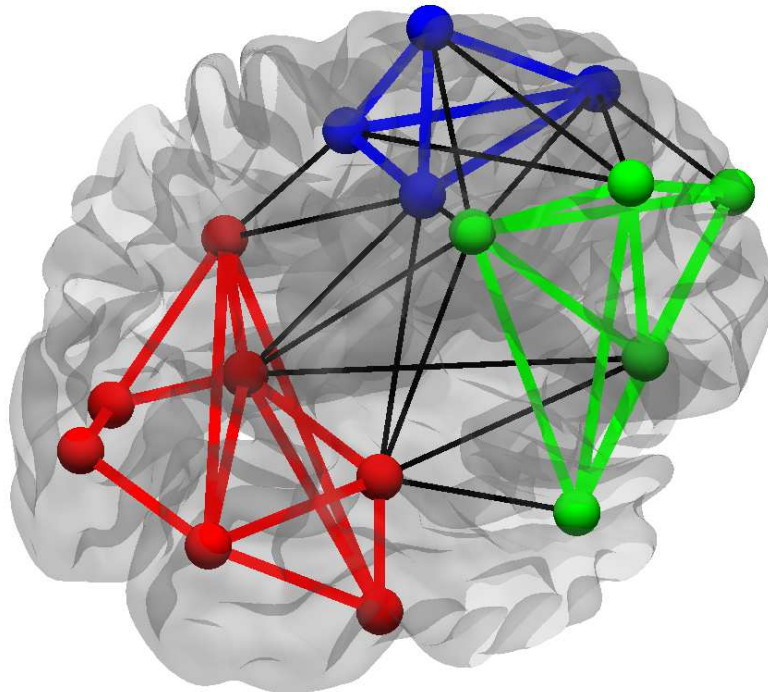


Figure 2.10: Low modularity. This graph corresponds to the graph plotted in Figure 2.9 with some extra between-community connections added. The graph can no longer be clearly separated into a collection of communities.

**Modularity** (global) quantifies the level to which a particular graph can be divided into communities (in other words subgraphs or modules) that are clearly separated. The modularity can be calculated only after the community structure

of the graph has been determined.

**Methodological notes:** The modularity is calculated as

$$\frac{1}{l} \sum_{ij} \left[ A_{ij} - \frac{k_i k_j}{l} \right] \delta_{ij}$$

where the sum is performed over all pairs of nodes in the graph,  $A_{ij}$  and  $l$  are the adjacency matrix and the total number of edges respectively,  $k_i$  and  $k_j$  are the degrees of node  $i$  and  $j$  and  $\delta_{ij}$  is a delta function specifying whether the nodes  $i$  and  $j$  belong to the same community (1 if they are and 0 if they are not).

### 2.3.13 Within-module z-score

**Within-module z-score** (nodal) reflects the level of connection of a node with the other nodes in the same community. It can be considered as a version of the degree calculated within-community. The calculation of z-score requires a previously calculated community structure.

**Within-module in-z-score** (nodal, D) is evaluated by considering only the contributions from the in-degrees of the node. **Within-module out-z-score** (nodal,D) is evaluated by considering only the contributions from the out-degrees of the node.

**Methodological notes:** The z-score for a node  $i$  belonging to the community  $S_i$  is evaluated as

$$Z_i = \frac{K_i - K_{S_i}}{\sigma_{S_i}}$$

where  $K_i$  is the degree of the node  $i$  when only within community connections are considered;  $K_{S_i}$  is the average degree of all nodes that belong in the community  $S_i$  and  $\sigma_{S_i}$  is the standard deviation of the degrees of the nodes that belong to the community  $S_i$ .

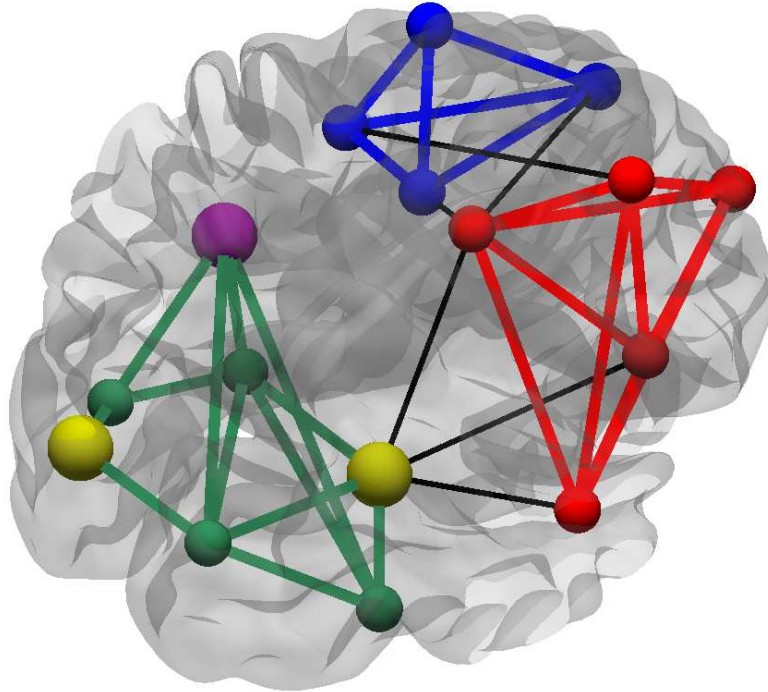


Figure 2.11: Within-module z-score of a node. A low z-score can result from a low degree (leftmost yellow node) or because of a high number of between-community connections (rightmost yellow node). Nodes that have lots of connections with nodes in the same community have high z-score (violet node).

### 2.3.14 Participation coefficient

**Participation coefficient** (nodal) shows how much connected a node is to various communities by comparing the between-communities connections of that node to its total number of connections. The calculation of this coefficient needs to have a previously determined community structure.

**Methodological notes:** The participation coefficient for a node  $i$  belonging to the community  $S_i$  can be calculated as

$$P_i = 1 - \sum_s \left( \frac{K_{S_i}}{K_i} \right)^2$$

where  $K_{S_i}$  denotes the number of edges that connect  $i$  with other nodes in the community  $S_i$ ,  $K_i$  is the total number of edges of node  $i$  and the sum is run over

all communities. High participation coefficient means that the node is connected to many communities. Such nodes could be facilitating global inter-modular interaction and are known as connector hubs.

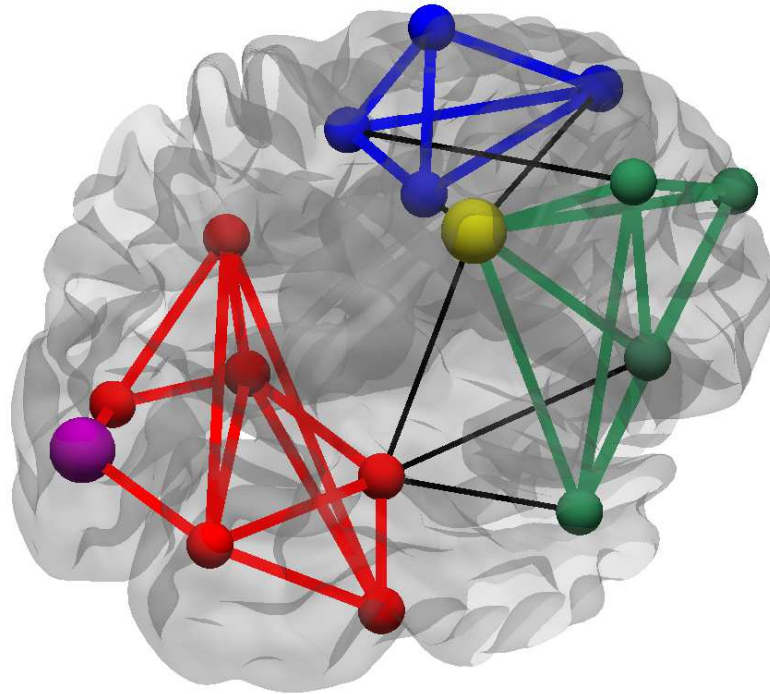


Figure 2.12: Participation coefficient of a node. A node with a low participation coefficient will have most of its connections with nodes belonging to the same community (violet node). The node will have a high participation coefficient if it makes a lot of its connections with nodes in different communities (yellow node).

### 2.3.15 Assortativity coefficient

**Assortativity coefficient** (global) is defined as the correlation coefficient between the degrees or strengths of all nodes that are on the two opposite ends of an edge [117]. In other words, this coefficient reflects the probability with which nodes tend to connect with other nodes that have similar degrees or strengths.



**Methodological notes:** The assortativity is calculated as

$$r = \frac{l^{-1} \sum_{i,j \in L} k_i k_j - [l^{-1} \sum_{i,j \in L} \frac{1}{2}(k_i + k_j)]^2}{l^{-1} \sum_{i,j \in L} \frac{1}{2}(k_i^2 + k_j^2) - [l^{-1} \sum_{i,j \in L} \frac{1}{2}(k_i + k_j)]^2}$$

where nodes  $i$  and  $j$  have degrees  $k_i$  and  $k_j$ , and  $l$  is the total number of edges in the graph. In the case of D and W graphs, the corresponding coefficient could be calculated by using the directed or weighted extensions for the nodal degree. A positive assortativity would mean that, on average, high degree nodes would prefer to connect to other nodes with high degree, while the negative assortativity means that nodes with high degree tend to connect with nodes of low degree.

### 2.3.16 Small-worldness

**Small-worldness** (global): A graph has the small-world property if it has a characteristic path length that is similar to the one observed in random graphs that have the same degree distribution, but has a significantly higher clustering coefficient (similar to the one observed for regular graphs) [52, 118].

**Methodological notes:** The small-worldness coefficient is calculated as

$$C_{\text{sw}} = \frac{C/C_{\text{rnd}}}{L/L_{\text{rnd}}}$$

where  $C$  and  $L$  denote the clustering coefficient and the characteristic path length of the graph.  $C_{\text{rnd}}$  and  $L_{\text{rnd}}$  represent the corresponding measures when calculated on random graphs; typically they are calculated as averages over 100 random graphs. If  $C_{\text{sw}} \gg 1$ , then the network has a small-world organization.

## Chapter 3

# Building the Networks of the Brain

The first step to carry out a brain connectivity analysis is to acquire some information about the *brain adjacency matrix*. To this end, the brain is segregated into multiple regions (typically the number of regions is between 50 and 1000) and then the strength of connections between all pairs of regions is measured. The particular method used to characterize this strength depends on the neuroimaging technique that is used to acquire the data. Most commonly, there are two wide categories of data that are used:

1. **Structural data** can be acquired by magnetic resonance imaging (MRI) or imaging **glucose metabolism data** by static positron emission tomography (PET). Once an image of the brain has been obtained for each subject in the group, a value (for example, cortical thickness, gray matter volume, glucose metabolism) can be extracted for each brain region of the corresponding subject. Then, the strength of the connection between two regions is calculated as the correlation of the values of the corresponding regions *across a group of subjects*. A possible justification for this process is the assumption that regions with strong connections will tend to show similar morphological qualities, for example they might grow or shrink together.

Therefore, for the structural data, one obtains a *single* brain adjacency matrix for a given group of subjects.

2. **Functional data** can be obtained by functional magnetic resonance imaging (fMRI) or electroencephalography measurements (EEG). These functional neuroimaging techniques provide a sequence of images for each subject, therefore each brain region is associated with a time series that measures its activation profile over time. The connection strength between two regions is calculated as the correlation between their corresponding time activation series. A possible justification for this process is that the regions with strong connections will show similar functional activity, for example they might activate or deactivate together. Therefore, for the functional data, one obtains an *individual* brain adjacency matrix for each subject.

In this chapter, I will discuss in more detail how to build the connectivity network of the brain from structural and functional data. I will first briefly describe the working principles of the relevant neuroimaging methods. Then, I will outline the general workflow that should be followed in order to perform a brain connectivity analysis, and explain the definitions of the nodes and the edges of the adjacency matrix as well as the statistical comparisons that can be performed between two groups in order to check whether the obtained results are genuine.

### 3.1 Imaging methods

Structural and functional data can be derived from various imaging techniques, ranging from diffusion MRI and DTI for structural data, to functional MRI, EEG or MEG for functional data. However, since the results presented in the following chapters are exclusively derived from structural and functional MRI, these two techniques will be the only ones I focus on.

### 3.1.1 MRI

The basis of the Magnetic Resonance Imaging (MRI) [119] is to make use of the magnetic properties of the atomic nuclei that are present in the brain tissue. One of the most abundant atoms present in the brain is  $^1\text{H}$  and as such, it is the element most frequently used for the purposes of MRI. Due to its unpaired proton,  $^1\text{H}$  has a net spin, hence it has a magnetic moment. However, in normal conditions, all magnetic moments are oriented randomly in the body, so that a net magnetization is not observed.

Taking an MRI image of a person entails placing that person in an external homogeneous magnetic field,  $B_0$ . In these conditions, all  $^1\text{H}$ s in the body will tend to align with the magnetic field, either parallel or anti-parallel. An excess of nuclei will align parallel to field, thus giving rise to a net magnetization,  $M_0$ , in the same direction as the external field. This alignment is not static, instead each nuclei precesses around the direction of  $B_0$  with a specific frequency, called *Larmor frequency*. This frequency is directly proportional to  $B_0$  and the constant of proportionality, called gyromagnetic ratio, is specific to each nucleus.

What makes MRI possible is the realization that the precessing nuclei can be excited by a radio-frequency (RF) pulse emitted perpendicularly to  $B_0$  and having exactly the Larmor frequency. In this case, some nuclei absorb the energy of the RF wave and change from low to high energy state. This, coupled with the fact that all nuclei start precessing in phase, results in the tilting of the direction of the net magnetization to be perpendicular to  $B_0$ .

Upon the removal of the external RF signal, the nuclei relax and return to their initial positions, emitting a RF signal of their own in the process. This *free-induction decay* (FID) signal can be detected by a receiver coil and the processing of this signal results in the MRI image. This above discussed sequence of events that results in an MRI image is illustrated in figure 3.1.

In order to be able to use this signal to create images, its origin needs to be encoded for each dimension. In particular, in order to choose an axial slice in

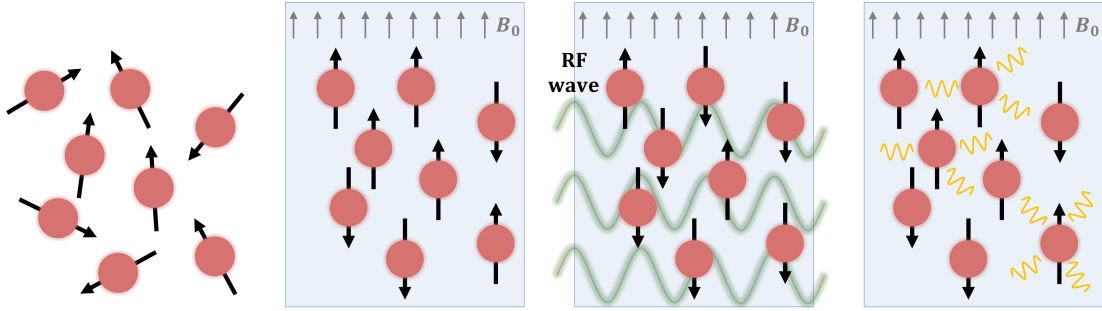


Figure 3.1: Workflow of MRI imaging procedure. MRI makes use of atomic nuclei that possess a magnetic moment. However, in normal conditions, all moments are oriented randomly and there is no net magnetization. After the application of an external magnetic field, an excess amount of atoms align parallel to the field, in their low-energy state. When perpendicular RF pulses at the right frequency are applied, the magnetic moments absorb their energy and are able to move to the high-energy state. After turning off the external RF pulses, the moments can relax, emitting FID signal in the process that can be subsequently used to produce the MRI images.

the direction of  $B_0$ , one additionally adds a gradient magnetic field in the same direction. This subjects the nuclei present in each slice along this gradient to slightly different magnetic fields, forcing them to precess at different frequencies. In turn, this means that by sending RF waves of different frequencies different nuclei can be selectively excited.

Since each axial slice is two dimensional, the x and y position within that slice need to be encoded. This is done by specifying the frequency and phase of each voxel; the y direction is commonly determined by phase, while the x is specified by frequency. For each frequency-phase pair then a 2D Fourier transform is used in order to translate them into the spatial domain.

The MRI contrast in single voxel will primarily depend on the density of atomic nuclei present in that voxel. In addition, the contrast can be also obtained based on two relaxation processes in the nuclei: the longitudinal or spin-lattice relaxation characterized by a relaxation time  $T_1$  and the transverse or spin-spin relaxation characterized by  $T_2$ . As discussed before, with the RF pulses switched on, the net magnetization is tilted perpendicularly to the constant magnetic field.

Once these pulses are switched off, as the nuclei return to their original configuration, the net magnetization in the axial direction will also slowly return to its initial value  $M_0$ . The time constant of this process is given by  $T_1$ ; in other words,  $T_1$  is the time at which the axial magnetization returns to 63% of  $M_0$ . The relaxing process of the nuclei can be also characterized by the loss of the transverse magnetization. This most commonly happens because of the dephasing of the spins' precession; one reason is the differences of the magnetic field at the position of each spin. This decay in the transverse magnetization is characterized by the time constant  $T_2$ .

One can choose between  $T_1$  and  $T_2$  weighted MRI images by adjusting the rate of the RF pulses (i.e. the repetition time, TR) and the time that elapses between the application of the RF pulse to the time of measurement (the echo delay time, TE). By adjusting both TR and TE, one could generate different pulse sequences that can be used to produce contrast between different tissue types.

In particular, the MRI can be used to contrast the structure of white and grey matter in the brain. Gray matter consists mostly of cell bodies, while the white matter contains mostly of long nerve fibers. Therefore, the MRI signals of the two are very different and they can be contrasted by taking into the account the different relaxation times of the protons that are present in both tissues.

### 3.1.2 Functional MRI

The functional MRI [77] is based on the same underlying principles explained in the previous section with its contrast derived from the different magnetic properties of oxygenated and deoxygenated blood, commonly termed as blood-oxygen-level dependent (BOLD) contrast. This contrast can occur locally, around the brain regions that are activated when some cognitive task is performed.

Upon such task, there is an increased energy requirement in the activated region due to the larger number of signaling and processing events, which leads to a locally increased oxygen consumption accompanied by a dilation of the vesicles.

This results in intensified oxygen rich blood flow to that area in order to counteract the need for more oxygen. However, these two processes do not cancel each other out, and the net result is the *oversupply* of oxygen rich blood around the activated region.

This phenomenon can be used to take fMRI images because the hemoglobin present in the blood has *different magnetic properties* under different circumstances. In particular, the oxygenated hemoglobin is a very weakly diamagnetic material with no effects on the external magnetic field while the deoxygenated hemoglobin is paramagnetic and slightly affects the field; a decrease in the concentration of the deoxyhemoglobin is accompanied by an increase in the signal.

Therefore, the activation of a particular region in the brain is accompanied by a decrease in the deoxygenated hemoglobin concentration, which can in turn result in local gradients in the magnetic field due to its paramagnetic nature. As discussed in section 3.1.1, such inhomogeneities in the magnetic field can alter the dephasing of the nuclear spins, i.e. they can modify the  $T_2$  relaxation time of the corresponding tissues. Then, this can be used to produce  $T_2$  weighted images for fMRI. Since the signal in fMRI is indicative of the whole series of changes that follow neural activity, it is considered to measure this activity only indirectly.

## 3.2 General workflow to analyze brain connectivity

Before the calculation of the adjacency matrix of the brain network, few pre-processing steps need to be applied to the images obtained from the neuroimaging techniques explained above. In short, some of these steps include the correction of any spatial distortions in the image due to the inhomogeneity of the magnetic field, the isolation of the background noise, the segmentation of the tissue and normalization to a template. These techniques are commonly applied by using an already existing software (for example, Freesurfer [120]). After carrying out

these pre-processing steps, one could proceed to calculate the adjacency matrix along few general series of steps exemplified in figure 3.2.

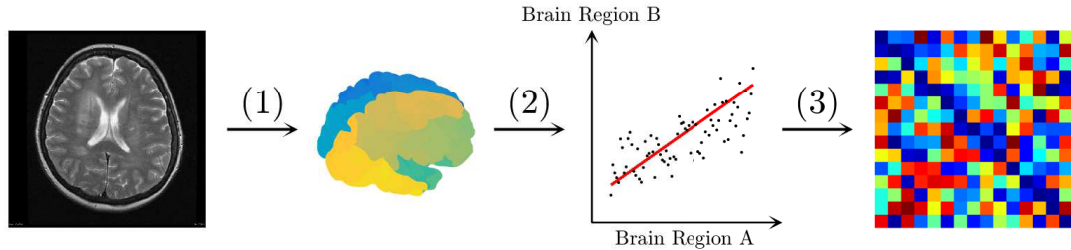


Figure 3.2: Construction of the adjacency matrix. Flowchart exemplifying the calculation of the adjacency matrices in the brain for neuroimaging data. (1) A T1-weighted MRI image needs to be pre-processed in order to correct it for existing artifacts. From this image, some meaningful variable (for example cortical thickness or subcortical volume) is obtained for each brain region that is defined by choosing a particular parcellation scheme. (2) For each pair of regions in the brain, the strength of their connection is calculated as the correlation coefficient between the obtained values. (3) The adjacency matrix is constructed such that each row and column represent different brain regions and each entry is the correlation coefficient between the corresponding pair of regions.

### 3.2.1 Definition of nodes

In the first step, a particular parcellation scheme is applied which divides the brain into multiple brain regions. Each brain region can be thought of as a small subnetwork, made up of multiple neurons and synapses between them, embedded in the large-scale brain network. Therefore, although all brain regions have a complex structure and their function is derived from the complex behavior of the many underlying neurons, in many applications it is suitable to represent them as compact neuronal masses that become the nodes of the complex brain network [121].

The nodes should be chosen to cover the whole volume of the brain and they should not overlap with each other [31]. Currently there is not a recognized standard for choosing the nodes, however their positions are commonly obtained from many existing anatomical atlases used in MRI, fMRI and PET or taken as



the position of the electrodes in EEG. This choice of nodes is very important because it directly affects the topology of the brain graphs, the strength of their connections and also the values of the graph measures that are calculated [122]. Consequently, two brain graphs can be meaningfully compared only if they are based on the *same brain atlas*.

After defining the brain regions in the brain, using some morphometry techniques, few characterization values (such as cortical thickness) can be extracted for each brain region. These values are then used to calculate the degree of association between the two regions, which I will discuss in the next section.

### 3.2.2 Definition of edges

The edges represent the connections between brain regions. As explained in section 2.2, the edges can indicate only the presence or the absence of the corresponding connections (binary graphs) or they can also specify the strength of the connections (weighted graphs). The edges have different interpretations that depend on the exact nature of the neuroimaging data. For example, when the data is obtained by structural MRI, the edges represent the statistical correlation of some structural parameters that are extracted for a couple of regions. On the other hand, for functional data, the edges represent the correlation between the time activation profiles of couple of regions over time. The strength of such correlations can be calculated using various measures, however the most commonly used are the following ones:

- The **Pearson correlation coefficient** between two regions  $j$  and  $k$  is calculated as

$$\rho_{jk} = \frac{\text{cov}(x_j, x_k)}{\sigma_j \sigma_k}, \quad (3.1)$$

where  $x_j$  and  $x_k$  are the series of values corresponding to each region,  $\text{cov}(x_j, x_k)$  is their covariance, and  $\sigma_j$  and  $\sigma_k$  represent the standard deviations of those series. This coefficient shows the degree of linear association that exists between the two sets of data. In other words, if  $x_j$  and

$x_k$  are plotted in a scatter plot and a best fit line is fitted for the data, the Pearson's coefficient will measure how far the data points are from this best fit line. This coefficient can have values in the range between  $-1$  and  $1$ . A value of  $1$  indicates a perfectly positive linear relation between the two sets of data, i.e. if one variable increases, the other increases linearly with it; while  $-1$  indicates a perfectly negative linear relation, i.e. if one value increases, the other one decreases linearly with it. A coefficient value of  $0$  is indicative of no linear correlation between the two sets of data; importantly, a value of  $0$  does not mean that there is no correlation between the two sets of data, only that any possible existing correlation is not linear. It should be noted that, as the Pearson's coefficient assumes a normal distribution of the data, it can be very sensitive to the presence of outliers or a skewed distribution and it cannot distinguish between the dependent and independent variables, i.e. it cannot give information about any causal or directed interactions.

- The **Spearman rank correlation coefficient** is a non-parametric version of the Pearson's coefficient and is defined as the Pearson's coefficient between two ranked variables. Spearman's coefficient is generally used in order to determine the degree of the monotonic relation between the two variables. To calculate this coefficient, the values in each set of data are ranked (the highest value is ranked  $1$  and, if there are two equal values, their average rank is assigned to both) and then the Pearson's coefficient is computed between the resulting ranks. The values of Spearman's coefficient range between  $-1$  and  $1$  and their interpretation is analogous with the one for the Pearson's coefficient; however while Pearson's coefficient reveals linear associations between two sets of data, Spearman's coefficient measures their monotonic relation and therefore can be considered as being less restrictive.
- The **Kendall rank correlation coefficient** is a non-parametric test that measures the correlation between two ranked quantities. This coefficient is expressed as

$$\tau = \frac{N_c - N_d}{\frac{1}{2}n(n-1)} \quad (3.2)$$

where the denominator denotes the total number of pairs and  $N_c$  and  $N_d$  are the numbers of concordant and discordant pairs respectively. Let  $x_i$  and  $x_j$  to be the corresponding ranks for the  $i^{th}$  and  $j^{th}$  values in the data series  $x$  and define the analogous quantities for the data series  $y$ . Then, consider the two pairs  $(x_i, y_j)$  and  $(x_j, y_i)$  between the two sets of data  $x$  and  $y$ . Then, in the case when  $x_i < x_j$  and  $y_i < y_j$ , or equivalently  $x_i > x_j$  and  $y_i > y_j$ , are true, the pair  $(x_i, y_j)$  is considered concordant or ordered in identical way. Otherwise, the pair is considered discordant. When  $x_i = x_j$  or  $y_i = y_j$  the pair is considered to be tied. The values for the Kendall correlation coefficient are in the range between  $-1$  to  $1$ . Higher coefficient values indicate good match between the pairs, i.e. it indicates that the pairs are ranked in similar order in both data series (they increase or decrease together).

- **Partial correlation coefficients.** Partial correlation coefficients can be calculated as the correlation coefficients between two sets of data, after regressing out the the effects of one or more other variables from both time series. Most commonly, Pearson’s and Spearman’s partial correlation coefficients are computed.

Although calculating the correlation coefficients is the most widely used method to characterize the association between two sets of data, other measures can be also utilized for the same purpose. In particular, for the analysis of functional data, measures such as coherence, Granger causality or mutual information can be computed as well [85].

### 3.2.3 Building the adjacency matrix

Each row and column of the adjacency matrix corresponds to the brain regions that are specified as described in section 3.2.1. Each entry in the adjacency matrix represents an edge between the corresponding brain regions whose strength can be derived using the methods outlined in section 3.2.2, with few additional steps:

- All self-connections are *eliminated* from the network. This is accomplished by setting the diagonal entries, which are calculated by the series' autocorrelations, of the adjacency matrix to zero.
- The negative correlations can be (1) equated to zero and, therefore, not included in the graph analysis, (2) substituted by their absolute values, or (3) left unchanged (however, in the latter case, this may result in inability to calculate some graph measures because they are not defined for negative correlations).

The adjacency matrix is built in different ways for the different imaging modalities:

### 1. **Structural data:**

The structural data resulting from images obtained with structural MRI in general consists of a single value (which may represent cortical thickness, subcortical volume or other measures of interest) that characterizes a brain region for each subject. Then, the edge between two brain regions is given by the statistical correlation of these values for the two regions across a group of subjects. Subjects typically are grouped according to some common characteristics they share (e.g. the same clinical diagnosis). As a result, a single connectivity matrix is obtained for each group of subjects and consequently all the measures that are calculated on structural brain networks reflect the properties of that group.

### 2. **Functional data:**

The functional information about the brain can be obtained for subjects performing some designed tasks (e.g. looking at a picture) or lying still without any cognitive tasks (resting state fMRI). In both cases, brain activity is monitored over time by obtaining multiple images; therefore each brain region is associated with a time series. As a result, the connection strength between two brain regions is given by the temporal correlation between the activation time series of the corresponding regions. As such, an

individual adjacency matrix can be obtained for each subject; consequently the graph measures that are calculated show the properties of individual subjects' networks. The subjects are grouped according to some common properties they share (e.g. same clinical diagnosis) and the properties of the group are derived as average of the measures calculated for individual subjects.

### 3.2.4 Calculation of graph measures

After constructing the adjacency matrices for each subject/group by following the steps discussed above, the topological properties of the resulting network can be calculated by using the various measures defined in chapter 2. Since the edges represent correlation coefficients that have continuous values, the resulting adjacency matrix is naturally weighted. From this point on, there are three different ways in which one can proceed to calculate the measures:

1. **Weighted analysis:** The weighted analogues are calculated for each measure.
2. **Binary analysis by specifying threshold:** The networks are first binarized by specifying a threshold value and the measures are calculated on the binary networks. A comparison between two groups in this analysis can be meaningful only if the groups' corresponding networks are binarized by specifying the same threshold value. One disadvantage of this method is apparent when one group has consistently lower connection strengths than the other; in this case, the specification of the same threshold for both groups will lead to different number of connections. Therefore, any significant result could be due to this difference rather than some underlying effect. In general, the results in this type of analysis are performed over some range of thresholds.
3. **Binary analysis by specifying density:** The networks are first binarized by specifying a threshold value so that a certain number of connections exist

in the graph, and the measures are calculated on the binary networks. In this type of analysis, a comparison between two groups can be meaningful only if the groups' corresponding binary networks have the same density of connections. Sometimes, this method is preferable because the analysis is done only on the corresponding percentage of strongest connections; as a result, the results are considered to reflect topological differences. This analysis is also commonly performed over some range of densities.

### 3.3 Between-group comparison

Typically, the connectivity analysis is performed by comparing the properties of a control group to a target group; for example in order to find the effect of a neurodegenerative disease one might compare a group of healthy subjects to patients having that particular disease. However, in order to determine whether the calculated differences are indeed genuine or they result from the randomness associated with the sample selection, statistical significance tests are commonly performed. One widely used procedure is the non-parametric permutation test which tests whether the differences between the two groups are significant (this is reported as p-values) and also determines the confidence intervals (generally calculated as 95% confidence intervals).

#### 3.3.1 Permutation test

The *null hypothesis* generally states that the observed effect is due to randomness. The decision of rejecting the null hypothesis can be evaluated with a permutation test by the calculation of the associated p-value (i.e. the probability to obtain a value that is equal to or more extreme than the real observed value just by chance). The p-value is then compared with a predetermined threshold value (which is typically taken to be  $p = 0.05$  or  $p = 0.01$ ). If the obtained p-value is lower than the threshold, the null hypothesis can be rejected as illustrated in figure 3.3.

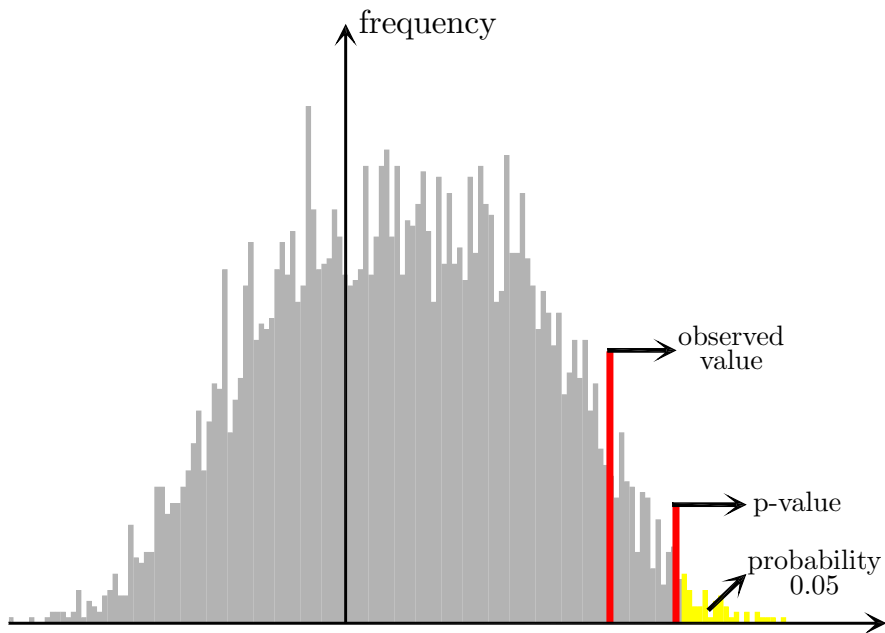


Figure 3.3: Permutation test and p-value. The permutation test calculates a p-value (defined as the probability to obtain a value that is equal to or greater than the observed value only by chance) and compares it to a predetermined threshold (for example,  $p = 0.05$  or  $p = 0.01$ ). If the calculated p-value is less than the threshold, the null hypothesis can be rejected.

In particular, the permutation test is used to compare the network measures calculated for two groups. It does so by following these steps:

1. Calculate the graph measures for each group and determine the difference between them.
2. Randomly permute the subjects between the two groups; calculate the measures for each of the permuted groups and obtain the difference between them.
3. Repeat the above step multiple times (typically, this is done 1000 times). After that, obtain the histogram of the differences.
4. Determine where the difference obtained from the two original groups falls within the histogram (i.e. calculate the p-value for the difference of the

original groups). Comparison of this value with the predetermined threshold (figure 3.2) will determine whether the null hypothesis can be rejected.

### 3.3.2 Comparison with random graphs

The measures calculated for a given group can also be compared with the ones calculated for the corresponding random graphs by following the procedure explained below:

1. Calculate the value of the particular measure for the group.
2. Calculate the measure for a set of random graphs (typically 1000); these graphs are calculated in a way that preserves the degree and strength distributions of the original graph. Based on this, obtain the histogram of the measure.
3. Determine where the value of the measure lies within the histogram.

### 3.3.3 False discovery rate (FDR)

When applying the permutation test to the nodal measures, one actually tests multiple null hypotheses simultaneously (one for each brain region). This results in the increase of the likelihood to obtain false significance; for example, with a 0.05 p-value threshold, one would expect to reject the null hypothesis 5% of the time just by chance, and this number increases if multiple hypothesis are tested. Therefore, the level of significance and the corresponding p-values need to be adjusted in order to account for the multiple comparisons. The *false discovery rate* (FDR) is used for this purpose and is applied by employing the Benjamini-Hochberg procedure (figure 3.4):



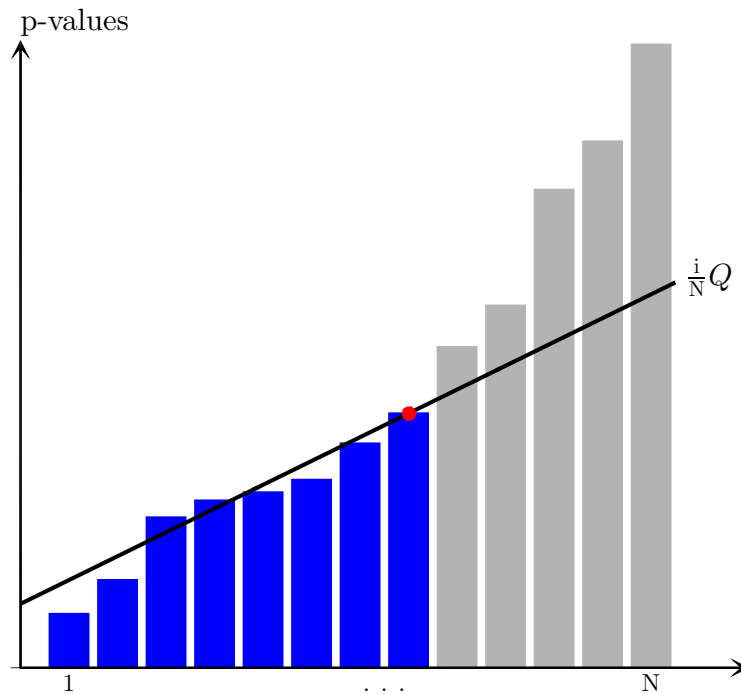


Figure 3.4: False discovery rate (FDR). The p-values are computed for each hypothesis testing and are arranged in ascending order. Each of these individual p-values is compared to their corresponding false-rate-corrected values given as  $\frac{i}{N}Q$  (here,  $Q = 0.10$ ). The first significant point is the largest p-value that is smaller than its corresponding false-rate-corrected value. Then, every hypothesis with smaller p-value, the blue bars in the figure, is also significant (regardless of whether the p-value is smaller or larger than the corresponding false rate corrected values).

1. Calculate the p-values for each individual hypothesis testing and sort them in ascending order (i.e. if one is testing a total of  $N$  hypotheses, the smallest p-value has rank  $i = 1$ , the largest has rank  $i = N$ ).
2. Choose the false discovery rate  $Q$  (usually,  $Q = 0.05$ ).
3. Each of the individual p-values are compared with their corresponding FDR corrected values, which can be calculated as  $\frac{i}{N}Q$ .
4. Identify the largest p-value that is smaller than the corresponding FDR corrected value.

5. The p-value identified in the previous step is the largest p-value that is significant; all smaller p-values are significant as well (regardless of whether they are larger than the corresponding false-rate-corrected values) as exemplified in figure 3.3.

# Chapter 4

## BRAPH – BRain Analysis using graPH theory

### 4.1 Introduction

Various toolboxes have been developed with the aim to apply graph theory to the study of brain connectivity networks, such as, eConnectome [123], BrainNet Viewer [124], GRETNA [125], CONN [126], GraphVar [127], the Brain Connectivity Toolbox [31] and GAT [128]. Additionally, it has been argued that time-varying brain networks offer valuable insights about the effects of mental illnesses [129], thereby prompting the development of toolboxes that allow the calculation of dynamic functional connectivity measures [130, 131]. Each of these toolboxes contributed to the field of the network neuroscience by providing the user with various options to visualize, build and characterize the brain network topology, however they mostly require some background in programming, are coded in a manner that does not allow for their straightforward adaptation or focus on only a single part of the analysis. As a result, a reliable, streamlined, user-friendly, fast, and scalable software that deals with all aspects of network organization is still lacking.

In this chapter, I will present *BRAPH – BRain Analysis using graPH theory* [132] (<http://www.braph.org/>), a toolbox that can be utilized to perform network analysis of the brain connectome. BRAPH is accompanied with a graphical user interface (GUI) and it is an open-source object-oriented software coded in MatLab. By benefiting from the object-oriented programming paradigm, this software provides a coherent modular structure that enables the addition of new objects even without an extensive knowledge of the underlying implementation, therefore permitting easy maintenance and modification of the existing code.

From the clinical point of view, BRAPH offers the following advantages: (a) in order to get the first impression of the data and any existing differences between groups before the actual network analysis, the regional mean values of each group can be compared between each other by using permutation testing; (b) individual and group adjacency matrices and network measures can be visualized by the user, which is pivotal for the detection of potential outliers, a major confound in neuroimaging studies; (c) it gives the user an insight into the topological changes of the brain networks over time by providing the option to carry out longitudinal analysis; (d) the community structure of the network can be calculated by employing a variety of algorithms and the user can also conduct subnetwork analyses within the pre-calculated communities, a very important tool for studies testing hypotheses within a particular structural or functional brain network; (e) BRAPH provides the basis for conducting a multi-modal graph theory analysis by integrating information from independent imaging modalities, which is arguably the next challenge in imaging connectomics; for example, both structural (MRI) and functional (fMRI) networks can be meaningfully compared by deriving them from the same brain atlas.

From the user's perspective, BRAPH is a vertically integrated software in which all steps of the analysis can be carried out sequentially, ranging from importing the neuroimaging data to saving the final results and the analysis parameters in a single file. Therefore, the organization of BRAPH is practical and it helps with the reliability and reproducibility of the results, which is an increasingly important issue within the research community.

In the following sections I will describe in detail the different options provided within BRAPH that can be used to perform the connectivity analysis of brain

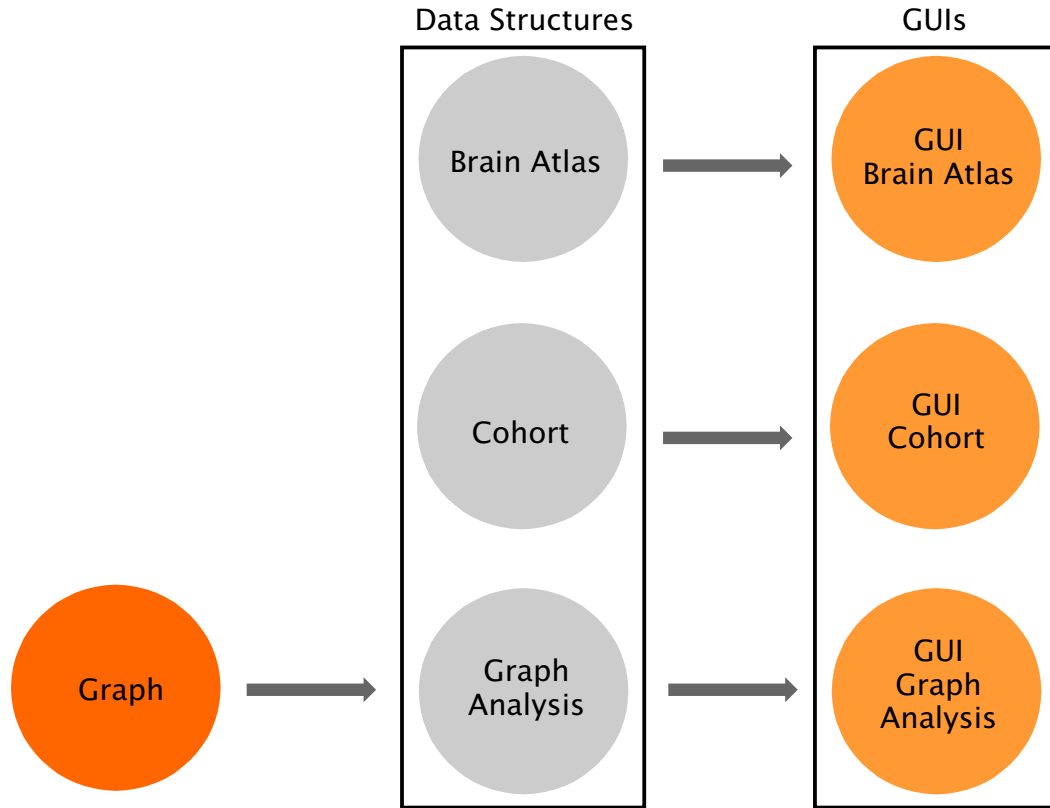


Figure 4.1: Overview of BRAPH software architecture. The structure of BRAPH is made up of three layers: Graph, Data Structures and Graphical User Interfaces (GUIs). Unidirectional interfaces (represented by arrows) are used to connect these layers as shown. Graph incorporates the functions that are needed to conduct the graph analysis. In the Data Structures layer, Brain Atlas is used to define the network’s nodes, Cohort allows the user to specify the subjects to be used in the analysis and divide them into groups and Graph analysis permits one to calculate the adjacency matrix, the network measures and the between-group comparisons. Each of the above is implement in an object, whose capabilities can be invoked by command line. Additionally, a GUI is made available for each object (i.e. GUI Brain Atlas, GUI Cohort and GUI Graph Analysis). Due to this organization, BRAPH can be customized, maintained and expanded very easily. Taken from [132].

networks. Such options include the building of the connectivity matrices, the analysis of binary and weighted networks, the implementation of between-group comparisons, and the normalization of the network measures by the ones computed from random networks. Although this software has already been applied in some previous graph theoretical studies on various neurodegenerative diseases [96, 97], to additionally demonstrate its ability, in this chapter I will also discuss the topological properties of structural networks built in patients with amnesic mild cognitive impairment (MCI) and AD, as well as functional networks derived from Parkinson's disease (PD) patients with MCI.

## 4.2 Materials and methods

### 4.2.1 Overview and analysis workflow

BRAPH is a complete software package that allows the user to perform all steps of a graph theoretical analysis (chapter 3), visualize the results by plotting high-quality images and save the whole analysis parameters in a single file. BRAPH can deal with data obtained from both structural (MRI, PET) and functional (fMRI and EEG) imaging techniques and can analyze this data by calculating binary and weighted brain connectivity networks. It also allows for the assessment of the community organization in the network by employing different algorithms; the calculated communities can be further extracted for a sub-network analysis. Between-group significant differences are tested by the non-parametric permutation test and the multiple hypothesis testing results are corrected by employing the false discovery rate (FDR) [133]. Additionally, it provides options to conduct longitudinal analysis, for which the statistical significance is also reported by permutation test, and also it gives the option to the user to normalize the network measures by random graphs.

As shown in figure 4.1, the software is made up of three independent layers:

Graph, Data Structures and Graphical User Interfaces (GUIs), all of them connected by software interfaces. The *Graph* package encompasses the set of fundamental functions that facilitate the calculation of the nodal and the global measures. The *Data Structures* package consists of functions that lay out the core functionalities of BRAPH, such as defining the brain atlas or the creation of cohorts by grouping the subject and the types of graphs; crucially each of them can be accessed by the command line and extended or modified by advanced users. The *GUIs* package provides the users without a computational background with a well-organized framework to perform the brain connectivity analysis. It consists of a series of GUIs, each of which allows for the execution of different task: (a) a selection and editing of the brain atlas can be accomplished by the *GUI Brain Atlas*; (b) the cohort of subjects can be specified in the *GUI Cohort*; (c) the *GUI Graph Analysis* facilitates the building of the adjacency matrix, the selection of the type of analysis (weighted or binary), the thresholding method (by specified a certain threshold or density) and the calculation and visualization of the network measures. In the case of GUI Cohort and GUI Graph Analysis, depending on the type of the imaging technique, four options can be chosen (MRI, fMRI, PET, EEG). By exploiting this three-layered structure, BRAPH can be further customized in order to address any emerging needs, for example, new graph measures or new approaches for building the adjacency matrix can be easily implemented. The workflow for performing a connectivity analysis in BRAPH is shown in figure 4.2; each step in this analysis is discussed in detail in the following sections.

#### 4.2.1.1 Defining the brain atlas

As discussed in section 3.2, the connectivity analysis starts by defining the nodes in the network, which represent the various regions in the brain (figure 4.2(A)). In BRAPH, the brain atlas is defined by the graphical interface *GUI Brain Atlas* and the corresponding set of objects (described in the sections 4.2.2.2 and 4.2.3.3). In order to be able to visualize the brain graph all regions need to be projected on the top of a 3D brain surface, therefore, for each brain region a name, label and

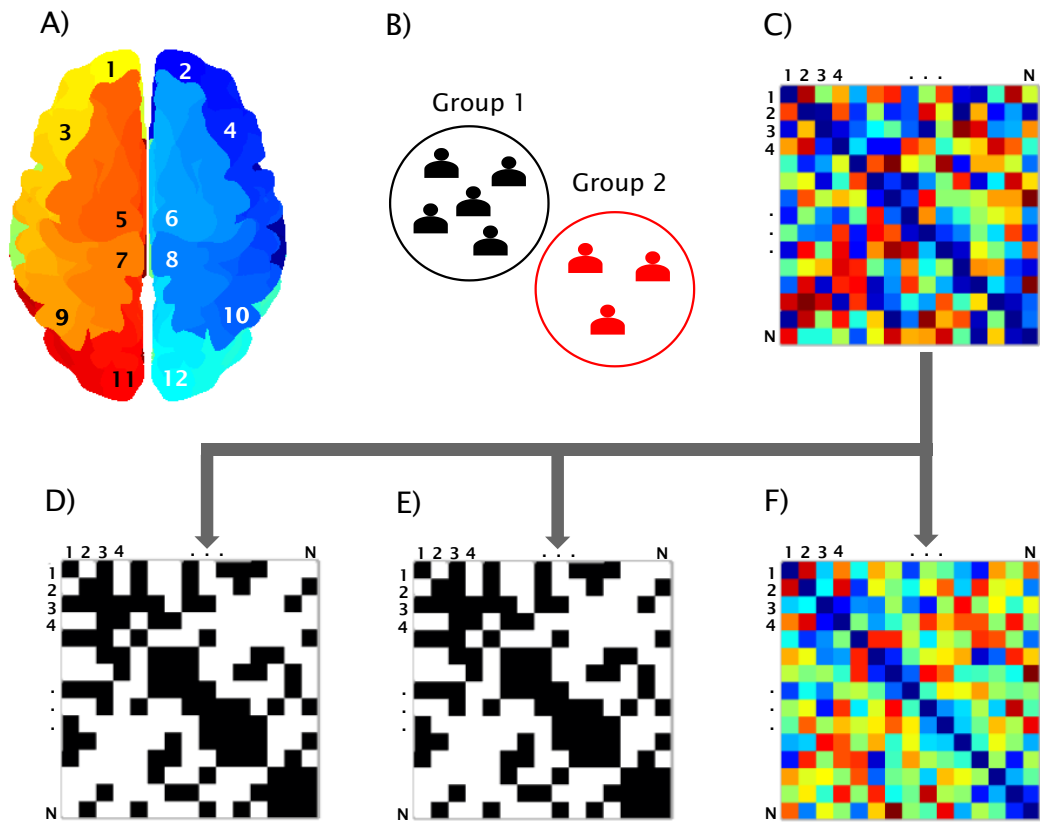


Figure 4.2: BRAPH workflow. Each step of the brain connectivity analysis in BRAPH can be performed by the corresponding graphical user interfaces (GUIs). A) *GUI Brain Atlas* allows the user to specify the brain regions. B) The user can import the data of the subjects, modify subject's relevant data and define subjects groups in *GUI Cohort*. C) *GUI Graph Analysis* allows the calculation of the adjacency matrix by allowing the user to choose how to deal with the negative correlation coefficients, specify the type of correlation and which type of graph to analyze. Based on the type of graph, three specialized GUIs are used to calculate and visualize the corresponding measures: D) *GUI Graph Analysis BUD*: binary undirected graphs at a fixed density; E) *GUI Graph Analysis BUT*: binary undirected graphs at a fixed threshold; *GUI Graph Analysis WU*: weighted undirected graphs. Taken from [132].

(x,y,z) coordinates should be specified. When structural networks are analyzed



(e.g. T1-weighted images obtained from structural MRI), the brain is generally divided by using an anatomical parcellation configuration that makes use of the sulci and gyri as anatomical markers. Some examples of anatomical atlases are Desikan [134], Destrieux [135] or Automated Anatomical Labeling (AAL) [136] atlas. In the case of functional data analysis (e.g. functional MRI data), in addition to defining the brain atlas from an anatomical parcellation, one could derive it by using a meta-analysis, or a method based on the clustering of the spatially coherent and homogeneous regions. Examples of functional atlases include the Power [137], Dosenbach [138] or Craddock [139] atlases. Additionally, the user could also define an atlas directly in *GUI Brain Atlas* or use a custom atlas from an external file.

#### 4.2.1.2 Defining the cohort

After creating or uploading the atlas, the corresponding cohort in the analysis needs to be defined (figure 4.2(B)). In BRAPH, the subject data can be uploaded through the *GUI Cohort* interface (sections 4.2.2.3 and 4.2.3.4). The subject data may consist, for example, of volume measures, of surface area, or cortical thickness in the case of structural MRI; time depended regional activation patterns in the case of functional MRI; electrophysiological signals in the case of EEG; and glucose metabolism in the case of PET. These values, in addition to the pre-processing steps of the images (section 3.2), are commonly obtained by using an external software, such as, the Statistical Parametric Mapping (SPM; <http://www.fil.ion.ucl.ac.uk/spm/>), FMRI Software Library (FSL; <https://fsl.fmrib.ox.ac.uk/fsl/fslwiki>) and FreeSurfer (<https://surfer.nmr.mgh.harvard.edu/>). Moreover, the obtained values may need to be corrected for the effects of confounding variables, for example, gender, age or subjects' motion in the scanner. This can be done by linear regression, in which case the residual values should replace the raw values in the analysis [140].

### 4.2.1.3 Defining the adjacency matrix

Once the brain atlas and subject data have been imported in BRAPH, the adjacency matrix is constructed by computing the edges that represent the relationships between all pairs of nodes (figure 4.2(C)). In the software, the edges are calculated in the interface *GUI Graph Analysis* (sections 4.2.2.4 and 4.2.3.5) by employing each of the correlation coefficients described in the sections 3.2.2 and 3.2.3. Additionally, in BRAPH, the user can handle the negative correlation coefficients in three different ways (section 3.2.3) and analyze three different types of graphs:

- **Weighted undirected analysis:** This analysis is performed on the adjacency matrix that is obtained by the symmetrization of the full weighted matrix (in which the elements are the corresponding correlation coefficients between two nodes) as described in section 2.2 (figure 4.2(F)). These networks are characterized by a single number in the case of the global measures and by an array of numbers (one number per brain region) in the case of nodal measures. This type of analysis is utilized by the *Graph Analysis WU* graphical interface (sections 4.2.2.5 and 4.2.3.5).

Furthermore, in order to perform binary network analysis, BRAPH can binarize the weighted undirected adjacency matrix in two ways, leading to the other two types of analyses:

- **Binary undirected threshold (BUT) analysis:** This analysis is performed by firstly selecting a correlation coefficient as a cut-off (or threshold) value. Then, the weighted adjacency matrix is binarized such that all edges below the cut-off value are excluded from the analysis and all edges above this value are set to 1 (figure 4.2(E)). These networks are commonly characterized over a range of thresholds which can be chosen by the user. This analysis is employed by the *Graph Analysis BUT* graphical interface (sections 4.2.2.5 and 4.2.3.5).

- **Binary undirected density (BUD) analysis:** This analysis is performed by binarizing the weighted adjacency matrix by choosing a cut-off correlation coefficient such that a certain fraction of edges (i.e., a specific density) is obtained in the graph (figure 4.2(D)). The user can also choose the range of densities that will be used to characterize the networks. This analysis is employed by the *Graph Analysis BUD* graphical interface (sections 4.2.2.5 and 4.2.3.5).

It should also be noted that even though BRAPH does not allow for the calculation of the directed networks through the graphical user interfaces, the directed analogues of the measures are already implemented in the *Graph* package and can be used from the command line in MatLab.

#### 4.2.1.4 Network construction and analysis

Each of the three interfaces described above allow for the calculation of both global and nodal network measures, on weighted or binary networks, using different thresholds or densities. BRAPH can calculate most of the measures defined in chapter 2 and all measures are implemented in the software package *Graph*. They are calculated by employing optimized and linear algebra based algorithms, some of which are adapted from the Brain Connectivity Toolbox (<http://www.brain-connectivity-toolbox.net/>) [31].

After the calculation of the measures for each group, BRAPH can test for significant differences between any two groups (cross-sectional analysis) as well as significant differences of the same group at two different points across time (longitudinal analysis). These results are obtained by performing non-parametric permutation tests and are reported as one-tailed and two-tailed p-values based on 95% confidence intervals. The permutation test for the longitudinal comparison is performed by permuting the data for each subject at the different time points, therefore enforcing that a group does not have the subjects data from two time points.

In the case of the nodal measures, the permutation tests are run for each brain region simultaneously. Therefore, they assess multiple null hypotheses at the same time, which in turn increases the chance of identifying false positives. In order to resolve this issue, BRAPH controls the multiple comparison p-values with the false discovery rate (FDR), implemented via the Benjamini-Hochberg procedure (section 3.3.3).

All network measures can be compared with their counterparts calculated on random graphs, for example, with the purpose to normalize the weighted measures. The random graphs used for this purpose are commonly derived to have the same weight or degree distribution as the original network. In BRAPH, the random graphs are computed by using the algorithms described in the Brain Connectivity Toolbox [31].

BRAPH also allows for the visualization of the calculated measures and comparisons and high quality and publication-ready images can be exported as a result. For global measures, BRAPH plots the difference of the measures calculated for two groups as well as the 95% confidence intervals derived from the permutation tests. In the case of nodal measures, the user can choose whether to view the raw results for each brain region, or alternatively, only the regions that pass the FDR corrections (have their corresponding null hypothesis rejected) can be visualized on a brain surface. Finally, the user can also plot both the binary network (for different thresholds/densities) and the weighted one (in which the strength of the edges is coded in the color and weight of the edges).

### 4.2.2 Graphical user interfaces in BRAPH

A series of GUIs (illustrated in figure 4.3) guide the user through the steps of the connectivity analysis. The analysis starts with *Brain Atlas* in which user can create and manipulate a brain atlas. In the next step, *Cohort* interface permits the user to create the subjects' cohort and upload their data. Afterwards, the type of the analysis can be specified in *Graph Analysis*; depending on this choice, a specialized GUI opens, *WU/BUD/BUT Graph Analysis*, in which the user

can calculate and visualize the measure. Although this workflow is implemented separately for each neuroimaging technique (figure 4.3), in the following sections I will only briefly present the corresponding GUIs for structural MRI data, while the complete description, including the one for the functional data, could be found at <http://www.brain.org/>.

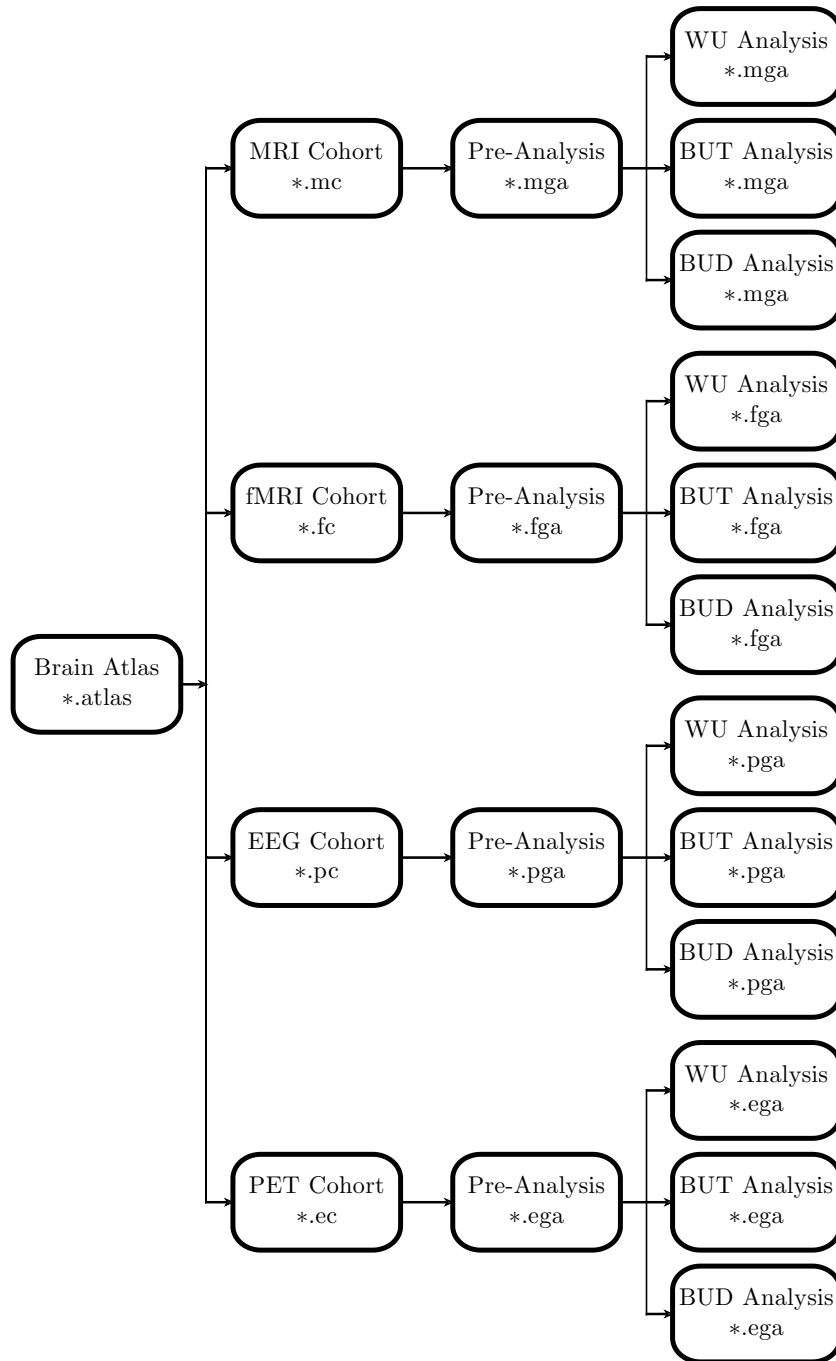


Figure 4.3: Connectivity analysis using the GUIs in BRAPH. A workflow of the connectivity analysis in BRAPH by using the GUIs for each of the four imaging modality. Each of the boxes indicates a GUI by specifying its name the format of the files that are outputted by that GUI. The arrows show the typical workflow between the GUIs. Taken from [141].

### 4.2.2.1 Initial GUI

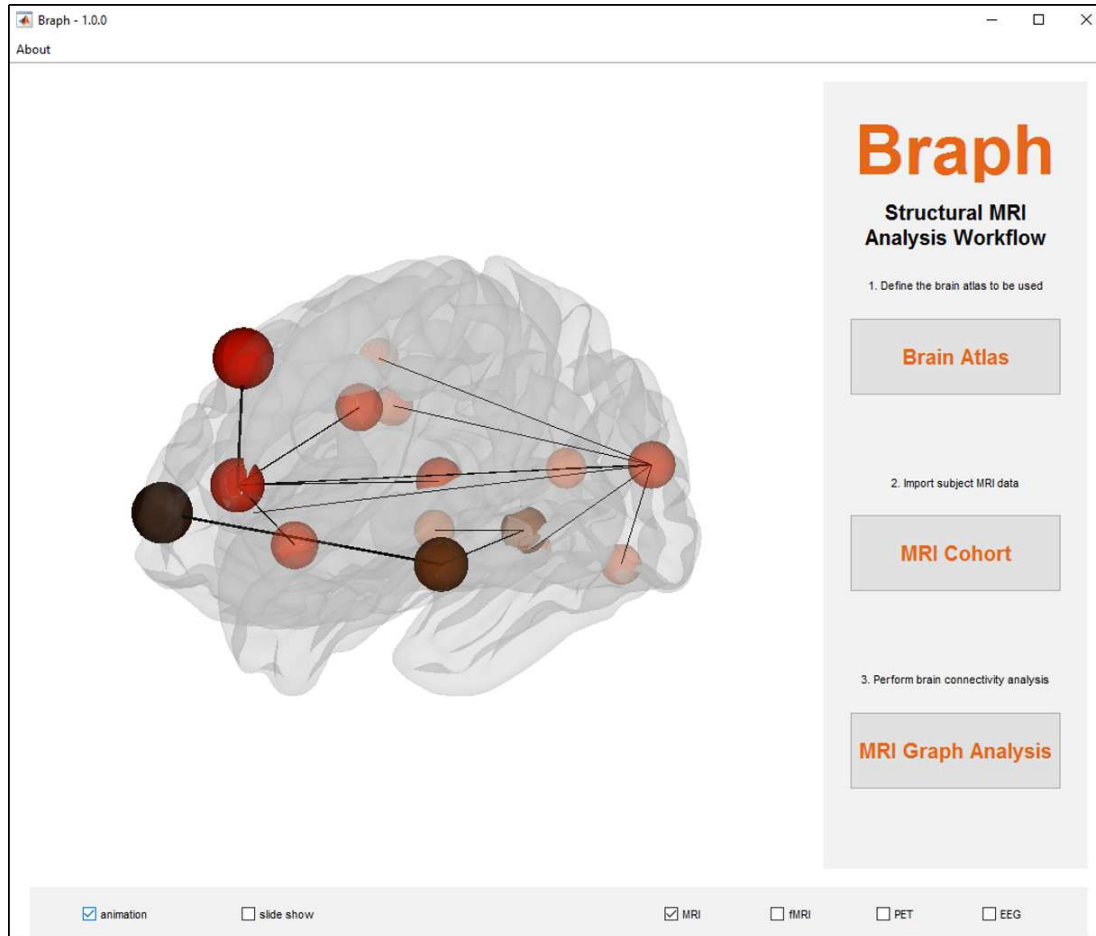


Figure 4.4: Initial GUI that becomes visible after launching BRAPH. This GUI allows the user to select the neuroimaging modality (via the checkboxes on the bottom right) and to start at various stages of the workflow: brain atlas, cohort or graph analysis (by pushing the appropriate button on the right). Taken from [141].

The initial GUI of BRAPH is illustrated in figure 4.4. This interface allows the user to:

- choose the imaging technique corresponding to the data that will be analyzed by selecting the appropriate checkbox on bottom right (the currently implemented imaging modalities are structural and functional MRI, PET and EEG).

- choose the stage at which to start the connectivity analysis by pressing the corresponding push button on the right (the analysis can be started from Brain Atlas, Cohort or Graph Analysis).
- visualize an animation of a rotating brain or slide show of selected measures in the animation panel on the left (the choice between the animation and slide show can be done via the checkboxes in the bottom left).

#### 4.2.2.2 The brain atlas GUI

*GUI Brain Atlas* is a GUI in which the user can visualize and manipulate a brain atlas. The atlas can be imported (in txt, xls or xml format) or a custom atlas can be created within the GUI. Finally, the brain atlas can be saved in a file with extension \*.atlas if intended for future BRAPH use, or it can be saved in txt or xml format that can be used within other applications.

An example of the GUIBrainAtlas is shown in figure 4.5, where four main work areas can be distinguished:

- **Menu** contains the fundamental actions that can be performed within GUI Brain Atlas such as the loading, saving, editing and visualizing of a brain atlas. It also allows the user to choose the type of cohort that needs to be built for the further analysis.
- **Toolbar** permits straight access to some of the most commonly used actions.
- **Table view** is a table that contains the properties (e.g. label, name and coordinates) of all brain regions. The buttons at the bottom allow the user to modify the brain atlas by adding, removing or changing the positions of the selected brain regions.
- **Brain view** is a panel that holds the 3D surface onto which the brain atlas is visualized. It permits the user to alter the visualization parameters of



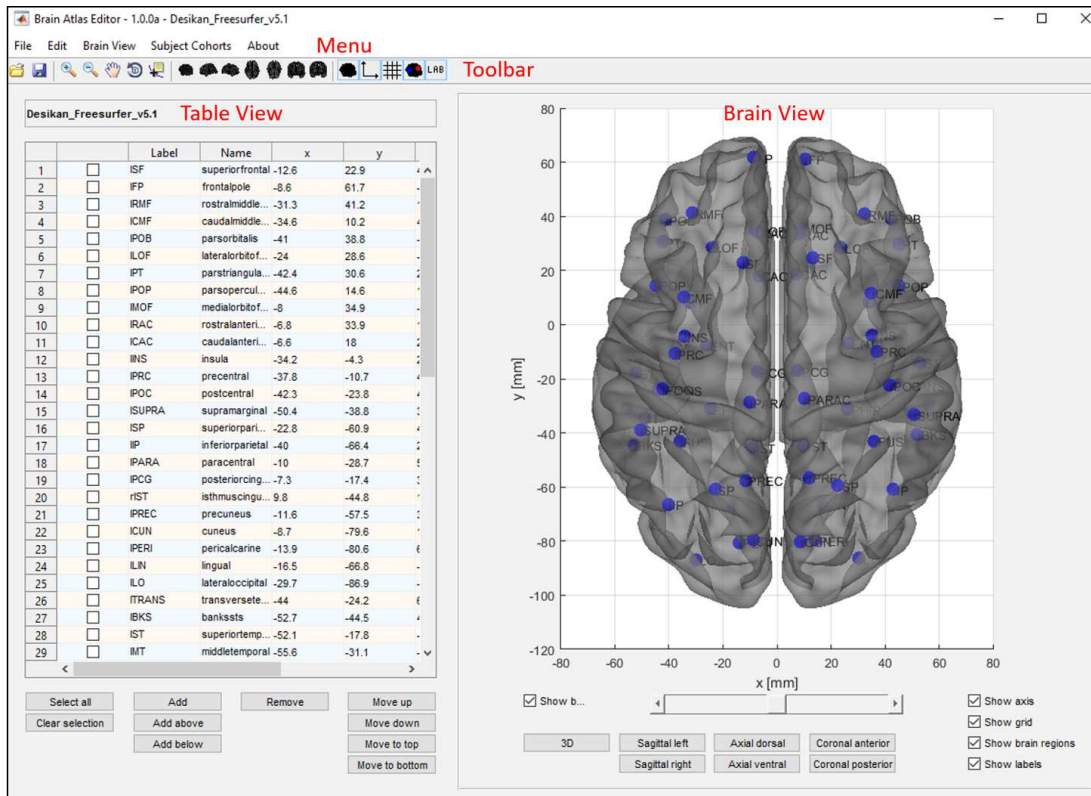


Figure 4.5: Screenshot of GUI Brain Atlas. Four main work areas can be distinguished: menu and toolbar at the top, a table view on the left and a brain view on the right. Taken from [141].

the plot. The plot in this panel can be eventually exported as a MatLab figure.

#### 4.2.2.3 The MRI cohort GUI

*GUI MRI Cohort* allows the building of an MRI cohort by importing individual or group of subjects from already prepared data files in xls, txt, or xlm format. The anagraphic information and the data of the subjects can be modified, and the subjects can be grouped into additional groups as needed. Furthermore, GUI MRI Cohort provides various option for the user to visualize the data of individual subjects, groups, and comparisons between groups. The MRI cohort can be saved in a file with extension \*.mc if intended for future BRAPH use, or it can be saved in xml format that can be used within other applications.

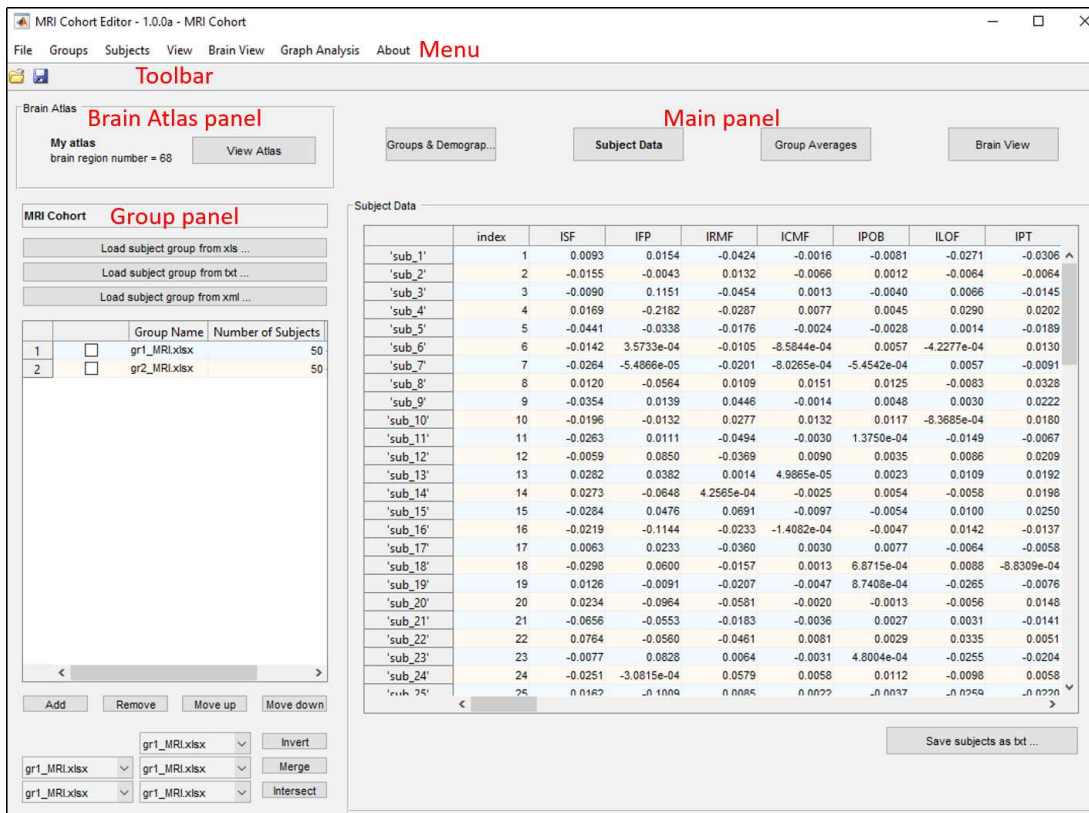


Figure 4.6: Screenshot of GUI MRI Cohort. Five main work areas can be distinguished: menu and toolbar on the top and a brain atlas panel on the top left. On the bottom left a group panel is located while the main panel is positioned on the right. Taken from [141].

An example of the GUIMRICohort is shown in figure 4.6 where five main work areas can be distinguished:

- **Menu** contains the fundamental actions that can be performed within GUI MRI Cohort such as the loading, saving, editing and visualizing of an MRI cohort. It also allows the user to start a new MRI graph analysis.
- **Toolbar** permits straight access to some of the most commonly used actions, for example, saving and loading of an MRI cohort.
- **Brain Atlas** allows the user to select an atlas that is going be used in the analysis (from a \*.atlas file). If an atlas has already been defined, it can be visualized by opening it in GUI Brain Atlas with restricted access.

- **Group panel** shows a table that contains the groups of subjects and their properties. This also allows the user to add new groups or remove existing ones; new groups can also be derived from the existing groups by performing some logical operations.
- **Main panel** is made up of four tabs: *Groups & Demographics* holds the group data; *Subject Data* can be used to edit the data of each subject; *Group Averages* allows the user to calculate the average or standard deviation of the group data; *Brain View* provides the visualization of the group or subject data on a brain surface, the final image can be further exported as a MatLab figure.

#### 4.2.2.4 The MRI graph analysis GUI

*GUI MRI Graph Analysis* allows the specification of the parameters used to compute the adjacency matrices for the analysis of structural MRI data. The resulting weighted adjacency matrices can be visualized directly, or they can be viewed as a function of both density and threshold. Additionally, the user can define a community structure and perform the connectivity analysis only within particular communities. A list of the measures available for calculation is shown at the bottom of the interface. The graph analysis file can be saved with extension \*.mga for further use in BRAPH or in xml format for use in other applications.

An example of the GUI MRI Graph Analysis is shown in figure 4.7 and six main work areas can be distinguished:

- **Menu** contains the fundamental actions that can be performed within GUI MRI Graph Analysis, such as the loading and saving of an MRI graph analysis. It also allows the user to generate a MatLab figure from the matrix shown in the main panel.
- **Toolbar** permits straight access to some of the most commonly used actions, for example, saving and loading of an MRI graph analysis; additionally the user can manipulate the graphic representations of the connectivity

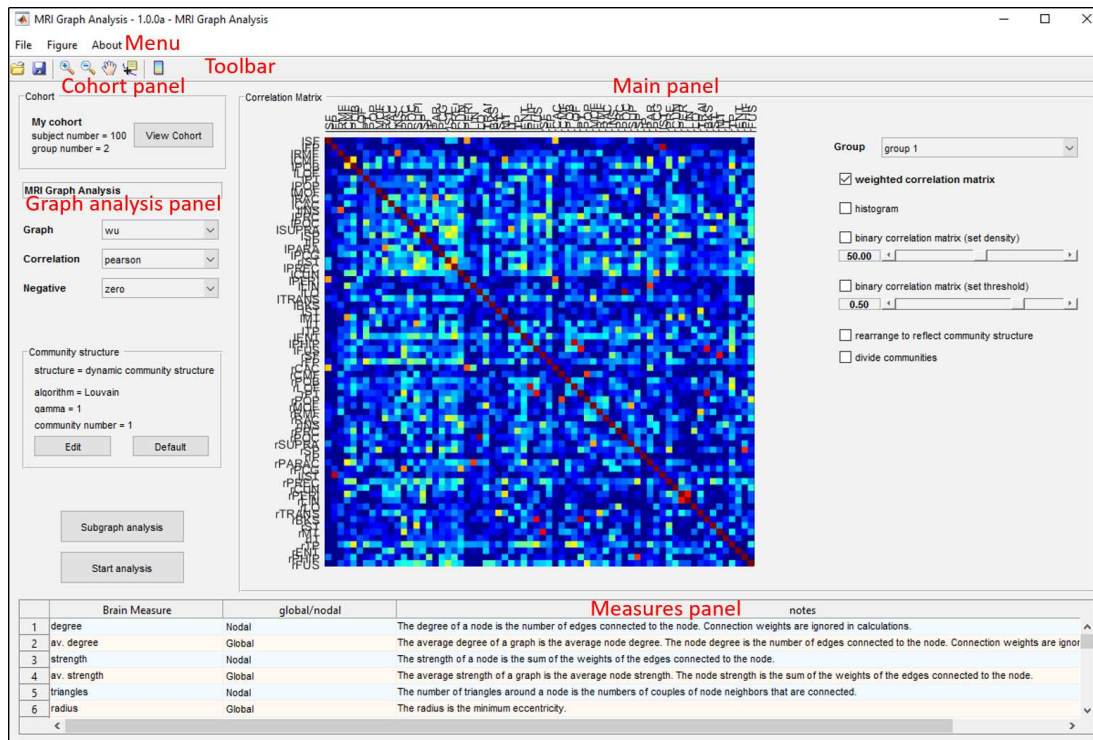


Figure 4.7: Screenshot of GUI MRI Graph Analysis. Six main work areas can be distinguished: menu and toolbar on the top, cohort and the graph analysis panel in the middle left. The main panel is located on the right and the measures panel can be found at the bottom. Taken from [141].

matrices.

- **Cohort panel** allows the user to select a cohort that is going to be used in the analysis (from a \*.mc file). If the cohort has already been defined, its properties can be visualized by opening it in GUI MRI Cohort with restricted access.
- **Graph analysis panel** permits one to choose the parameters of the analysis. In particular, the user can choose the properties of the graph analysis (weighted or binary), the correlation that characterizes the strength of between-node connections (section 3.2.2) and how to deal with the negative correlations (section 3.2.3). Furthermore, one can perform the calculation of the community structure (via the interface *Community structure*, visualized in figure 4.8) and choose whether to continue the analysis on the full graph or any other subset of nodes.

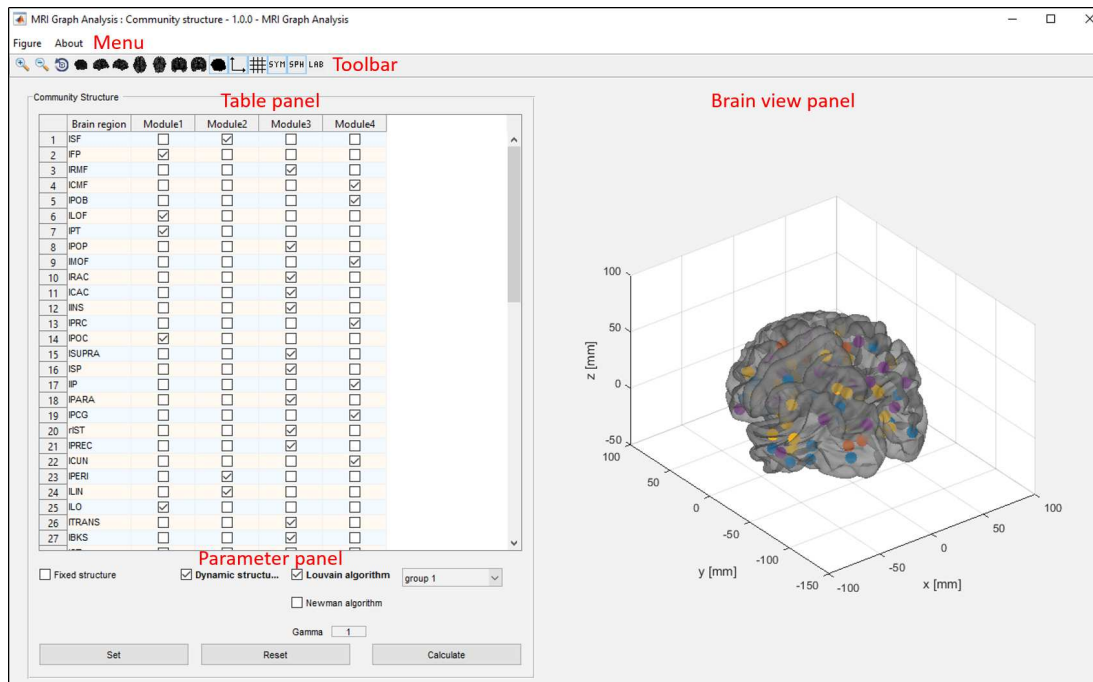


Figure 4.8: GUI Community structure. Snapshot of the interface that can be used to specify the community structure. Taken from [141].

- **Main panel** visualizes the adjacency matrix that will be used in the analysis. It allows the user to view weighted as well as binary matrices as function of density or threshold, moreover, the matrices' rows and columns can be rearranged in order to better reflect the community structure of the network.
- **Measures panel** show the measures that are available for each type (weighted or binary) of graph.

#### 4.2.2.5 The MRI graph analysis BUD GUI

Once the type of analysis has been decided in the *GUI MRI Graph Analysis*, the user is redirected to a specialized GUI that performs that particular analysis (*MRI Graph Analysis WU* for weighted analysis, *MRI Graph Analysis BUT* for binary analysis at a fixed threshold and *MRI Graph Analysis BUD* for binary analysis at a fixed density of connections. In this section I will describe the GUI

*MRI Graph Analysis BUD*, a detailed information for the other two interfaces can be found at <http://www.brgraph.org/>.

*GUI MRI Graph Analysis BUD* enables the user to conduct a brain graph analysis of MRI data by binary undirected graphs at fixed density of connections (BUD = Binary Undirected Density). Within this GUI, the group measures can be calculated and compared with random graphs. Additionally, the measures of two groups can be compared with each other by the permutation tests. Both single and double-tailed p-values are calculated (FDR correction is applied for nodal measures) and the user can visualize the 95% significance intervals. The global and nodal measures are showed separately; in the case of nodal measures, the results can be visualized on a brain surface. The graph analysis file can be saved with extension \*.mga for further use in BRAPH or in xml format for use in other applications.

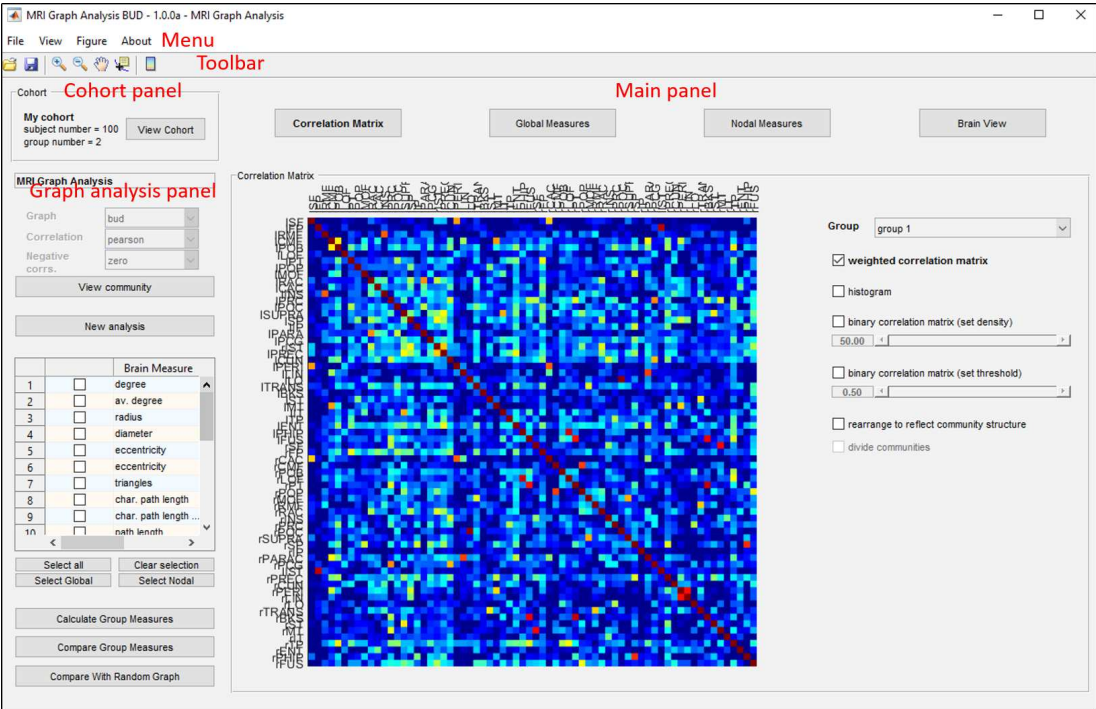


Figure 4.9: Snapshot of GUI MRI Graph Analysis BUD. Five main work areas can be distinguished: menu and toolbar on the top, main panel on the right and the cohort and graph analysis panels on the left. Taken from [141].

An example of the GUI MRI Graph Analysis BUD is shown in figure 4.9 where

five main work areas can be distinguished:

- **Menu** contains the fundamental actions that can be performed within GUI MRI Graph Analysis BUD such as the loading and saving of an MRI graph analysis. It also allows the user to generate a MatLab figure from the matrix shown in the main panel.
- **Toolbar** permits straight access to some of the most commonly used actions, for example, saving and loading of an MRI graph analysis; additionally the user can manipulate the graphic representations of the connectivity matrices.
- **Cohort panel** allows the user to visualize the properties of the cohort used in the analysis by opening it in GUI MRI Cohort with restricted access.
- **Graph analysis panel** allows the user to visualize the community structure of the graph by opening it in the Community structure GUI (figure 4.8). Moreover, the user can choose which measures to calculate or compare; the details of the comparison, such as the density range or the number of permutations can be specified inside the new interface that opens once the corresponding button is pushed (an example of the interface that allows for between-group comparison is shown in figure 4.10).
- **Main panel** is made up of four tabs: *Correlation Matrix* allows the user to visualize the matrix used in the analysis; *Global Measures* shows and plots the information about the global measures; *Nodal Measures* allows the visualization of individual results for each brain regions; *Brain View* allows the nodal measures or comparisons to be plotted on a brain surface. Each of the plots in the main panel can be further exported as a MatLab figure.

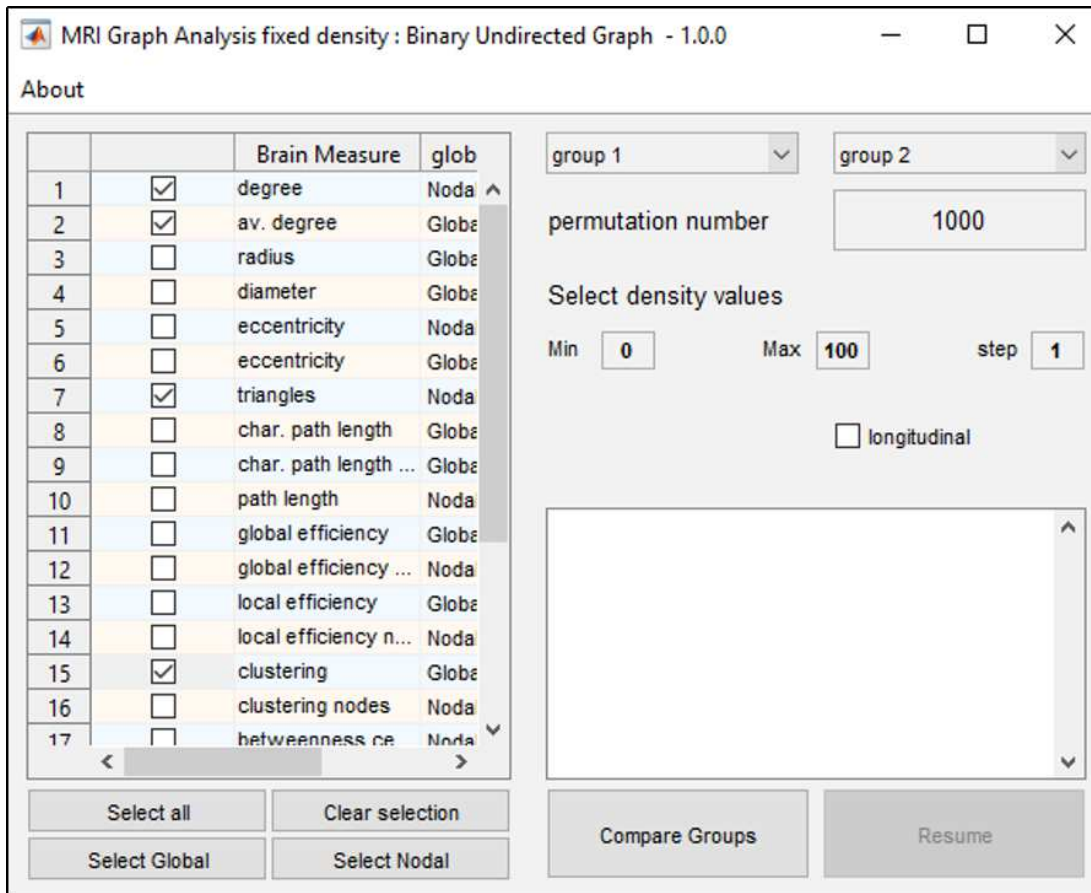


Figure 4.10: Snapshot of the interface that can be used to perform a between-group comparison. Taken from [141].

### 4.2.3 The underlying BRAPH architecture

All actions that can be performed by the graphical user interfaces have their bases in the implementation of few objects. Each object has a specific set of methods and properties that achieve a particular purpose. However, while the *Brain Atlas* marks the start of the connectivity analysis for all neuroimaging modalities, the *Cohort* and *Graph Analysis* are implemented separately for each of the four imaging techniques (MRI, fMRI, EEG and PET).

Although in this section I will illustrate the objects' organization and interaction by using the structural MRI as an example, the other imaging modalities are implemented analogously. The main differences exist in the different structure



of few properties and methods of the relevant objects due to the fact that they have to handle different data types in the structural and functional analysis. In particular, the data of an MRI subject will be an array (one value per brain region) while the data of an fMRI subject is a matrix (multiple values per brain region). In another example, the calculated measures in structural data reflect group properties; however, in functional data they are indicative of the properties of the individual subjects, and as such, the measures need to be further averaged over all subjects.

#### 4.2.3.1 The *graph* package

*Graph* is a stand-alone package that consists of few objects with the aim to facilitate the calculation of the graph measures and transformation between different graph types (e.g. weighted to binary, directed to undirected). All of these are achieved by the methods of the class **Graph**, which creates a graph and implements the set of measures that can be calculated on this graph. These measures are defined as the constant properties of the graph; additional properties include its adjacency matrix and **Structure**. The **Structure** property is implemented as a separate object, which facilitates the calculation of the community structure of the graph by various algorithms (for example, structure can be calculated by Newman and Louvain algorithms, or the user can define a custom structure).

**Graph** is an abstract class, therefore, instances of this class cannot be created. Instead, one of the sub-classes (e.g., **GraphBD**, **GraphBU**, **GraphWD**, **GraphWU**) should be used to implement the methods for that particular graph type. Additional properties for each of these sub-classes include a list of all measures for the relevant graph type and the parameters needed to obtain that graph from the most general weighted directed graph; for example, to obtain binary undirected graph, one needs to specify threshold or density as well as symmetrization rule (section 2.2).

### 4.2.3.2 Data structure classes

All objects that are used to define the brain atlas, cohort and graph analysis are instances of a group of abstract classes that provide the general framework of properties and methods that are needed in the higher levels of the hierarchical architecture of BRAPH. This group consists of:

- **List Element** represents an element of a **List**. Each List Element has a property which is defined by its tag, format and value. The methods in this class serve to access and set the properties of each element of the list.
- **List** represents a list of indexed elements. The properties of a list include a catalogue of its elements. List's methods involve the manipulation of the elements of the list, such as the addition, removal or changing the position of given element.
- **Group** is a group of list elements. A group has a name, notes and data, which is represented as a series of ones and zeros that indicate the participation of each element in the corresponding group.
- **Group List** represents a list of groups.
- **List With Groups** is a list of elements that are grouped into various groups. This class is a child of **List** and it has a list of the groups as its additional property. Therefore, all list elements can be manipulated individually, while at the same time they are assigned to different groups.
- **Hash List Element** represents an element of a hash list. This class is mainly used to define the hash value of a certain element of a list.

### 4.2.3.3 The brain atlas object

Few hierarchically organized objects provide the foundations to execute the actions for the creation and manipulation of a Brain Atlas. These objects can be split into two broad categories, as objects that build and plot the brain atlas.

Building of a brain atlas is accomplished by two objects:

- **Brain Region** is defined as list element (see section 4.2.3.2). This object represents a brain region with the properties: name, label, (x, y, z) coordinates and hemisphere participation. Its methods are mostly inherited from the **List Element** class and they include the setting and the retrieval of the values assigned to each of its properties.
- **Brain Atlas** is defined as list (section 4.2.3.2), where the elements of this list are the individual brain regions. Atlas' properties include the name and the brain surface (the default brain surface in BRAPH is based on the ICBM 152 template [142]). The majority of Brain Atlas' methods are inherited from the **List** class and they involve various actions to manipulate the list elements, such as addition, removal or changing the position of an element, as well as saving and loading the brain atlas to an external file.

On the other hand, the plotting of a brain atlas is achieved by the following three objects:

- **Plot Brain Surf** is an object that plots and manages the brain surface based on the ICBM 152 template [142]. Its properties involve the different options to visualize the brain surface (such as, color, transparency, orientation) while its methods achieve the manipulation of the axis of the graph, such as, setting the axis limits, turning the grid on/off or setting the desired view.
- **Plot Brain Atlas** plots and manages the brain regions that make up a brain atlas. The brain regions can be plotted by using symbols, spheres or labels, therefore, most of the methods of Plot Brain Atlas are used to apply their corresponding plot properties. Additionally, since the brain regions are plotted on a brain surface, Plot Brain Atlas is a child of the object **Plot Brain Surf** and inherits all of its properties and methods.

- **Plot Brain Graph** plots a brain graph by manipulating the links between brain regions. The links can be plotted by using lines, arrows or cylinders, therefore, most of the methods of Plot Brain Graph are used to apply their corresponding plot properties. This object is a child of **Plot Brain Atlas** and, therefore, inherits the properties of both objects described above. As a result, Plot Brain Graph provides all essential methods needed for the visualization of a brain graph (brain regions and connections between them) on a brain surface.

#### 4.2.3.4 The MRI cohort object

The MRI Cohort is implemented by the properties and methods of two objects:

- **MRI Subject** is defined as list element (see section 4.2.3.2). This object represents a subject with MRI data that has the properties: code, age, gender and data. Its methods are mostly inherited from the **List Element** class and they include the setting and the retrieval of the values assigned to each of its properties.
- **MRI Cohort** represents a cohort of subjects with MRI data. The properties of MRI Cohort object include the MRI subjects, various groups that subjects can belong to, and Brain Atlas (as a result, one cannot initialize an MRI Cohort without previously defining the Brain Atlas object). MRI Cohort is defined as a list with groups (section 4.2.3.2; all the subjects in the cohort are arranged into a list and each group is associated with a data (a series of ones and zeros) corresponding to a participation decision for each subject. Therefore, MRI Cohort inherits its methods from the class **List With Groups** which include methods to manipulate the individual subjects and groups (to add, remove or change their positions in the list) as well as methods to change the participation status of each subject to any group.

#### 4.2.3.5 MRI graph analysis

**MRI Graph Analysis** is an abstract class that represents a list of measures used for graph analysis of MRI data. Instances of this class cannot be initiated, instead, one of its sub-classes (**MRI Graph Analysis BUD**, **MRI Graph Analysis BUT** or **MRI Graph Analysis WU**) should be used. **MRI Graph Analysis** inherits the properties and methods of the class **List** (section 4.2.3.2), its list elements are the measures (graph measures used to characterize the brain network; one measure can be calculated per group), the comparisons (between group or longitudinal comparisons of given measures) or random comparisons (comparison of the measure with the one calculated for random networks) that can be calculated for the corresponding graphs.

The properties of this class include the cohort, the subject data, the adjacency matrix (one per group), the community structure and hashtables for each measure, comparison and random comparison. Additional properties of an **MRI Graph Analysis** include the ones that define the adjacency matrix of a given group, such as graph and correlation types and variable specifying how to deal with the negative correlations. The main method of this class is the calculation of the adjacency matrix, additional methods achieve the retrieval of the various properties of the class.

#### 4.2.3.6 The MRI graph analysis BUD object

In this sections I describe the series of objects that are invoked to perform binary undirected analysis at fixed density (BUD). The objects that are utilized to perform the BUT and WU analysis follow analogous pattern to the ones discussed in this section.

- **MRI Measure** is an abstract class that represents a measure of MRI data. This class inherits the properties and methods of **Hash List Element** (section 4.2.3.2). As this class cannot be initiated, one of its sub-classes

(**MRI Measure BUD**, **MRI Measure BUT** or **MRI Measure WU**) should be used.

- **MRI Measure BUD** represents MRI measure of binary undirected graph with fixed density. This object is an instance of **MRI Measure** and it inherits its properties and methods. Each Measure BUD has few properties the include its code, group, value, density and threshold at which the measure is calculated. Its most important method involves assigning a hash value to the measure based on its properties so that it can be located within the graph analysis list. In order to save computational time the measures are not calculated repeatedly, therefore if a measure is located in the list, it is not recalculated again.
- **MRI Comparison BUD** represents MRI comparison of binary undirected graph with fixed density. It is a child of **MRI Measure BUD** thereby inheriting its properties and methods. Additional methods involve the calculation of the difference between the measure values of two groups and the corresponding confidence intervals. The additional properties of MRI Comparison BUD are introduced to reflect the features of the performed comparison, such as number of permutations, single and double tailed p-values.
- **MRI Random Comparison BUD**, represents MRI comparison of binary undirected graph at fixed density with random graphs. It is defined analogously to the MRI Comparison BUD.
- **MRI Graph Analysis BUD** is a graph analysis of fixed density binary undirected MRI. Its properties are inherited from the abstract class **MRI Graph Analysis**. The methods of MRI Graph Analysis BUD include the calculation of network measures for a given group or the implementation of the permutation test in order to compare two groups or single group with random graph. After the calculation of each measure or comparison, it is added to the list. Before calculation, the list is checked to see whether a measure exists, thus, a measure is calculated only if it is not present in the list.

#### 4.2.3.7 Utility objects

- **BNC** defines set of constants and auxiliary methods for BRAPH.
- **Check** is used to validate certain inputs. In particular, it checks whether an input is real, integer or object, and in the case of multiple inputs, it validates whether they have the same size.
- **GUI** defines a set of constants and methods of general use in the graphical user interfaces of BRAPH.
- **Plot Data Element** creates and manages an element which data is to be plotted. This object inherits the properties and methods of **List Element**. Its additional properties hold the information about the elements' x and y values and the plot properties of the markers and lines used to plot them.
- **Plot Data Area** creates and manages an area element which data is to be plotted. It inherits the properties and methods of **Plot Data Element**. Additional properties hold the information about the plot and data (for example, the x and y values of the area boundaries) properties of the plotted area.
- **Plot Data** manages and plots the data of elements in a list. It is a subclass of **List** and it inherits its properties and methods used to manipulate the elements of the list. Plot Data's methods allow the plotting of single or multiple elements by using symbols and lines as well as setting the axis properties.

#### 4.2.4 Subjects

In order to demonstrate BRAPH's capabilities, we performed structural and functional connectivity analysis in two unrelated studies. In the structural study, we examined the possible differences in network topology between healthy subjects, amnesic MCI patients and AD patients (the details for each group are given in table 4.1) from the Alzheimer's Disease Neuroimaging Initiative (ADNI) database

(adni.loni.usc.edu). Being led by Principal Investigator Michael W. Weiner, MD, ADNI started in 2003 in the form of public-private partnership with the aim to investigate whether the clinical evaluation can be combined with some biological markers in order to assess the development of MCI and early AD. The participants were scanned by using a sagittal 3D T1-weighted MPRAGE sequence on a 1.5 Tesla MRI imaging system. The details of the sequence are as follows: echo time ( $TE$ ) = 3.0 – 4.1 ms; repetition time ( $TR$ ) = 9 – 13 ms; flip angle ( $FA$ ) =  $8^\circ$ ; inversion time ( $IT$ ) = 1000 ms; voxel size =  $1.1 \times 1.1 \times 1.2$  mm<sup>3</sup>.

Table 4.1: Characteristics of the structural MRI sample. CTR - controls; MCI - Mild Cognitive Impairment; AD - Alzheimer’s disease; MMSE - minimal state examination. The gender differences were evaluated using the  $\chi^2$  test while the differences between the other variables (age, education and MMSE scores) were estimated using an analysis of variance (ANOVA). In each cell, the means of the sample are followed by the standard deviations in the parentheses [132].

	<b>CTR</b> - 210 subjects	<b>MCI</b> - 377 subjects	<b>AD</b> - 181 subjects	<b>F</b> or $\chi^2$ tests (p value)
Age (y)	76.1(5.0)	74.5(7.5)	75.6 (7.0)	0.017
Sex (M/F)	110/100	243/134	97/84	0.005
Education(y)	16.0(2.9)	15.7(3.0)	14.8(3.2)	< 0.001
MMSE	29.1(0.9)	27.0(1.8)	23.2(2.0)	< 0.001



Table 4.2: Characteristics of the fMRI sample. CTR - controls; PD-CN - Parkinson’s disease cognitively normal; PD-MCI - Parkinson’s disease with mild cognitive impairment; UPDRS-III - Unified Parkinson’s disease rating scale–Part III; HY stage - Hoehn and Yahr stage; MoCA - Montreal cognitive assessment scale. The gender differences were evaluated using the  $\chi^2$  test while the differences between the other variables (age, education and MoCA scores) were estimated using Student’s T test. In each cell, the means of the sample are followed by the standard deviations in the parentheses [132].

	<b>CTR - 15</b> subjects	<b>PD-CN - 69</b> subjects	<b>PD-MCI - 15</b> subjects
Age (y)	66.4(9.1)	61.0(10.4)	63.5(8.2)
Sex (M/F)	13/2	46/23	11/4
Education (y)	16.5(2.3)	15.3(2.9)	14.2(3.1)
UPDRS-III	-	18.2(9.1)	21.8(8.9)
HY stage	-	1.7(0.5)	1.8(0.4)
MoCA	27.9(1.6)	27.6(1.9)	24.0(3.7)
Disease time (y)	-	1.2(0.9)	2.4(1.5)
	<b>CTR vs</b> <b>PD-CN (p</b> value)	<b>CTR vs</b> <b>PD-MCI (p</b> value)	<b>PD-CN vs</b> <b>PD-MCI (p</b> value)
Age (y)	0.066	0.372	0.378
Sex (M/F)	0.125	0.361	0.616
Education (y)	0.112	0.024	0.204
UPDRS-III	-	-	0.161
HY stage	-	-	0.297
MoCA	0.615	0.001	< 0.001
Disease time (y)	-	-	< 0.001

In the second study, the analysis was performed on the resting-state fMRI data obtained from healthy controls, PD patients that were cognitively normal and PD patients with MCI (the details for each group are given in table 4.2). The patients were from the Parkinson’s Progression Markers Initiative (PPMI) (2011) [143] ([www.ppmiinfo.org/data](http://www.ppmiinfo.org/data); accessed in November, 2015), which was started in 2010 as an international and multicenter study with the goal to establish biomarkers for PD progression. Following already established criteria for diagnosis of PD-MCI in the PPMI cohort [144], PD patients were categorized as PD-MCI (i.e. they have MCI) if their scores on two cognitive tests are 1.5 standard deviation below the scaled mean scores. Conversely, if the patients do not meet the conditions to be classified as PD-MCI, they were considered to be cognitively normal (PD-CN). The images of all participants were taken in Erlangen, Germany on a 3 Tesla scanner by using an echo-planar imaging sequence with the following details: echo time = 25 ms; repetition time = 2400 ms; voxel size =  $3.25 \times 3.25 \times 3.25$  mm<sup>3</sup>; matrix =  $68 \times 68$ ; flip angle = 80°; total scan time was 8 minutes and 29 seconds which included 210 volumes.

Each participating site in ADNI and PPMI received approval from an ethical standards committee before study initiation and obtained written informed consent from all participants.

#### **4.2.5 Network construction and analysis**

In order to examine the topological properties of the structural networks in controls, amnesic MCI patients, and AD patients from ADNI the adjacency matrices were built in the following way:

- MRI T1-weighted images were preprocessed using FreeSurfer (version 5.3), following the steps detailed in Pereira et al [96].
- 82 regions were assigned as nodes in the networks and cortical thickness and subcortical volumes were extracted for each region.

- The connection strength between all pairs of regions were calculated by the Pearson's correlation coefficient, and the negative correlations were set to zero.
- By fixing the density of connections, binary undirected graphs were analyzed in the density range 5% to 25%, in steps of 0.5%.

The functional network topologies of elderly controls from PPMI, PD-CN and PD-MCI patients were assessed by the following steps:

- Their fMRI images were preprocessed by SPM8 (<http://www.fil.ion.ucl.ac.uk/spm>). In shortly, this step involved removing of the first five volumes, realignment, slice-timing correction, filtering to retain only low frequency signals (0.01 – 0.08 Hz), normalization to the Montreal Neurological Institute (MNI) template (voxel size  $3 \times 3 \times 3$  mm<sup>3</sup>) and regression of white matter and cerebrospinal fluid signals as well as the six head motion parameters.
- For each subject, 200 brain regions derived from the Craddock atlas [139] were assigned as nodes in the network and time-series values for each brain region were extracted.
- The connection strength between all pairs of regions were calculated by the Pearson's correlation coefficient, and the negative correlations were set to zero.
- The graph theoretical analysis was performed on the weighted undirected graphs.

In order to asses statistical differences between groups in both studies, non-parametric permutation tests with 10000 permutations were conducted. The differences were considered to be statistically significant for a two-tailed test of the null hypothesis at  $p < 0.05$ . In the case of the nodal results, the number of multiple comparisons were controlled by applying the FDR procedure at  $q < 0.05$ .

## 4.3 Results

### 4.3.1 Structural network topology in amnesic MCI and AD

The structural adjacency matrices and brain graphs of patients and controls can be found in figure 4.11. All groups showed strong correlations between bilaterally homologous regions.

Concerning the global network topology (figure 4.12), the characteristic path length and local efficiency increased in MCI and AD patients compared to controls over various network densities. The most pronounced changes were observed in transitivity and modularity: transitivity decreased while modularity increased in MCI and AD patients when compared to controls over almost all densities of the network. Furthermore, the AD patients, when compared to the MCI patients, exhibited increases in the characteristic path length at some network densities while showing widespread changes in the transitivity and modularity.

In the case of the local topology (figure 4.13), significant increases in the nodal degree are shown in the left medial orbitofrontal, right insula, bilateral rostral anterior cingulate and posterior cingulate gyri, while decreases are shown in the left middle temporal, right precentral and right inferior parietal gyri in AD patients compared to controls. When compared to MCI, AD patients also presented a higher nodal degree in the left rostral anterior cingulate and isthmus cingulate gyri.

In addition to the nodal degree, the nodal local efficiency was compared between groups. It significantly increased in the left transverse temporal gyrus in MCI patients compared to controls. In AD patients, the local efficiency increased in the bilateral temporal pole and left entorhinal cortex and decreased in few regions from the frontal (bilateral superior frontal, left pars triangularis, bilateral pars opercularis, right postcentral gyri), temporal (bilateral inferior temporal gyri, amygdala, hippocampus) and parietal (left inferior parietal, right precuneus)

lobes. When AD patients were compared with MCI patients, the efficiency of the right rostral anterior cingulate increased in AD patients.

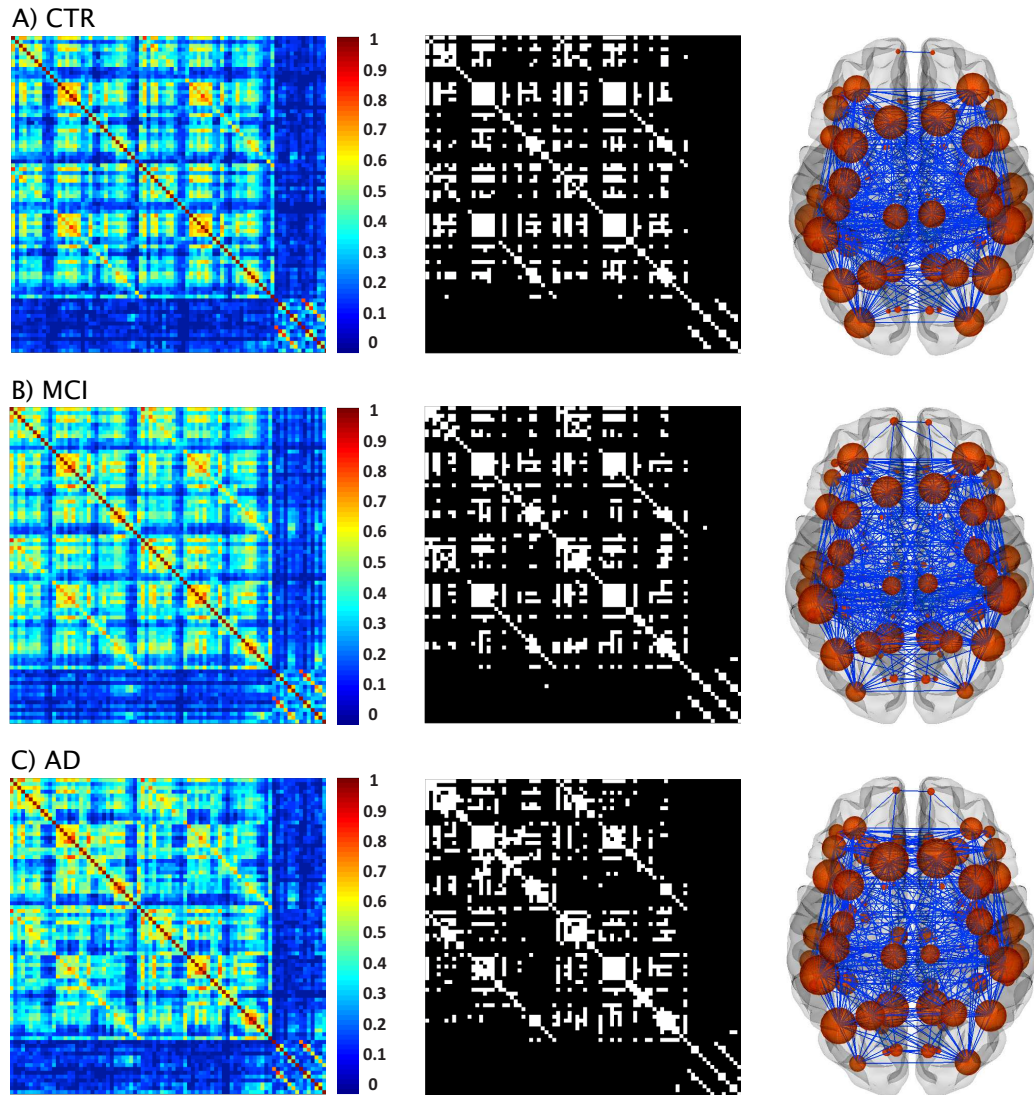


Figure 4.11: Structural brain networks in controls, MCI patients, and AD patients. The 82 region weighted adjacency matrices (left), the binary adjacency matrices at 15% density of connections (center) and the corresponding binary undirected graphs (right) are shown for A) controls (CTR), B) patients with amnesic mild cognitive impairment (MCI), and C) Alzheimer's disease (AD) patients. Taken from [132].

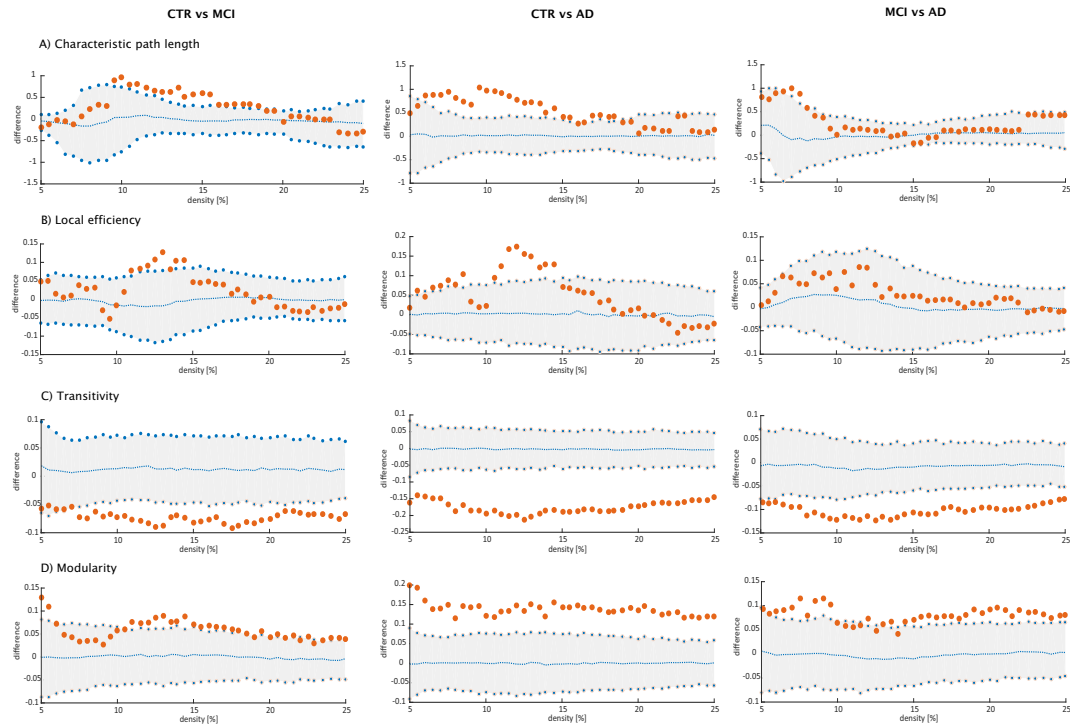


Figure 4.12: Differences between groups in global structural topology. The differences in A) characteristic path length, B) local efficiency, C) transitivity and D) modularity are calculated between: controls (CTR) and Alzheimer’s disease (AD) patients (left); controls (CTR) and patients with mild cognitive impairment (MCI) in the center; patients with mild cognitive impairment (MCI) and Alzheimer’s disease (AD) patients (right). The plot indicate the lower and upper bounds (blue circles) of the 95% Confidence Intervals (CI) (gray shade) as a function of density. The differences between groups are indicated by the orange circles; they are considered to be statistically significant at  $p < 0.05$  when they fall outside of the confidence interval. The blue dots plotted in the middle of the CI (around zero) show the mean values of the difference between the randomized groups while performing the permutation test. Taken from [132].

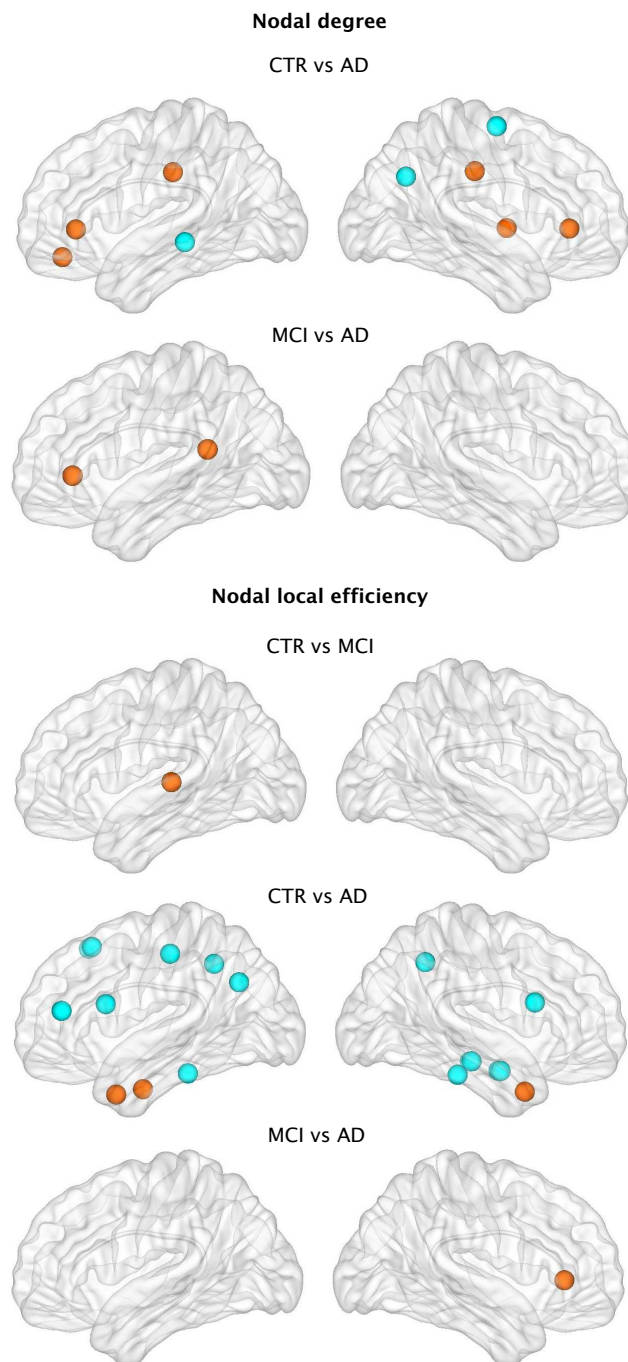


Figure 4.13: Differences between groups in nodal structural measures. Only the nodes that show significant differences between the corresponding groups after FDR corrections are plotted. Orange designates increases in the relevant nodal measures, while blue designates decreases. Taken from [132].

### 4.3.2 Functional network topology in PD-MCI

The functional adjacency matrices of controls, PD-CN and PD-MCI patients are illustrated in figure 4.14. We compared the weighted average degree (section 2.3) between the both groups of patients and controls. The results showed that PD-CN and PD-MCI patients have less connections (controls = 183.7; PD-CN = 175.2; PD-MCI = 172.6) than the controls. This difference was statistically significant in the case of PD-MCI (p-value = 0.027) and showed a tendency in the direction of significance in the case of PD-CN (p-value = 0.081).

Furthermore, we conducted an analysis of the community structure of each group (based on their weighted graphs shown in figure 4.14) in order to evaluate the presence of smaller communities (or modules) of regions within their corresponding networks. We could identify five modules in all three groups which were quite similar to each other. Module I consisted of medial frontal areas, the posterior cingulate and bilateral angular gyri, resembling the default-mode network. Module II included temporal and cerebellar areas. Module III comprised several middle, inferior frontal and parietal regions, similarly to the fronto-parietal network usually found in resting-state studies [70, 145]. Module IV included most of the visual cortex similarly to the previously reported visual network. Finally, Module V was mainly made up of temporal and inferior frontal areas as well as the insula.

The calculation of the average degree within each module revealed that PD-CN patients had a lower number of connections compared to controls in Module II, which included temporal and cerebellar areas (PD-CN = 49.02; controls = 51.89; p-value = 0.020). The same trend was observed in Module V consisting of insular, temporal and inferior frontal regions (PD-CN = 28.39; controls = 28.93; p-value = 0.040). None of the regions present in these modules showed significant difference between PD-CN patients and controls after correcting for FDR.

We also observed that, when compared to controls, PD-MCI patients had less connections in Module III that consists of fronto-parietal areas (PD-MCI = 54.87; controls = 57.95; p-value = 0.002) and Module V including insular, temporal



and inferior frontal areas (PDMCI = 28.37; controls = 28.93; p-value = 0.040). After FDR corrections, few regions in Module III had significantly smaller degree in PD-MCI patients: the bilateral superior frontal, bilateral superior parietal gyri, precuneus, left middle frontal gyrus, inferior frontal gyrus and left anterior cingulate (figure 4.15(a)). On the other hand, in module V, the left insula, right frontal orbital gyrus and bilateral transverse temporal gyri (figure 4.15(b)) showed significantly lower degree in PD-MCI patients.

In order to check whether the results of the PD-MCI group were influenced by the existence of various MCI subtypes, we compared the nodal and average degree of Modules III and V between each subtype and controls. In the current study, the PD-MCI group was made up of 9 patients that had multiple-domain MCI and 6 patients with single-domain MCI (5 amnesic, 1 patient non-amnesic). Both subtypes had lower average degree when compared with controls in Module III (multipledomain MCI = 54.6; single-domain MCI = 55.3; controls = 58.0) and Module V (multipledomain MCI = 28.4; single-domain MCI = 28.3; controls = 28.9). With the exception of right transverse temporal gyrus, which had a similar degree in controls and single-domain MCI patients, all other regions in the two modules showed smaller nodal degrees in both MCI subtypes when compared with controls (tables 4.3 and 4.4) .

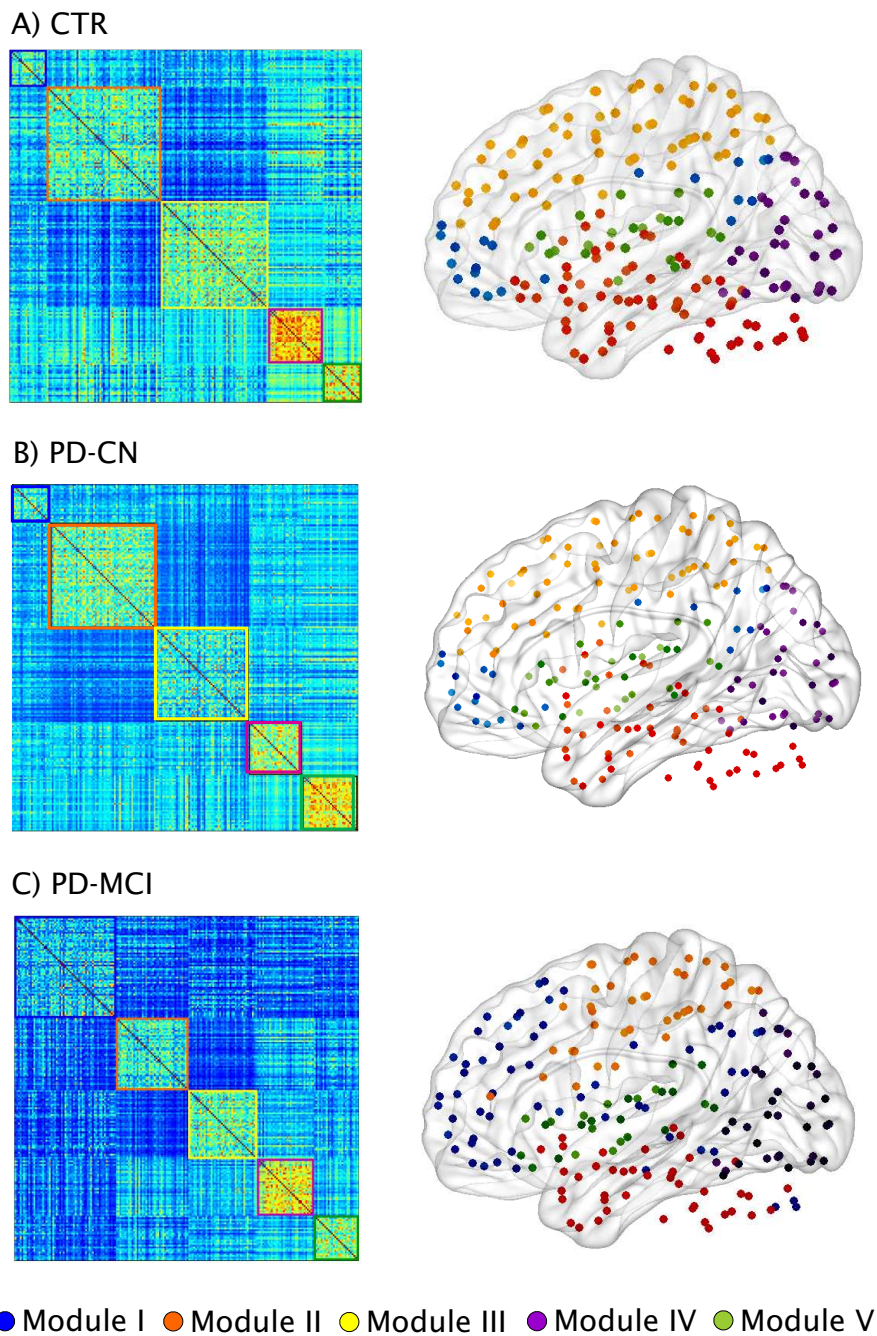


Figure 4.14: Functional brain networks and modules in controls and PD-MCI patients. Weighted connectivity matrices (on the left) and modules (on the right) are shown for A) controls (CTR) and Parkinson's disease patients B) with normal cognition (PD-CN) and C) with mild cognitive impairment (PD-MCI). Five modules were identified in each group. Taken from [132].

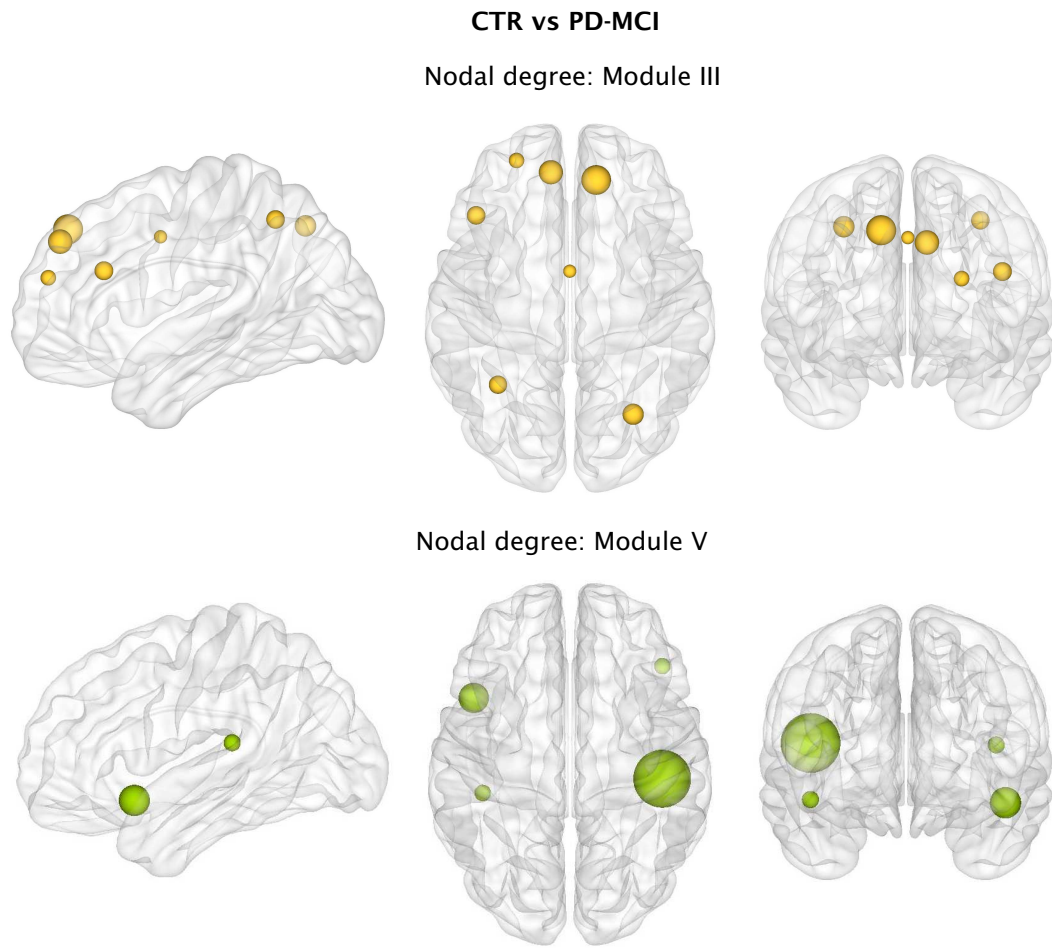


Figure 4.15: Differences between groups in the nodal functional degree. The plotted spheres indicate the regions from Modules III and V that exhibit significant decreases in the nodal degree in Parkinson’s disease patients with mild cognitive impairment (PD-MCI) compared to controls (CTR) after FDR corrections. Taken from [132].

Table 4.3: Nodal degree for regions in Module III in PD-MCI subtypes and controls. CTR - controls; PD-MCI - Parkinson’s disease with mild cognitive impairment. In each cell, the means of the sample are followed by the standard deviations in the parentheses [132].

Module III regions	CTR - 15 subjects	Multiple-domain PD - MCI - 9 subjects	Single-domain PD - MCI - 6 subjects
Lh Superior Frontal G	59.7 (0.8)	58.0 (3.0)	56.7 (4.7)
Lh Anterior Cingulate	59.8 (0.6)	58.0 (4.0)	55.7 (5.9)
Lh Superior Frontal G	58.7 (2.7)	52.0 (13.9)	53.6 (4.7)
Lh Middle Frontal G	59.4 (1.5)	55.7 (6.5)	54.4 (7.5)
Lh Superior Parietal G	59.7 (0.6)	57.5 (4.8)	56.4 (3.9)
Lh Inferior Frontal G	59.1 (1.6)	54.0 (7.0)	56.3 (3.3)
Lh Precuneus	60.0 (0.0)	58.0 (4.9)	56.6 (4.5)
Rh Superior Frontal G	58.8 (1.8)	53.2 (13.8)	50.9 (8.7)
Rh Superior Parietal G	59.0 (2.0)	54.7 (5.8)	53.4 (7.4)
Rh Precuneus	59.7 (0.6)	57.5 (4.8)	56.4 (3.9)

Table 4.4: Nodal degree for regions in Module V in PD-MCI subtypes and controls. CTR - controls; PD-MCI - Parkinson’s disease with mild cognitive impairment. In each cell, the means of the sample are followed by the standard deviations in the parentheses [132].

Module V regions	CTR - 15 subjects	Multiple- domain PD - MCI - 9 subjects	Single- domain PD - MCI - 6 subjects
Lh Insula	29.0 (0.0)	28.8 (0.4)	28.6 (1.3)
Lh Transverse Temporal G	29.0 (0.0)	28.7 (0.8)	28.6 (1.3)
Rh Frontal Orbital G	29.0 (0.0)	28.5 (1.2)	28.7 (0.7)
Rh Transverse Temporal G	29.0 (0.0)	29.0 (0.0)	28.7 (1.0)

## 4.4 Discussion

In this chapter, I described BRAPH, the first object-oriented software that provides the necessary tools for all researchers, irrespective of their scientific background, to perform graph theory analysis. Since the network science is a dynamic subject that evolves at an increasing rate, it is vital to have a very-well structured software that can be modified or expanded easily, so that the existing methods can be extended and integrated with the new topological analyses and graph theory measures. One of the BRAPH’s main advantages is the fact that it allows the user to deal with all stages in the connectivity analysis by providing a considerable help at each step, ranging from the definition of nodes and edges to producing the final high resolution images of the results as well as saving all

results and analysis parameters in a dedicated file. In order to get an idea of BRAPH's capabilities, in the following sections I discuss the results obtained by analyzing structural and functional data obtained from patients with amnesic MCI, AD and PD-MCI.

#### **4.4.1 Large-scale structural networks in amnesic MCI and AD**

Alzheimer's disease is one of the most widespread neurodegenerative disorders that places a significant burden on the caregiver and has a very significant impact on society [146]. Although a lot of effort has been dedicated in order to better understand and diagnose AD, its underlying effects on the topological organization of the brain networks remain poorly understood. An increasing number of studies offer evidence proposing that the amyloid plaques neurofibrillary tangles, which are pathological indicators of AD, might use the neural connections and synapses in order to spread through the brain. Therefore, the graph theoretical study of the brain connectivity could be used to shed light on the disease spreading mechanisms in AD.

In this study, we found that the global network topology of the brain networks in AD patients has abnormal organization that is demonstrated by decreases of transitivity accompanied by increases in modularity, local efficiency and path length. These changes point out that the regions in AD patients' network have less efficient communication with each other and between separate brain communities. Especially, the transitivity and modularity showed the most extensive changes in the network organization. The decreases in the transitivity observed in AD patients show that the neighboring areas in AD patients are poorly connected with each other. Moreover, the modularity increases indicate that the communities in AD patients have much higher within-community connectivity and worse inter-community connectivity. Patients that have amnesic MCI, and are possibly on the path to develop AD, also showed similar, albeit less extensive, network changes suggesting that amnesic MCI might be indeed an intermediate stage

between healthy aging and dementia. The above results agree with the findings reported by various studies [147, 96].

By comparing the nodal degree in AD network with controls and patients with MCI, we observe that the most extensive changes in the number of connections are observed in regions that are part of the default-mode network, including the medial orbitofrontal, the anterior cingulate and posterior cingulate gyri. Since these regions correspond to areas that show amyloid deposition, gray matter atrophy and glucose hypometabolism in AD patients [148], the default-mode network is commonly associated with AD. As a result, the changes in the nodal degree obtained in this study, may partially be indicative of pathological and metabolic abnormalities that frequently are present in AD patients.

On the contrary, both MCI and AD patients displayed changes in the nodal local efficiency. While these alterations were only present in a sole region in the left temporal lobe in MCI patients, the AD patients showed changes in local efficiency across few regions in frontal, temporal and parietal areas, including the hippocampus and amygdala, which have roles in AD pathology [149]. Since the local efficiency quantifies the efficiency of information transfer between a given region and its neighbors, the decreasing of this measure could possibly reflect the loss of local connections. On the contrary, the increases in the local efficiency might reveal a compensatory process by which the number of connections between close brain areas increases in order to counterbalance the connection loss between remote brain areas.

To conclude, all of our findings discussed above point to the direction that graph theory is a convenient method that can be used to evaluate abnormalities in the brain networks organization in the prodromal and clinical stages of AD.

#### **4.4.2 Large-scale functional networks in PD**

One of the key non-motor symptoms that can affect the quality of life in Parkinson's disease patients is cognitive impairment. Throughout the progression of

PD, the patients can receive the diagnosis of MCI if they start to experience cognitive impairment in one or more domains, which can be associated with a greater risk to progress to dementia [150]. Therefore, there exists a crucial need to identify the underlying mechanisms of MCI in order to prevent the cognitive decline in PD patients.

By analyzing PD patients' weighted networks in BRAPH, we observed that PD-MCI patients exhibited lower number of connections in the whole brain network than healthy controls, which stipulates that, in general, PD-MCI have more disconnected brain regions. However, after determining their community structure and performing the analogous analysis within each community, we found that these effects were mostly driven by the lower degrees observed in the fronto-parietal network and in a network involving temporal and inferior frontal regions in the PD-MCI group. The regions that were most affected in these networks were the superior frontal gyri, superior parietal gyri, precuneus, transverse temporal gyri and insula, which have already been shown to present decreased connectivity in PD [151] and recognized as important brain hubs [152]. The hubs are considered to be the most central regions of a network that take part in a lot of long-distance connections. As a result, they possibly have higher metabolic costs along with an increased vulnerability to oxidative stress [152]. In a previous study [153], it was shown that the pathological brain lesions are concentrated in hub regions of the connectome in several neurodegenerative disorders, including PD, in line with our findings. The analysis was repeated separately in single-domain and multiple-domain MCI groups; we observed that the above regions exhibited diminished connectivity in both subtypes, therefore indicating that our findings were not driven by any specific subgroup of PD-MCI.

In addition to the above results concerning the PD-MCI group, we identified that PD-CN patients have lower number of connections in two networks that consisted of temporo-cerebellar areas and temporo-frontal regions, which agrees with earlier fMRI studies that established abnormalities in these brain areas in patients with PD [151]. Furthermore, the inferior temporal gyri and inferior frontal cortex are among the initial cortical areas that are affected by Lewy body pathology in autopsy cases with PD [154]. This indicates that they possibly play a relevant



role in the progression of the disease from brainstem structures to cortical brain areas. The fact that both PD-CN and PD-MCI patients showed abnormalities in the same network of inferior temporal and frontal areas provides support to this assumption and suggests that these regions are important to understand disconnectivity in PD regardless of cognitive status.

### 4.4.3 BRAPH features

The application of network science to study the brain's structure and function is still a new field that faces few crucial challenges. One of the most important challenge is whether the complex brain connectome with billions of neurons and synapses between them, can be reduced and accurately represented by relatively low number of nodes (typically few hundred to thousand) and edges. Although currently there is a limited knowledge on how to solve this issue, BRAPH can help in addressing few other challenges.

In particular, given that the true connectome is a sparse network, it is important to threshold the structural or functional edges, which typically consist of continuous association indices [155]. This process of thresholding can be accomplished via various methods. On one hand, the threshold can be applied by specifying some significance level, such that only the connections that surpass this level are considered in the analysis. Therefore, all weak connections are regarded to be not genuine and are eliminated from the analysis. As a result, this thresholding scheme yields uneven number of connections for various individuals or groups. On other hand, one can enforce the equal number of connections across various networks by applying threshold that would result in a fixed value of density. Therefore, the analysis is done by considering only a fixed percentage of edges which results in the measures being independent of the number of edges [155]. Both thresholding schemes are made available in BRAPH and they can be easily compared by the user.

Additional important challenge is the choice of the threshold value. As currently there is no accepted consensus of what is the best threshold value, BRAPH allows

the user to test the hypothesis across different levels of significance in order to establish the reproducibility of the results. Since some authors believe that the choice of the threshold range is an arbitrary process that has a heavy influence on the results we also provide the option to carry out weighted network analysis. In this case, the user can analyze both strong and weak connections in a network, obtaining results that do not depend on a particular thresholding scheme.

Moreover, the realization that different node definitions can lead to different results in the graph theory analysis poses yet another challenge. To help in this regard, BRAPH provided six anatomical and functional brain atlases that can be employed within the same study in order to check the dependency of the results on the different parcellation schemes. Furthermore, a new brain atlas can be easily created or uploaded in BRAPH that adjusts to the user needs.

The final challenge that BRAPH can deal with is the normalization of the network measures by their counterparts calculated on networks with random organization (that preserve the degree and/or weight distribution). Various options are provided in BRAPH that can help the user to perform this normalization.

# Chapter 5

## Disrupted Network Topology in Patients with Stable and Progressive MCI and Alzheimer's Disease

### 5.1 Introduction

Alzheimer's disease (AD) is a highly damaging neurodegenerative disorder that deprives the affected individuals of most of their cognitive functions (for example, language, visuospatial and executive abilities) as well as their memories over the course of the disease. It has been observed that the development of these symptoms commonly occurs in a well ordered manner, and the stage of the symptoms may indicate the degree of the amyloid deposits' accumulation and the spatial distribution of neurofibrillary tangles [156]. For example, while the early phases of the disease are associated with a memory loss that is a consequence of the existence of tangles in medial temporal regions [157, 158, 159], aphasia and apraxia take place at later points which can be due to the spread of tangles and plaques into neocortical areas [160, 161]. Due to this progressive spread of pathology

between interconnected regions of the brain, AD can be considered as a disconnection syndrome that can result in abnormalities in brain networks [162]. Such abnormalities are exhibited through the loss of connections in various regions (for example, in the default mode network) that is thought to occur due to the accumulation of amyloid plaques in these regions [163, 164].

In order to apply graph theory to study the brain networks of AD patients in vivo, one can utilize various neuroimaging techniques, such as DTI, structural, and functional MRI (these methods are reviewed in [147, 165, 166]) or PET [167, 168]. By analyzing structural MRI data, it has been demonstrated that the global organization of the brain networks in AD patients is altered when compared with healthy controls [166, 169]. However, there is a disagreement about the characteristics of such changes; some studies found that the path length and clustering coefficient increase in the AD patients' networks while other studies have shown decreases or even no changes in these measures [166, 170]. Similarly, some studies found that the network topology in AD patients shows small-world characteristics, while others identified random or regular network topologies [166]. One possible reason for these inconsistencies could be the inclusion of small sample sizes that consist of patients that have heterogeneous clinical characteristics. Although there is great interest to analyze the brain connectivity in AD, to date, there are no studies that have studied the community structure of the structural MRI networks built in AD patients.

As a transition state between AD and normal aging, a patient with amnesic mild cognitive impairment (MCI) has a very high risk to progress to dementia [171]. While patients with MCI have exhibited abnormal functional connectivity and disrupted integrity of the white matter [172, 173, 174, 175], the direct link between the above features and the altered network topology are not completely clear. While one study could not find differences in the clustering coefficient and path length when MCI patients were compared to controls [176], another study could identify significant differences that were very diverse and changed in line with the method of network construction. There is increasing evidence showing that MCI patients progress to AD at a rate of approximately 15% per year [177]. Therefore, it is important to study the organization of brain networks in stable

MCI as well as networks in patients who show fast or slow advance to dementia in order to understand the particular changes in the network that indicate the transition to AD, thereby understanding the effects the disease continuation has on brain networks.

In this chapter, I will discuss the usage of graph theory to characterize the organization abnormalities that occur in the structural brain networks in subjects with stable MCI (sMCI), patients who show a slow (late MCI converters, lMCIc) and fast (early MCI converters, eMCIc) progression to dementia and AD patients. The subject cohort consisted of over 1000 subjects from 2 multicenter cohorts: the Alzheimer's Disease Neuroimaging Initiative (ADNI) and the AddNeuroMed study. Few global (the small-worldness, the characteristic path length and the mean clustering coefficient) and local (the nodal closeness centrality and the nodal clustering) network measures were calculated in order to characterize these networks. Unlike the previous studies, I will also show how the transitivity and modularity (which are for example, indicative of the network's ability to perform specialized processing tasks within local, very well connected groups of regions) vary across patient groups. The starting hypothesis is that all patient groups would show altered behavior in the global measures; when compared with controls, more pronounced changes in the network topology were expected in lMCIc, eMCIc, and AD patients than sMCI patients. Moreover, since the series of abnormalities occurring between regions of the default-mode network are suggestive of the expanding of the tangle pathology in AD [148, 178], we hypothesized that these regions will show the most noticeable changes in the local network measures.

## 5.2 Materials and methods

### 5.2.1 Subjects

In this cohort, a total of 1008 subjects from the ADNI database (adni.loni.usc.edu) and the AddNeuroMed study were studied. 301 of these subjects were healthy controls, 452 were diagnosed as MCI while 282 were AD patients. The MCI group consisted of: 87 patients were diagnosed as early MCI converters (eMCIc, they converted to AD after 1 year), 71 progressed to AD after 3 years (late MCI converters, lMCIc) while 110 of them did not convert to AD in the 3 years of monitoring (stable MCI, sMCI). Another subgroup of MCI was sMCI-1y, which consisted of subjects that were stable after 1 year but they did not have any follow-up data after that year. Finally, because they did not have a precise diagnosis, eight subjects were not included in the analysis. The characteristics of these subjects are summarized in table 5.1.

The ADNI started in 2003 with the aim to study whether various biological markers can be combined with some clinical assessment in order to quantify the advance of MCI and early AD. In order for a subject to be included in the ADNI cohort as a healthy control, the subject would need to obtain a score in the range 24 - 30 from the Mini-Mental State Examination (MMSE), a score of 0 from Clinical Dementia Rating-Sum of Boxes (CDR - SB) and not show signs of dementia, MCI or depression. The MCI group patients were included based on the Peterson criteria [171] for amnesic MCI. The AD patients who were included in this cohort fulfilled the criteria of the National Institute for Neurological and Communicative Disorders and Stroke - Alzheimer's Disease and Related Disorder Association (NINDS/ADRDA) for probable AD, scored in the range of 18 - 26 from the MMSE and had a CDR-SB score in the range 0.5 - 1.0. The patients who had other notable disease (different from incipient AD), used some medications that could result in memory impairment or had history of head trauma or structural brain lesions were excluded from ADNI cohort.

AddNeuroMed is an Integrated Project (funded by the European Union Sixth

Table 5.1: Characteristics of the sample. CTR, controls; sMCI, stable mild cognitive impairment after 1 year (sMCI-1y) or 3 years (sMCI); lMCIc, late mild cognitive impairment converters; eMCIc, early mild cognitive impairment converters; AD, Alzheimer’s disease; MMSE, mini-mental state examination; CDR, clinical dementia rating scale. Differences in age, years of education, and MMSE scores were assessed using an analysis of variance (ANOVA). Differences in CDR scores were assessed using a Kruskal–Wallis test and differences in gender were assessed using a  $\chi^2$  test In each cell, the means of the sample are followed by the standard deviations in the parentheses [96].

	<b>CTR</b> (n = 301)	<b>sMCI-1y</b> (n = 157)	<b>sMCI</b> (n = 110)	<b>lMCIc</b> (n = 71)	<b>eMCIc</b> (n = 87)	<b>AD</b> (n = 282)	<b>F or <math>\chi^2</math> tests</b> (p value)
Age (years)	75.1 (5.7)	75.0 (6.5)	74.7 (7.5)	74.8 (7.0)	74.1 (6.7)	75.6 (7.0)	0.9 (0.475)
Gender (male/female)	156/145	88/69	74/36	43/28	54/33	130/152	19.2 (0.002)
Education (years)	14.2 (4.4)	11.8 (5.2)	15.7 (3.0)	16.1 (3.0)	13.9 (4.2)	12.2 (4.9)	21.2 ( $< 0.001$ )
MMSE scores	29.1 (1.1)	27.0 (1.6)	27.6 (1.7)	26.7 (1.7)	26.6 (1.8)	22.4 (3.5)	272.8 ( $< 0.001$ )
CDR scores	0	0.5	0.5	0.5	0.5	0.9 (0.4)	880.2 ( $< 0.001$ )

Denoting the significant differences at level  $p < 0.001$  as: **a** - CTR and sMCI; **b** - sMCI-1y and AD; **c** - sMCI and AD; **d** - lMCIc and AD; **e** - eMCIc and AD; **f** - CTR and sMCI-1y; **g** - CTR and lMCIc; **h** - CTR and AD; **i** - sMCI-1y and sMCI; **j** - sMCI-1y and lMCIc; **k** - sMCI-1y and eMCIc; **l** - sMCI and eMCIc; **m** - lMCIc and eMCIc; **n** - CTR and eMCIc; **o** - sMCI and lMCIc. The groups statistical differences for each property are as follow: Gender - **a,b,c,d,e**; Education - **f,a,g,h,i,j,k,l,c,m,d,e**; MMSE - **f,a,g,n,h,i,b,o,l,c,d,e**; CDR - **f,a,g,n,h,b,c,d,e**.

Framework program) [179, 180] with the task to produce and validate various novel models of AD disease and its treatment on the basis on in vivo and in vitro models in humans and animals. In humans, AddNeuroMed makes use of MRI magnetic resonance spectroscopy (MRS) in order to ratify imaging markers that would help diagnose and detect the disease early as well as evaluate the effectiveness of various therapies. The data were contributed by 6 different imaging sites: University of Kuopio (Finland), University of Perugia (Italy), Aristotle University of Thessaloniki (Greece), King’s College London (United Kingdom), University of Lodz (Poland), and University of Toulouse (France) [179, 181, 182]. In order for a subject to be included in AddNeuroMed cohort as a healthy control, the subject would need to obtain a score in the range 24 - 30 from the Mini-Mental State Examination (MMSE), a score of 0 from Clinical Dementia Rating (CDR), would need to be aged 65 years or older and not show signs of any neurological diseases, including dementia, depression, organ failure or other unsteady systematic disease. The MCI group patients were included by following the similar criteria as the control group, the difference being a CDR score of 0.5 and reported problems in the memory by the informant or the patient. The AD patients who were included in this cohort fulfilled the criteria of NINDS/ADRDA and DSM-IV for probable AD, scored in the range of 12 - 28 from the MMSE, were 65 years or older and did not have any unsteady systematic diseases, organ failure or other psychiatric or neurological disease in addition to AD.

### 5.2.2 MRI acquisition

Data acquisition for the AddNeuroMed study was designed to be compatible with ADNI [181, 182, 183]. All participants from both cohorts were scanned in an MRI system of 1.5 Tesla (5 scanning sites were used to acquire data for AddNeuroMed, while 58 sites were used for the ADNI data) with a a sagittal 3D T1-weighted MPRAGE sequence with the following parameters: echo time ( $TE$ ) = 3.0 – 4.1 ms; repetition time ( $TR$ ) = 9 – 13 ms; flip angle (FA) =  $8^\circ$ ; inversion time (IT) = 1000 ms; voxel size =  $1.1 \times 1.1 \times 1.2 \text{ mm}^3$ . These cohorts were combined in few studies [184, 185], thereby demonstrating that the patients



from both cohorts show very similar atrophy patterns and have comparable predictive power to differentiate AD and MCI patients from healthy controls.

### 5.2.3 Image preprocessing

The obtained T1-weighted MRI images were preprocessed by using the version 5.1 of the FreeSurfer software. The preprocessing steps included the following: adjustment for the spatial distortions and motion artifacts that can arise because of the non-linearity of the magnetic gradient and inhomogeneity of the B1 magnetic field; taking away the nonbrain tissue by employing a hybrid watershed/surface deformation procedure [186]; automated conversion to the standard Talairach space; normalization of the intensity [187]; tessellation of the gray/white matter boundary; automated topology correction [188]; and deformation of the surface according to the intensity gradients, with the aim to position the gray/white and gray/CSF borders at the place where the transition between tissue classes is indicated by the greatest shift in intensity. After the completion of the cortical models, registration to a spherical atlas took place, that makes use of the cortical folding patterns of each individual in order to match their cortical geometry across subjects [189]. Finally, the cerebral cortex was parcellated into 68 regions via the brain atlas Desikan et al. [134]; additionally, 7 subcortical structures were also included: hippocampus, amygdala, thalamus, caudate, putamen, accumbens, and pallidum (illustrated in figure 5.1). The HiveDB database system [190] was used to preprocess all data, and 8 subjects who were designated as outliers in the cortical thickness and subcortical volume measures were excluded from the analysis.

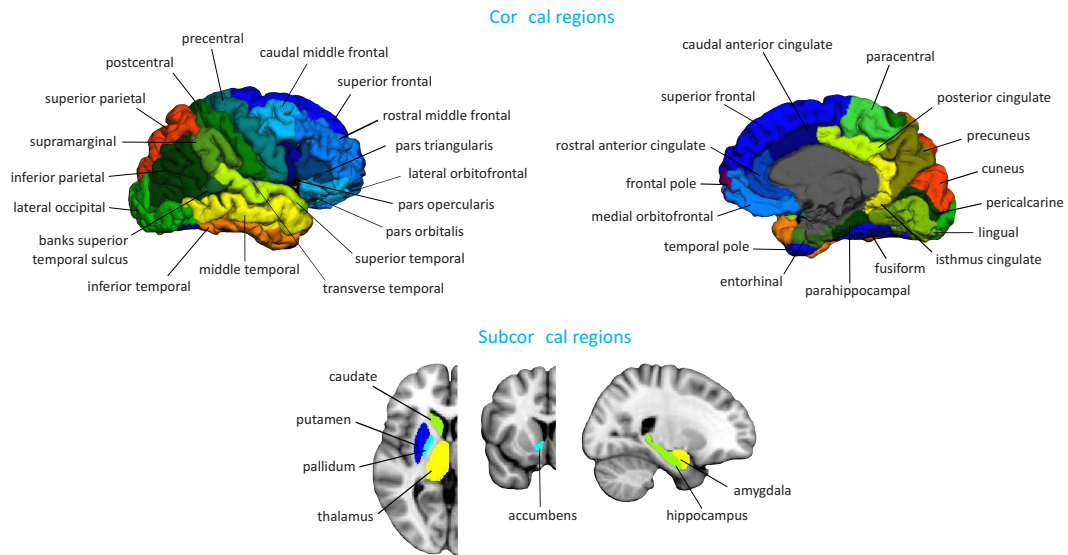


Figure 5.1: Brain regions that were used in network construction and analysis. From each of these regions for every subject, the cortical thickness and subcortical volumes were extracted. Taken from [96].

## 5.2.4 Network construction and analysis

In order to control for the effects of gender, age and education of the individual subjects, linear regression was performed for all cortical regions [90]. By including the intracranial volume as an another covariate, the same procedure was also performed for subcortical regions. Furthermore, in order to be certain that the scanning location of the subjects (63 scanning center in total) would not have effect on the results, we performed a regression analysis with the scanning site as an additional covariate (the results are presented in appendix A.1.1).

The raw values were substituted by the residuals from the regression analysis which were subsequently used to calculate the connectivity network. This network was build such that each brain region was represented as a node and the edges represented inter-regional correlations [90]. In here, we used both cortical thicknesses and subcortical volumes in order to build the networks, similarly to earlier studies [97].

Each group was associated with an  $82 \times 82$  adjacency matrix. Each entry in this matrix was calculated as the Pearson correlation coefficient between the corrected anatomical measures of the corresponding regions across the group of subjects (figure 5.2). Each adjacency matrix was further binarized by fixing the density of connections for every group (chapter 3); we analyzed the binary matrices across a range of densities (the minimum density was 5%, the maximum was 35%, in the steps of 1%) and compared the resulting network topologies for different groups across this range. For densities greater than 35%, the networks did not have small-world properties (the small-world coefficient for these networks was near 1), thus, they were similar to random networks. On the other hand, for densities lower than 5%, these networks had very low number of edges and became widely disconnected. The self-connections were excluded from the analysis and all negative correlation coefficients were equated to 0.

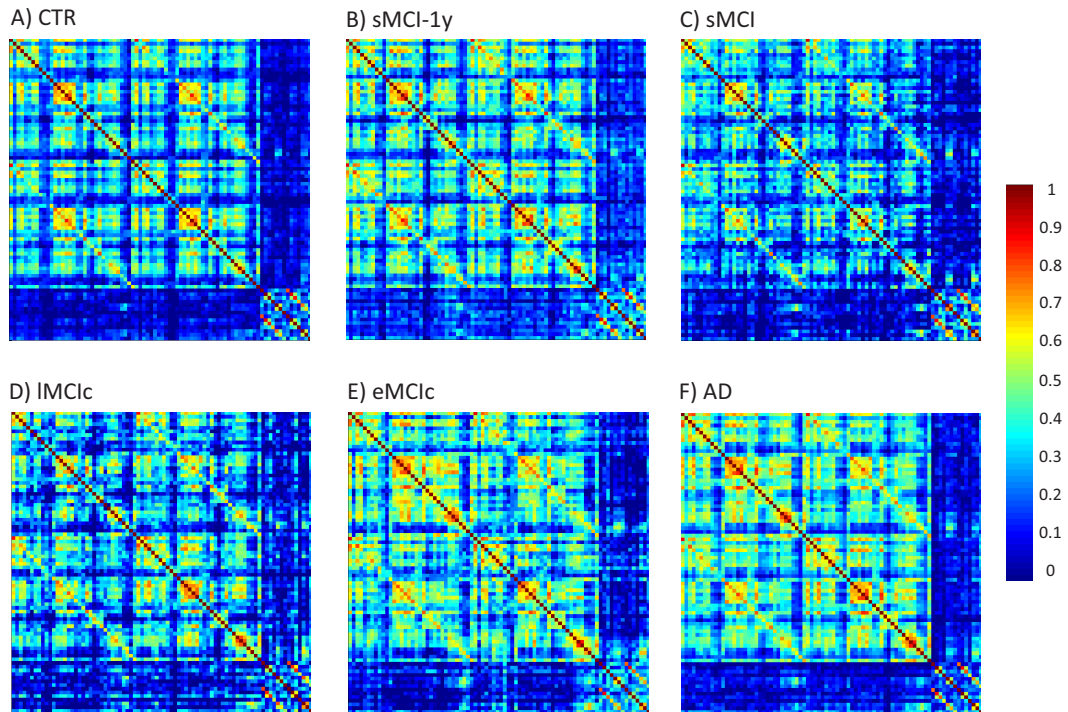


Figure 5.2: Structural adjacency matrices are shown for: (A) controls (CTR), (B) sMCI patients after 1 year (sMCI-1y), (C) sMCI patients (after 3 years), (D) IMCIc, (E) eMCIc, and (F) AD patients. In these matrices, the last rows and columns correspond to the relations between the subcortical areas, while the rest correspond to relations between cortical regions. The strength of the connections is indicated by the corresponding color; stronger (weaker) correlations are shown by warmer (colder) colors. Taken from [96].

We calculated the mean clustering coefficient, the characteristic path length, the transitivity, modularity and small-worldness in order to characterize the global network topology. On the other hand, the regional network properties were evaluated by the calculation of the closeness centrality and the nodal clustering, which can be indicators of different network features and have not been extensively studied in MCI and AD. In order to assess the nodes' roles in each community, we calculated the participation coefficient and the within-community nodal degree (chapter 2). All measures were calculated by using BRAPH [132] (chapter 4) and the visualization of the networks was accomplished by using BrainNet Viewer

[124] ([http://www.nitrc.org/projects/ bnv/](http://www.nitrc.org/projects/bnv/)).

### 5.2.5 Comparison of network measures between groups

The statistical significance of the between-group differences was evaluated by using the non-parametric permutation test with 1000 simulations, as described in section 3.3. The results were reported by using the 95% confidence intervals (CI) as a critical values for a 2-tailed test of the null hypothesis at  $p < 0.05$ . The nodal measures were corrected for the multiple hypothesis testing by using the false discovery rate (FDR) at  $q < 0.05$  (section 3.3.3).

## 5.3 Results

The sample characteristics are summarized in table 5.1. Since we found significant differences in the education years and gender between the groups ( $p < 0.001$ ), the data for the cortical thickness and subcortical measures were corrected for these variables. In general, all groups of patients had significantly lower MMSE scores ( $p < 0.001$ ) and higher CDR scores ( $p < 0.001$ ) than controls. The AD patients had lower MMSE scores than sMCI, lMCIc, eMCIc patient groups ( $p < 0.05$ ), furthermore, lMCIc and eMCIc had worse MMSE scores when compared with the sMCI patients ( $p < 0.05$ ). Finally, sMCI-1y scored lower on the MMSE than sMCI group ( $p < 0.05$ ).

### 5.3.1 Global network analysis

For each group, the weighted adjacency matrices are plotted in figure 5.2. From the correlation patterns of all groups, it can be observed that all reciprocally homologous regions have strong correlations between them. In general, we could observe that all groups showed a small-world topology. Moreover, with increasing

values of the density of the networks ( $D$ ), the transitivity and the mean clustering coefficient increased while the modularity and the characteristic path length decreased (as illustrated in figure 5.3).

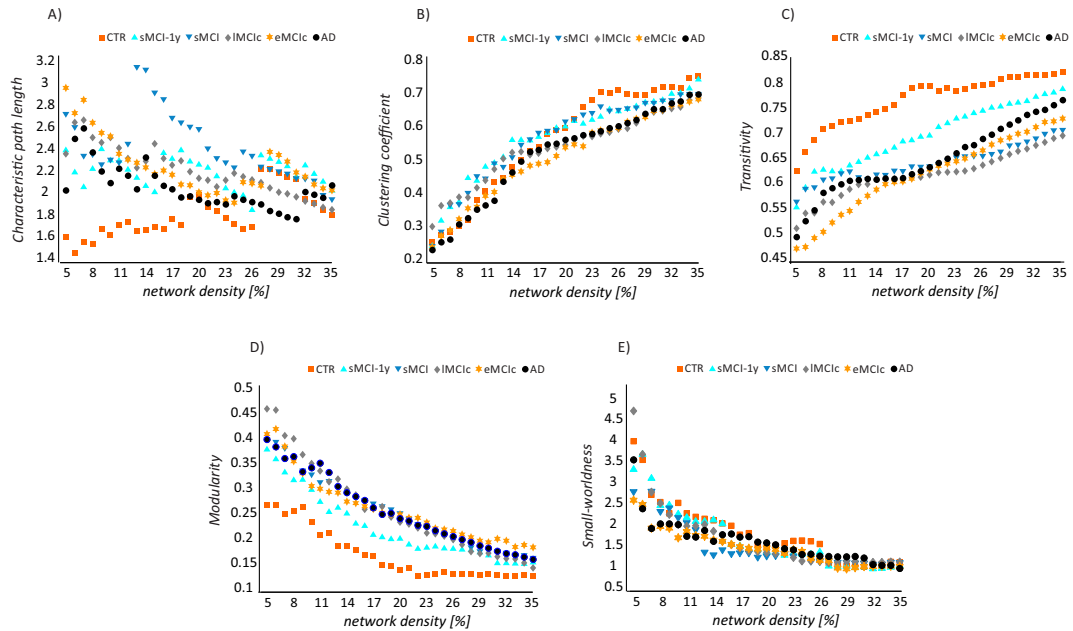


Figure 5.3: Changes in global network measures as a function of network density. Characteristic path length (A), clustering coefficient (B), transitivity (C), modularity (D), and small-worldness (E) calculated for the following groups: CTR - Controls; sMCI-1y - patients with stable mild cognitive impairment after 1 year; sMCI - patients with sMCI after 3 years; eMCIc and IMCIc - MCI patients that converted early (after 1 year) and late (after 3 years) to AD; and AD - Alzheimer’s patients. Taken from [96].

When analyzing the differences between various groups, we observed that, over several densities of the networks, the characteristic path lengths increases in the sMCI, IMCIc, eMCIc, and AD groups when compared with the controls (P range, 0.043 – 0.001). The clustering coefficient decreases at few different densities in IMCIc, eMCIc, and AD (P range, 0.043 – 0.001) when compared with controls; however it shows no changes for the sMCI patients. The most widespread differences between patients and controls were observed for the transitivity and

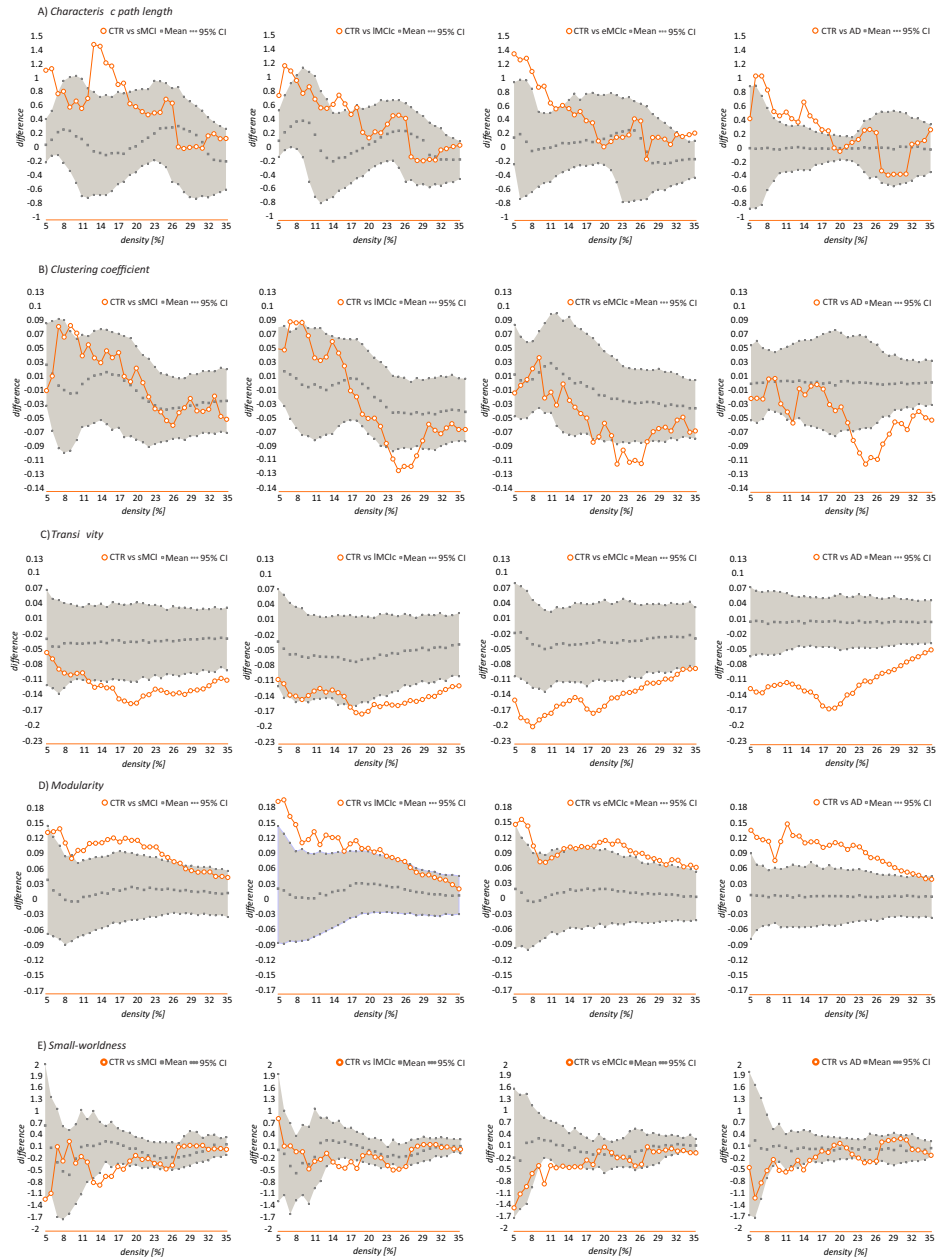


Figure 5.4: Differences between controls and sMCI, IMCIc, eMCIc, and AD patients in global network measures. From left to right, the plots show the differences between: controls (CTR) and sMCI patients; CTR and IMCIc; CTR and eMCIc; CTR and AD patients for the following global network measures: characteristic path length (A), clustering coefficient (B), transitivity (C), modularity (D), and smallworldness (E). If the difference between two groups (orange circles) fall outside of the CI (gray area), they are statistically significant at the level of  $p < 0.05$ . Taken from [96].

modularity; at most densities of the network, the transitivity significantly decreased (P range, 0.049 – 0.001) while modularity significantly increased (P range, 0.049 – 0.001) in the patients groups. Finally, we could also find that the small-worldness significantly decreases, albeit for only few network thresholds, in the patients groups when compared with controls (P range, 0.040 – 0.010). All of the above results are summarized in figure 5.4.

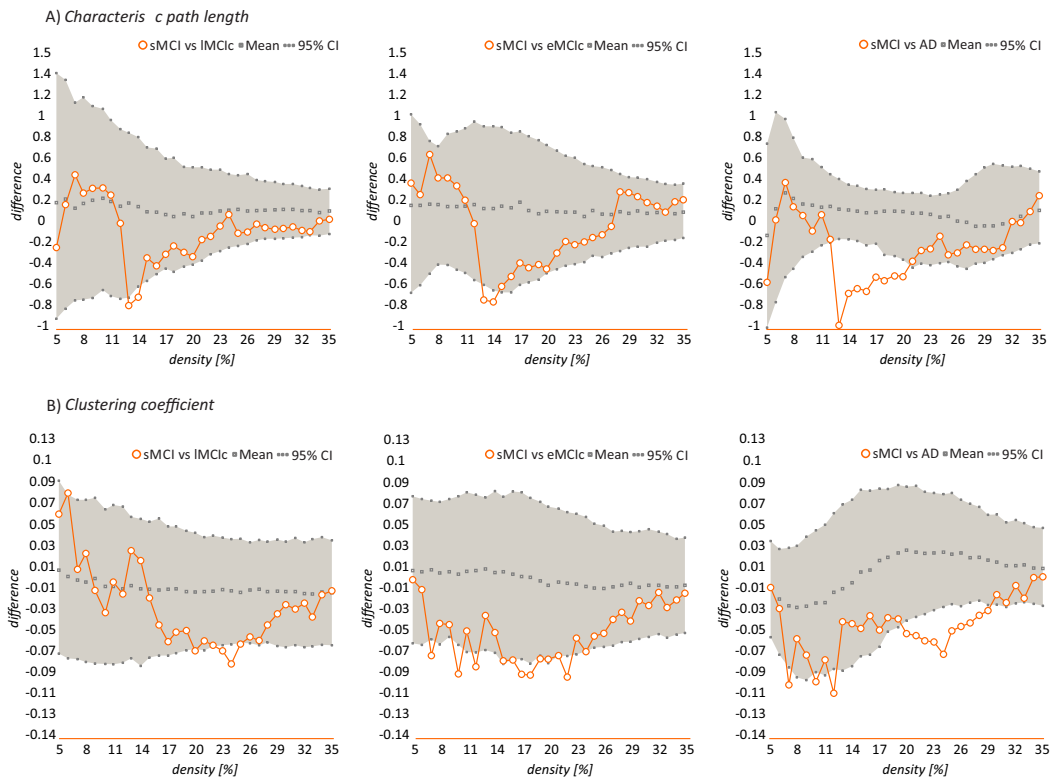


Figure 5.5: Differences between sMCI and IMCIc, eMCIc, and AD patients in global network measures. From left to right, the plots show the differences between: sMCI and IMCIc patients; sMCI and eMCIc patients; sMCI and AD patients; for the following global network measures: characteristic path length (A) and clustering coefficient (B). If the difference between two groups (orange circles) fall outside of the CI (gray area), they are statistically significant at the level of  $p < 0.05$ . Taken from [96].

In the comparison between the various patient groups, we found that the IMCIc,



eMCIc, and AD patients exhibited lower clustering coefficient (P range, 0.042 – 0.001) and characteristic path length (P range, 0.048 – 0.001) than sMCI patients (figure 5.5). Between these groups, there were no significant differences in the modularity or transitivity. Moreover, in the global network organization, we did not observe any significant differences between lMCIc, eMCIc, and AD patients.

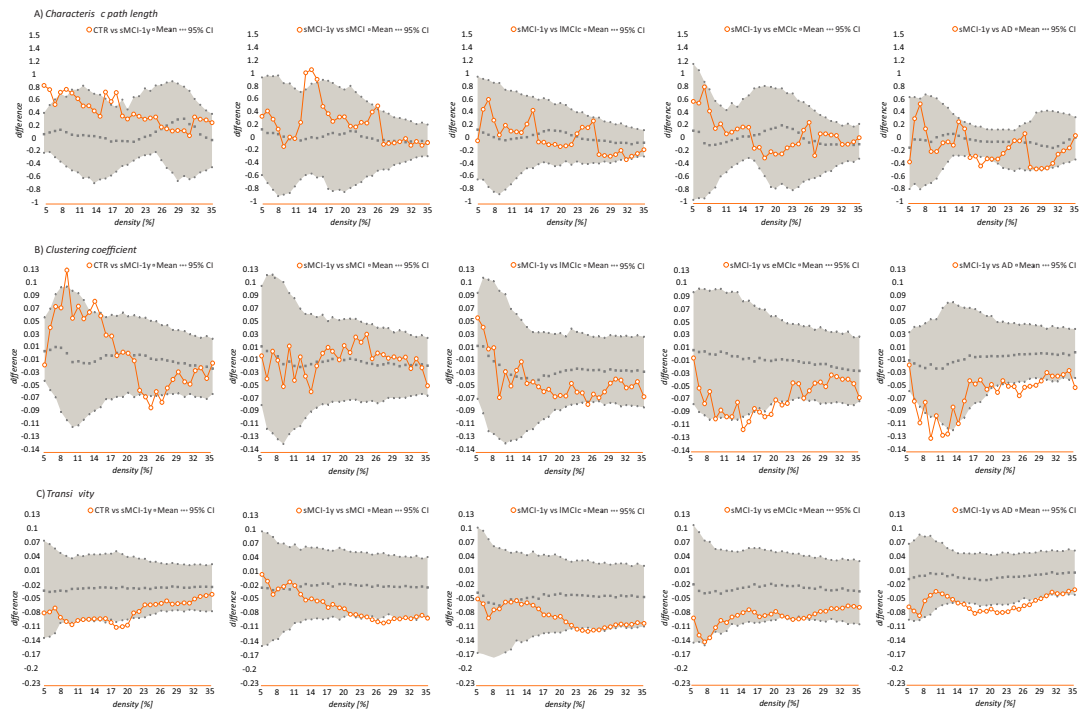


Figure 5.6: Differences between sMCI-1y and sMCI, lMCIc, eMCIc and AD patients in global network measures. From left to right, the plots show the differences between: sMCI-1y and sMCI patients; sMCI-1y and lMCIc; sMCI-1y and eMCIc; sMCI-1y and AD patients; for the following global network measures: the characteristic path length (A), clustering coefficient (B), transitivity (C). If the difference between two groups (orange circles) fall outside of the CI (gray area), they are statistically significant at the level of  $p < 0.05$ . Taken from [96].

Differently with the other MCI groups, we observed no significant changes of the modularity and transitivity in sMCI-1y patients when compared to controls. However, at few network densities, sMCI-1y patients exhibited increased path lengths (P range, 0.045 – 0.004) and changes in the clustering coefficient (P

range, 0.044 – 0.018). Additionally, they had higher transitivity (P range, 0.048 – 0.019) than AD patients and also higher clustering than both, eMCIc (P range, 0.046 – 0.018) and AD patients (P range, 0.043 – 0.016). The sMCI-1y patients did not exhibit changes in the small-worldness and modularity when compared with the other patient groups. The results for the comparison of sMCI-1y with the other patient groups and controls are summarized in figure 5.6.

In order to evaluate if these results are influenced by the fact that patients were scanned in various scanning centers, the controls were also compared to the patient groups after including the scanning sites as a covariate in the analysis. These analyses between controls and patient groups showed analogous differences in the mean clustering, the characteristic path length, the transitivity and modularity to the results presented above, therefore, indicating that the scanning centers did not have an effect on our results.

### **5.3.2 Nodal network analysis**

Nodal network measures also exhibited several changes between different groups. In general, the nodal clustering coefficient was lower in patients groups when compared to controls, while showing widespread changes solely in the AD group. Moreover, all patient groups exhibited decreased nodal closeness centrality in the bilateral hippocampi and amygdala, while increased centrality, with level that varied across the different patient groups, was observed in medial parietal, medial temporal, and limbic regions. In this section, I will discuss these general changes in more detail.

After we corrected the results for multiple hypothesis testing (FDR,  $q < 0.05$ ), we observed a decrease in the clustering coefficient in the left superior frontal gyrus in the case of sMCI patients, and in the right postcentral gyrus in the case of eMCIc patients comparison with controls. In the comparison between AD patients and controls, the AD patients exhibited decreased nodal clustering in the following regions: the bilateral precuneus, superior frontal gyri, lateral orbitofrontal gyri,

middle temporal gyri, inferior temporal gyri, fusiform, hippocampi, and amygdala; the left pars triangularis gyrus, postcentral gyrus; and the right caudal middle frontal gyrus, pars opercularis gyrus, and lateral occipital gyrus (figure 5.7 and table 5.2). Furthermore, the clustering decreased in the left postcentral gyrus of AD patients when compared with sMCI patients (FDR,  $q < 0.05$ ).

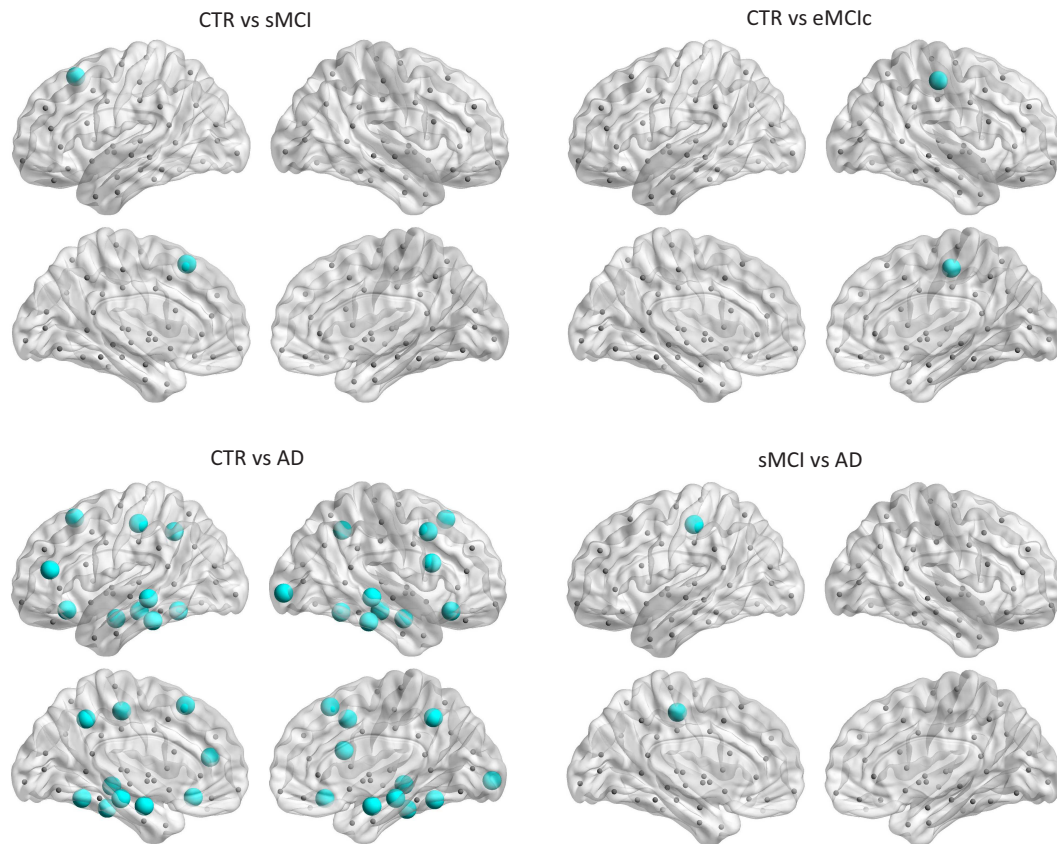


Figure 5.7: Significant decreases in the nodal clustering coefficient in sMCI, eMCIc, and AD patients. CTR - controls; sMCI - stable MCI; eMCIc - early MCI converters, AD - Alzheimer’s disease. All regions that exhibit the decrease in the clustering coefficients are listed in table 5.2. Taken from [96].

Table 5.2: List of the regions showing significant differences in the nodal clustering coefficient between groups (FDR - corrected). Note: CTR - controls; sMCI - stable mild cognitive impairment; lMCIc - late mild cognitive impairment converters; eMCIc - early mild cognitive impairment converters; AD - Alzheimer’s disease; Lh - left hemisphere; Rh - right hemisphere; G - gyrus [96].

Region	CTR	sMCI	P value
Lh Superior frontal G	0.83	0.50	0.002
Region	CTR	eMCIc	P value
Rh Postcentral	0.94	0.56	0.001
Region	CTR	AD	P value
Lh Superior frontal G	0.83	0.57	0.001
Lh Lateral orbitofrontal G	0.81	0.5	0.001
Lh Pars triangularis G	0.90	0.65	0.001
Lh Postcentral G	0.96	0.68	0.001
Lh Precuneus	0.78	0.58	0.001
Lh Middle temporal G	0.78	0.62	0.017
Lh Inferior temporal G	0.94	0.64	0.002
Lh Fusiform	0.79	0.56	0.004
Lh Hippocampus	1	0.33	0.001
Lh Amygdala	1	0.33	0.001
Rh Superior frontal G	0.78	0.52	0.001
Rh Caudal middle frontal G	0.92	0.77	0.009
Rh Lateral orbitofrontal G	0.71	0.45	0.003
Rh Pars opercularis G	0.96	0.62	0.001
Rh Precuneus	0.80	0.62	0.017
Rh Lateral occipital G	0.74	0.60	0.007
Rh Middle temporal G	0.81	0.61	0.016
Rh Inferior temporal G	0.90	0.66	0.003
Rh Fusiform	0.84	0.53	0.001
Rh Hippocampus	1	0.33	0.001
Rh Amygdala	1	0.33	0.001
Region	sMCI	AD	P value
Lh Postcentral	0.95	0.68	0.001

The closeness centrality showed decreases in the hippocampi and amygdala in all patient groups when compared to controls. Additionally, significant decreases were also observed in the right pericalcarine gyrus in sMCI and lMCIc patients and in the right accumbens in eMCIc patients. Closeness centrality increased in the left posterior cingulate in sMCI patients; the left pallidum, right insula, right temporal pole, right entorhinal in lMCIc patients; the left posterior cingulate, right lateral orbitofrontal gyrus, bilateral insula, bilateral entorhinal in AD patients (figure 5.8 and table 5.3). Moreover, closeness centrality showed significant differences in the comparison between the patient groups, most notably in the temporal, occipital, and subcortical regions (for further details, see table 5.3).

Table 5.4, shows a summary of the results about the behavior of the global and nodal measures for different groups.

Table 5.3: List of the regions showing significant differences in the nodal closeness centrality between groups (FDR - corrected). CTR - controls; sMCI - stable mild cognitive impairment; lMCIc - late mild cognitive impairment converters; eMCIc - early mild cognitive impairment converters; AD - Alzheimer’s disease; Lh - left hemisphere; Rh - right hemisphere; G - gyrus [96].

Region	CTR	sMCI	P value
Lh Posterior cingulate	0.30	0.48	0.001
Lh Hippocampus	1	0.29	0.001
Lh Amygdala	1	0.34	0.001
Rh Pericalcarine	0.38	0.28	0.001
Rh Hippocampus	1	0.38	0.001
Rh Amygdala	1	0.33	0.001
Region	CTR	lMCIc	P value
Lh Pallidum	0.39	1	0.001
Lh Hippocampus	1	0.39	0.001
Lh Amygdala	1	0.34	0.001
Rh Insula	0.28	0.53	0.001
Rh Pericalcarine	0.38	0.30	0.001

Continued

Table 5.3 – Continued

Rh Temporal pole	0.29	0.46	0.001
Rh Entorhinal	0.22	0.45	0.001
Rh Hippocampus	1	0.44	0.001
Rh Amygdala	1	0.33	0.001
Region	CTR	eMCIc	P value
Lh Posterior cingulate	0.30	0.54	0.001
Lh Lingual G	0.43	0.56	0.001
Lh Temporal pole	0.39	0.49	0.001
Lh Hippocampus	1	0.26	0.001
Lh Amygdala	1	0.35	0.001
Lh Accumbens	0.36	1	0.001
Rh Insula	0.28	0.49	0.001
Rh Temporal pole	0.29	0.45	0.001
Rh Entorhinal	0.22	0.46	0.001
Rh Hippocampus	1	0.32	0.001
Rh Amygdala	1	0.32	0.001
Rh Accumbens	0.54	1	0.001
Region	CTR	AD	P value
Lh Insula	0.38	0.51	0.001
Lh Posterior cingulate	0.30	0.55	0.001
Lh Entorhinal	0.29	0.44	0.001
Lh Hippocampus	1	0.31	0.001
Lh Amygdala	1	0.31	0.001
Rh Lateral orbitofrontal G	0.47	0.58	0.006
Rh Insula	0.28	0.53	0.001
Rh Entorhinal	0.22	0.44	0.001
Rh Hippocampus	1	0.31	0.001
Rh Amygdala	1	0.31	0.001
Region	sMCI	IMCIc	P value
Lh Postcentral G	0.41	0.58	0.005

Continued

Table 5.3 – Continued

Lh Pallidum	0.21	1	0.001
Rh Postcentral	0.41	0.61	0.001
Region	sMCI	eMCIc	P value
Lh Pericalcarine	0.26	0.41	0.001
Lh Transverse temporal G	0.40	0.54	0.001
Lh Accumbens	0.21	1	0.001
Rh Lingual G	0.32	0.50	0.001
Rh Accumbens	0.21	1	0.001
Region	sMCI	AD	P value
Lh Postcentral G	0.41	0.60	0.001
Lh Pallidum	0.21	1	0.001
Rh Pericalcarine	0.28	0.37	0.001
Rh Pallidum	0.21	1	0.001
Region	lMCIc	eMCIc	P value
Lh Accumbens	0.30	1	0.001
Region	eMCIc	AD	P value
Lh Lingual	0.55	0.43	0.001
Rh Frontal pole	0.34	0.45	0.001

---

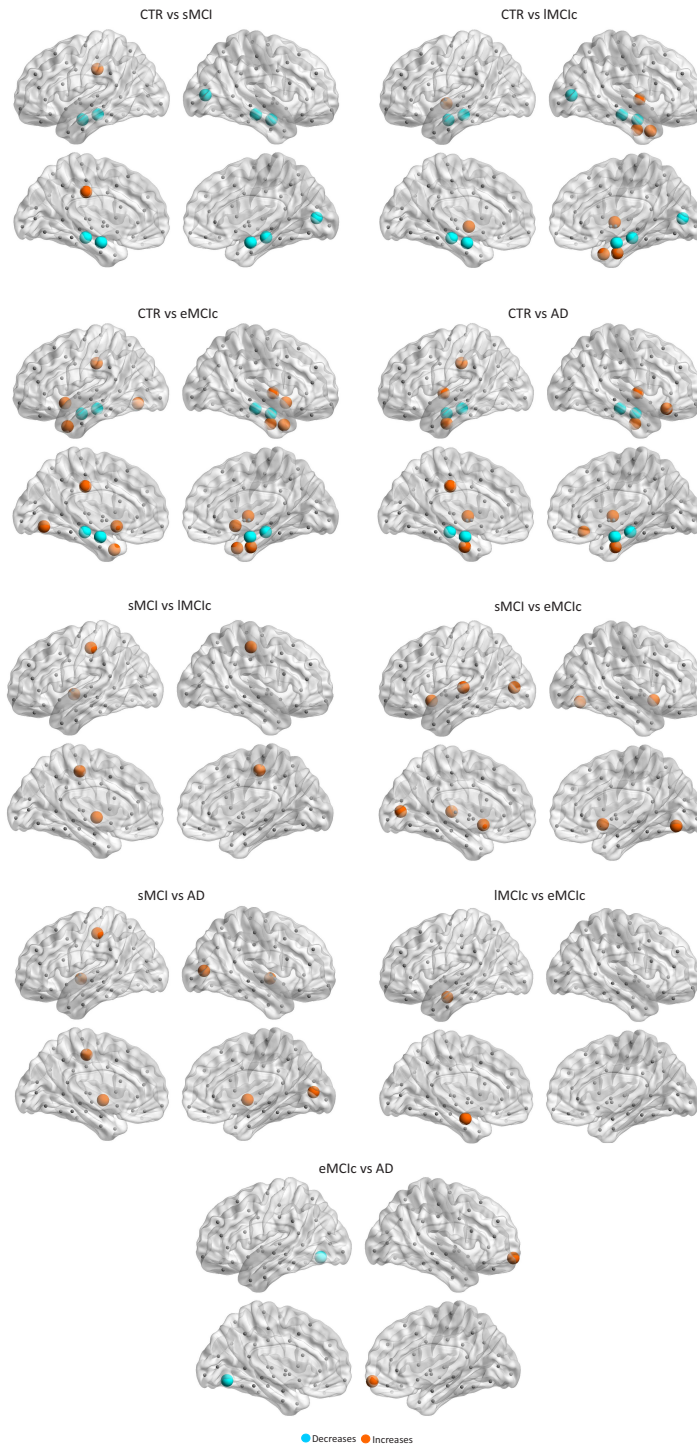


Figure 5.8: Significant differences in the nodal closeness centrality between controls and patients. CTR - controls; sMCI - stable MCI; eMCIc - early MCI converters, AD - Alzheimer’s disease. The regions that exhibit significant decreases (increases) in the closeness centrality are shown in blue (orange). These regions are listed in table 5.3. Taken from [96].



Table 5.4: Summary of the global and nodal network results. When compared with controls, all patient groups manifested an increased path length and modularity as well as decreases in the transitivity and small-worldness. While the global clustering coefficient showed decreases in lMCIc, eMCIc, and AD groups, the nodal clustering coefficient showed notable changes only in AD patients, by being decreased in 21 regions when compared with controls. When compared with sMCI patients, the remaining patient groups exhibited an increased closeness centrality and a decreased path length and mean clustering coefficient. The nodal clustering coefficient decreased only in 1 region in AD patients when compared with sMCI patients [96].

Measures	CTR vs. sMCI	CTR vs. lMCIc	CTR vs. eMCIc	CTR vs. AD	sMCI vs. lMCIc	sMCI vs. eMCIc	sMCI vs. AD
Characteristic path length	↑	↑	↑	↑	↓	↓	↓
Clustering coefficient	—	↓	↓	↓	↓	↓	↓
Transitivity	↓	↓	↓	↓	—	—	—
Modularity	↑	↑	↑	↑	—	—	—
Small-worldness	↓	↓	↓	↓	—	—	—
Nodal clustering	↓	—	↓	↓	—	—	↓
	1 region		1 region	21 regions			1 region
Nodal closeness centrality	↓	↓	↓	↓	—	—	—
	5 regions	5 regions	4 regions	4 regions			
	↑	↑	↑	↑	↑	↑	↑
	1 region	4 regions	8 regions	6 regions	3 regions	5 regions	4 regions

### 5.3.3 Brain communities

Four communities (or modules) were identified in the control groups; 3 communities were identified in sMCI, lMCIC, and eMCIC patients; and 5 communities were present in AD patients (figure 5.9). The full list of communities and the regions belonging to each community is presented in table 5.5.

In the controls, Module I consisted of the superior frontal gyri, posterior cingulate, and supramarginal gyri, which are part of the default-mode network. The entorhinal gyri and subcortical regions were present in Module II. Module III was the largest, including several lateral frontal, parietal, and occipital regions while Module IV included the parahippocampal gyri.

The community structure of sMCI, lMCIC, and eMCIC patients was similar to the one of the controls. The differences being that Module I did not include the superior frontal, lateral parietal, or posterior parietal regions while Module II comprised additional regions in the patients groups. In the case of AD patients, several regions were detached from Module II and formed 2 new communities; one was composed of the caudate, putamen, accumbens, and pallidum (Module IV) while the other contained the bilateral thalami (Module V).

In order to evaluate the between-groups differences in the communities described above, we calculated the within-module degree and participation coefficient. After FDR corrections, we observed that the AD patients show increases in the within-module degree and decreases in the participation coefficient when compared with controls. The regions that showed increases in the within-module degree were part of Modules I and III and included the left postcentral, left superior parietal, right pars opercularis gyri, and right insula. On the other hand, decreases in the participation coefficient were shown by the left pars orbitalis and bilateral cuneus, which were present in Module III. Furthermore, when lMCIC and eMCIC patients were compared to controls, some of these regions also exhibited increase in the within-module degree and decrease in the participation coefficient, however, these differences did not survive the correction for the multiple comparisons (table 5.6).

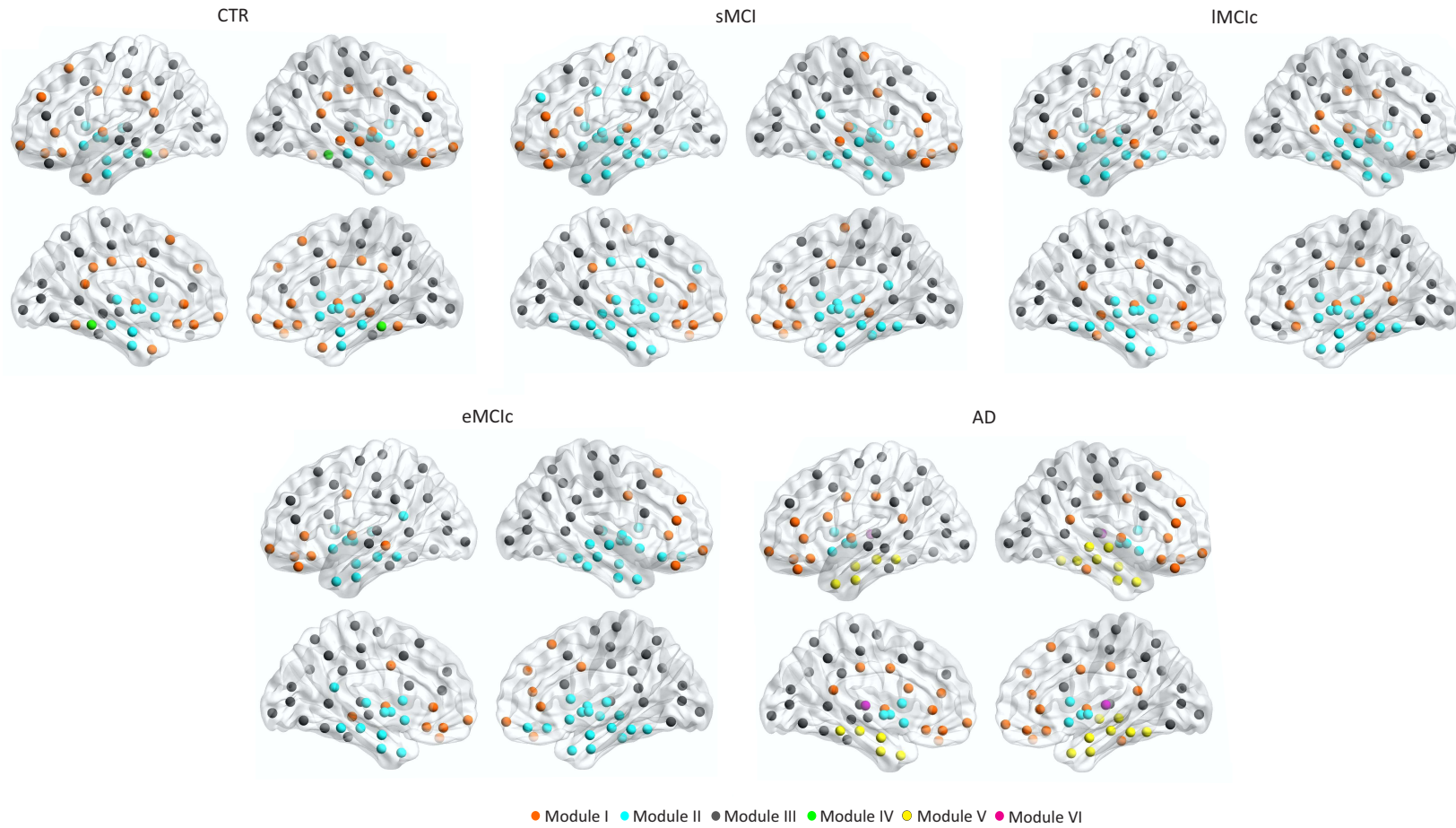


Figure 5.9: Brain communities in controls and sMCI, lMCIc, eMCIc, and AD patients. CTR - controls; sMCI - stable mild cognitive impairment; lMCIc - late mild cognitive impairment converters; eMCIc - early mild cognitive impairment converters; AD - Alzheimer's disease. Different communities are shown in different colors. For each group, the left and right lateral (top) and medial (bottom) brain views are shown. Taken from [96].

Table 5.5: Brain communities in controls, sMCI, lMCIc, eMCIc, and AD patients. CTR - controls; sMCI - stable mild cognitive impairment; lMCIc - late mild cognitive impairment converters; eMCIc - early mild cognitive impairment converters; AD - Alzheimer’s disease [96].

Hemisphere	Brain region	Modules CTR	Modules sMCI	Modules lMCIc	Modules eMCIc	Modules AD
Left	Superiorfrontal	I	III	III	III	III
Left	Frontalpole	I	I	III	I	I
Left	Rostralmiddlefrontal	I	II	III	III	III
Left	Caudalmiddlefrontal	III	III	III	III	III
Left	Parsorbitalis	III	I	III	I	I
Left	Lateralorbitofrontal	I	I	I	I	I
Left	Parstriangularis	III	I	III	III	I
Left	Parsopercularis	III	I	III	III	I
Left	Medialorbitofrontal	I	I	I	I	I
Left	Rostralanteriorcingulate	I	I	I	I	I
Left	Caudalanteriorcingulate	I	II	I	I	I
Left	Insula	I	II	I	I	I
Left	Precentral	III	I	III	III	III
Left	Postcentral	III	III	III	III	III
Left	Supramarginal	I	I	III	III	III

Continued

Table 5.5 – Continued

Left	Superiorparietal	III	III	III	III	III
Left	Inferiorparietal	III	III	III	III	III
Left	Paracentral	III	III	III	III	III
Left	Posteriorcingulate	I	II	III	III	I
Left	Isthmuscingulate	I	II	I	III	I
Left	Precuneus	III	III	III	III	III
Left	Cuneus	III	III	III	III	III
Left	Pericalcarine	III	III	III	III	III
Left	Lingual	III	II	III	III	III
Left	Lateraloccipital	III	III	III	III	III
Left	Transversetemporal	III	I	III	III	III
Left	Bankssts	III	III	III	III	III
Left	Superiortemporal	III	II	II	III	III
Left	Middletemporal	III	II	I	I	III
Left	Inferiortemporal	III	II	I	III	III
Left	Temporalpole	I	II	II	II	V
Left	Entorhinal	II	II	II	II	V
Left	Parahippocampal	IV	II	II	II	V
Left	Fusiform	I	II	II	III	III
Left	Thalamus	II	II	II	II	VI

Continued

Table 5.5 – Continued

Left	Caudate	II	II	II	II	II	II
Left	Putamen	II	II	II	II	II	II
Left	Pallidum	II	II	II	II	II	II
Left	Hippocampus	II	II	II	II	II	V
Left	Amygdala	II	II	II	II	II	V
Left	Accumbens	II	II	II	II	II	II
Right	Superiorfrontal	I	III	III	I	I	I
Right	Frontalpole	I	I	III	I	I	I
Right	rostralmiddlefrontal	I	III	III	I	I	I
Right	Caudalmiddlefrontal	III	III	III	III	III	III
Right	Parsorbitalis I	I	III	I	I	I	
Right	Lateralorbitofrontal	I	I	I	II	II	I
Right	Parstriangularis	III	I	III	I	I	I
Right	Parsopercularis	III	III	III	III	III	III
Right	Medialorbitofrontal	I	I	III	II	II	I
Right	Rostralanteriorcingulate	I	I	I	I	I	I
Right	Caudalanteriorcingulate	I	I	I	I	I	I
Right	Insula	I	II	I	II	II	I
Right	Precentral	III	I	III	III	III	III
Right	Postcentral	III	III	III	III	III	III

Continued

Table 5.5 – Continued

Right	Supramarginal	I	III	III	III	III	III
Right	Superiorparietal	III	III	III	III	III	III
Right	Inferiorparietal	III	III	III	III	III	III
Right	Paracentral	III	III	III	III	III	III
Right	Posteriorcingulate	I	III	I	III	III	I
Right	Isthmuscingulate	I	III	I	II	III	I
Right	Precuneus	III	III	III	III	III	III
Right	Cuneus	III	III	III	III	III	III
Right	Pericalcarine	III	III	III	III	III	III
Right	Lingual	III	III	III	III	III	III
Right	Lateraloccipital	III	III	III	III	III	III
Right	Transversetemporal	III	I	I	III	III	III
Right	Bankssts	III	III	I	III	III	III
Right	Superiortemporal	I	II	II	II	II	V
Right	Middletemporal	I	I	II	II	II	V
Right	Inferiortemporal	III	II	I	II	II	I
Right	Temporalpole	I	II	II	II	II	V
Right	Entorhinal	II	II	II	II	II	V
Right	Parahippocampal	IV	II	II	II	II	V
Right	Fusiform	I	II	II	II	II	V

Continued

Table 5.5 – Continued

Right	Thalamus	II	II	II	II	VI
Right	Caudate	II	II	II	II	II
Right	Putamen	II	II	II	II	II
Right	Pallidum	II	II	II	II	II
Right	Hippocampus	II	II	II	II	V
Right	Amygdala	II	II	II	II	V
Right	Accumbens	II	II	II	II	II

---



Table 5.6: Differences in the within-module degree and participation coefficient between groups. CTR - controls; sMCI - stable mild cognitive impairment; lMCIc - late mild cognitive impairment converters; eMCIc - early mild cognitive impairment converters; AD - Alzheimer’s disease; Lh - left hemisphere; Rh - right hemisphere; G - gyrus. The differences between controls and AD patients survived corrections for multiple comparisons with FDR, while the other differences between groups were significant at an uncorrected level ( $< 0.05$ ) [96].

Within - module degree			
Region	CTR	sMCI	P value
Rh Pars opercularis G	-3.29	0.53	0.002
Within - module degree			
Region	CTR	eMCIc	P value
Lh Postcentral G	-0.35	1.22	0.004
Lh Superior Parietal G	-0.35	0.99	0.017
Within - module degree			
Region	CTR	AD	P value
Lh Postcentral G	-1.12	0.70	0.001
Lh Superior Parietal G	-1.12	0.89	0.002
Lh Superior Temporal G 0.39	1.86	0.003	
Rh Pars Opercularis G	-2.81	0.42	0.001
Participation coefficient			
Region	CTR	AD	P value
Lh Lateral Occipital G	0.66	0.23	0.004
Rh Postcentral G	0.66	0.24	0.008
Rh Lateral Occipital G	0.66	0.32	0.001

## 5.4 Discussion

In this chapter, I presented the largest study, to date, that assesses the topological organization of brain networks in MCI patients that remain stable, show slow or

fast progress to AD and AD patients. We observed an abnormal network organization all patient groups, that is indicated by the increased path length, decreased transitivity and increased modularity relative to the controls. Additionally, the clustering coefficient is decreased in the lMCIc, eMCIc, and AD patients, but do not show any differences between sMCI patients and controls. Taken together, all these observations point to the direction that the prodromal and clinical stages of AD are correlated with diminished ability of spatially distinct brain regions to integrate information and altered communication patterns between neighboring regions as well as communities.

In this study, all patient groups had increased path length relative to controls, which is an indication of an abnormal global organization of their respective networks. Short path lengths allow quick and efficient distribution of the information between remote brain regions, which is considered to be essential for cognitive functioning [191]. Therefore, our findings indicate that, on average, the distance between two remote brain areas was larger in the networks of the patients, which in turn results in less efficient communication between them. This agrees with earlier graph theoretical studies in AD, which also identified increased path lengths in the networks of AD patients built from structural and functional data [105, 176, 192, 193, 194]. One study used DTI to build individual subjects' networks and found that increases in path lengths correlate with worse MMSE scores [194], thereby proposing that path length can be considered as markers of cognitive dysfunction in AD.

Another observation from this study is the decrease in the mean clustering coefficient in lMCIc, eMCIc, and AD patients when compared to controls, which is indicative of lower number of connections between the neighboring areas in the patients' networks. This observation is in agreement with some [147, 165], but not all earlier studies [105, 176], suggesting that the results can be influenced by different methodologies, sample sizes or characteristics of the patient groups. Li et al. [170] studied MCI patients which converted to AD and found longitudinal decreases of the clustering coefficient, which may suggest that reducing of the clustering in the network is related with conversion to dementia in AD.

Additionally, this is the first study to evaluate the transitivity and modularity in the structural networks of MCI and AD patients. These two measures were significant across almost all densities of the network, therefore being indicative of greater abnormalities than the path length or clustering. The transitivity measures the level of connectivity of a given brain region within its local environment similarly to the clustering coefficient. However, nodes that have very few connections have smaller effect on the transitivity when compared with the clustering coefficient [31], making it a superior measure for poorly inter-connected networks. As such, we recommend that this measure is used in future studies evaluating structural networks in amnesic MCI and AD as it provides greater sensitivity to the effects of the disease.

The modularity describes the level at which the network can be subdivided into different sub-network (or communities, modules) [195]. Larger modularity indicates that the brain regions are very well connected with other regions within the same community, however, they are poorly connected to brain regions that belong to other communities. The significant increase in the modularity we observed in sMCI, lMCIc, eMCIc, and AD patients compared with controls, suggests that patients' networks have higher intra-community connectivity and lower number of connections between communities. This suggests that the whole-brain networks in the patients are fragmented into small number of large and isolated components. These observations of the patients' connectivity patterns were further supported by the increases of the within-module degree and decreases of the participation coefficient in the frontal, parietal, and occipital regions of the patient groups, when compared with controls. Significant increase in the modularity was also identified in the functional networks of patients with Parkinson's disease with mild cognitive impairment, who have a higher risk of developing dementia [196]. Such increases were explained to be an abnormal process which leads to the increase of the number of connections between brain regions in a certain module that subsequently leaves the other communities relatively isolated. The same study related the increases in modularity with worse memory and visuospatial performance in Parkinson's patients, indicating that these modularity changes are pathological and related to larger clinical decline [196].

Moreover, we also found that, even though the patients had similar community structure with controls, the exact regions that belonged to each community changed across the patient groups. In particular, the AD patients had 2 communities that were not present in the other group. As a result, our findings indicate the reorganization of the communities in sMCI, IMCIc, eMCIc, and AD patients. Also, analogous to some earlier studies that studied modularity in structural MRI networks [92, 197], we did not observe an exact agreement between the brain modules and resting-state fMRI networks [198].

In addition to the changes in the global network topologies, we also identified alterations in the properties of some specific brain regions. In particular, few areas in AD patients had decreased nodal clustering when compared with controls, suggesting worse communication patterns with their neighboring regions. Few of these areas belonged to the default-mode network, for example the precuneus and superior frontal gyri [198], which can be explained by the pathological changes within this network that occur in AD [148, 178, 199]. We also found decreased clustering in few other frontal and temporal regions in AD patients; this indicates that the clustering changes in AD patients were quite extensive which is in agreement with previous studies that offered evidence of extended brain atrophy at advanced stages of AD [200]. In contrast with these extensive changes exhibited by AD patients, the MCI patients displayed decreases in the clustering coefficient only by few frontal and parietal regions.

The nodal closeness centrality exhibited more heterogeneous changes, showing both increases and decreases, in all patient groups compared with controls. The decreases of the centrality in all patient groups were mainly found in the bilateral hippocampi and amygdala, which suggests the loss of connections between these regions and the rest of the network. This might be explained by the loss of the integrity of white matter or alternatively by the disruption of white matter fibers that connect these regions in MCI and AD patients that has been observed in various DTI studies [201]. On the other hand, the closeness centrality increased mainly in the posterior cingulate, temporal pole, entorhinal cortex, insula, and orbitofrontal regions. Since the closeness centrality is a measure that quantifies

the level of interaction between regions; its increase in regions that exhibit pathological changes in AD [149, 156, 158] can be explained by the shared mechanisms in neurodegeneration [202]. In particular, within the graph theory framework, while 2 regions could show high correlation if they have structural or functional connection between them, they could also correlate if they become atrophied at the same rate [203]. As a result, since medial temporal, medial parietal, and limbic regions show atrophy starting with the early stages of AD, it is possible that they will have strong interaction with other regions in the network that become atrophied as the disease progresses.

In this study, we also compared the global and local network characteristics of the different patient groups between each other. We found that, when compared with the other patients groups, sMCI patients exhibited a larger path length (figure 5.5). Additionally, sMCI patients showed reduced nodal closeness centrality in several regions, including the postcentral gyrus, pallidum and accumbens (for a full list, see table 5.3). These results suggest that the sMCI patients show considerable abnormalities in the interactions between two remote brain areas. Previous studies found that the initial pathological changes in AD target distant brain areas [204], which can be usually connected by long and poorly myelinated axons. Therefore, our results may indicate that such pathological changes are more notable in sMCI patients, which are potentially at earlier stages of AD. On the contrary to the path length, the clustering coefficient was reduced in IMCIc, eMCIc, and AD patients compared with sMCI patients. This in turn, proposes that the connections loss in the neighboring area is indicative of the changes that occur in patients that are on the path to develop AD or already have dementia.

There is increasing evidence of the considerable heterogeneity that exists among the MCI patients; for example, while many MCI subjects stay stable for many years, others show progression to AD while some others return to normal cognition [205]. Furthermore, amnesic MCI can be also produced by few pathologies other than AD, including frontotemporal dementia [206], vascular dementia [207], and hippocampal sclerosis [208]. The results presented in this chapter support the notion of the heterogeneity in the abnormalities of the network topology between the MCI groups. In particular, in contrast to the other MCI groups, sMCI-1y

patients showed increased clustering with respect to controls while showing almost no changes in the modularity and transitivity (figure 5.6). Therefore, it is possible that the sMCI-1y group was comprised of a mixture of subjects that progressed to dementia after few years, remained stable or had a different non-AD related disease. This variance might be able to explain the lack of changes in the transitivity and modularity in sMCI-1y, as opposed to the other patients groups which had more homogeneous structure. Studies assessing network topology in MCI subjects should consider their results with respect to this important heterogeneity.

Although the brain network are inherently sparse, building the brain networks from neuroimaging data results in continuous adjacency matrices [155]. Therefore, in order to identify the true connections while remove the potentially spurious ones, many studies apply a threshold to the adjacency matrices. One particular way to apply this threshold, is to make the analysis only by considering the connections that overcome a level of significance. However, this approach will result in different number of connections for different subject groups. In this study, the threshold was applied so that the most significant connections were retained, while keeping the number of connections across various groups fixed. Since currently there is no consensus to determine which threshold value is best [155], we tested the group differences for a particular range of densities, following some previous studies [105, 176]. We choose the range in order to analyze networks that were meaningfully organized. The top boundary of this range was chosen because the networks above this particular density were exhibiting random organization. On the other hand, the lower bound was chosen such that the analyzed network had enough connections between the regions, i.e. network at lower densities were widely disconnected. Our findings indicated that significant differences between groups can be observed for different densities, suggesting that the results were consistent.

It should be noted also that the present study has few limitations. Firstly, using correlations between structural measures to obtain adjacency matrices, results in a single network per group. As a result, since individual networks are not

calculated and characterized, this method does not allow for the correlation analysis with clinical measures. Nevertheless, some studies [209, 210] have provided a method that allows the calculation of single-subject structural matrices from structural MRI; this method could be considered in studies that assess structural networks in large cohorts of AD and MCI patients. The second limitation is the fact that only longitudinal data of the patients' clinical diagnosis up to 3 years was obtained. Hence, in particular for the sMCI patients, it is possible that some of the individuals in this group converted to AD shortly after this period.

# Chapter 6

## Directed Networks in Parkinson's and Alzheimer's Patients

### 6.1 Introduction

As discussed in the previous chapters, studying the organization of complex brain networks in patients can reveal a substantial information about the effect that neurodegenerative diseases might have on their connectivity patterns. In particular, as shown in chapter 5, the structural undirected networks in Alzheimer's patients show abnormal organization that is manifested through changes in the global topological measures (decreases in transitivity and mean clustering coefficient, accompanied by increases in modularity and characteristic path length) as well as changes in the local network properties of several regions (decreases in the nodal clustering coefficient and changes in the closeness centrality that varied across different regions) [96].

However, results and observations can change between different studies. This can, in part, be attributed to the size of the sample and the heterogeneous clinical characteristic of patients [96]. In particular, for some samples, undirected networks in patients do not show any changes in the topological properties when compared



with healthy controls [96]. Therefore, there is a need to explore alternative methods of building the complex brain networks that can detect any alterations in the brain connectivity arising due to the presence of various neurological disorders, for example, Parkinson's or Alzheimer's disease (for a review, see [211] and [212]).

Studying directed networks in the brain may offer this possibility. Directed networks are commonly used to understand the degree to which one region can influence the activity pattern of another one; this connectivity patterns are sometimes termed as effective connectivity [83, 84]. Currently, Granger causality [86, 87] is the most widely used method to derive the effective connectivity patterns in the brain. This approach has been applied to a wide range of studies that used functional MRI resting-state data in order to evaluate some causal relations that occur between various regions in the resting state networks [213] as well as the default mode networks [214]. Furthermore, by using graph theoretical approaches, it has been demonstrated that these directed networks also show small-world characteristics [215].

In this chapter, I will present a new method of building directed networks in the brain that uses the temporal delays in the interaction between two brain regions in order to estimate a directed link between the corresponding regions. I will further demonstrate that this method can successfully reveal abnormal topological organizations in Parkinson's and Alzheimer's disease patients, even in the cases in which such changes cannot be identified by undirected networks analysis. However, it should be noted that, since our method uses Pearson's correlation to quantify the between-region interaction, it assigns a direction of the edge based only on temporal precedence. As such, this method is not suggestive of any causation or influence in the interaction between the regions.

## 6.2 Materials and methods

### 6.2.1 Analysis overflow

Resting-state functional MRI data was obtained for each subject (representative time series are shown in figure 6.1(a)). The connection strength between two regions was characterized by calculating the *delayed* Pearson’s correlation coefficient between the corresponding time series. The delay was introduced by shifting the two time series by a certain amount and calculating the Pearson’s coefficient between the shifted time series. Since the time series in our analysis are discrete, the delay between two series is defined as the number of time steps one series is shifted relative to the other, i.e. if the fMRI repetition time is  $\Delta t = 1\text{s}$ , and we want to calculate the correlation at delay  $d = 3$ , the actual time delay between the two series is  $d\Delta t = 3\text{s}$ .

The correlation coefficient between all pairs of regions (all calculated at the same delay) were assembled in a matrix, representing the weighted delayed network (figure 6.1(b), shown for  $d = 3$ ). In order to retain only one-directional connections <sup>1</sup> we extract the anti-symmetric part of this matrix by substituting the matrix’s transpose (figure 6.1(c)) from itself, (figure 6.1(b)), therefore, obtaining the weighted adjacency matrix of the network (figure 6.1(d)).

The weighted adjacency matrices were further binarized (figure 6.1(e) and 6.1(f)) by fixing the density of connections for every group (chapter 3). The binary matrices were analyzed over the complete range of densities available for binarization (1% - 50%) and the resulting network topologies across this range were compared between the various groups. The self-connections were excluded from the analysis and all negative correlation coefficients were equated to 0.

The statistical significance of the between-group differences was evaluated by

---

<sup>1</sup>Consider two regions, A and B. In the delayed weighted network, A has a directed connection to B with strength  $W_1$  and B has a directed connection to A with strength  $W_2$ . We substitute these two connections with one effective connection that has the strength  $|W_1 - W_2|$  and the direction of the stronger connection

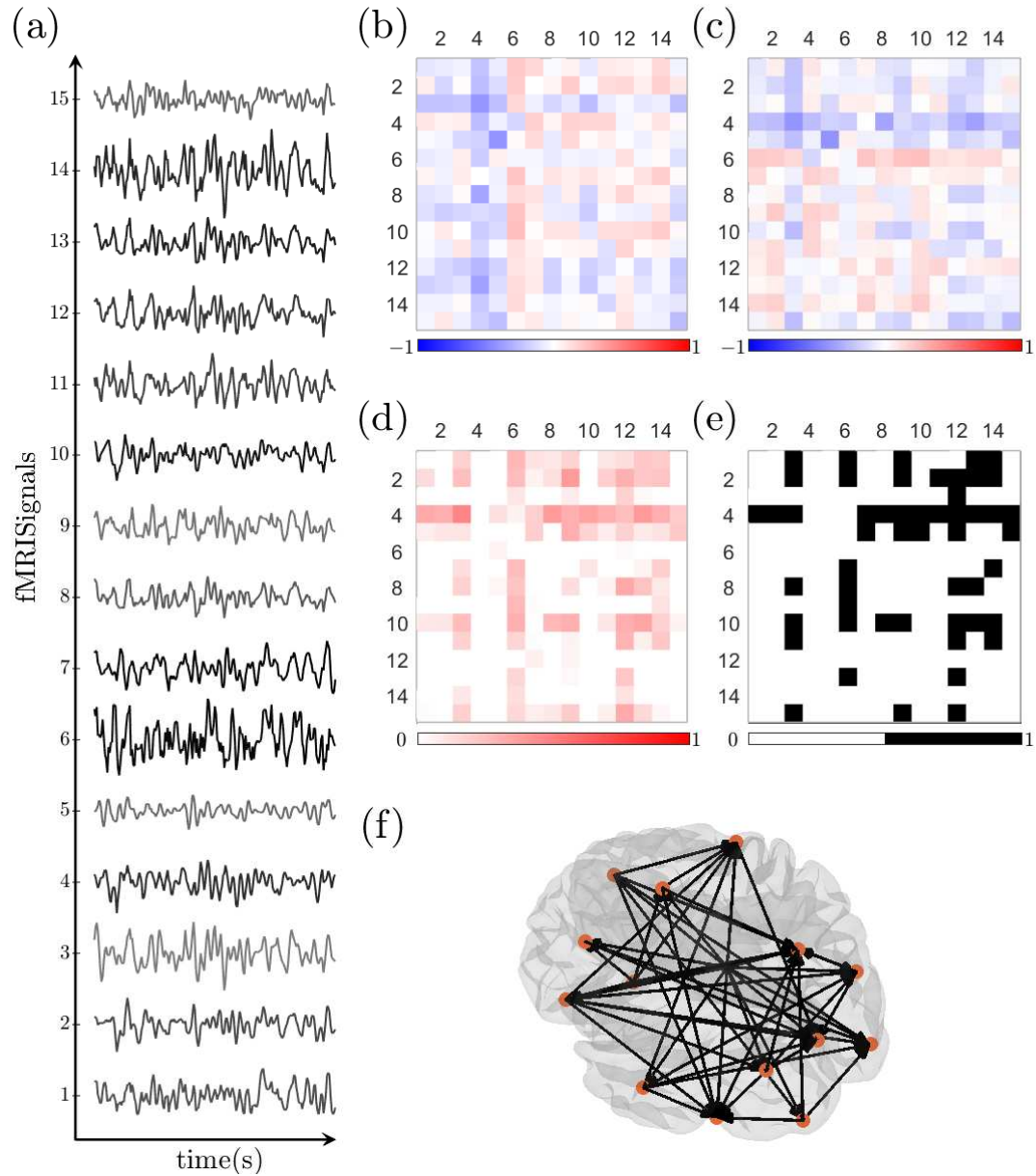


Figure 6.1: Directed network analysis overview. Resting-state fMRI data was obtained for each subject(a). The connection strength between any two regions was obtained by calculating their delayed Pearson’s correlation coefficient, resulting in the weighted delayed matrix shown in (b). The adjacency matrix is taken as the anti-symmetric part of this matrix (d), given by the difference of the delayed connectivity matrix (b) with its transpose (c). The adjacency matrix (d) was further binarized; an example of the resulting binary matrix and its corresponding graph are shown in (e) and (f).

using the non-parametric permutation test with 10000 simulations, as described in section 3.3. The results were reported by using the 95% confidence intervals (CI) as a critical values for a 2-tailed test of the null hypothesis at  $p < 0.05$ .

In order to assess whether the amount of shift (delay) between the time series affects our results, we repeated our analysis over wide range of delays. Furthermore, to check for consistency over various parcellation schemes, the analysis was conducted over two brain atlases; the low and high resolution analysis was performed on Craddock atlases [139] consisting of 200 and 840 brain regions respectively.

## 6.2.2 Network measures

Since we analyzed binary directed networks, the global network topology was characterized by calculating the directed analogues of the mean clustering coefficient, transitivity, modularity, global and local efficiency. The clustering coefficient is defined as the number of triangles that can be formed around a node (chapter 2). Taking into account the direction of the edges, there are 8 possible ways to form a triangle [114]. In our analysis, we chose to consider a triangle as completed only if the edges forming the triangle are arranged in a close directed cycle (i.e. each node in this triangle has one incoming and one outgoing edge). Similarly, we employed the same procedure to calculate the transitivity, by identifying the number of directed cycles in the network.

The global efficiency is defined as the average of the inverses of the path length for each node, while the local efficiency is defined as the global efficiency calculated only within the node's neighborhood. Their directed counterparts are calculated as averages of their in and out variants (chapter 2). These measures were chosen over the path length in order to be able to characterize the disconnected networks that are obtained for small densities. The directed version of modularity was implemented according to the definitions presented in [31, 216].

### 6.2.3 Subjects

The analysis was repeated on two separate cohorts. In the first cohort, 25 healthy controls were compared to 71 cognitively normal Parkinson’s Disease (PD) patients. Among the patients, 46 were taking various doses of medication while 25 patients were not on any medication when the fMRI scan was conducted. Furthermore, longitudinal data of a group of 46 patients (not overlapping with the patients taking the medication) was obtained around one and a half year after the first scan. By the time of the follow-up scan, 31 of the 46 patients starting taking the medication at different times during this period.

In order to control for the effects of gender and age of the individual subjects, linear regression was performed for all network regions [90]. Furthermore, since the head motion (translational and rotational) was significant in the two groups, it was additionally included as a covariate in the analysis. In the case of the longitudinal analysis, the time interval between the two scans was added as a covariate in order to account for the different scan events between patients. The characteristics of the PD patients are shown in table 6.1.

Table 6.1: Characteristics of Parkinson’s Disease sample. CTR - Controls; PD-CN - cognitively normal Parkinson’s Disease patients. The characteristics of the sample are shown in terms of age, gender, education, status of medication and average time of the follow-up scan after the first one. \* Longitudinal data was obtained only from 46 patients.

	CTR (n = 13)	PD-CN (n = 71)
Age (years)	65.54 (8.03)	60.25 (10.38)
Gender (M/F)	11/2	46/25
Education (years)	16.92 (2.49)	15.23 (3.03)
Medicated (Y/N)	0/13	46/25
Longitudinal* (months)	—	15.93 (6.37)

The second cohort comprised of 25 controls, 45 patients that were diagnosed as Mild Cognitive Impairment (MCI) and 24 Alzheimer’s Disease (AD) patients.

The MCI groups consisted of 19 patients who were designated as early MCI (eMCI) and 16 patients who were late MCI converters (lMCI). 9 controls had an amyloid pathology (henceforth, referred as CTR – A1), 16 of the controls did not have any pathology (CTR – A0), while all subjects in the patient groups showed signs of amyloid pathology. In this study, we compared the controls without any pathology to the remaining 4 groups (CTR – A1, eMCI, lMCI and AD patients).

There were no significant differences in the head motion between groups. Therefore, the regional time series were regressed only to control for the age, gender and education differences of the individual subjects. The characteristics of the AD cohort are shown in table 6.2.

Table 6.2: Characteristics of Alzheimer’s sample. CTR - Controls; eMCI - early MCI converters; lMCI - late MCI converters; AD - Alzheimer’s Disease patients. The characteristics of the sample are shown in terms of age, gender, education, and amyloid pathology status. Based on the amyloid pathology, the control groups is split into two groups: CTR – A0 and CTR – A1.

	<b>CTR</b> (n = 25)	<b>eMCI</b> (n = 19)	<b>lMCI</b> (n = 16)	<b>AD</b> (n = 24)
<b>Age (years)</b>	75.24(7.56)	71.42(5.31)	75.31(5.59)	73.86(6.48)
<b>Gender (M/F)</b>	10/15	9/10	10/6	11/13
<b>Education (years)</b>	16.72(2.05)	15.89(2.82)	16.31(2.66)	15.04(2.35)
<b>Amyloid (Y/N)</b>	9/16	19/0	16/0	24/0

### 6.3 Results and discussion

In order to evaluate whether our results emerge only in the case of directed networks, we firstly analyzed both cohorts by constructing undirected networks. These networks were analyzed by following a procedure analogous to the one detailed in chapters 4 and 5: the Pearson’s correlation coefficient (at delay of zero) was used to quantify the strength of connections between any two regions;

only the positive connections were used in the analysis; the weighted matrices were binarized by fixing the density of connections between groups in the density range 1% - 50%; the binary matrices were compared by the non-parametric permutation test.

Furthermore, in order to check whether both steps are essential into the construction of directed networks (calculating the delayed correlation matrix followed by taking the asymmetric part of this matrix) we constructed the directed adjacency matrix only by calculating delayed Pearson's correlation coefficient between all pairs of regions at various delays (figure 6.1(b)) and analyzed them by following the steps described above.

Both analyses did not reveal any consistent significant differences between controls and patient groups in both cohorts. This suggests that the following results are inherent to our proposed method of calculating adjacency matrices to analyze brain connectivity and cannot be revealed by analyzing undirected networks.

### **6.3.1 Parkinson's Disease patients**

The results of the comparison between controls and PD-CN group are shown in figure 6.2. The figure shows the differences in the corresponding measures between the two groups (the orange circles), along with the 95% confidence intervals (the gray area). The box-plots illustrate the actual values of the measures for each group (PD-CN, red and CTR, black) as a function of the delay, averaged over the range of densities for which the between-group differences are significant. The results shown in figure 6.2 are calculated for the low resolution network.

We observed that differences between controls and patients depend on the delay used to quantify the strength of connections between regions. In particular, no changes were observed for small delays (delay 1 to delay 5). The most widespread changes appeared for delays 6 to 8 and only some measures showed significant differences in delays 9 and 10 (figures 6.2 and 6.3).

Our results indicate that delays 6-8 capture intrinsic patterns of interaction in the brains of the PD-CN patients. Except for modularity, which increases in patients at small densities and decreases in the higher densities when compared to controls, all other measures showed increases in the PD-CN networks over wide density range. Most notably, the global efficiency showed increases at small densities; the local efficiency, clustering and transitivity showed increases in the higher density range.

This behavior can be understood if one considers the number of connections in the networks at various densities. High densities result in very well connected networks. Therefore, most of the nodes are connected with every other node in the network, making the two networks virtually indistinguishable in this regard; this is reflected by the fact that the difference in the global efficiency values of the two groups tends to zero as density increases. On the other hand, the remaining measures require a certain pattern of connections in order to give a contribution. At small densities, there are not enough connections to make any contribution to the clustering, as a result, the networks cannot be distinguished in this regime since both will have exceptionally low clustering coefficient. Thus, these measures start to show differences as the number of connections grow with the density and more clusters form in the networks.

In order to show that these results can be reproduced with alternative parcellation schemes, the analysis was also performed with a high resolution atlas of 840 regions. The results of this analysis are shown in figures A.1 and A.2. These results are equivalent with the ones obtained for the low resolution atlas, which suggests that the application of our method does not depend on the particular parcellation scheme used in the analysis.

Furthermore, to assess the clinical relevance of our results we performed correlation analysis with various clinical tests. In short, we calculated the partial Pearson's correlation coefficient between the measures calculated for each individual subject and subjects' respective scores on various clinical assessment tests, while keeping age, gender and motion as covariates. We found that over many



delays, all global measures correlate significantly with the unified Parkinson's disease rating scale (UPDRS) at wide density ranges [217]. A sample of the p-values obtained from this calculation, for delay of 7, are shown in tables A.2 and A.3.

After the initial scan, some of the PD-CN patients had a follow-up fMRI scan around one and a half year later. We compared the baseline and longitudinal networks of this subgroup in order to assess any changes in their directed brain networks over time. The results of this analysis are summarized in figure 6.4. In line with our previous results, delays 6 and 7 show widespread changes in this subgroup, suggesting that the topological network properties indeed change over time. Interestingly, these results show a decrease in all measures in the longitudinal group, i.e. with time, the network topology of the Parkinson's patients tends to become similar to the one of the healthy controls in this cohort. Since the majority of this subgroup have taken medication in the period leading up to the follow-up scan (31 out of 46 patients), these results might be an indication of an effect that medicine has on brain networks in PD-CN patients. We repeated this analysis in the high resolution parcellation scheme and obtained similar results (figure A.3).

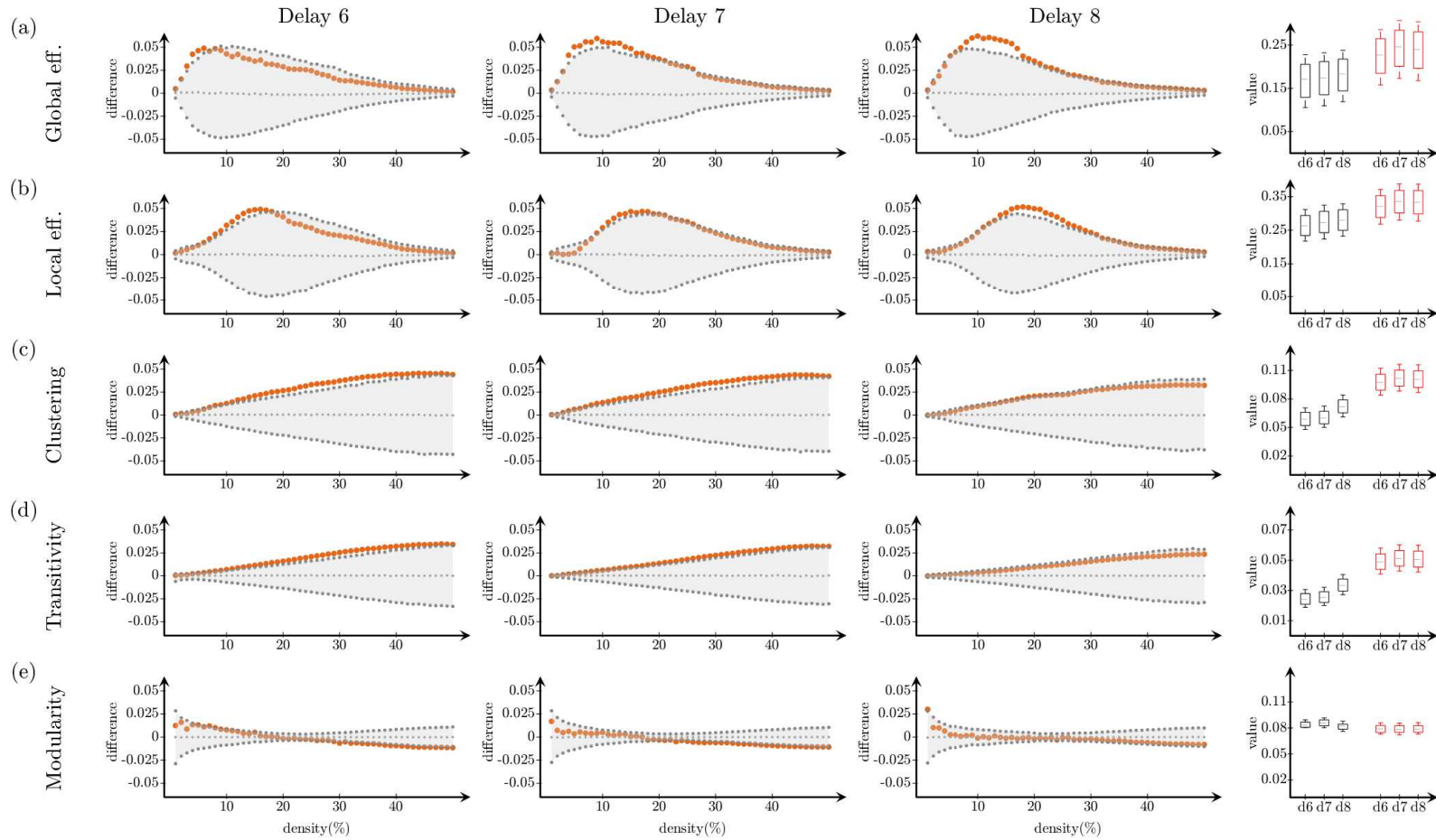


Figure 6.2: Changes in global network measures as a function of network density. PD-CN group is compared to healthy controls for low resolution networks. Global efficiency (a), local efficiency (b), clustering coefficient(C), transitivity (D), and modularity (E) are calculated for delays of 6 (leftmost), 7 (left-center) and 8 (right-center). Rightmost: The values of the corresponding measures for PD-CN (red) and controls (black) over a selected range of densities.

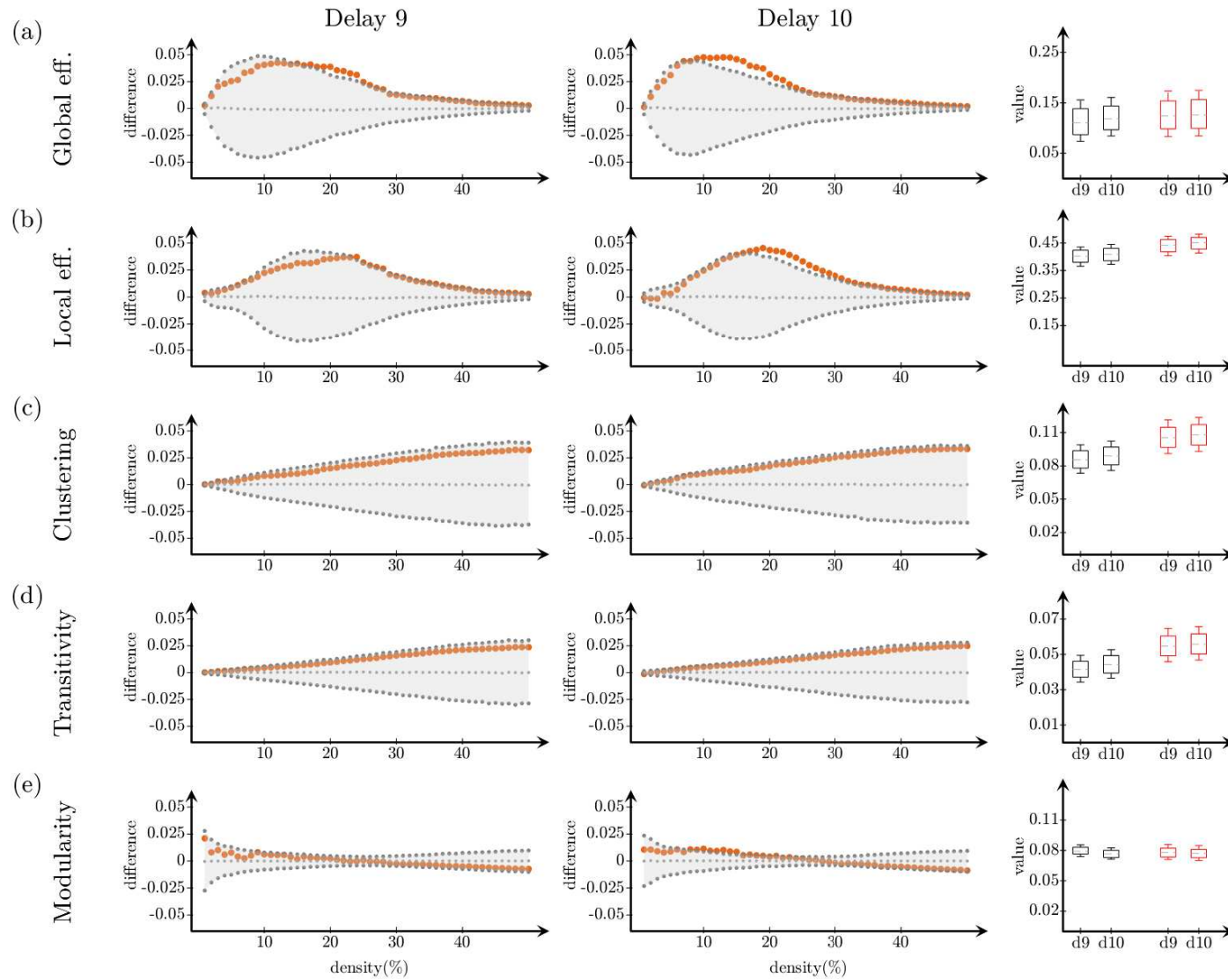


Figure 6.3: Changes in global network measures as a function of network density. PD-CN group is compared to healthy controls for low resolution networks. Global efficiency (a), local efficiency (b), clustering coefficient (C), transitivity (D), and modularity (E) are calculated for delays of 9 (left) and 10 (center). Right: The values of the corresponding measures for PD-CN (red) and controls (black) over a selected range of densities.

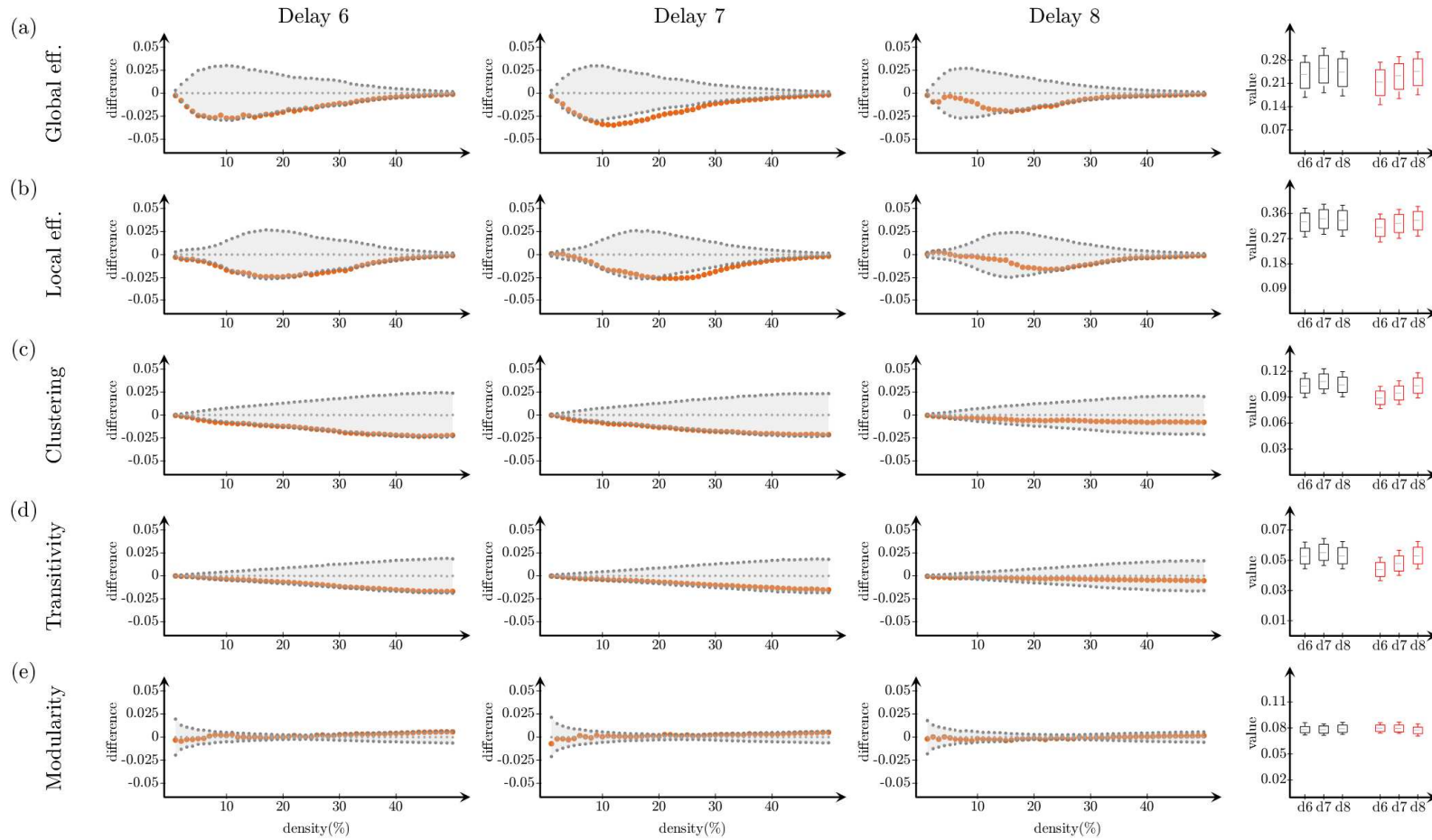


Figure 6.4: Changes in global network measures as a function of network density for longitudinal data. The baseline and longitudinal networks are compared for the PD-CN subgroup for low resolution networks. Global efficiency (a), local efficiency (b), clustering coefficient (C), transitivity (D), and modularity (E) are calculated for delays of 9 (left) and 10 (center). Right: The values of the corresponding measures for baseline (red) and longitudinal (black) data over a selected range of densities. These results were calculated based on the low resolution parcellation scheme.

### 6.3.2 Alzheimer’s Disease patients

The results of the comparison between healthy controls and various patient groups (CTR – A1, eMCI, lMCI and AD) for the global and local efficiency, clustering, transitivity and modularity are shown in figures 6.5 to 6.9 respectively. In each figure, the differences between the two groups are plotted by the orange circles, on the top of the 95% confidence intervals (the gray area). The box-plots illustrate the actual values of the measures for each group (CTR – A0 are plotted in black, the patient groups are plotted in red) as a function of the delay, averaged over the range of density for which the between-group differences are significant. The results in these figures are calculated for delays 1-3. For the corresponding results in higher delays, 4-6, see figures A.4 to A.8.

CTR – A1, eMCI and lMCI patient groups did not show any significant differences when compared with healthy controls. On the other hand, widespread changes were observed for AD patients relative to controls. Contrary to the PD-CN patients, these changes appeared at smaller delays. On the other hand, similarly to the PD-CN patients, the global efficiency differences occur at small densities; all other measures tend to show significant results at higher densities.

We observed decreases in global efficiency, local efficiency, clustering coefficient and transitivity for delays 1 and 2; at the same delays the modularity tended to show increases at higher densities. Crucially, since decreases in global efficiency can be interpreted as increases in the characteristic path length, these results mirror the results presented in chapter 5 for undirected network analysis [96]. These findings validate our method as a possible option to analyze the abnormal network organization in Alzheimer’s patients while hinting that the directed networks in these patients are more susceptible to changes due to this disease.

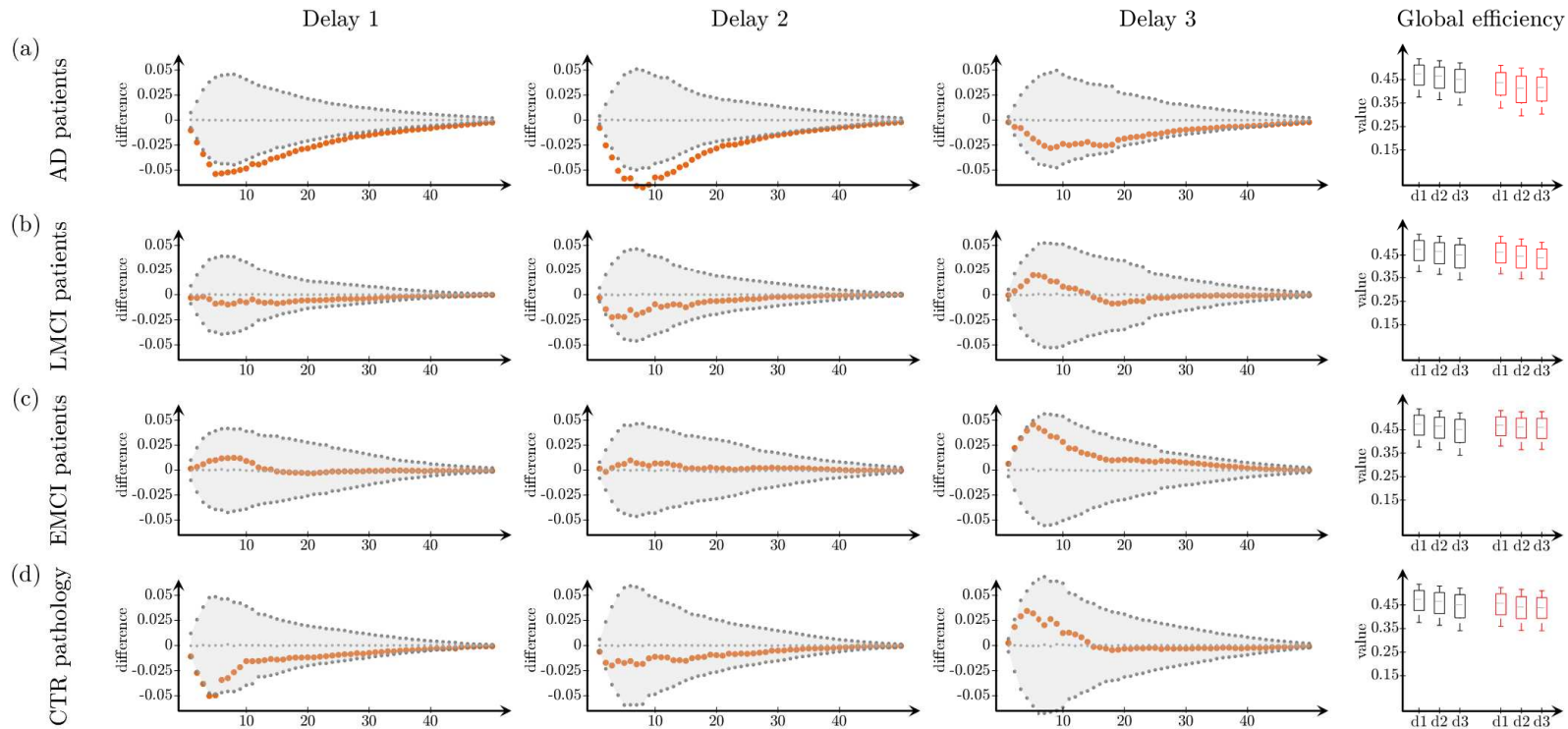


Figure 6.5: Changes in global efficiency as a function of network density for delays 1-3. CTR – A0 group is compared to CTR – A1 (a), eMCI (b), lMCI (c) and AD (d) patients for delays of 1 (leftmost), 2 (left-center) and 3 (right-center). Rightmost: The values of the global efficiency for the corresponding groups (controls shown in black).

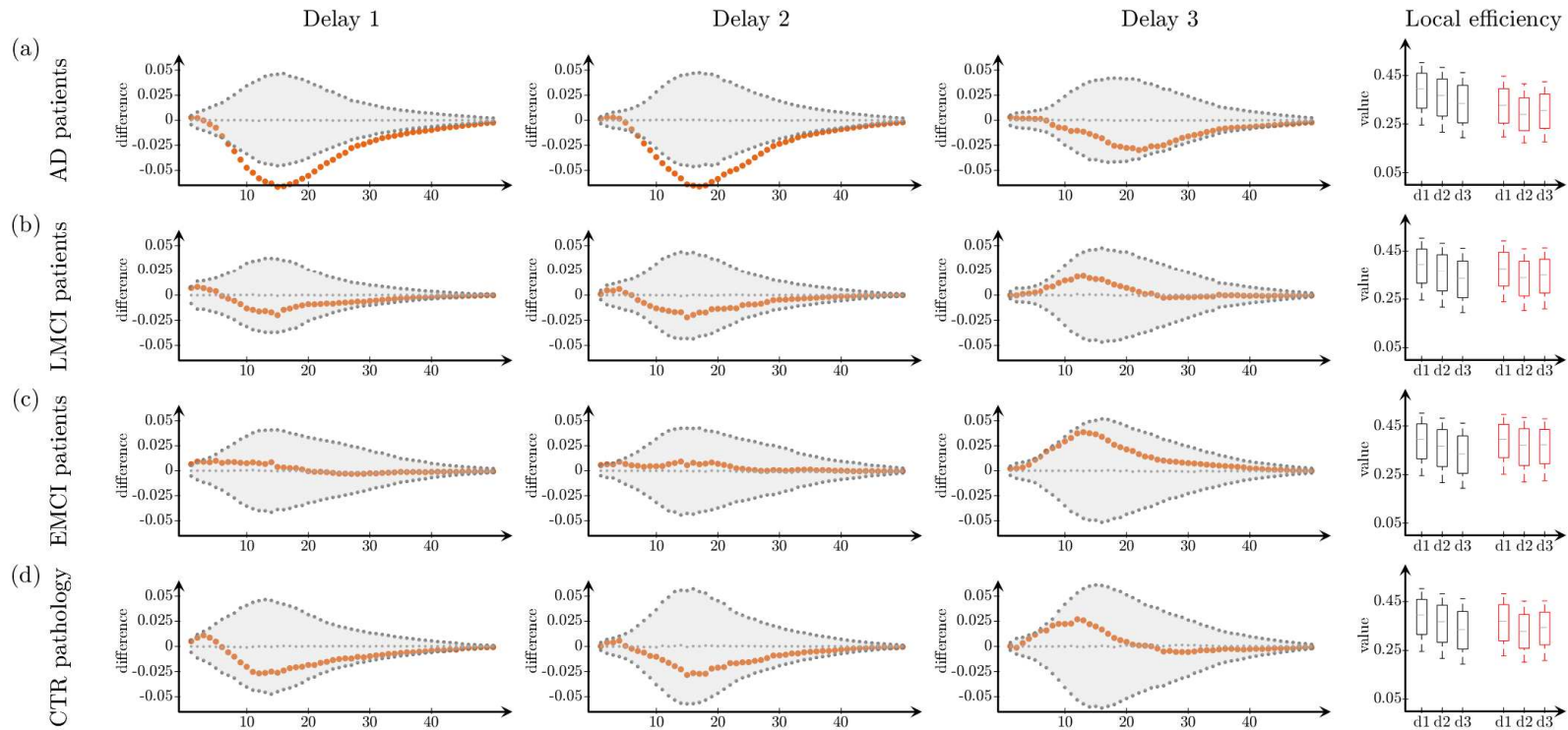


Figure 6.6: Changes in local efficiency as a function of network density for delays 1-3. CTR – A0 group is compared to CTR – A1 (a), eMCI (b), lMCI(C) and AD (D) patients for delays of 1 (leftmost), 2 (left-center) and 3 (right-center). Rightmost: The values of the local efficiency for the corresponding groups (controls shown in black).

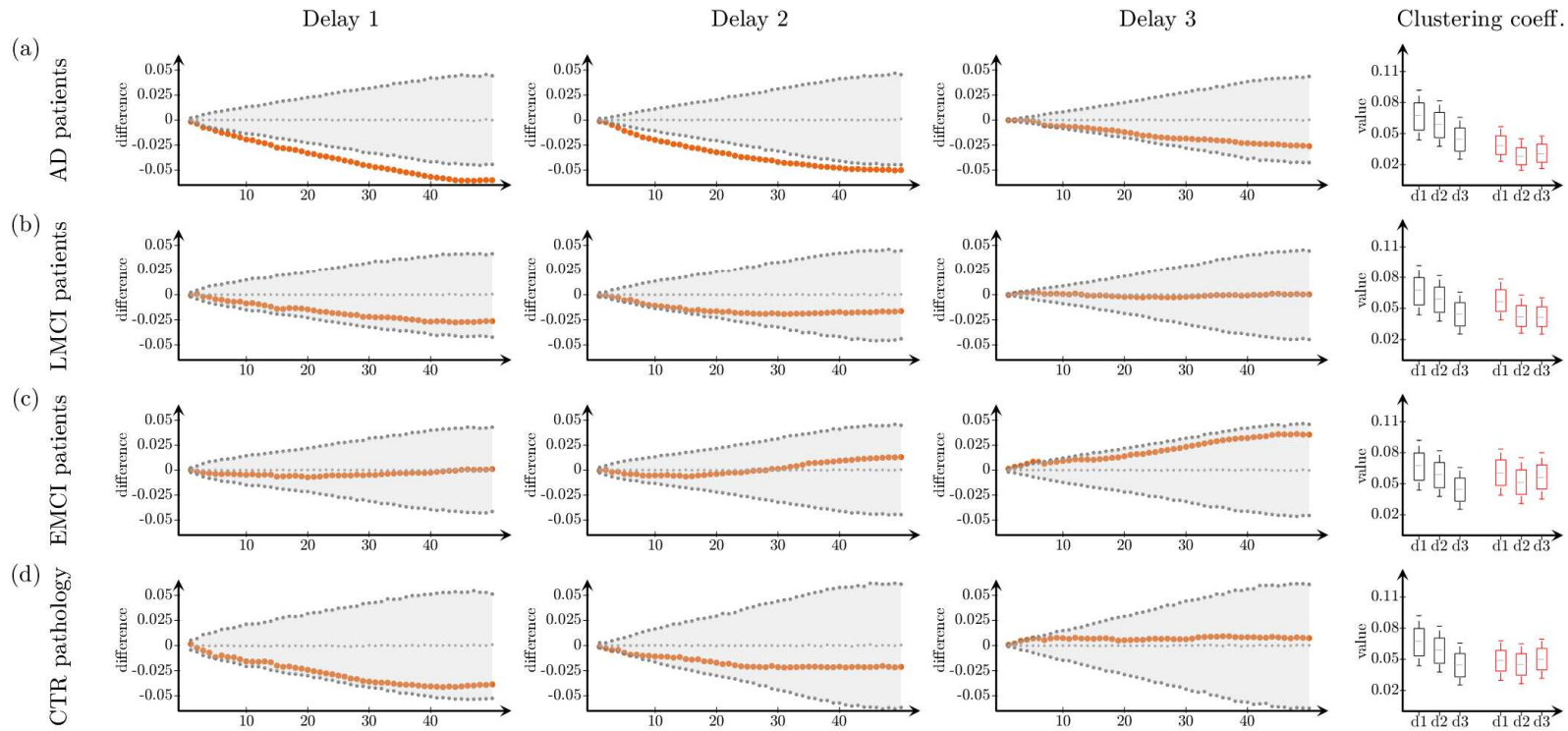


Figure 6.7: Changes in clustering coefficient as a function of network density for delays 1-3. CTR – A0 group is compared to CTR – A1 (a), eMCI (b), lMCI (c) and AD (d) patients for delays of 1 (leftmost), 2 (left-center) and 3 (right-center). Rightmost: The values of the clustering coefficient for the corresponding groups (controls shown in black).



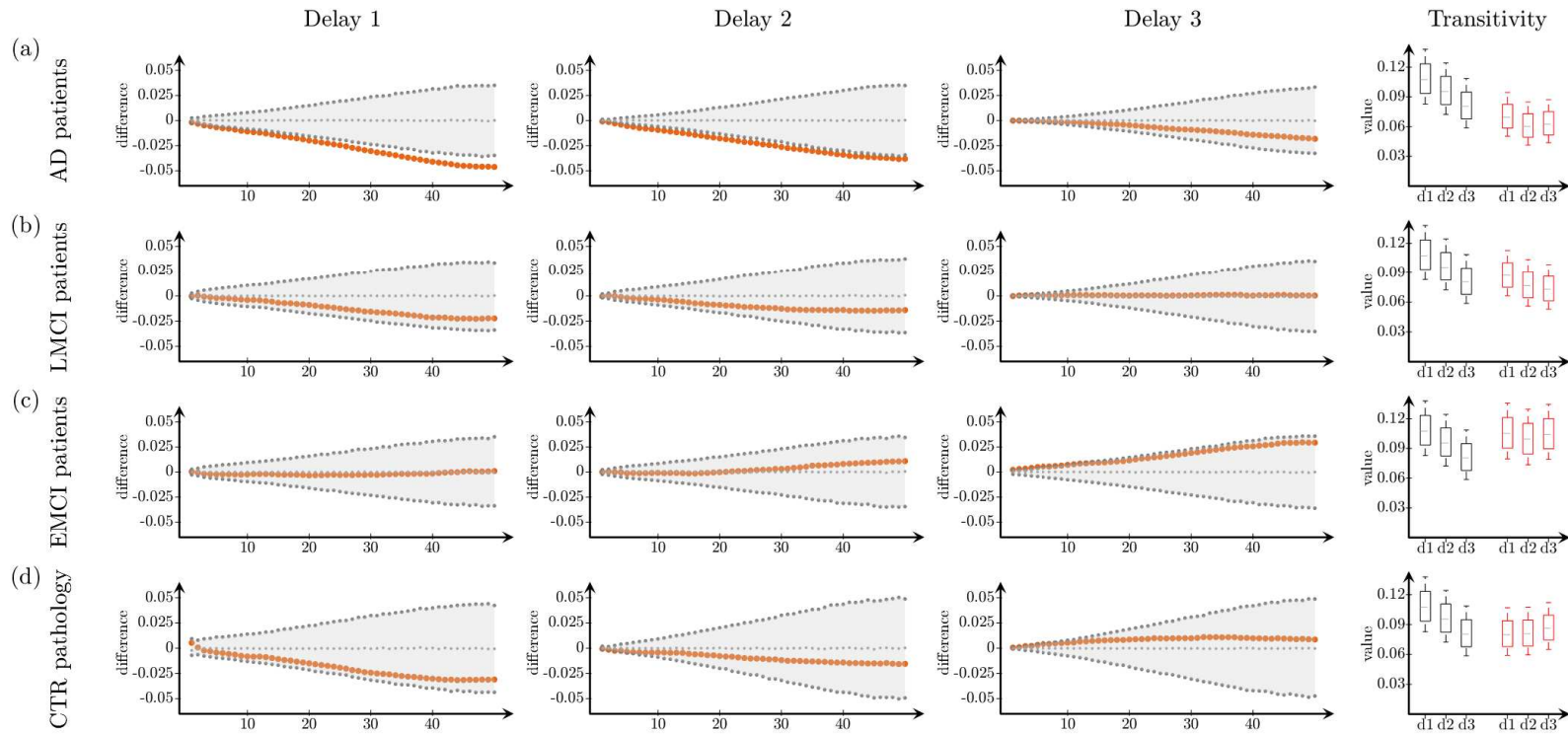


Figure 6.8: Changes in transitivity as a function of network density for delays 1-3. CTR – A0 group is compared to CTR – A1 (a), eMCI (b), lMCI (c) and AD (d) patients for delays of 1 (leftmost), 2 (left-center) and 3 (right-center). Rightmost: The values of the transitivity for the corresponding groups (controls shown in black).

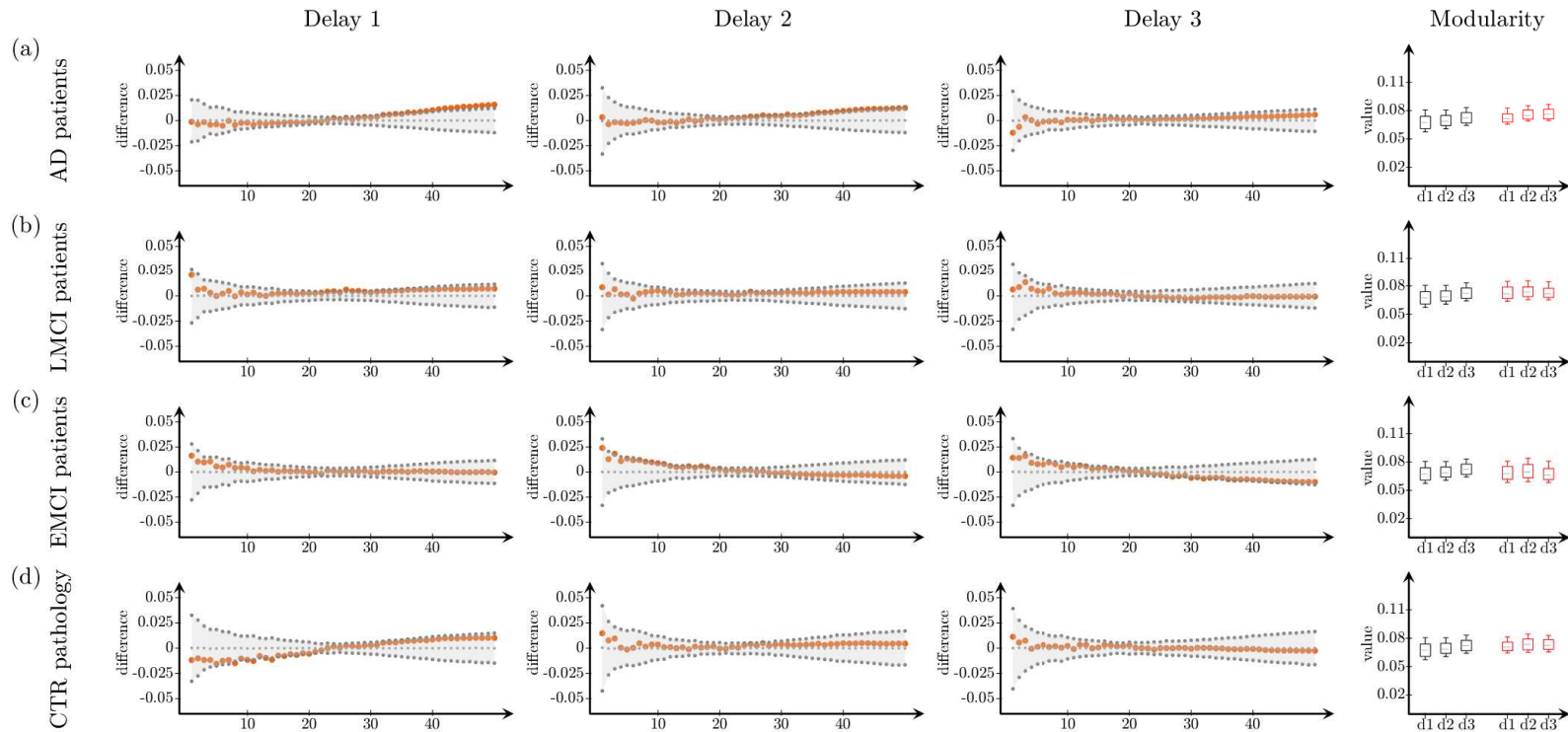


Figure 6.9: Changes in modularity as a function of network density: delays 1-3. CTR – A0 group is compared to CTR – A1 (a), eMCI (b), LMCI (c) and AD (d) patients for delays of 1 (leftmost), 2 (left-center) and 3 (right-center). Rightmost: The values of the modularity for the corresponding groups (controls shown in black).

## 6.4 Future perspectives

The results presented in this chapter suggest that directed networks built by delayed correlations are good indicators of any topological changes that might result from a particular neurodegenerative disease. However, further discussions and investigations are needed in order to understand certain features of this model.

Firstly, the question of why PD-CN and AD patients show significant results at different temporal delays needs further investigation. In particular, we need to understand whether these delays are significant for the relevant disease because possibly, the most affected regions by that disease show the strongest mutual correlation at these delays. Additionally, a detailed study of any potential changes in the regional topology will also be conducted.

Finally, in this chapter I presented differences of the global network measures in the full range of density that is available for this analysis. However, it is possible that the networks for very low densities can become highly disconnected, while the networks at high densities show characteristics similar to random networks, which makes them unsuitable for the analysis. Further evaluations are needed in order to check which network densities result in meaningful networks.

# Chapter 7

## Delayed Correlations Improve Reconstruction of the Brain Connectome

### 7.1 Introduction

The large-scale complex network of the brain, also known as the *connectome* [81], consists of intricate patterns of anatomical pathways connecting the spatially distributed neuron populations. This structural network is widely considered to act as a scaffold that facilitates the vast range of dynamic behaviors exhibited by the neurons, reflected in the observation of the functional networks of the brain [94, 218]. In contrast to the structural networks, functional networks are calculated as statistical associations between the set of all anatomically separated regions that exhibit correlated activity [83], and as such, the functional networks do not correspond to any physical connections. Nevertheless, it has been shown that these networks are reliable and robust over a wide range of working conditions of the brain [219, 220].

One of the challenges in neuroscience is to understand the nature of the relation between the structural and functional organization of the brain and study whether we can infer the properties of one organization by having knowledge of the other. Previous studies have already shown that structural architecture shapes the functional activation on many levels, ranging from small neuronal networks to large-scale networks in the brain [107, 221]. They also demonstrated that strong structural connections are a good indicator of strong functional ones [108], while also arguing that inferring structural networks from functional ones is possible [222], but less reliable [108, 223].

One major caveat of the functional networks is their strong dependence on the measure used to quantify the temporal correlations; such measures include correlation, coherence, Shannon entropy or phase-locking values (for a review, see [85]). While each model offers certain advantages and disadvantages for their use, currently there is not a unique standard or validation for the usage of one over the others [85]. In spite of that, defining the connection strength between two regions as the Pearson's correlation coefficient between their corresponding activation time series remains one of the most widely used method. This measure relies on the assumption that the two regions' activation is reciprocal, direct and simultaneous.

While the Pearson's correlation is computationally fast and simple to interpret, it has a few major disadvantages. For example, it cannot account for the indirect connections in the brain, which have been shown to have an effect on the functional connectivity [108]; nor takes into consideration the temporal delays, which play a role in the synchronization of neural networks [224, 225, 226] and brain organization [227]. In addition, the origin and interpretation of the negative correlation coefficients is still a debated topic. While some studies argue that negative correlation are a corollary of the data analysis process, others ascribe them to purely physiological origin [228, 229]. In order to avoid this issue, sometimes it is preferable to include only the positive connections in the analysis, by setting the negative coefficients to zero or to their absolute value.

In this chapter, I will demonstrate that the functional networks derived from the

standard correlation methods do not faithfully represent the primary structural networks. Instead, we propose a method, the *delayed correlation*, to reconstruct the structural brain connectome by utilizing the temporal delays in the dynamic behavior of the neurons. We show that the delayed correlation method correctly identifies 70% to 80% of the connections in simulated networks and performs well in the identification of the global and nodal network properties, especially at low densities which are relevant for the connectome. This method suggests that the underlying network architecture invariably introduces temporal delays in the dynamic behavior of the neurons and harvesting this information is necessary for its reconstruction.

## 7.2 Materials and methods

### 7.2.1 Model of neuronal activity

In order to simulate the spontaneous activity of each neuron, we used a linear model, suggested by Galán [230, 108]. The activity of each neuron is expressed as

$$\vec{\mathbf{u}}(t + \Delta t) = A\vec{\mathbf{u}}(t) + \eta(t), \quad (7.1)$$

where  $A$  is a generalized connection matrix that is given by

$$A = (1 - \alpha\Delta t)I + C\Delta t \quad (7.2)$$

In this equation,  $\alpha$  is a variable that specifies the amount of leakage of each neurons,  $I$  is the identity matrix, and  $C$  is the matrix specifying the connection strengths between the neurons; in place of  $C$  we use the simulated weighted real matrix that specifies the coupling strength between any pair of neurons (figure 7.1(a)).

There are no external sources in this system, instead, the neurons are driven by spatially and temporally independent Gaussian noise, denoted by  $\eta$ . In order to achieve stability in the simulations,  $C$  was normalized to have a unit norm,

$\|C\| = 1$ . By setting  $\Delta t = 0.5$ , for a wide range of connectivity matrices, we obtain stable simulations for  $1 \geq \alpha \leq 3$ . In what follows, we use  $(\alpha, \Delta t) = (2, 0.5)$  in order to obtain a model in which the neuron’s behavior does not depend on its state at previous times.

## 7.2.2 Analysis overview

By using the linear model of neuronal dynamics described in the previous section, we simulated the spontaneous activity of a neuronal network with a small-world architecture. The organization of this “*real network*” of neurons was derived from the Watts-Strogatz model (chapter 1), while the inter-neuron synaptic strengths were drawn from a symmetric Gaussian distribution (figure 7.1(a)). Each node (neuron) of this network is endowed with a dynamic behavior by using the linear model described in the previous section with the real matrix employed in the place of  $C$ , a sample of the neurons’ activation patterns is shown in figure 7.1(c). From each neuron’s time series, one can build a “*reconstructed network*” by choosing a certain measure of association between any pair of time series; this network is indicative of the functional connections between each pair of neural elements.

We propose a new method of building this network, the *delayed correlation* method, which utilizes the temporal delays in the correlation of the neurons’ time series. In particular, we define the connection strength between two neurons as the inverse of the delay at which the absolute value of the cross-correlation function between the two neurons is maximal. In this way, we obtain a weighted reconstructed network in which the strongest functional connections occur for pairs that are activated simultaneously or with small temporal delays.

In order to evaluate whether this method is a good predictor of the structural architecture, we compared the real and the reconstructed networks by using few parameters as benchmarks. Specifically, we calculated the percentage of common connections in the two networks, and evaluated the extent to which global and local characteristics of the real network are replicated in the reconstructed network. This comparison was performed by binarizing both matrices by ensuring

that they both have the same number of connections, and subsequently comparing the resulting binary matrices (for example, the network in figure 7.1(d) is compared to the one in figure 7.1(b)).

To check how the delayed correlation method fares against the commonly used correlation procedures, we also calculated the reconstructed networks by using Pearson's correlation coefficient (which assumes synchronicity between the time series) by treating the negative coefficients in two ways: substituting them with their absolute values (henceforth referred to as *absolute correlation* method, figure 7.1(e)) or setting them equal to zero (*zero correlation method*, figure 7.1(f)). After calculating these networks, they were also binarized and compared to the binary real network in figure 7.1(b). Furthermore, in order to assess whether the obtained results can be explained by chance alone, the three models were gauged against a null model, in which the edges in the reconstructed matrix are built at random.



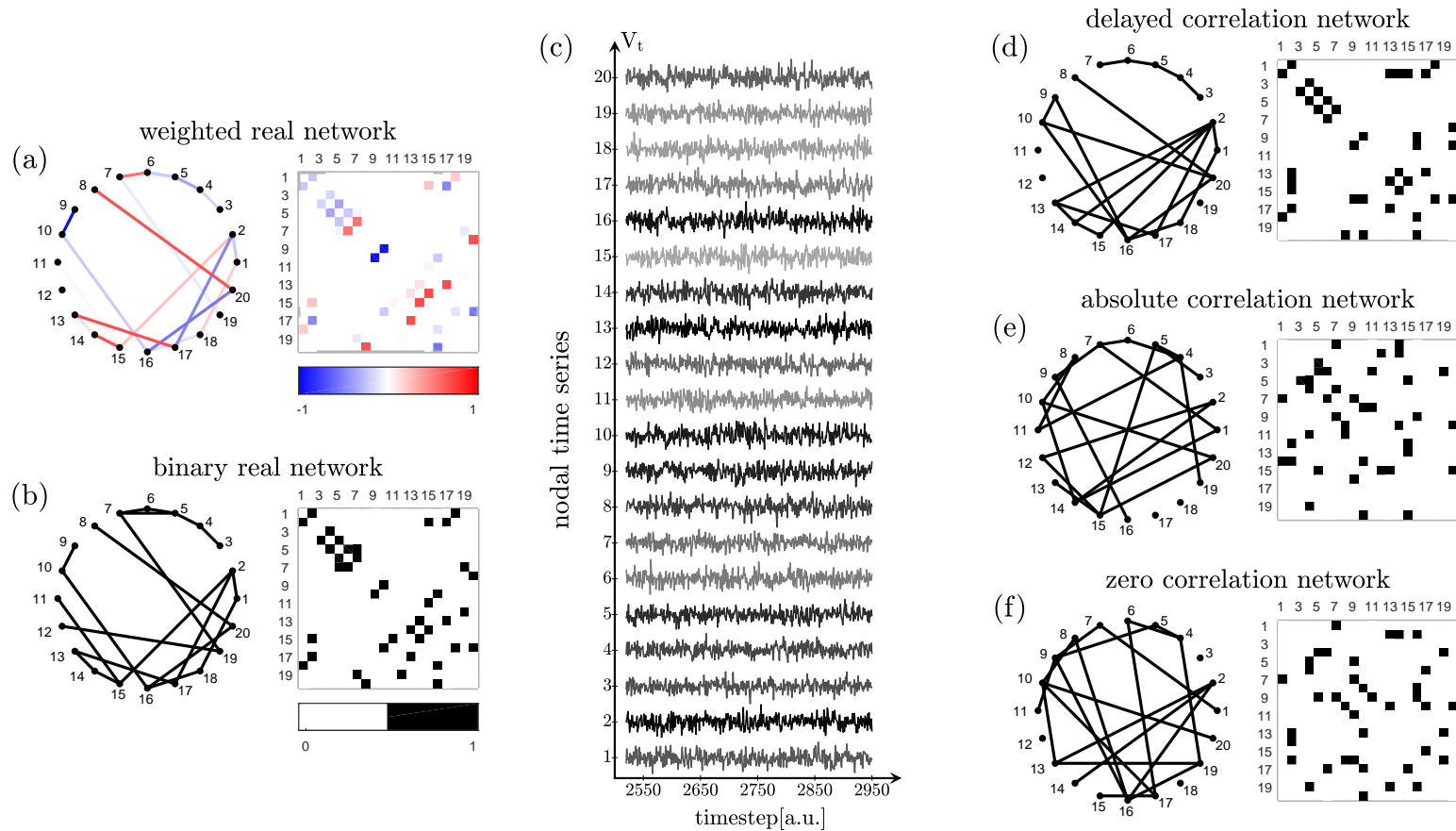


Figure 7.1: Overview of the network reconstruction procedure. (a) An example of weighted, small-world structural network of 20 nodes derived from the Watts-Strogatz model, showing the 10% of the strongest connections. (b) The corresponding binary network at the same density of connections as in (a), after all of its edges have been assigned a weight of 1. Each node of this structural network is endowed with dynamic behavior by using a Simple Autoregressive model (SAR) with the network in (a) defining the between-node coupling strengths. A sample of each node's representative time series is shown in (c). Using the time series, a network at the same density as (b) is reconstructed by the following methods to calculate the metric specifying the between-node connection strength: (d) delayed correlation approach; pairwise Pearson's correlation coefficient in which negative coefficients are set to (e) zero and (f) their absolute values. To assess each method's accuracy, the reconstructed binary networks (shown in (d),(e) and (f)) are compared with the real binary network shown in (b).

## 7.3 Results and discussion

### 7.3.1 Network reconstruction accuracy

Figure 7.2 shows the percentage of successfully reconstructed connections (edges in the reconstructed network that are also present in the real one), for each of the four methods described in the previous section. The reported results are calculated for networks of 100 nodes (figure 7.2(a)), of 200 nodes (figure 7.2(b)) and of 500 nodes (figure 7.2(c)), over the range of densities for which the real networks are sparse. Each real network is simulated by the Watts-Strogatz model with  $\beta = 0.05$  and the plotted results are the average of 100 trials. We show that the delayed correlation method builds reconstructed networks that overlap around 60% to 80% with the real neuronal networks over the whole density range and for different network sizes. The absolute correlation method performs in the range of 5% to 25% and shows slightly better results than the zero correlation. All three methods perform better than the null model, indicating that these results are not due to chance alone.

These results show that the functional networks calculated by the widely used correlation methods do not represent the structural networks faithfully. On the contrary, the delayed correlation method can reconstruct up to 80% of the real network, with the best performance shown in sparse networks, i.e. lower resolution networks at small densities. This behavior can be explained by considering the efficiency of communication within the neuronal network.

Two neurons that interact and communicate strongly are expected to show highly correlated activation patterns (either synchronous or at small temporal delays). In this context, strong interaction implies very short and clearly defined paths (section 2.3) between the two neurons. In sparse networks, due to the very low number of connections, two neurons can communicate only through few different paths; i.e. one node can be reached from the other in only few different ways. Therefore, the communication pathway between any two nodes in a sparse network is very well defined; as a result, the temporal delays (which can be thought

to occur due to the finite speed of information transmission) will be indicative of the distances between the nodes. In particular, two nodes with shorter distances between them will correlate with smaller temporal delays.

On the contrary, as the density and the number of nodes in the network increase, the number of connections in the network and, consequently, the number of paths that can be used for communication between two nodes increases. Each of these possible paths involves different number of edges that need to be crossed, therefore, a clearly preferred pathway of interaction is not available. As a result, the communication between the two nodes is scrambled, without a clear transmission delay. Therefore, the calculated delay conveys less information about the distance between nodes which, in turn, makes the reconstruction of the real network less efficient.

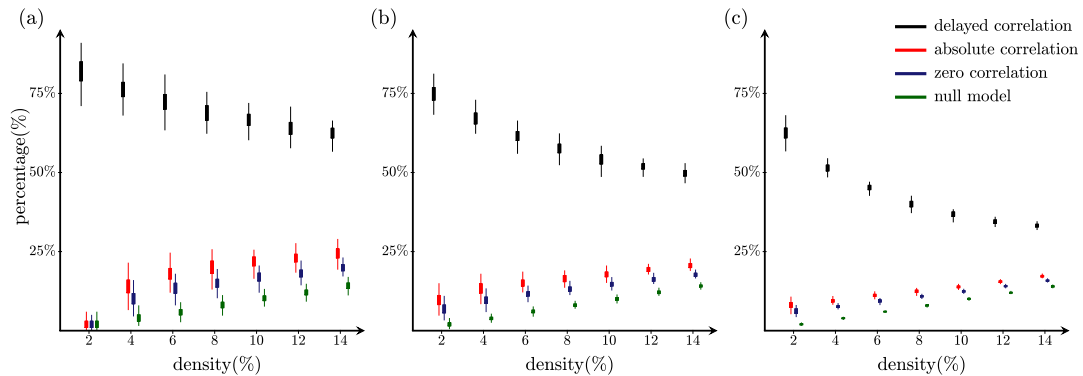


Figure 7.2: Accuracy of network reconstruction. Percentage of edges in the real network that can be correctly identified by each method (black - delayed correlation; red - absolute correlation; blue - zero correlation; green - null model) for networks of (a) 100 nodes, (b) 200 nodes and (c) 500 nodes. The bottom and top edges of the boxes show the 25<sup>th</sup> and 75<sup>th</sup> percentiles while the vertical lines extend to the furthest observations that are not designated as outliers. The plots were obtained as an average of 100 trials.

The reason that the real network cannot be reconstructed perfectly can be traced to the inherent drawbacks of the correlation procedure. In particular, two nodes can show highly correlated activation patterns if they have a strong interaction

between them (i.e. they have a direct connection). Alternatively, highly correlated activation can be also exhibited if both nodes have no connection between them, instead, they are both influenced from a third node in a similar way (i.e. they have indirect connection, mediated by a third node). This inability of the correlation methods to make difference between direct and indirect connections is one of the main reasons that not all real connections can be inferred from the functional data. Indeed, Honey et al [108] demonstrated that there can be functional connectivity between two regions even if they do not have a physical link between each other, attributing this property to the indirect connections between the nodes.

### 7.3.2 Features of the delayed correlation model

We carried out a detailed analysis to investigate the robustness of the delayed correlation method against different models of the real matrix and inter-neuronal strength. Our reference model was a real small-world network of 200 nodes, with the synaptic strengths drawn from a Gaussian distribution centered around zero. Then, we proceeded to investigate how varying each of these parameters affected the performance of the delayed correlation method.

Figure 7.3(a) shows the method's accuracy as a function of the small-worldness of the real network. The corresponding reconstructed networks have a 50% overlap with the real network for every intermediate network interpolated between a regular network and a random one, shown in inset. Furthermore, the method shows good performance as a function of the heterogeneity of the nature of the synapses, figure 7.3(b). We demonstrate this by varying the percentage of excitatory synapses present in the real network. It can be seen that the percentage of correctly identified connections is symmetric around the point of 50% excitatory synapses; the model performs equally well regardless of whether the network is mostly excitatory or inhibitory. Moreover, the accuracy of the model improves as the homogeneity of the synapses increases. Finally, we draw the synaptic weights from a q-Gaussian distribution that we vary from bounded to heavy tailed by

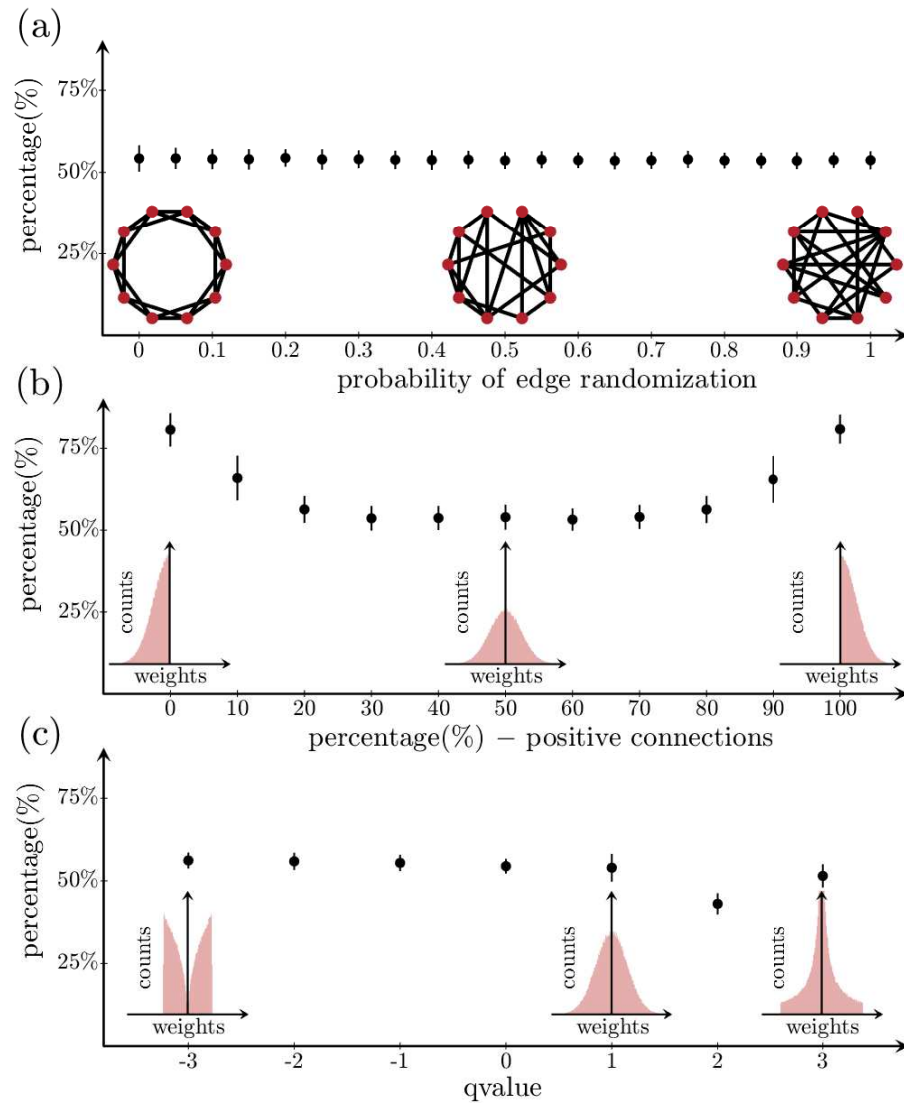


Figure 7.3: Network reconstruction efficiency of the delayed correlation method. Reconstruction efficiency as a function of (a) probability to randomize an edge in the Watts-Strogatz model, (b) percentage of positive weights in the weighted real network and (c) different distribution of weights in the real network represented by the  $q$  parameter in a  $q$ -Gaussian distribution. Insets: (a) An example of structural network for different randomization parameter in the Watts-Strogatz model. From left to right the networks vary from regular to random networks. (b) Histograms of the structural weights distribution when there are (from left to right) 0%, 50% and 100% positive weights. (c) The weight distribution changes ranging from bounded  $q$ -Gaussian for  $q = -3$ , Gaussian function for  $q = +1$  to heavy tail distribution for  $q = +3$ .

setting different values to the parameter  $q$ , insets in figure 7.3(c). The results in figure 7.3(c) show that the model's performance is not dependent on the particular shape of the synaptic strength distribution used.

All of these results taken together, indicate that the ability of the delayed correlation method to reconstruct the real network, does not depend on the models from which the real matrices and synaptic strengths are drawn. Instead, the only limiting factor to this method's performance is due to the number of connections within the network.

### 7.3.3 Global network properties

The global topology of the real network was evaluated by the calculation of the clustering coefficient, transitivity, characteristic path length and the global efficiency (chapter 2). The real network had 200 nodes and small-world characteristics ( $\beta = 0.05$ ), as such, it is characterized by high clustering coefficients coupled with low path lengths, or analogously by high transitivity and high global efficiency as shown in figure 7.4 (orange boxes). Only the delayed correlation method results in reconstructed networks with similar clustering and transitivity as the real ones for small densities, however, all methods perform close in the reconstruction of the network's clustering for higher densities (figure 7.4(a) and 7.4(b)). On the other hand, all methods are able to reconstruct equally well the short path lengths and high global efficiencies in the real network (figure 7.4(c) and 7.4(d)). Due to the high reproducibility of the results, the boxes in figure 7.4 are centered around the corresponding median with constant standard deviation. Detailed information about the mean and standard deviation of each point can be found in table 7.1.

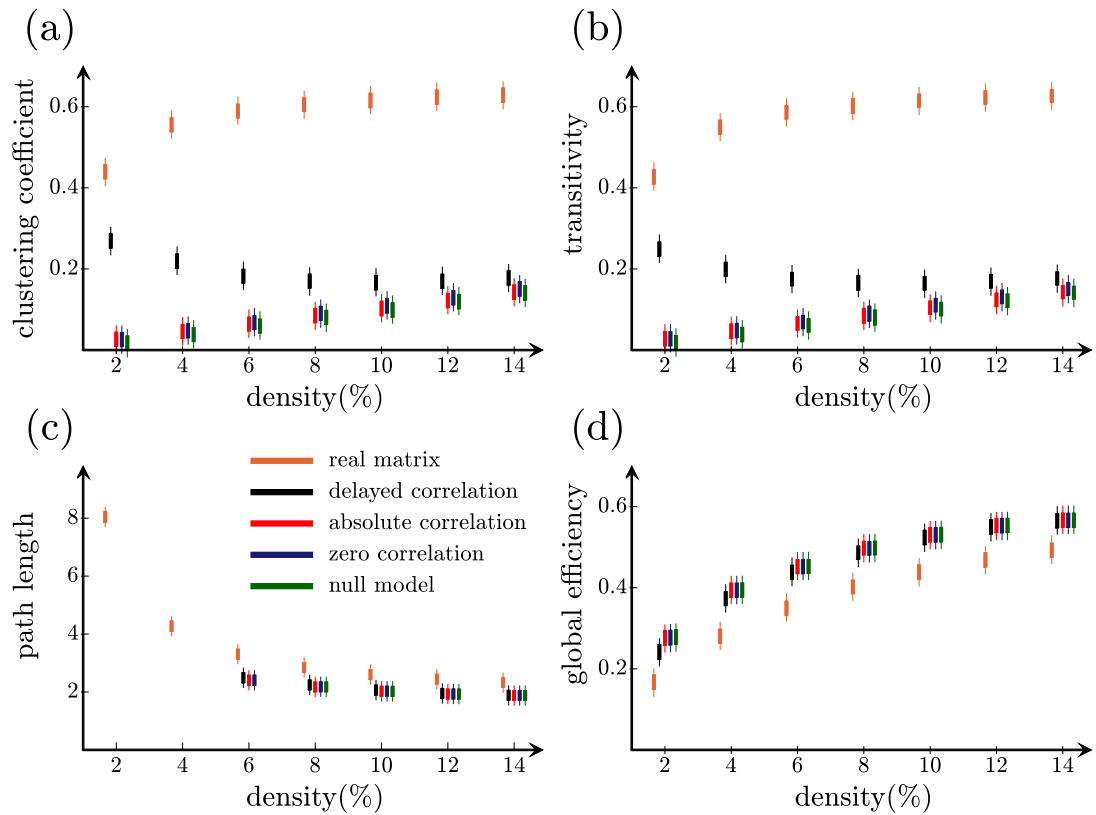


Figure 7.4: Global network measures as a function of network density. (a) Clustering coefficient, (b) transitivity, (c) characteristic path length and (d) global efficiency calculated for real network (orange), delayed correlation (black), absolute correlation (red), zero correlation (blue) and null model (green). The boxes are centered around the median and the spread of the data is fixed at the same values for each point. Detailed information about the mean and standard deviation is summarized in table 7.1.

The nodal clustering coefficient is a measure of the fraction of triangles that can be formed around a node; the average of this coefficient over all nodes in the network gives the global clustering coefficient (section 2.3). Since the formation of a triangle around a particular node involves the arrangement of 3 edges in a particular order, in order to observe similar clustering in the reconstructed network all 3 connections need to be correctly reconstructed. However, as discussed above, the real matrix cannot be completely reproduced and around 20% to 30%

of the connections remain wrongly reconstructed. Therefore, for each wrongly reconstructed connection, a number of triangles they were part of get broken down, and the clustering coefficient invariably decreases due to the reconstruction. For the delayed correlation method, the clustering coefficient decreases as function of density; this is due to the fact that the number of wrongly reconstructed connections increases with density (figure 7.2(a)), as a result, more triangles are broken down with density. Since the transitivity is very similar to the clustering coefficient (section 2.3), the same line of reasoning can be applied in order to explain its behavior shown in figure 7.4(b).

On the contrary, the wrongly reconstructed edges do not have such profound effect on the path length and global efficiency. In particular, in the case of clustering, a wrongly reconstructed edge results in breaking down a triangle in the real network, but does not necessarily result in building of a triangle in the reconstructed network, therefore making no contribution to the overall clustering. On the contrary, since path length and global efficiency are calculated as averages over all nodes in the network, every edge (rightly or wrongly reconstructed) makes contribution to their calculation, resulting in similar values for the real and reconstructed networks (figure 7.4(c-d)).

Furthermore, the path lengths calculations show that even though the real network is a connected one, the reconstructed networks can be disconnected (especially for small densities). Therefore, instead of the path length, the global efficiency needs to be used to characterize sparse networks, indicating that it is indeed a superior measure with respect to the path length (chapter 2).



Table 7.1: Global network measures as a function of network density. For each density, the mean and standard deviation (in the parentheses) are shown for all methods. These results correspond to the ones plotted in figure 7.4.

<b>Clustering coefficient</b>							
Density	2%	4%	6%	8%	10%	12%	14%
real matrix	0.437 (0.016)	0.557 (0.012)	0.589 (0.013)	0.605 (0.011)	0.617 (0.009)	0.624 (0.008)	0.628 (0.007)
delayed corr.	0.268 (0.043)	0.219 (0.030)	0.183 (0.017)	0.171 (0.014)	0.166 (0.010)	0.171 (0.006)	0.177 (0.005)
absolute corr.	0.027 (0.008)	0.047 (0.006)	0.065 (0.004)	0.084 (0.003)	0.103 (0.003)	0.123 (0.002)	0.142 (0.002)
zero corr.	0.028 (0.009)	0.048 (0.006)	0.069 (0.004)	0.090 (0.003)	0.110 (0.003)	0.130 (0.002)	0.150 (0.002)
null model	0.018 (0.008)	0.039 (0.005)	0.061 (0.004)	0.080 (0.003)	0.100 (0.003)	0.121 (0.002)	0.141 (0.002)
<b>Transitivity</b>							
Density	2%	4%	6%	8%	10%	12%	14%
real matrix	0.426 (0.016)	0.550 (0.013)	0.584 (0.013)	0.602 (0.011)	0.615 (0.010)	0.621 (0.008)	0.626 (0.007)
delayed corr.	0.245 (0.043)	0.201 (0.028)	0.174 (0.016)	0.166 (0.013)	0.163 (0.009)	0.168 (0.006)	0.176 (0.005)
absolute corr.	0.030 (0.009)	0.047 (0.005)	0.065 (0.004)	0.084 (0.003)	0.103 (0.003)	0.123 (0.002)	0.142 (0.002)
zero corr.	0.029 (0.007)	0.048 (0.005)	0.069 (0.004)	0.090 (0.003)	0.110 (0.003)	0.130 (0.002)	0.150 (0.002)
null model	0.020 (0.006)	0.039 (0.004)	0.060 (0.003)	0.080 (0.003)	0.100 (0.003)	0.120 (0.002)	0.141 (0.002)

Continued

Table 7.1 – Continued

	<b>Path Length</b>						
Density	2%	4%	6%	8%	10%	12%	14%
real matrix	8.128 (0.848)	4.294 (0.182)	3.312 (0.088)	2.851 (0.051)	2.602 (0.034)	2.440 (0.019)	2.321 (0.016)
delayed corr.	—	—	2.489 (0.013)	2.243 (0.011)	2.062 (0.007)	1.949 (0.003)	1.884 (0.002)
absolute corr.	—	—	2.402 (0.003)	2.176 (0.003)	2.022 (0.002)	1.929 (0.002)	1.876 (0.001)
zero corr.	—	—	2.403 (0.003)	2.178 (0.003)	2.023 (0.003)	1.930 (0.002)	1.876 (0.001)
null model	—	—	—	2.174 (0.003)	2.020 (0.002)	1.927 (0.002)	1.876 (0.001)
	<b>Global Efficiency</b>						
Density	2%	4%	6%	8%	10%	12%	14%
real matrix	0.165 (0.010)	0.280 (0.008)	0.351 (0.007)	0.402 (0.005)	0.438 (0.004)	0.467 (0.003)	0.493 (0.003)
delayed corr.	0.240 (0.010)	0.373 (0.004)	0.440 (0.002)	0.486 (0.002)	0.523 (0.001)	0.549 (0.001)	0.566 (0.001)
absolute corr.	0.275 (0.004)	0.394 (0.001)	0.453 (0.001)	0.498 (0.001)	0.530 (0.001)	0.552 (0.001)	0.568 (0.001)
zero corr.	0.276 (0.003)	0.394 (0.001)	0.453 (0.001)	0.497 (0.001)	0.530 (0.001)	0.552 (0.001)	0.567 (0.001)
null model	0.277 (0.003)	0.395 (0.001)	0.454 (0.001)	0.498 (0.001)	0.530 (0.001)	0.552 (0.001)	0.568 (0.001)

### 7.3.4 Nodal network properties

We also calculated the percentage of nodes that possess similar topological properties in the real and reconstructed networks. As quantifying properties, we considered the degree, the global efficiency and the nodal clustering (figure 7.5). A node is considered to have similar degree in the reconstructed and real networks, if its degree in the reconstructed network is  $\pm 1$  of its degree in the real one; the corresponding value for the clustering and global efficiency is  $\pm 50\%$  of their value in the real network. The advantage of the delayed correlation method is clear for sparse networks; with this method up to  $\pm 75\%$  of the nodes have similar degrees in both reconstructed and real network, the other methods can result in only approximately  $\pm 50\%$  (figure 7.5(a)). Figure 7.5(b - leftmost) shows a sample real network in which each node is represented by a circle and the circle's sizes are proportional to the node's degree (the connections between nodes are not shown for clarity). The colored nodes in the networks shown in figure 7.5(b) represent the particular nodes correctly identified by each method; since most of the unidentified nodes have small degrees it follows that the delayed correlation method is able to correctly reconstruct the hubs, i.e. the nodes in the network with unusually high degrees.

Similar results follow for the global efficiency in sparse networks. Up to 85% of the nodes can be reconstructed by the delayed correlation compared to a maximum of 70% reconstructed by other methods, figure 7.5(c), while all methods perform equally well for higher densities. The most pronounced differences are observed in the nodal clustering coefficient; while the delayed correlation can identify a maximum of 50% of the nodes in sparse networks, other methods only can do so only for the 5% of the nodes (figure 7.5(e)).

These differences are due to the fact that only a low number of connections are correctly identified by the correlation methods. In particular, since the global measures reflect an aggregate result which is averaged over all nodes, the fact that some connections are not overlapping in both networks is offset to a certain degree by the averaging procedure for all nodes. However, since this averaging is

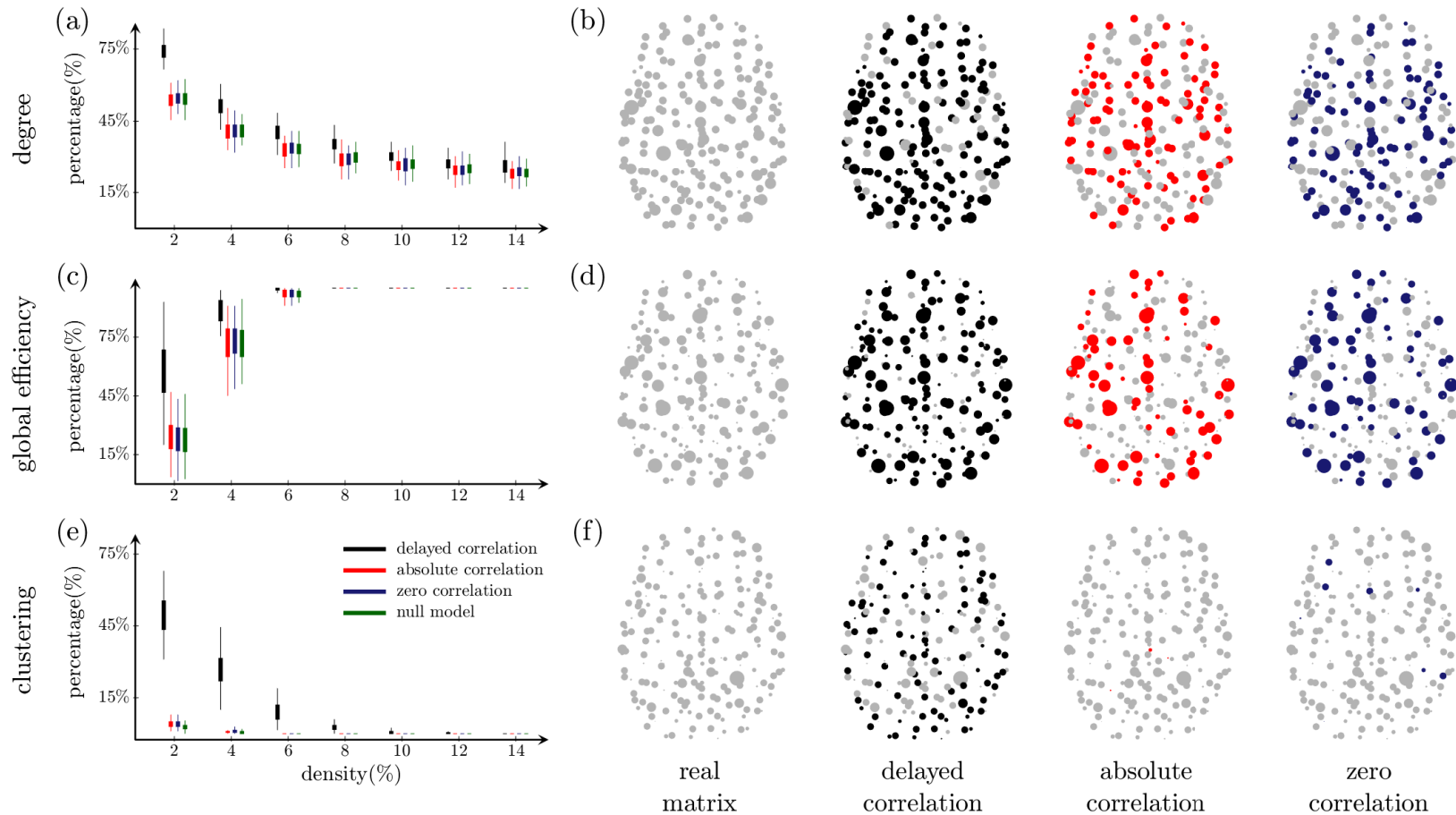


Figure 7.5: Nodal network measures as a function of density. Percentage of correctly identified nodes by the method of delayed correlation (black), absolute correlation (red), zero correlation (blue) and null model (green) as a function of density for (a) nodal degree, (b) nodal global efficiency and (c) nodal clustering. A node is considered to be successfully reconstructed if its value in the reconstructed network is within the tolerance range from its value in the real network. The tolerance range is defined as  $\pm 1$  for the nodal degree and  $\pm 50\%$  of the measure's value in the real network for clustering and global efficiency. (b-e) An example of single trial real network illustrating which nodes are reconstructed by each method based on the degree, global efficiency and clustering respectively. The real network is plotted in gray and the colored nodes have been successfully reconstructed by the corresponding method. The size of the nodes in the network is proportional to the node's value of the measure.

not present in the local topological measures, the fact that the majority of the connections are not reconstructed properly is translated into the incapability to replicate the nodal properties. Moreover, for each measure, the performance of the correlation methods over the whole range of densities is equal to the one of the null model, leading to the conclusion that their behavior is mainly due to chance alone. This indicates that the usual correlation methods do not relay any crucial information about the local network topology.

On the contrary, the delay correlation method performs very well in wide range of circumstances, with the difference being most pronounced for sparse networks. In particular, the fact that it performs much better than the null model, suggests that time delays convey a certain information about the network that goes beyond chance.

### 7.3.5 Community structure

To explore whether a given community structure of the real network can be faithfully reproduced by the delayed correlation method, we studied the reconstruction of modular networks. We created a modular network of 200 nodes that consisted of 5 isolated small-world sub-networks of 40 nodes each, therefore ensuring its maximum modularity (figure 7.6(a - left)). Then, we progressively added random connections to this network, as a result, the modularity of the network decreases with the number of connections that are added (the orange boxes in figure 7.6(d)).

Although the modularity of the real network decreases, the 5 original communities are largely preserved for the whole range of added random connections; the majority of the connections remain within the same community (the colored connections in figure 7.6(a-c)), however the modularity is decreased due to the increased number of between-community connections (connections plotted in black in figure 7.6(b and c)). When reconstructing this behavior, we observed that, while the delayed correlation performs much better than the other methods, it still results in slightly lower modularity values than the real network. The reason for this behavior (similar to the case of the reconstruction of network measures)

is the fact that although the delayed correlation successfully reconstructs the majority of real connections, it does not reconstruct all of them. Therefore, some of the connections that were running within community in the original network, can occur between nodes in different communities in the reconstructed one, therefore decreasing the modularity, as illustrated in figure 7.6(a,b,c - right).

In order to quantify the goodness of fit between the real and reconstructed communities, we evaluated the percentage of same-community pairs in the reconstructed network, that were also in the same community in the real network. The results of this parameters are shown in figure 7.6(e). We see that the delayed correlation is very successful into identifying such pairs, reaching up to 95% success for highly modular networks, while on the other hand, other methods can identify at most around 25% of such pairs. This parameter suggests that, on average, the communities formed in the reconstructed networks by the delayed correlation are meaningful and close to the real communities. However, it does not show whether the integrity of the communities in the original network was preserved, i.e. it cannot distinguish the cases when a community in real network is split into smaller communities in the reconstructed ones.

To that end, we proceed to calculate how many same-community pairs in the real networks remained in the same community after the reconstruction, showing the results in figure 7.6(f). For highly modular networks, the communities are largely preserved by the delayed correlation method, with more than 90% of the nodes remaining in their communities. As the modularity of the real networks decreases, the real communities tend to split due to the reconstruction process. However, the delayed correlation method still places 40% to 70% of the nodes in the same community, while for the other methods only 30% of the nodes remain.

Moreover, from figure 7.6(d-f), we can observe that while the delayed correlation performs much better than the null model, the other correlation methods perform similarly to it; this shows that the communities that result from these methods are entirely due to chance. The spread of the data in figure 7.6 is fixed in order to provide better visualization, the exact means and standard deviations for each point are given in table 7.2.

The community reconstruction results by the delayed correlation are summarized in figure 7.6(a - c) by plotting the community structure of a sample real (left) and reconstructed (right) network for different number of random connections. The corresponding communities are shown in the same color, the black lines represent inter-communities connections while the colored ones show connections running only within the same communities. From these plots, we can observe that in the case of  $N_{\text{conn}} = 0$ , the communities are preserved and only few nodes are not identified in the correct community. However, for  $N_{\text{conn}} = 1200$  the community division becomes less clear, and while most of the nodes retain their within community neighbors, each of the 5 communities in the real network is split into smaller ones.

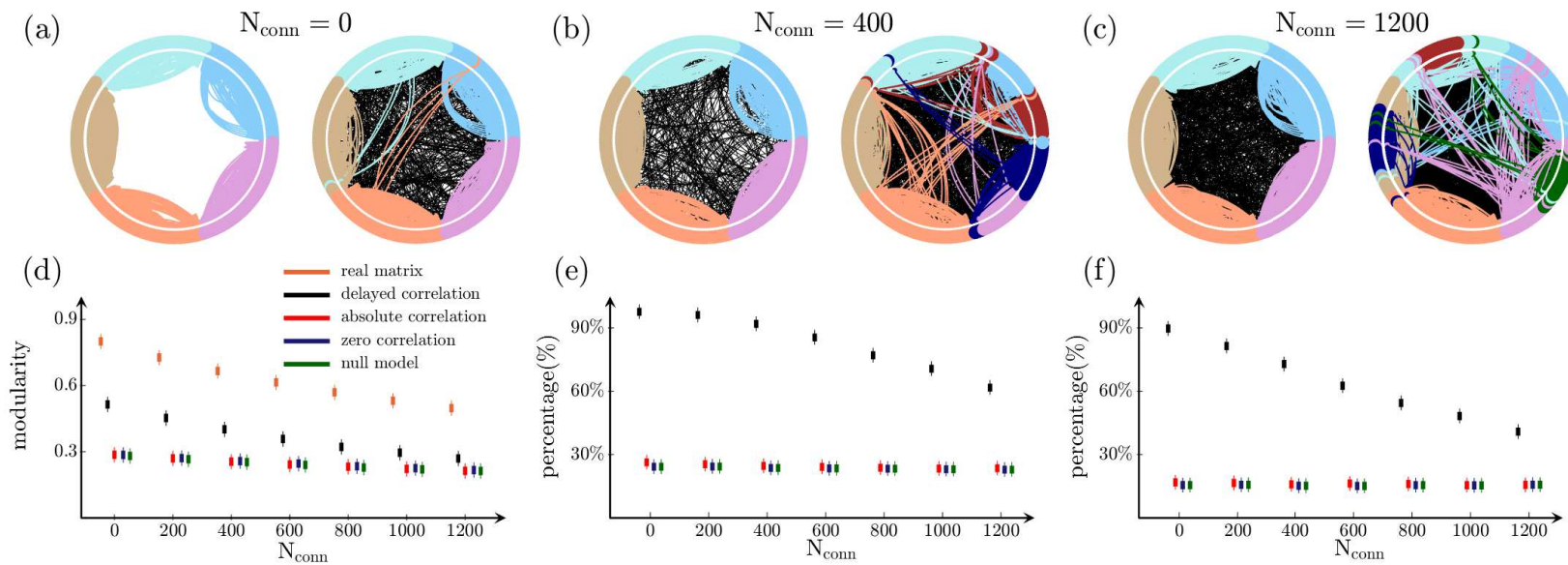


Figure 7.6: Community structure in a modular graph. A modular network of 200 nodes is built by clustering together 5 distinctive equal size communities with no connections between them (shown in (a), left) resulting in a maximum modularity of 0.8. The number of connections between communities is further increased (an example of the resulting networks is shown in (b) and (c) left) resulting in decreasing of the network modularity (d). (e) Percentage of same community paired nodes in the reconstructed network that were also in a same community in the real network as a function of the number of between community connections. (f) Percentage of pairs in a same community in the real network that are also in the same community in the reconstructed network. The matrices on the right in (a), (b) and (c) illustrate the reconstruction of the modular graph on the left by the delayed correlation method. The boxes are centered around the median and the spread of the data is fixed at the same values for each point. Detailed information about the mean and standard deviation is summarized in table 7.2.



Table 7.2: Community structure in a modular graph. For each number of inter-community connections, the mean and standard deviation (in the parentheses) are shown for all methods. These results correspond to the ones plotted in figure 7.6.

<b>Modularity</b>							
Density	2%	4%	6%	8%	10%	12%	14%
real matrix	0.800 (0.000)	0.727 (0.003)	0.666 (0.005)	0.614 (0.005)	0.569 (0.005)	0.532 (0.006)	0.497 (0.006)
delayed corr.	0.513 (0.027)	0.452 (0.022)	0.399 (0.019)	0.358 (0.015)	0.321 (0.015)	0.295 (0.013)	0.270 (0.013)
absolute corr.	0.286 (0.007)	0.270 (0.006)	0.254 (0.006)	0.242 (0.005)	0.231 (0.006)	0.222 (0.005)	0.213 (0.005)
zero corr.	0.285 (0.007)	0.271 (0.006)	0.257 (0.005)	0.246 (0.005)	0.234 (0.006)	0.226 (0.005)	0.217 (0.005)
null model	0.281 (0.006)	0.265 (0.005)	0.252 (0.005)	0.241 (0.006)	0.229 (0.005)	0.221 (0.006)	0.212 (0.005)
<b>Percentage of conserved reconstructed pairs</b>							
Density	2%	4%	6%	8%	10%	12%	14%
delayed corr.	97.72 (0.24)	96.33 (0.47)	92.16 (0.52)	84.83 (3.18)	77.84 (2.08)	70.76 (1.61)	61.85 (1.46)
absolute corr.	26.38 (0.27)	25.75 (0.55)	24.75 (0.20)	24.13 (0.24)	23.81 (0.10)	23.50 (0.12)	23.50 (0.33)
zero corr.	24.40 (0.23)	24.50 (0.21)	23.78 (0.18)	23.51 (0.13)	23.34 (0.23)	23.11 (0.13)	23.00 (0.11)
null model	24.40 (0.23)	24.50 (0.21)	23.78 (0.18)	23.51 (0.13)	23.34 (0.23)	23.11 (0.13)	23.00 (0.11)

---

Continued

Table 7.2 – Continued

Density	Percentage of conserved structural pairs						
	2%	4%	6%	8%	10%	12%	14%
delayed corr.	90.16 (1.33)	81.32 (1.63)	72.41 (2.48)	62.19 (2.30)	54.39 (1.49)	48.17 (1.76)	41.61 (2.17)
absolute corr.	16.76 (0.33)	16.55 (0.17)	16.00 (0.37)	16.33 (0.13)	16.26 (0.45)	15.45 (0.28)	15.72 (0.23)
zero corr.	15.61 (0.23)	15.71 (0.21)	15.26 (0.21)	15.07 (0.29)	15.55 (0.15)	15.49 (0.26)	15.75 (0.17)
null model	15.61 (0.23)	15.71 (0.21)	15.26 (0.21)	15.07 (0.29)	15.55 (0.15)	15.49 (0.26)	15.75 (0.17)

---

### 7.3.6 Diffusion tensor imaging networks

We also assessed the performance of each method in the reconstruction of structural networks derived from Diffusion Tensor Imaging (DTI). These networks were obtained from 11 healthy individuals, by using the Automated Anatomical Labeling brain atlas with 116 regions. The results are summarized in figure 7.7.

The results for DTI networks are in line with the results obtained for simulated small-world topologies. The delayed correlation method performs strikingly better than the other models when attempting to reconstruct the real network (figure 7.7(a)). With regards to the global measures, the reconstructed networks have lower clustering and higher global efficiency at higher densities, however both match well with the real networks at low densities. Finally, the delayed correlation is able to reconstruct much higher percentage of nodes that have similar topologies in the reconstructed and real networks, as evaluated by the degree, global efficiency and the clustering coefficient (figures 7.7(c), 7.7(d) and 7.7(e) respectively).

## 7.4 Future perspectives

In order to complete this study, some further investigations are needed. To be specific, in this chapter, I showed that the delayed correlation method is superior to the other commonly used correlation approaches and showed that it is very robust with the topology of the real network as well as with the distribution and sign of weights used to specify synaptic strengths. However, the question of whether this model is robust against the method of simulating the neuronal dynamics still remains. Additional methods need to be tested in order to check for the reproducibility of the results, some possible choices for the simulation of the neuronal dynamics are presented in Abdelnour et al. [231], Pernice et al. [232], Belykh et al. [233]. In addition, the DTI networks reconstruction I presented in this chapter is based on the networks constructed only on 11 subjects, which makes the above results possibly biased due to the small sample size. In order

to obtain more sound observations, the analysis needs to be repeated with larger and more heterogeneous sample of subjects.

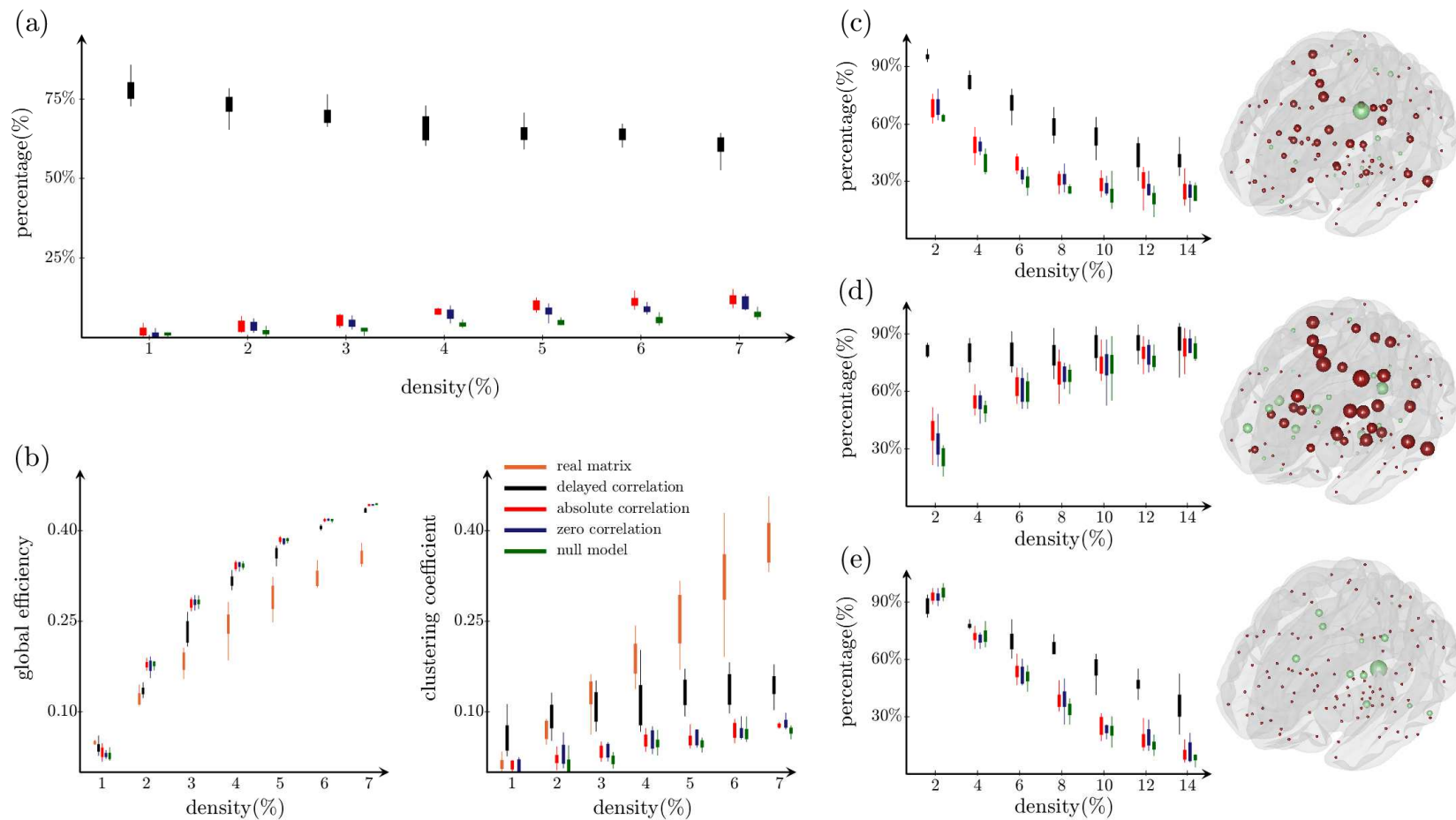


Figure 7.7: Reconstruction of structural networks derived from DTI data. (a) Percentage of edges in a real network that can be correctly identified by each method (black - delayed correlation; red - absolute correlation; blue - zero correlation; green - null model). The networks are derived from DTI data from 11 healthy subjects using the AAL116 atlas. (b) Global clustering coefficient (left) and global efficiency (right) as a function of network density. (c) Percentage of correctly identified nodes as function of network density (left) and a single network illustration on a brain surface (right, the reconstructed nodes are shown in red) based on the nodal degree, (d) global efficiency and (e) clustering coefficient. The bottom and top edges of the boxes show the 25<sup>th</sup> and 75<sup>th</sup> percentiles while the vertical lines extend to the furthest observations that are not designated as outliers.

# Chapter 8

## Conclusion

The tools of graph theory can be employed in order to study and understand the brain as a complex system that is built up from mutually interacting elements. This framework has been able to identify some fundamental aspects of network organization that the human brain relies on, including a small-world topological architecture, community structure and the presence of hubs. These properties enable our brain to continuously evolve and adapt within an environment that presents ever increasing cognitive demands. On the other hand, the disruption in some of these properties can account for few key aspects that form the basis of pathology in neurological diseases.

In order to address the growing demands in the field of brain connectivity analysis, we developed *BRAPH - BRain Analysis using graPH theory*. Being an object-oriented freeware, BRAPH can be easily altered and expanded, for example by adding new objects or modifying the current ones, and therefore, can be customized to suit any future needs. Additionally, BRAPH encompasses a series of user-friendly graphical user interfaces, that allow the users without programming background an effortless way to conduct their analyses. Both structural and functional data can be analyzed by BRAPH in few steps, ranging from defining the brain parcellation scheme, building the adjacency matrices, calculating and visualizing various global and nodal measures, performing non-parametric tests

to quantify the significance of the results, to the saving of all analysis in a single file that then can be used by BRAPH or any external software as needed.

To demonstrate the various strengths of BRAPH, we performed two independent studies. In the first one, we analyzed the topological properties of networks in patients with amnesic MCI and AD that were built from structural MRI data. We found that the networks of these patients exhibited abnormal global topology, which led to less effective communication between any two regions, when compared to healthy subjects' networks. On a regional level, we identified changes in the local topology of various regions. Importantly, these regions coincided with the areas in the brain that showed most pronounced amyloid deposition, gray matter atrophy and glucose hypometabolism, suggesting that these local topology changes can be indicative of pathological and metabolic abnormalities that commonly occur in AD patients.

In the second study, we analyzed functional networks in PD patients with, and without MCI. Our results showed that, across many thresholds, PD-MCI patients have more disconnected networks when compared to controls. A more detailed analysis of the community structure in these networks revealed that the absence of connections was most pronounced in the temporal and inferior frontal regions. Previous studies have already shown that these regions play the role of important brain hubs and are among the regions most affected by PD. The fact that we obtained similar results for both, PD-CN and PD-MCI patients, indicates that the temporal and inferior frontal regions are key to understand the effects of PD to the brain connectivity, regardless of the patients' cognitive status.

Furthermore, we involved 1008 individuals from 2 multicenter cohorts in order to investigate the topological properties of the structural networks in stable and progressive MCI, and AD patients. We demonstrated that modularity and transitivity show much greater sensitivity to MCI and AD when compared with the path length and clustering coefficient. Contrary to earlier studies, we also assessed the changes in the nodal network properties in stable MCI, late MCI converters, early MCI converters, and AD patients. In particular, changes in nodal clustering

were detected only in AD patients, while the closeness centrality exhibited alterations in all groups for various regions. All results taken together offer insight into the development of AD, that starts by affecting distinct brain regions and eventually alters the global network organization.

However, it is possible that different samples of patients with various clinical characteristics could lead to slightly different observations. While some studies found significant organizational abnormalities in the undirected networks in AD patients, others did not identify any differences in AD patients when compared to controls. To address this issue, we proposed the use of directed networks as a more sensitive indicator of any disease related changes in the brain connectivity. The method to build these directed networks is based on temporal precedence, by calculating delayed correlation coefficients between all pairs of regions. We demonstrated that directed networks show abnormal global network organization in cognitively normal PD patients (indicated by increases in the global and local efficiency, transitivity and clustering) when compared to controls. In addition, AD patients had altered global topology that showed decreases in these measures. Importantly, undirected networks calculated in these patients did not exhibit any differences when compared to controls, which suggests that directed networks might be more sensitive to PD and AD related pathological effects.

Finally, we put forward a method, the delayed correlation method, that harvests the information contained in the temporal delays between the brain regions' activation patterns in order to reconstruct the structural brain connectome. We showed that the commonly used correlation methods build functional networks that are not faithful representations of the underlying structural organization, with only 5% to 25% overlap between the two networks. Instead, the delayed correlation method correctly identifies 70% to 80% of the connections in simulated structural brain networks; this result is robust against changes in the network parameters (small-worldness, excitatory vs. inhibitory connection ratio, weight distribution). Moreover, although all methods perform equally well in predicting the global network properties (characteristic path length, global efficiency, clustering coefficient, transitivity), the delayed correlation method predicts more accurately the nodal network properties (nodal degree, nodal clustering, nodal



global efficiency), particularly at lower network densities.

# Bibliography

- [1] S. Camazine, *Self-organization in biological systems*. Princeton University Press, 2003.
- [2] J. Feret, V. Danos, J. Krivine, R. Harmer, and W. Fontana, “Internal coarse-graining of molecular systems,” *Proceedings of the National Academy of Sciences*, vol. 106, no. 16, pp. 6453–6458, 2009.
- [3] J. A. Shapiro, “Thinking about bacterial populations as multicellular organisms,” *Annual Reviews in Microbiology*, vol. 52, no. 1, pp. 81–104, 1998.
- [4] H. C. Berg, *E. coli in Motion*. Springer Science & Business Media, 2008.
- [5] G. M. Viswanathan, M. G. Da Luz, E. P. Raposo, and H. E. Stanley, *The physics of foraging: an introduction to random searches and biological encounters*. Cambridge University Press, 2011.
- [6] J. K. Parrish, S. V. Viscido, and D. Grunbaum, “Self-organized fish schools: an examination of emergent properties,” *The biological bulletin*, vol. 202, no. 3, pp. 296–305, 2002.
- [7] W. Bialek, A. Cavagna, I. Giardina, T. Mora, E. Silvestri, M. Viale, and A. M. Walczak, “Statistical mechanics for natural flocks of birds,” *Proceedings of the National Academy of Sciences*, vol. 109, no. 13, pp. 4786–4791, 2012.

- [8] M. Moussaïd, D. Helbing, S. Garnier, A. Johansson, M. Combe, and G. Theraulaz, “Experimental study of the behavioural mechanisms underlying self-organization in human crowds,” *Proceedings of the Royal Society of London B: Biological Sciences*, vol. 276, no. 1668, pp. 2755–2762, 2009.
- [9] M. Mijalkov, A. McDaniel, J. Wehr, and G. Volpe, “Engineering sensorial delay to control phototaxis and emergent collective behaviors,” *Physical Review X*, vol. 6, no. 1, p. 011008, 2016.
- [10] S. Maslov, K. Sneppen, and A. Zaliznyak, “Detection of topological patterns in complex networks: correlation profile of the internet,” *Physica A: Statistical Mechanics and its Applications*, vol. 333, pp. 529–540, 2004.
- [11] K. Park and W. Willinger, *The Internet as a large-scale complex system*, vol. 3. Oxford University Press on Demand, 2005.
- [12] G. A. Pagani and M. Aiello, “The power grid as a complex network: a survey,” *Physica A: Statistical Mechanics and its Applications*, vol. 392, no. 11, pp. 2688–2700, 2013.
- [13] A.-L. Barabási, R. Albert, and H. Jeong, “Scale-free characteristics of random networks: the topology of the world-wide web,” *Physica A: statistical mechanics and its applications*, vol. 281, no. 1-4, pp. 69–77, 2000.
- [14] T. Vicsek and A. Zafeiris, “Collective motion,” *Physics Reports*, vol. 517, no. 3-4, pp. 71–140, 2012.
- [15] M. Ballerini, N. Cabibbo, R. Candelier, A. Cavagna, E. Cisbani, I. Giardina, V. Lecomte, A. Orlandi, G. Parisi, A. Procaccini, *et al.*, “Interaction ruling animal collective behavior depends on topological rather than metric distance: Evidence from a field study,” *Proceedings of the national academy of sciences*, vol. 105, no. 4, pp. 1232–1237, 2008.
- [16] G. F. Young, L. Scardovi, A. Cavagna, I. Giardina, and N. E. Leonard, “Starling flock networks manage uncertainty in consensus at low cost,” *PLoS computational biology*, vol. 9, no. 1, p. e1002894, 2013.

- [17] A. Davis, B. B. Gardner, and M. R. Gardner, *Deep South: A social anthropological study of caste and class*. Univ of South Carolina Press, 2009.
- [18] A. Rapoport and W. J. Horvath, “A study of a large sociogram,” *Systems Research and Behavioral Science*, vol. 6, no. 4, pp. 279–291, 1961.
- [19] G. F. Davis, M. Yoo, and W. E. Baker, “The small world of the american corporate elite, 1982-2001,” *Strategic organization*, vol. 1, no. 3, pp. 301–326, 2003.
- [20] S. Redner, “How popular is your paper? an empirical study of the citation distribution,” *The European Physical Journal B-Condensed Matter and Complex Systems*, vol. 4, no. 2, pp. 131–134, 1998.
- [21] A. Broder, R. Kumar, F. Maghoul, P. Raghavan, S. Rajagopalan, R. Stata, A. Tomkins, and J. Wiener, “Graph structure in the web,” *Computer networks*, vol. 33, no. 1-6, pp. 309–320, 2000.
- [22] L. A. N. Amaral, A. Scala, M. Barthelemy, and H. E. Stanley, “Classes of small-world networks,” *Proceedings of the national academy of sciences*, vol. 97, no. 21, pp. 11149–11152, 2000.
- [23] W. Aiello, F. Chung, and L. Lu, “A random graph model for massive graphs,” in *Proceedings of the thirty-second annual ACM symposium on Theory of computing*, pp. 171–180, Acm, 2000.
- [24] M. Boss, H. Elsinger, M. Summer, and S. Thurner, “Network topology of the interbank market,” *Quantitative finance*, vol. 4, no. 6, pp. 677–684, 2004.
- [25] H. Jeong, S. P. Mason, A.-L. Barabási, and Z. N. Oltvai, “Lethality and centrality in protein networks,” *Nature*, vol. 411, no. 6833, p. 41, 2001.
- [26] H. Jeong, B. Tombor, R. Albert, Z. N. Oltvai, and A.-L. Barabási, “The large-scale organization of metabolic networks,” *Nature*, vol. 407, no. 6804, p. 651, 2000.

- [27] N. D. Martinez, “Artifacts or attributes? effects of resolution on the little rock lake food web,” *Ecological monographs*, vol. 61, no. 4, pp. 367–392, 1991.
- [28] G. Alexanderson, “About the cover: Euler and königsberg’s bridges: A historical view,” *Bulletin of the american mathematical society*, vol. 43, no. 4, pp. 567–573, 2006.
- [29] L. Euler, “Solutio problematis ad geometriam situs pertinens,” *Comm. Acad. Sci. Imper. Petropol.*, vol. 8, pp. 128–140, 1736.
- [30] A.-L. Barabási, *Network science*. Cambridge university press, 2016.
- [31] M. Rubinov and O. Sporns, “Complex network measures of brain connectivity: uses and interpretations,” *Neuroimage*, vol. 52, no. 3, pp. 1059–1069, 2010.
- [32] M. E. Newman, “The structure of scientific collaboration networks,” *Proceedings of the national academy of sciences*, vol. 98, no. 2, pp. 404–409, 2001.
- [33] J.-P. Onnela, J. Saramäki, J. Hyvönen, G. Szabó, M. A. De Menezes, K. Kaski, A.-L. Barabási, and J. Kertész, “Analysis of a large-scale weighted network of one-to-one human communication,” *New journal of physics*, vol. 9, no. 6, p. 179, 2007.
- [34] Y. Ding, “Scientific collaboration and endorsement: Network analysis of coauthorship and citation networks,” *Journal of informetrics*, vol. 5, no. 1, pp. 187–203, 2011.
- [35] O. Sporns, “Structure and function of complex brain networks,” *Dialogues in clinical neuroscience*, vol. 15, no. 3, p. 247, 2013.
- [36] C. v. Stam and E. Van Straaten, “The organization of physiological brain networks,” *Clinical neurophysiology*, vol. 123, no. 6, pp. 1067–1087, 2012.
- [37] S. Boccaletti, V. Latora, Y. Moreno, M. Chavez, and D.-U. Hwang, “Complex networks: Structure and dynamics,” *Physics reports*, vol. 424, no. 4-5, pp. 175–308, 2006.

- [38] U. Alon, “Network motifs: theory and experimental approaches,” *Nature Reviews Genetics*, vol. 8, no. 6, p. 450, 2007.
- [39] R. Milo, S. Shen-Orr, S. Itzkovitz, N. Kashtan, D. Chklovskii, and U. Alon, “Network motifs: simple building blocks of complex networks,” *Science*, vol. 298, no. 5594, pp. 824–827, 2002.
- [40] M. Girvan and M. E. Newman, “Community structure in social and biological networks,” *Proceedings of the national academy of sciences*, vol. 99, no. 12, pp. 7821–7826, 2002.
- [41] G. W. Flake, S. Lawrence, C. L. Giles, and F. M. Coetzee, “Self-organization and identification of web communities,” *Computer*, vol. 35, no. 3, pp. 66–70, 2002.
- [42] R. Guimera and L. A. N. Amaral, “Functional cartography of complex metabolic networks,” *nature*, vol. 433, no. 7028, p. 895, 2005.
- [43] V. Latora and M. Marchiori, “Efficient behavior of small-world networks,” *Physical review letters*, vol. 87, no. 19, p. 198701, 2001.
- [44] S. Achard and E. Bullmore, “Efficiency and cost of economical brain functional networks,” *PLoS computational biology*, vol. 3, no. 2, p. e17, 2007.
- [45] V. Latora and M. Marchiori, “Vulnerability and protection of infrastructure networks,” *Physical Review E*, vol. 71, no. 1, p. 015103, 2005.
- [46] O. Sporns, C. J. Honey, and R. Kötter, “Identification and classification of hubs in brain networks,” *PloS one*, vol. 2, no. 10, p. e1049, 2007.
- [47] P. Erdős and A. Rényi, “On random graphs, i,” *Publicationes Mathematicae (Debrecen)*, vol. 6, pp. 290–297, 1959.
- [48] M. Molloy and B. Reed, “A critical point for random graphs with a given degree sequence,” *Random structures & algorithms*, vol. 6, no. 2-3, pp. 161–180, 1995.

- [49] F. Chung and L. Lu, “The average distances in random graphs with given expected degrees,” *Proceedings of the National Academy of Sciences*, vol. 99, no. 25, pp. 15879–15882, 2002.
- [50] M. E. Newman, S. H. Strogatz, and D. J. Watts, “Random graphs with arbitrary degree distributions and their applications,” *Physical review E*, vol. 64, no. 2, p. 026118, 2001.
- [51] D. M. Pennock, G. W. Flake, S. Lawrence, E. J. Glover, and C. L. Giles, “Winners don’t take all: Characterizing the competition for links on the web,” *Proceedings of the national academy of sciences*, vol. 99, no. 8, pp. 5207–5211, 2002.
- [52] D. J. Watts and S. H. Strogatz, “Collective dynamics of ‘small-world’ networks,” *nature*, vol. 393, no. 6684, p. 440, 1998.
- [53] D. J. Watts, “Networks, dynamics, and the small-world phenomenon,” *American Journal of sociology*, vol. 105, no. 2, pp. 493–527, 1999.
- [54] M. E. Newman and D. J. Watts, “Renormalization group analysis of the small-world network model,” *Physics Letters A*, vol. 263, no. 4-6, pp. 341–346, 1999.
- [55] D. d. S. Price, “A general theory of bibliometric and other cumulative advantage processes,” *Journal of the Association for Information Science and Technology*, vol. 27, no. 5, pp. 292–306, 1976.
- [56] A.-L. Barabási and R. Albert, “Emergence of scaling in random networks,” *science*, vol. 286, no. 5439, pp. 509–512, 1999.
- [57] M. E. Newman, “The structure and function of complex networks,” *SIAM review*, vol. 45, no. 2, pp. 167–256, 2003.
- [58] M. Karoński, “A review of random graphs,” *Journal of Graph Theory*, vol. 6, no. 4, pp. 349–389, 1982.
- [59] A.-L. Barabási, “Scale-free networks: a decade and beyond,” *science*, vol. 325, no. 5939, pp. 412–413, 2009.

- [60] R. Albert and A.-L. Barabási, “Statistical mechanics of complex networks,” *Reviews of modern physics*, vol. 74, no. 1, p. 47, 2002.
- [61] E. Bullmore and O. Sporns, “The economy of brain network organization,” *Nature Reviews Neuroscience*, vol. 13, no. 5, p. 336, 2012.
- [62] G. Buzsaki, *Rhythms of the Brain*. Oxford University Press, 2006.
- [63] S. L. Bressler, “Large-scale cortical networks and cognition,” *Brain Research Reviews*, vol. 20, no. 3, pp. 288–304, 1995.
- [64] O. Sporns, *Networks of the Brain*. MIT press, 2010.
- [65] N. Fliesler, “New human neuron core to analyze ‘disease in a dish,’” 2015. [Online; accessed 15-March-2018].
- [66] M. Tirrell, “Treating psychiatric disorders through neuron stimulation,” 2016. [Online; accessed 15-March-2018].
- [67] H. Care, “Epilepsy,” 2017. [Online; accessed 15-March-2018].
- [68] G. Tononi, O. Sporns, and G. M. Edelman, “A measure for brain complexity: relating functional segregation and integration in the nervous system,” *Proceedings of the National Academy of Sciences*, vol. 91, no. 11, pp. 5033–5037, 1994.
- [69] B. Biswal, F. Zerrin Yetkin, V. M. Haughton, and J. S. Hyde, “Functional connectivity in the motor cortex of resting human brain using echo-planar mri,” *Magnetic resonance in medicine*, vol. 34, no. 4, pp. 537–541, 1995.
- [70] J. Damoiseaux, S. Rombouts, F. Barkhof, P. Scheltens, C. Stam, S. M. Smith, and C. Beckmann, “Consistent resting-state networks across healthy subjects,” *Proceedings of the national academy of sciences*, vol. 103, no. 37, pp. 13848–13853, 2006.
- [71] E. Bullmore and O. Sporns, “Complex brain networks: graph theoretical analysis of structural and functional systems,” *Nature Reviews Neuroscience*, vol. 10, no. 3, p. 186, 2009.



- [72] M. Catani and D. H. ffytche, “The rises and falls of disconnection syndromes,” *Brain*, vol. 128, no. 10, pp. 2224–2239, 2005.
- [73] M. F. Bear, B. W. Connors, and M. A. Paradiso, *Neuroscience*, vol. 2. Lippincott Williams & Wilkins, 2007.
- [74] Z. J. Koles, “Trends in eeg source localization,” *Clinical Neurophysiology*, vol. 106, no. 2, pp. 127–137, 1998.
- [75] N. K. Logothetis, “What we can do and what we cannot do with fmri,” *Nature*, vol. 453, no. 7197, p. 869, 2008.
- [76] J. Goense, Y. Bohraus, and N. K. Logothetis, “fmri at high spatial resolution: implications for bold-models,” *Frontiers in computational neuroscience*, vol. 10, p. 66, 2016.
- [77] R. B. Buxton, “The physics of functional magnetic resonance imaging (fmri),” *Reports on Progress in Physics*, vol. 76, no. 9, p. 096601, 2013.
- [78] D. Le Bihan, J.-F. Mangin, C. Poupon, C. A. Clark, S. Pappata, N. Molko, and H. Chabriat, “Diffusion tensor imaging: concepts and applications,” *Journal of magnetic resonance imaging*, vol. 13, no. 4, pp. 534–546, 2001.
- [79] P. J. Basser, S. Pajevic, C. Pierpaoli, J. Duda, and A. Aldroubi, “In vivo fiber tractography using dt-mri data,” *Magnetic resonance in medicine*, vol. 44, no. 4, pp. 625–632, 2000.
- [80] A. Mechelli, C. J. Price, K. J. Friston, and J. Ashburner, “Voxel-based morphometry of the human brain: methods and applications,” *Current medical Imaging reviews*, vol. 1, no. 2, pp. 105–113, 2005.
- [81] O. Sporns, G. Tononi, and R. Kötter, “The human connectome: a structural description of the human brain,” *PLoS computational biology*, vol. 1, no. 4, p. e42, 2005.
- [82] S. B. Laughlin and T. J. Sejnowski, “Communication in neuronal networks,” *Science*, vol. 301, no. 5641, pp. 1870–1874, 2003.

- [83] K. J. Friston, “Functional and effective connectivity in neuroimaging: a synthesis,” *Human brain mapping*, vol. 2, no. 1-2, pp. 56–78, 1994.
- [84] K. J. Friston, “Functional and effective connectivity: a review,” *Brain connectivity*, vol. 1, no. 1, pp. 13–36, 2011.
- [85] S. M. Smith, K. L. Miller, G. Salimi-Khorshidi, M. Webster, C. F. Beckmann, T. E. Nichols, J. D. Ramsey, and M. W. Woolrich, “Network modelling methods for fmri,” *Neuroimage*, vol. 54, no. 2, pp. 875–891, 2011.
- [86] C. W. Granger, “Investigating causal relations by econometric models and cross-spectral methods,” *Econometrica: Journal of the Econometric Society*, pp. 424–438, 1969.
- [87] A. Roebroeck, E. Formisano, and R. Goebel, “Mapping directed influence over the brain using granger causality and fmri,” *Neuroimage*, vol. 25, no. 1, pp. 230–242, 2005.
- [88] K. J. Friston, L. Harrison, and W. Penny, “Dynamic causal modelling,” *Neuroimage*, vol. 19, no. 4, pp. 1273–1302, 2003.
- [89] A. McIntosh and F. Gonzalez-Lima, “Structural equation modeling and its application to network analysis in functional brain imaging,” *Human brain mapping*, vol. 2, no. 1-2, pp. 2–22, 1994.
- [90] Y. He, Z. J. Chen, and A. C. Evans, “Small-world anatomical networks in the human brain revealed by cortical thickness from mri,” *Cerebral cortex*, vol. 17, no. 10, pp. 2407–2419, 2007.
- [91] Y. Iturria-Medina, R. C. Sotero, E. J. Canales-Rodríguez, Y. Alemán-Gómez, and L. Melie-García, “Studying the human brain anatomical network via diffusion-weighted mri and graph theory,” *Neuroimage*, vol. 40, no. 3, pp. 1064–1076, 2008.
- [92] Z. J. Chen, Y. He, P. Rosa-Neto, J. Germann, and A. C. Evans, “Revealing modular architecture of human brain structural networks by using cortical thickness from mri,” *Cerebral cortex*, vol. 18, no. 10, pp. 2374–2381, 2008.

- [93] C. C. Hilgetag and M. Kaiser, “Clustered organization of cortical connectivity,” *Neuroinformatics*, vol. 2, no. 3, pp. 353–360, 2004.
- [94] P. Hagmann, L. Cammoun, X. Gigandet, R. Meuli, C. J. Honey, V. J. Wedeen, and O. Sporns, “Mapping the structural core of human cerebral cortex,” *PLoS biology*, vol. 6, no. 7, p. e159, 2008.
- [95] M. P. van den Heuvel, R. S. Kahn, J. Goñi, and O. Sporns, “High-cost, high-capacity backbone for global brain communication,” *Proceedings of the National Academy of Sciences*, vol. 109, no. 28, pp. 11372–11377, 2012.
- [96] J. B. Pereira, M. Mijalkov, E. Kakaei, P. Mecocci, B. Vellas, M. Tsolaki, I. Kłoszewska, H. Soininen, C. Spenger, S. Lovestone, *et al.*, “Disrupted network topology in patients with stable and progressive mild cognitive impairment and alzheimer’s disease,” *Cerebral Cortex*, vol. 26, no. 8, pp. 3476–3493, 2016.
- [97] J. B. Pereira, D. Aarsland, C. E. Ginestet, A. V. Lebedev, L.-O. Wahlund, A. Simmons, G. Volpe, and E. Westman, “Aberrant cerebral network topology and mild cognitive impairment in early parkinson’s disease,” *Human brain mapping*, vol. 36, no. 8, pp. 2980–2995, 2015.
- [98] V. M. Eguiluz, D. R. Chialvo, G. A. Cecchi, M. Baliki, and A. V. Apkarian, “Scale-free brain functional networks,” *Physical review letters*, vol. 94, no. 1, p. 018102, 2005.
- [99] S. Achard, R. Salvador, B. Whitcher, J. Suckling, and E. Bullmore, “A resilient, low-frequency, small-world human brain functional network with highly connected association cortical hubs,” *Journal of Neuroscience*, vol. 26, no. 1, pp. 63–72, 2006.
- [100] D. Meunier, S. Achard, A. Morcom, and E. Bullmore, “Age-related changes in modular organization of human brain functional networks,” *Neuroimage*, vol. 44, no. 3, pp. 715–723, 2009.
- [101] M. E. Raichle, A. M. MacLeod, A. Z. Snyder, W. J. Powers, D. A. Gusnard, and G. L. Shulman, “A default mode of brain function,” *Proceedings of the National Academy of Sciences*, vol. 98, no. 2, pp. 676–682, 2001.

- [102] M. Guye, G. Bettus, F. Bartolomei, and P. J. Cozzone, “Graph theoretical analysis of structural and functional connectivity mri in normal and pathological brain networks,” *Magnetic Resonance Materials in Physics, Biology and Medicine*, vol. 23, no. 5-6, pp. 409–421, 2010.
- [103] B. J. He, G. L. Shulman, A. Z. Snyder, and M. Corbetta, “The role of impaired neuronal communication in neurological disorders,” *Current opinion in neurology*, vol. 20, no. 6, pp. 655–660, 2007.
- [104] D. S. Bassett, E. Bullmore, B. A. Verchinski, V. S. Mattay, D. R. Weinberger, and A. Meyer-Lindenberg, “Hierarchical organization of human cortical networks in health and schizophrenia,” *Journal of Neuroscience*, vol. 28, no. 37, pp. 9239–9248, 2008.
- [105] Y. He, Z. Chen, and A. Evans, “Structural insights into aberrant topological patterns of large-scale cortical networks in alzheimer’s disease,” *Journal of Neuroscience*, vol. 28, no. 18, pp. 4756–4766, 2008.
- [106] C. J. Stam, B. Jones, G. Nolte, M. Breakspear, and P. Scheltens, “Small-world networks and functional connectivity in alzheimer’s disease,” *Cerebral cortex*, vol. 17, no. 1, pp. 92–99, 2006.
- [107] C. J. Honey, J.-P. Thivierge, and O. Sporns, “Can structure predict function in the human brain?,” *Neuroimage*, vol. 52, no. 3, pp. 766–776, 2010.
- [108] C. Honey, O. Sporns, L. Cammoun, X. Gigandet, J.-P. Thiran, R. Meuli, and P. Hagmann, “Predicting human resting-state functional connectivity from structural connectivity,” *Proceedings of the National Academy of Sciences*, vol. 106, no. 6, pp. 2035–2040, 2009.
- [109] G. Arroyo Otori, “Higher-dimensional modelling of geographic information,” 2016.
- [110] J. Kepner and J. Gilbert, *Graph algorithms in the language of linear algebra*. SIAM, 2011.
- [111] A. Barrat, M. Barthelemy, and A. Vespignani, “The architecture of complex weighted networks: Measurements and models,” in *Large Scale Structure*

*And Dynamics Of Complex Networks: From Information Technology to Finance and Natural Science*, pp. 67–92, World Scientific, 2007.

- [112] J. M. Harris, J. L. Hirst, and M. J. Mossinghoff, *Combinatorics and graph theory*, vol. 2. Springer, 2008.
- [113] J.-P. Onnela, J. Saramäki, J. Kertész, and K. Kaski, “Intensity and coherence of motifs in weighted complex networks,” *Physical Review E*, vol. 71, no. 6, p. 065103, 2005.
- [114] G. Fagiolo, “Clustering in complex directed networks,” *Physical Review E*, vol. 76, no. 2, p. 026107, 2007.
- [115] M. E. Newman, “Ego-centered networks and the ripple effect,” *Social Networks*, vol. 25, no. 1, pp. 83–95, 2003.
- [116] S. Kintali, “Betweenness centrality: Algorithms and lower bounds,” *arXiv preprint arXiv:0809.1906*, 2008.
- [117] M. E. Newman, “Assortative mixing in networks,” *Physical review letters*, vol. 89, no. 20, p. 208701, 2002.
- [118] M. D. Humphries and K. Gurney, “Network ‘small-world-ness’: a quantitative method for determining canonical network equivalence,” *PloS one*, vol. 3, no. 4, p. e0002051, 2008.
- [119] R. W. Brown, E. M. Haacke, Y.-C. N. Cheng, M. R. Thompson, and R. Venkatesan, *Magnetic resonance imaging: physical principles and sequence design*. John Wiley & Sons, 2014.
- [120] B. Fischl, “Freesurfer,” *Neuroimage*, vol. 62, no. 2, pp. 774–781, 2012.
- [121] S. L. Bressler and V. Menon, “Large-scale brain networks in cognition: emerging methods and principles,” *Trends in cognitive sciences*, vol. 14, no. 6, pp. 277–290, 2010.
- [122] J. Wang, L. Wang, Y. Zang, H. Yang, H. Tang, Q. Gong, Z. Chen, C. Zhu, and Y. He, “Parcellation-dependent small-world brain functional networks:

- a resting-state fmri study,” *Human brain mapping*, vol. 30, no. 5, pp. 1511–1523, 2009.
- [123] B. He, Y. Dai, L. Astolfi, F. Babiloni, H. Yuan, and L. Yang, “econnectome: A matlab toolbox for mapping and imaging of brain functional connectivity,” *Journal of neuroscience methods*, vol. 195, no. 2, pp. 261–269, 2011.
- [124] M. Xia, J. Wang, and Y. He, “Brainnet viewer: a network visualization tool for human brain connectomics,” *PloS one*, vol. 8, no. 7, p. e68910, 2013.
- [125] J. Wang, X. Wang, M. Xia, X. Liao, A. Evans, and Y. He, “Gretna: a graph theoretical network analysis toolbox for imaging connectomics,” *Frontiers in human neuroscience*, vol. 9, p. 386, 2015.
- [126] S. Whitfield-Gabrieli and A. Nieto-Castanon, “Conn: a functional connectivity toolbox for correlated and anticorrelated brain networks,” *Brain connectivity*, vol. 2, no. 3, pp. 125–141, 2012.
- [127] J. Kruschwitz, D. List, L. Waller, M. Rubinov, and H. Walter, “Graphvar: A user-friendly toolbox for comprehensive graph analyses of functional brain connectivity,” *Journal of neuroscience methods*, vol. 245, pp. 107–115, 2015.
- [128] S. H. Hosseini, F. Hoefft, and S. R. Kesler, “Gat: a graph-theoretical analysis toolbox for analyzing between-group differences in large-scale structural and functional brain networks,” *PloS one*, vol. 7, no. 7, p. e40709, 2012.
- [129] V. D. Calhoun, R. Miller, G. Pearlson, and T. Adali, “The chronnectome: time-varying connectivity networks as the next frontier in fmri data discovery,” *Neuron*, vol. 84, no. 2, pp. 262–274, 2014.
- [130] W. Liao, G.-R. Wu, Q. Xu, G.-J. Ji, Z. Zhang, Y.-F. Zang, and G. Lu, “Dynamicbc: a matlab toolbox for dynamic brain connectome analysis,” *Brain connectivity*, vol. 4, no. 10, pp. 780–790, 2014.
- [131] J. Cui, L. Xu, S. L. Bressler, M. Ding, and H. Liang, “Bsmart: a matlab/c toolbox for analysis of multichannel neural time series,” *Neural Networks*, vol. 21, no. 8, pp. 1094–1104, 2008.

- [132] M. Mijalkov, E. Kakaei, J. B. Pereira, E. Westman, G. Volpe, A. D. N. Initiative, *et al.*, “Braph: A graph theory software for the analysis of brain connectivity,” *PloS one*, vol. 12, no. 8, p. e0178798, 2017.
- [133] Y. Benjamini and Y. Hochberg, “Controlling the false discovery rate: a practical and powerful approach to multiple testing,” *Journal of the royal statistical society. Series B (Methodological)*, pp. 289–300, 1995.
- [134] R. S. Desikan, F. Ségonne, B. Fischl, B. T. Quinn, B. C. Dickerson, D. Blacker, R. L. Buckner, A. M. Dale, R. P. Maguire, B. T. Hyman, *et al.*, “An automated labeling system for subdividing the human cerebral cortex on mri scans into gyral based regions of interest,” *Neuroimage*, vol. 31, no. 3, pp. 968–980, 2006.
- [135] C. Destrieux, B. Fischl, A. Dale, and E. Halgren, “Automatic parcellation of human cortical gyri and sulci using standard anatomical nomenclature,” *Neuroimage*, vol. 53, no. 1, pp. 1–15, 2010.
- [136] N. Tzourio-Mazoyer, B. Landeau, D. Papathanassiou, F. Crivello, O. Etard, N. Delcroix, B. Mazoyer, and M. Joliot, “Automated anatomical labeling of activations in spm using a macroscopic anatomical parcellation of the mni mri single-subject brain,” *Neuroimage*, vol. 15, no. 1, pp. 273–289, 2002.
- [137] J. D. Power, A. L. Cohen, S. M. Nelson, G. S. Wig, K. A. Barnes, J. A. Church, A. C. Vogel, T. O. Laumann, F. M. Miezin, B. L. Schlaggar, *et al.*, “Functional network organization of the human brain,” *Neuron*, vol. 72, no. 4, pp. 665–678, 2011.
- [138] N. U. Dosenbach, K. M. Visscher, E. D. Palmer, F. M. Miezin, K. K. Wenger, H. C. Kang, E. D. Burgund, A. L. Grimes, B. L. Schlaggar, and S. E. Petersen, “A core system for the implementation of task sets,” *Neuron*, vol. 50, no. 5, pp. 799–812, 2006.
- [139] R. C. Craddock, G. A. James, P. E. Holtzheimer, X. P. Hu, and H. S. Mayberg, “A whole brain fmri atlas generated via spatially constrained spectral clustering,” *Human brain mapping*, vol. 33, no. 8, pp. 1914–1928, 2012.

- [140] O. Voevodskaya, A. Simmons, R. Nordenskjöld, J. Kullberg, H. Ahlström, L. Lind, L.-O. Wahlund, E.-M. Larsson, E. Westman, A. D. N. Initiative, *et al.*, “The effects of intracranial volume adjustment approaches on multiple regional mri volumes in healthy aging and alzheimer’s disease,” *Frontiers in aging neuroscience*, vol. 6, p. 264, 2014.
- [141] M. M. et al., “Braph - brain analysis using graph theory,” 2017. [Online; accessed 15-March-2018].
- [142] J. C. Mazziotta, A. W. Toga, A. Evans, P. Fox, J. Lancaster, *et al.*, “A probabilistic atlas of the human brain: theory and rationale for its development,” *Neuroimage*, vol. 2, no. 2, pp. 89–101, 1995.
- [143] K. Marek, D. Jennings, S. Lasch, A. Siderowf, C. Tanner, T. Simuni, C. Coffey, K. Kieburtz, E. Flagg, S. Chowdhury, *et al.*, “The parkinson progression marker initiative (ppmi),” *Progress in neurobiology*, vol. 95, no. 4, pp. 629–635, 2011.
- [144] D. Weintraub, T. Simuni, C. Caspell-Garcia, C. Coffey, S. Lasch, A. Siderowf, D. Aarsland, P. Barone, D. Burn, L. M. Chahine, *et al.*, “Cognitive performance and neuropsychiatric symptoms in early, untreated parkinson’s disease,” *Movement Disorders*, vol. 30, no. 7, pp. 919–927, 2015.
- [145] M. P. Van Den Heuvel and H. E. H. Pol, “Exploring the brain network: a review on resting-state fmri functional connectivity,” *European neuropsychopharmacology*, vol. 20, no. 8, pp. 519–534, 2010.
- [146] B. Winblad, P. Amouyel, S. Andrieu, C. Ballard, C. Brayne, H. Brodaty, A. Cedazo-Minguez, B. Dubois, D. Edvardsson, H. Feldman, *et al.*, “Defeating alzheimer’s disease and other dementias: a priority for european science and society,” *The Lancet Neurology*, vol. 15, no. 5, pp. 455–532, 2016.
- [147] B. M. Tijms, A. M. Wink, W. de Haan, W. M. van der Flier, C. J. Stam, P. Scheltens, and F. Barkhof, “Alzheimer’s disease: connecting findings from graph theoretical studies of brain networks,” *Neurobiology of aging*, vol. 34, no. 8, pp. 2023–2036, 2013.



- [148] R. L. Buckner, A. Z. Snyder, B. J. Shannon, G. LaRossa, R. Sachs, A. F. Fotenos, Y. I. Sheline, W. E. Klunk, C. A. Mathis, J. C. Morris, *et al.*, “Molecular, structural, and functional characterization of alzheimer’s disease: evidence for a relationship between default activity, amyloid, and memory,” *Journal of Neuroscience*, vol. 25, no. 34, pp. 7709–7717, 2005.
- [149] H. Braak and E. Braak, “Neuropathological stageing of alzheimer-related changes,” *Acta neuropathologica*, vol. 82, no. 4, pp. 239–259, 1991.
- [150] P. Svenningsson, E. Westman, C. Ballard, and D. Aarsland, “Cognitive impairment in patients with parkinson’s disease: diagnosis, biomarkers, and treatment,” *The Lancet Neurology*, vol. 11, no. 8, pp. 697–707, 2012.
- [151] H. C. Baggio, B. Segura, and C. Junque, “Resting-state functional brain networks in parkinson’s disease,” *CNS neuroscience & therapeutics*, vol. 21, no. 10, pp. 793–801, 2015.
- [152] M. P. van den Heuvel and O. Sporns, “Network hubs in the human brain,” *Trends in cognitive sciences*, vol. 17, no. 12, pp. 683–696, 2013.
- [153] N. A. Crossley, A. Mechelli, J. Scott, F. Carletti, P. T. Fox, P. McGuire, and E. T. Bullmore, “The hubs of the human connectome are generally implicated in the anatomy of brain disorders,” *Brain*, vol. 137, no. 8, pp. 2382–2395, 2014.
- [154] H. Braak, K. Del Tredici, U. Rüb, R. A. De Vos, E. N. J. Steur, and E. Braak, “Staging of brain pathology related to sporadic parkinson’s disease,” *Neurobiology of aging*, vol. 24, no. 2, pp. 197–211, 2003.
- [155] A. Fornito, A. Zalesky, and M. Breakspear, “Graph analysis of the human connectome: promise, progress, and pitfalls,” *Neuroimage*, vol. 80, pp. 426–444, 2013.
- [156] G. B. Frisoni, N. C. Fox, C. R. Jack Jr, P. Scheltens, and P. M. Thompson, “The clinical use of structural mri in alzheimer disease,” *Nature Reviews Neurology*, vol. 6, no. 2, p. 67, 2010.

- [157] R. I. Scahill, J. M. Schott, J. M. Stevens, M. N. Rossor, and N. C. Fox, “Mapping the evolution of regional atrophy in alzheimer’s disease: unbiased analysis of fluid-registered serial mri,” *Proceedings of the National Academy of Sciences*, vol. 99, no. 7, pp. 4703–4707, 2002.
- [158] D. R. Thal, U. Rüb, M. Orantes, and H. Braak, “Phases of  $\alpha\beta$ -deposition in the human brain and its relevance for the development of ad,” *Neurology*, vol. 58, no. 12, pp. 1791–1800, 2002.
- [159] P. M. Thompson, K. M. Hayashi, G. I. De Zubicaray, A. L. Janke, S. E. Rose, J. Semple, M. S. Hong, D. H. Herman, D. Gravano, D. M. Doddrell, *et al.*, “Mapping hippocampal and ventricular change in alzheimer disease,” *Neuroimage*, vol. 22, no. 4, pp. 1754–1766, 2004.
- [160] H. Braak, I. Alafuzoff, T. Arzberger, H. Kretschmar, and K. Del Tredici, “Staging of alzheimer disease-associated neurofibrillary pathology using paraffin sections and immunocytochemistry,” *Acta neuropathologica*, vol. 112, no. 4, pp. 389–404, 2006.
- [161] C. McDonald, L. McEvoy, L. Gharapetian, C. Fennema-Notestine, D. Hagler, D. Holland, A. Koyama, J. Brewer, A. Dale, A. D. N. Initiative, *et al.*, “Regional rates of neocortical atrophy from normal aging to early alzheimer disease,” *Neurology*, vol. 73, no. 6, pp. 457–465, 2009.
- [162] M. Pievani, W. de Haan, T. Wu, W. W. Seeley, and G. B. Frisoni, “Functional network disruption in the degenerative dementias,” *The Lancet Neurology*, vol. 10, no. 9, pp. 829–843, 2011.
- [163] Y. I. Sheline and M. E. Raichle, “Resting state functional connectivity in preclinical alzheimer’s disease,” *Biological psychiatry*, vol. 74, no. 5, pp. 340–347, 2013.
- [164] Y. I. Sheline, M. E. Raichle, A. Z. Snyder, J. C. Morris, D. Head, S. Wang, and M. A. Mintun, “Amyloid plaques disrupt resting state default mode network connectivity in cognitively normal elderly,” *Biological psychiatry*, vol. 67, no. 6, pp. 584–587, 2010.

- [165] B. M. Tijms, C. Möller, H. Vrenken, A. M. Wink, W. de Haan, W. M. van der Flier, C. J. Stam, P. Scheltens, and F. Barkhof, “Single-subject grey matter graphs in alzheimer’s disease,” *PloS one*, vol. 8, no. 3, p. e58921, 2013.
- [166] Z. Dai and Y. He, “Disrupted structural and functional brain connectomes in mild cognitive impairment and alzheimer’s disease,” *Neuroscience bulletin*, vol. 30, no. 2, pp. 217–232, 2014.
- [167] G. Sanabria-Diaz, E. Martínez-Montes, and L. Melie-Garcia, “Glucose metabolism during resting state reveals abnormal brain networks organization in the alzheimer’s disease and mild cognitive impairment,” *PloS one*, vol. 8, no. 7, p. e68860, 2013.
- [168] J. Sepulcre, M. R. Sabuncu, A. Becker, R. Sperling, and K. A. Johnson, “In vivo characterization of the early states of the amyloid-beta network,” *Brain*, vol. 136, no. 7, pp. 2239–2252, 2013.
- [169] D. J. Phillips, A. McGlaughlin, D. Ruth, L. R. Jager, A. Soldan, A. D. N. Initiative, *et al.*, “Graph theoretic analysis of structural connectivity across the spectrum of alzheimer’s disease: The importance of graph creation methods,” *NeuroImage: Clinical*, vol. 7, pp. 377–390, 2015.
- [170] Y. Li, Y. Wang, G. Wu, F. Shi, L. Zhou, W. Lin, and D. Shen, “Discriminant analysis of longitudinal cortical thickness changes in alzheimer’s disease using dynamic and network features,” *Neurobiology of aging*, vol. 33, no. 2, pp. 427–e15, 2012.
- [171] R. C. Petersen, G. E. Smith, S. C. Waring, R. J. Ivnik, E. G. Tangalos, and E. Kokmen, “Mild cognitive impairment: clinical characterization and outcome,” *Archives of neurology*, vol. 56, no. 3, pp. 303–308, 1999.
- [172] D. Medina, F. Urresta, J. D. Gabrieli, M. Moseley, D. Fleischman, D. A. Bennett, S. Leurgans, D. A. Turner, G. T. Stebbins, *et al.*, “White matter changes in mild cognitive impairment and ad: a diffusion tensor imaging study,” *Neurobiology of aging*, vol. 27, no. 5, pp. 663–672, 2006.

- [173] Y. Zhang, N. Schuff, G.-H. Jahng, W. Bayne, S. Mori, L. Schad, S. Mueller, A.-T. Du, J. Kramer, K. Yaffe, *et al.*, “Diffusion tensor imaging of cingulum fibers in mild cognitive impairment and alzheimer disease,” *Neurology*, vol. 68, no. 1, pp. 13–19, 2007.
- [174] J. Petrella, F. Sheldon, S. Prince, V. Calhoun, and P. Doraiswamy, “Default mode network connectivity in stable vs progressive mild cognitive impairment,” *Neurology*, vol. 76, no. 6, pp. 511–517, 2011.
- [175] M. A. Binnewijzend, M. M. Schoonheim, E. Sanz-Arigita, A. M. Wink, W. M. van der Flier, N. Tolboom, S. M. Adriaanse, J. S. Damoiseaux, P. Scheltens, B. N. van Berckel, *et al.*, “Resting-state fmri changes in alzheimer’s disease and mild cognitive impairment,” *Neurobiology of aging*, vol. 33, no. 9, pp. 2018–2028, 2012.
- [176] Z. Yao, Y. Zhang, L. Lin, Y. Zhou, C. Xu, T. Jiang, A. D. N. Initiative, *et al.*, “Abnormal cortical networks in mild cognitive impairment and alzheimer’s disease,” *PLoS computational biology*, vol. 6, no. 11, p. e1001006, 2010.
- [177] M. Grundman, R. C. Petersen, S. H. Ferris, R. G. Thomas, P. S. Aisen, D. A. Bennett, N. L. Foster, C. R. Jack Jr, D. R. Galasko, R. Doody, *et al.*, “Mild cognitive impairment can be distinguished from alzheimer disease and normal aging for clinical trials,” *Archives of neurology*, vol. 61, no. 1, pp. 59–66, 2004.
- [178] R. L. Buckner, J. Sepulcre, T. Talukdar, F. M. Krienen, H. Liu, T. Hedden, J. R. Andrews-Hanna, R. A. Sperling, and K. A. Johnson, “Cortical hubs revealed by intrinsic functional connectivity: mapping, assessment of stability, and relation to alzheimer’s disease,” *Journal of neuroscience*, vol. 29, no. 6, pp. 1860–1873, 2009.
- [179] S. Lovestone, P. Francis, I. Kloszewska, P. Mecocci, A. Simmons, H. Soininen, C. Spenger, M. Tsolaki, B. Vellas, L.-O. Wahlund, *et al.*, “Addneuromed—the european collaboration for the discovery of novel biomarkers for alzheimer’s disease,” *Annals of the New York Academy of Sciences*, vol. 1180, no. 1, pp. 36–46, 2009.

- [180] S. Lovestone, P. Francis, and K. Strandgaard, “Biomarkers for disease modification trials—the innovative medicines initiative and addneuromed,” *The journal of nutrition, health & aging*, vol. 11, no. 4, p. 359, 2007.
- [181] A. Simmons, E. Westman, S. Muehlboeck, P. Mecocci, B. Vellas, M. Tsolaki, I. Kłoszewska, L.-O. Wahlund, H. Soininen, S. Lovestone, *et al.*, “The addneuromed framework for multi-centre mri assessment of alzheimer’s disease: experience from the first 24 months,” *International journal of geriatric psychiatry*, vol. 26, no. 1, pp. 75–82, 2011.
- [182] A. Simmons, E. Westman, S. Muehlboeck, P. Mecocci, B. Vellas, M. Tsolaki, I. Kłoszewska, L.-O. Wahlund, H. Soininen, S. Lovestone, *et al.*, “Mri measures of alzheimer’s disease and the addneuromed study,” *Annals of the New York Academy of Sciences*, vol. 1180, no. 1, pp. 47–55, 2009.
- [183] C. R. Jack, M. A. Bernstein, N. C. Fox, P. Thompson, G. Alexander, D. Harvey, B. Borowski, P. J. Britson, J. L Whitwell, C. Ward, *et al.*, “The alzheimer’s disease neuroimaging initiative (adni): Mri methods,” *Journal of magnetic resonance imaging*, vol. 27, no. 4, pp. 685–691, 2008.
- [184] G. Spulber, A. Simmons, J.-S. Muehlboeck, P. Mecocci, B. Vellas, M. Tsolaki, I. Kłoszewska, H. Soininen, C. Spenger, S. Lovestone, *et al.*, “An mri-based index to measure the severity of alzheimer’s disease-like structural pattern in subjects with mild cognitive impairment,” *Journal of internal medicine*, vol. 273, no. 4, pp. 396–409, 2013.
- [185] F. Falahati, D. Ferreira, H. Soininen, P. Mecocci, B. Vellas, M. Tsolaki, I. Kłoszewska, S. Lovestone, M. Eriksdotter, L.-O. Wahlund, *et al.*, “The effect of age correction on multivariate classification in alzheimer’s disease, with a focus on the characteristics of incorrectly and correctly classified subjects,” *Brain topography*, vol. 29, no. 2, pp. 296–307, 2016.
- [186] F. Ségonne, A. M. Dale, E. Busa, M. Glessner, D. Salat, H. K. Hahn, and B. Fischl, “A hybrid approach to the skull stripping problem in mri,” *Neuroimage*, vol. 22, no. 3, pp. 1060–1075, 2004.

- [187] J. G. Sled, A. P. Zijdenbos, and A. C. Evans, "A nonparametric method for automatic correction of intensity nonuniformity in mri data," *IEEE transactions on medical imaging*, vol. 17, no. 1, pp. 87–97, 1998.
- [188] F. Ségonne, J. Pacheco, and B. Fischl, "Geometrically accurate topology-correction of cortical surfaces using nonseparating loops," *IEEE transactions on medical imaging*, vol. 26, no. 4, pp. 518–529, 2007.
- [189] B. Fischl, M. I. Sereno, and A. M. Dale, "Cortical surface-based analysis: Ii: inflation, flattening, and a surface-based coordinate system," *Neuroimage*, vol. 9, no. 2, pp. 195–207, 1999.
- [190] J. Muehlboeck, E. Westman, A. Simmons, *et al.*, "Thehivedb image data management and analysis framework," *Frontiers in neuroinformatics*, vol. 7, p. 49, 2014.
- [191] O. Sporns and J. D. Zwi, "The small world of the cerebral cortex," *Neuroinformatics*, vol. 2, no. 2, pp. 145–162, 2004.
- [192] C.-Y. Lo, P.-N. Wang, K.-H. Chou, J. Wang, Y. He, and C.-P. Lin, "Diffusion tensor tractography reveals abnormal topological organization in structural cortical networks in alzheimer's disease," *Journal of Neuroscience*, vol. 30, no. 50, pp. 16876–16885, 2010.
- [193] E. J. Sanz-Arigita, M. M. Schoonheim, J. S. Damoiseaux, S. A. Rombouts, E. Maris, F. Barkhof, P. Scheltens, and C. J. Stam, "Loss of 'small-world' networks in alzheimer's disease: graph analysis of fmri resting-state functional connectivity," *PLoS one*, vol. 5, no. 11, p. e13788, 2010.
- [194] N. Shu, Y. Liang, H. Li, J. Zhang, X. Li, L. Wang, Y. He, Y. Wang, and Z. Zhang, "Disrupted topological organization in white matter structural networks in amnesic mild cognitive impairment: relationship to subtype," *Radiology*, vol. 265, no. 2, pp. 518–527, 2012.
- [195] M. E. Newman, "Fast algorithm for detecting community structure in networks," *Physical review E*, vol. 69, no. 6, p. 066133, 2004.

- [196] H.-C. Baggio, R. Sala-Llonch, B. Segura, M.-J. Marti, F. Valldeoriola, Y. Compta, E. Tolosa, and C. Junqué, “Functional brain networks and cognitive deficits in parkinson’s disease,” *Human brain mapping*, vol. 35, no. 9, pp. 4620–4634, 2014.
- [197] K. Wu, Y. Taki, K. Sato, S. Kinomura, R. Goto, K. Okada, R. Kawashima, Y. He, A. C. Evans, and H. Fukuda, “Age-related changes in topological organization of structural brain networks in healthy individuals,” *Human brain mapping*, vol. 33, no. 3, pp. 552–568, 2012.
- [198] M. D. Greicius, G. Srivastava, A. L. Reiss, and V. Menon, “Default-mode network activity distinguishes alzheimer’s disease from healthy aging: evidence from functional mri,” *Proceedings of the National Academy of Sciences of the United States of America*, vol. 101, no. 13, pp. 4637–4642, 2004.
- [199] X. Li, T.-Q. Li, N. Andreasen, M. K. Wiberg, E. Westman, and L.-O. Wahlund, “Ratio of a $\beta$ 42/p-tau 181p in csf is associated with aberrant default mode network in ad,” *Scientific reports*, vol. 3, p. 1339, 2013.
- [200] M. Lehmann, S. J. Crutch, G. R. Ridgway, B. H. Ridha, J. Barnes, E. K. Warrington, M. N. Rossor, and N. C. Fox, “Cortical thickness and voxel-based morphometry in posterior cortical atrophy and typical alzheimer’s disease,” *Neurobiology of aging*, vol. 32, no. 8, pp. 1466–1476, 2011.
- [201] T. C. Chua, W. Wen, M. J. Slavin, and P. S. Sachdev, “Diffusion tensor imaging in mild cognitive impairment and alzheimer’s disease: a review,” *Current opinion in neurology*, vol. 21, no. 1, pp. 83–92, 2008.
- [202] W. Zhu, W. Wen, Y. He, A. Xia, K. J. Anstey, and P. Sachdev, “Changing topological patterns in normal aging using large-scale structural networks,” *Neurobiology of aging*, vol. 33, no. 5, pp. 899–913, 2012.
- [203] A. Alexander-Bloch, J. N. Giedd, and E. Bullmore, “Imaging structural co-variance between human brain regions,” *Nature Reviews Neuroscience*, vol. 14, no. 5, p. 322, 2013.

- [204] J. Zhou, E. D. Gennatas, J. H. Kramer, B. L. Miller, and W. W. Seeley, “Predicting regional neurodegeneration from the healthy brain functional connectome,” *Neuron*, vol. 73, no. 6, pp. 1216–1227, 2012.
- [205] T. D. Koepsell and S. E. Monsell, “Reversion from mild cognitive impairment to normal or near-normal cognition risk factors and prognosis,” *Neurology*, vol. 79, no. 15, pp. 1591–1598, 2012.
- [206] K. Yaffe, R. C. Petersen, K. Lindquist, J. Kramer, and B. Miller, “Subtype of mild cognitive impairment and progression to dementia and death,” *Dementia and geriatric cognitive disorders*, vol. 22, no. 4, pp. 312–319, 2006.
- [207] M. Zanetti, C. Ballabio, C. Abbate, C. Cutaia, C. Vergani, and L. Bergamaschini, “Mild cognitive impairment subtypes and vascular dementia in community-dwelling elderly people: A 3-year follow-up study,” *Journal of the American Geriatrics Society*, vol. 54, no. 4, pp. 580–586, 2006.
- [208] D. W. Dickson, P. Davies, C. Bevona, K. Van Hoesven, S. Factor, E. Grober, M. Aronson, and H. Crystal, “Hippocampal sclerosis: a common pathological feature of dementia in very old ( $\geq 80$  years of age) humans,” *Acta neuropathologica*, vol. 88, no. 3, pp. 212–221, 1994.
- [209] B. M. Tijms, P. Seriès, D. J. Willshaw, and S. M. Lawrie, “Similarity-based extraction of individual networks from gray matter mri scans,” *Cerebral Cortex*, vol. 22, no. 7, pp. 1530–1541, 2012.
- [210] B. M. Tijms, M. ten Kate, A. M. Wink, P. J. Visser, M. Ecury, M. Clerique, A. Estanga, M. G. Sebastian, A. Izagirre, J. Villanua, *et al.*, “Gray matter network disruptions and amyloid beta in cognitively normal adults,” *Neurobiology of aging*, vol. 37, pp. 154–160, 2016.
- [211] M. Pievani, N. Filippini, M. P. Van Den Heuvel, S. F. Cappa, and G. B. Frisoni, “Brain connectivity in neurodegenerative diseases—from phenotype to proteinopathy,” *Nature Reviews Neurology*, vol. 10, no. 11, p. 620, 2014.
- [212] Y. Iturria-Medina and A. C. Evans, “On the central role of brain connectivity in neurodegenerative disease progression,” *Frontiers in aging neuroscience*, vol. 7, p. 90, 2015.



- [213] W. Liao, D. Mantini, Z. Zhang, Z. Pan, J. Ding, Q. Gong, Y. Yang, and H. Chen, “Evaluating the effective connectivity of resting state networks using conditional granger causality,” *Biological cybernetics*, vol. 102, no. 1, pp. 57–69, 2010.
- [214] Q. Jiao, G. Lu, Z. Zhang, Y. Zhong, Z. Wang, Y. Guo, K. Li, M. Ding, and Y. Liu, “Granger causal influence predicts bold activity levels in the default mode network,” *Human brain mapping*, vol. 32, no. 1, pp. 154–161, 2011.
- [215] W. Liao, J. Ding, D. Marinazzo, Q. Xu, Z. Wang, C. Yuan, Z. Zhang, G. Lu, and H. Chen, “Small-world directed networks in the human brain: multivariate granger causality analysis of resting-state fmri,” *Neuroimage*, vol. 54, no. 4, pp. 2683–2694, 2011.
- [216] E. A. Leicht and M. E. Newman, “Community structure in directed networks,” *Physical review letters*, vol. 100, no. 11, p. 118703, 2008.
- [217] C. Ramaker, J. Marinus, A. M. Stiggelbout, and B. J. Van Hilten, “Systematic evaluation of rating scales for impairment and disability in parkinson’s disease,” *Movement Disorders*, vol. 17, no. 5, pp. 867–876, 2002.
- [218] H.-J. Park and K. Friston, “Structural and functional brain networks: from connections to cognition,” *Science*, vol. 342, no. 6158, p. 1238411, 2013.
- [219] S. M. Smith, P. T. Fox, K. L. Miller, D. C. Glahn, P. M. Fox, C. E. Mackay, N. Filippini, K. E. Watkins, R. Toro, A. R. Laird, *et al.*, “Correspondence of the brain’s functional architecture during activation and rest,” *Proceedings of the National Academy of Sciences*, vol. 106, no. 31, pp. 13040–13045, 2009.
- [220] M. D. Fox, A. Z. Snyder, J. L. Vincent, M. Corbetta, D. C. Van Essen, and M. E. Raichle, “The human brain is intrinsically organized into dynamic, anticorrelated functional networks,” *Proceedings of the National Academy of Sciences of the United States of America*, vol. 102, no. 27, pp. 9673–9678, 2005.

- [221] M. P. Van Den Heuvel, R. C. Mandl, R. S. Kahn, H. Pol, and E. Hilleke, “Functionally linked resting-state networks reflect the underlying structural connectivity architecture of the human brain,” *Human brain mapping*, vol. 30, no. 10, pp. 3127–3141, 2009.
- [222] C. J. Honey, R. Kötter, M. Breakspear, and O. Sporns, “Network structure of cerebral cortex shapes functional connectivity on multiple time scales,” *Proceedings of the National Academy of Sciences*, vol. 104, no. 24, pp. 10240–10245, 2007.
- [223] M. A. Koch, D. G. Norris, and M. Hund-Georgiadis, “An investigation of functional and anatomical connectivity using magnetic resonance imaging,” *Neuroimage*, vol. 16, no. 1, pp. 241–250, 2002.
- [224] Q. Wang, M. Perc, Z. Duan, and G. Chen, “Synchronization transitions on scale-free neuronal networks due to finite information transmission delays,” *Physical Review E*, vol. 80, no. 2, p. 026206, 2009.
- [225] M. Dhamala, V. K. Jirsa, and M. Ding, “Enhancement of neural synchrony by time delay,” *Physical review letters*, vol. 92, no. 7, p. 074104, 2004.
- [226] D. Guo, Q. Wang, and M. Perc, “Complex synchronous behavior in interneuronal networks with delayed inhibitory and fast electrical synapses,” *Physical Review E*, vol. 85, no. 6, p. 061905, 2012.
- [227] A. Mitra, A. Z. Snyder, T. Blazey, and M. E. Raichle, “Lag threads organize the brain’s intrinsic activity,” *Proceedings of the National Academy of Sciences*, vol. 112, no. 17, pp. E2235–E2244, 2015.
- [228] G. Goelman, N. Gordon, and O. Bonne, “Maximizing negative correlations in resting-state functional connectivity mri by time-lag,” *PloS one*, vol. 9, no. 11, p. e111554, 2014.
- [229] G. Chen, G. Chen, C. Xie, and S.-J. Li, “Negative functional connectivity and its dependence on the shortest path length of positive network in the resting-state human brain,” *Brain connectivity*, vol. 1, no. 3, pp. 195–206, 2011.

- [230] R. F. Galán, “On how network architecture determines the dominant patterns of spontaneous neural activity,” *PloS one*, vol. 3, no. 5, p. e2148, 2008.
- [231] F. Abdelnour, H. U. Voss, and A. Raj, “Network diffusion accurately models the relationship between structural and functional brain connectivity networks,” *Neuroimage*, vol. 90, pp. 335–347, 2014.
- [232] V. Pernice, M. Deger, S. Cardanobile, and S. Rotter, “The relevance of network micro-structure for neural dynamics,” *Frontiers in computational neuroscience*, vol. 7, p. 72, 2013.
- [233] I. Belykh, E. de Lange, and M. Hasler, “Synchronization of bursting neurons: What matters in the network topology,” *Physical review letters*, vol. 94, no. 18, p. 188101, 2005.

# Appendix A

## Data

### A.1 Chapter 5

#### A.1.1 Differences in global measures after controlling for scanning centers

Table A.1: Differences in global network measures between controls and patients after controlling for scanning site. D - density of the network; CTR - controls; sMCI - stable mild cognitive impairment (sMCI); lMCIc - late mild cognitive impairment converters; eMCIc - early mild cognitive impairment converters; AD - Alzheimer’s disease [96].

<i>Characteristic path length</i>									
D	CTR	sMCI-3y	lMCIc	eMCIc	AD	CTR-sMCI p value	CTR-lMCIc p value	CTR-eMCIc p value	CTR-AD p value
5	1.5845	2.7304	2.3518	3.0140	2.0183	0.003	0.017	0.006	0.444
6	1.6790	2.5520	2.7738	2.8021	2.6171	0.015	0.012	0.059	0.082
7	1.5567	2.3543	2.6419	2.6831	2.6296	0.051	0.026	0.013	0.004
8	1.5438	2.3631	2.5191	2.6536	2.3915	0.118	0.090	0.010	0.009
9	1.6820	2.2803	2.4485	2.5449	2.2578	0.428	0.336	0.010	0.027
10	1.7357	2.3155	2.4950	2.4729	2.3602	0.477	0.347	0.017	0.005
11	1.6816	2.2758	2.3931	2.3818	2.3218	0.384	0.342	0.044	0.002
12	1.7398	2.4715	2.3119	2.2830	2.1696	0.198	0.319	0.108	0.025
13	1.6727	3.1611	2.2269	2.2865	2.0461	0.006	0.128	0.066	0.059
14	1.6606	3.1556	2.5465	2.2456	2.3345	0.004	0.008	0.094	< 0.001
15	1.6719	2.9224	2.3967	2.3178	2.1887	0.014	0.026	0.071	< 0.001
16	1.7764	2.8681	2.2983	2.2192	2.1258	0.022	0.070	0.292	0.030
17	1.7778	2.6959	2.3519	2.1333	2.0345	0.024	0.041	0.525	0.060
18	1.8619	2.6469	2.2953	2.1254	2.0177	0.035	0.161	0.790	0.247

Continued

Table A.1 – Continued

19	2.0555	2.6289	2.1832	2.0775	1.9832	0.139	0.753	0.649	0.538
20	1.9738	2.5825	2.1387	2.0000	1.9476	0.131	0.826	0.613	0.835
21	1.8879	2.4036	2.1052	1.9815	1.9232	0.315	0.772	0.787	0.765
22	1.8437	2.3276	2.1670	1.9094	1.9303	0.475	0.619	0.740	0.461
23	1.7804	2.2865	2.1161	1.9426	2.0179	0.555	0.676	0.929	0.125
24	1.7240	2.2365	2.1846	2.1347	1.9808	0.554	0.386	0.544	0.167
25	1.6722	2.3920	2.1563	2.1321	1.9495	0.202	0.301	0.473	0.266
26	2.0252	2.3522	2.1201	2.0886	1.9313	0.901	0.601	0.974	0.548
27	2.2212	2.2515	2.0930	2.0599	1.9031	0.476	0.316	0.887	0.345
28	2.2291	2.2333	2.0533	2.3755	1.8440	0.613	0.364	0.657	0.293
29	2.1885	2.2096	2.0262	2.3502	1.8142	0.848	0.609	0.550	0.325
30	2.1620	2.1802	1.9958	2.3228	1.7719	0.941	0.762	0.306	0.337
31	2.0063	2.1457	1.9678	2.1879	1.7516	0.815	0.932	0.190	0.611
32	1.9335	2.1445	1.9371	2.1587	2.0158	0.480	0.591	0.092	0.859
33	1.9125	2.1232	1.9015	2.1331	1.9914	0.311	0.508	0.059	0.818
34	1.8520	1.9810	1.8802	2.0509	1.9680	0.36	0.297	0.051	0.694
35	1.8121	1.9581	1.8621	2.0051	2.0831	0.217	0.211	0.042	0.216

---

Continued

Table A.1 – Continued

D	<i>Clustering coefficient</i>								
	CTR	sMCI-3y	lMCIc	eMCIc	AD	CTR-sMCI p value	CTR-lMCIc p value	CTR-eMCIc p value	CTR-AD p value
5	0.2559	0.2447	0.3067	0.2461	0.2325	0.325	0.289	0.571	0.476
6	0.2683	0.3027	0.3396	0.2703	0.2548	0.693	0.132	0.882	0.801
7	0.2846	0.3741	0.3917	0.2946	0.2699	0.089	0.019	0.877	0.642
8	0.3048	0.3730	0.3799	0.3304	0.2970	0.212	0.166	0.537	0.673
9	0.3243	0.4030	0.3926	0.3593	0.3411	0.070	0.171	0.541	0.478
10	0.3894	0.4453	0.4143	0.3667	0.3608	0.131	0.606	0.197	0.267
11	0.4151	0.4573	0.4454	0.4023	0.3696	0.274	0.567	0.385	0.104
12	0.4379	0.4863	0.4728	0.4054	0.3808	0.230	0.454	0.326	0.067
13	0.4467	0.4836	0.5050	0.4473	0.4379	0.485	0.168	0.832	0.764
14	0.4817	0.5201	0.5266	0.4574	0.4625	0.498	0.224	0.623	0.538
15	0.5120	0.5520	0.5206	0.4667	0.4921	0.533	0.877	0.393	0.615
16	0.5296	0.5689	0.5112	0.4884	0.5126	0.458	0.590	0.449	0.661
17	0.5417	0.5866	0.5215	0.4951	0.5353	0.382	0.560	0.368	0.883
18	0.5796	0.5995	0.5378	0.5105	0.5445	0.666	0.291	0.178	0.462
19	0.5975	0.5912	0.5455	0.5295	0.5529	0.982	0.255	0.241	0.385
20	0.5981	0.6149	0.5541	0.5412	0.5655	0.453	0.500	0.352	0.529
21	0.6455	0.6248	0.5578	0.5408	0.5684	0.958	0.086	0.036	0.071

Continued

Table A.1 – Continued

22	0.6616	0.6458	0.5714	0.5414	0.5690	0.657	0.106	0.010	0.024
23	0.6748	0.6574	0.5766	0.5858	0.5782	0.565	0.083	0.095	0.012
24	0.7041	0.6564	0.5775	0.5893	0.5896	0.708	0.007	0.016	0.001
25	0.7062	0.6527	0.5901	0.5906	0.6007	0.618	0.018	0.008	0.003
26	0.7063	0.6549	0.5934	0.5988	0.6079	0.599	0.029	0.020	0.005
27	0.6914	0.6579	0.6114	0.6277	0.6167	0.880	0.244	0.251	0.024
28	0.6985	0.6619	0.6127	0.6251	0.6253	0.914	0.166	0.149	0.013
29	0.7056	0.6737	0.6181	0.6344	0.6314	0.964	0.158	0.182	0.006
30	0.7153	0.6789	0.6453	0.6423	0.6502	0.870	0.414	0.192	0.014
31	0.7181	0.6763	0.6527	0.6538	0.6582	0.634	0.424	0.312	0.012
32	0.7218	0.6873	0.6684	0.6699	0.6777	0.785	0.620	0.521	0.030
33	0.7233	0.7045	0.6767	0.6794	0.6894	0.788	0.804	0.772	0.078
34	0.7533	0.6979	0.6861	0.6809	0.7016	0.333	0.315	0.146	0.018
35	0.7558	0.7046	0.6891	0.7015	0.7022	0.330	0.311	0.414	0.009

*Transitivity*

D	CTR	sMCI-3y	lMCIc	eMCIc	AD	CTR-sMCI p value	CTR-lMCIc p value	CTR-eMCIc p value	CTR-AD p value
5	0.6256	0.5682	0.5097	0.4805	0.4957	0.681	0.211	0.020	0.002
6	0.6599	0.5870	0.5243	0.4699	0.5242	0.577	0.161	0.001	0.001

Continued



Table A.1 – Continued

7	0.6848	0.5963	0.5333	0.4964	0.5531	0.458	0.136	0.003	0.001
8	0.7128	0.6073	0.5648	0.5140	0.5780	0.260	0.157	0.003	0.001
9	0.7154	0.6102	0.5587	0.5317	0.5905	0.201	0.116	0.005	0.001
10	0.7216	0.6258	0.5703	0.5388	0.5957	0.246	0.117	0.007	0.001
11	0.7206	0.6215	0.5862	0.5501	0.6095	0.186	0.204	0.008	0.001
12	0.7308	0.6145	0.5929	0.5654	0.6082	0.082	0.180	0.010	0.001
13	0.7373	0.6118	0.5942	0.5773	0.6113	0.059	0.142	0.009	0.001
14	0.7414	0.6162	0.6059	0.5894	0.6125	0.060	0.223	0.026	0.001
15	0.7492	0.6202	0.6021	0.5999	0.6127	0.062	0.153	0.018	0.001
16	0.7527	0.6268	0.6035	0.5998	0.6122	0.064	0.155	0.018	0.001
17	0.7738	0.6244	0.6041	0.6005	0.6141	0.016	0.089	0.003	0.001
18	0.7890	0.6346	0.6110	0.6094	0.6178	0.015	0.066	0.001	0.001
19	0.7935	0.6375	0.6088	0.6184	0.6286	0.008	0.038	0.002	0.001
20	0.7945	0.6348	0.6145	0.6280	0.6353	0.008	0.036	0.006	0.001
21	0.7866	0.6405	0.6177	0.6325	0.6432	0.013	0.044	0.012	0.001
22	0.7890	0.6491	0.6177	0.6372	0.6499	0.023	0.017	0.010	0.001
23	0.7836	0.6529	0.6158	0.6427	0.6582	0.029	0.032	0.022	0.001
24	0.7894	0.6563	0.6185	0.6485	0.6726	0.026	0.017	0.021	0.001
25	0.7908	0.6583	0.6269	0.6573	0.6787	0.018	0.019	0.034	0.001
26	0.7991	0.6566	0.6339	0.6679	0.6932	0.006	0.014	0.018	0.001

Continued

Table A.1 – Continued

27	0.7982	0.6598	0.6414	0.6771	0.7019	0.011	0.010	0.033	0.001
28	0.8085	0.6679	0.6455	0.6823	0.7095	0.007	0.008	0.017	0.001
29	0.8109	0.6776	0.6527	0.6938	0.7189	0.008	0.007	0.039	0.001
30	0.8124	0.6808	0.6597	0.7009	0.7296	0.012	0.014	0.046	0.001
31	0.8163	0.6837	0.6645	0.7016	0.7404	0.003	0.007	0.039	0.003
32	0.8181	0.6921	0.6681	0.7146	0.7442	0.010	0.006	0.070	0.003
33	0.8196	0.7015	0.6786	0.7227	0.7498	0.020	0.019	0.077	0.009
34	0.8214	0.7052	0.6860	0.7209	0.7605	0.030	0.026	0.047	0.028
35	0.8240	0.7110	0.6891	0.7282	0.7663	0.021	0.019	0.090	0.023

*Modularity*

D	CTR	sMCI-3y	lMCIc	eMCIc	AD	CTR-sMCI p value	CTR-lMCIc p value	CTR-eMCIc p value	CTR-AD p value
5	0.2813	0.3979	0.4849	0.4241	0.3972	0.047	0.011	0.092	0.016
6	0.2524	0.3876	0.4632	0.4236	0.3872	0.040	0.002	0.013	0.002
7	0.2619	0.3836	0.4309	0.3936	0.3571	0.035	0.003	0.028	0.009
8	0.2587	0.3617	0.4131	0.3551	0.3404	0.076	0.006	0.096	0.017
9	0.2661	0.3436	0.3775	0.3300	0.3410	0.051	0.031	0.194	0.024
10	0.2470	0.3285	0.3655	0.3130	0.3308	0.047	0.019	0.208	0.011
11	0.2290	0.3192	0.3525	0.3027	0.3539	0.021	0.012	0.174	0.001

Continued

Table A.1 – Continued

12	0.2089	0.3118	0.3295	0.2966	0.3350	0.030	0.012	0.118	0.001
13	0.2026	0.3020	0.3291	0.2947	0.3015	0.029	0.009	0.105	0.004
14	0.1941	0.2939	0.2988	0.2703	0.3015	0.020	0.028	0.138	0.001
15	0.1812	0.2933	0.2806	0.2777	0.2791	0.037	0.036	0.087	0.007
16	0.1815	0.2774	0.2813	0.2778	0.2681	0.020	0.044	0.082	0.023
17	0.1701	0.2770	0.2639	0.2549	0.2674	0.017	0.064	0.120	0.008
18	0.1565	0.2594	0.2630	0.2543	0.2610	0.018	0.030	0.055	0.002
19	0.1489	0.2607	0.2415	0.2438	0.2478	0.008	0.083	0.050	0.001
20	0.1402	0.2579	0.2306	0.2490	0.2438	0.022	0.077	0.049	0.003
21	0.1415	0.2379	0.2302	0.2490	0.2339	0.020	0.086	0.036	0.001
22	0.1397	0.2358	0.2250	0.2471	0.2326	0.017	0.082	0.015	0.001
23	0.1371	0.2322	0.2133	0.2387	0.2278	0.079	0.093	0.034	0.001
24	0.1312	0.2082	0.2113	0.2261	0.2167	0.060	0.053	0.027	0.004
25	0.1364	0.2081	0.2120	0.2185	0.2109	0.054	0.071	0.046	0.008
26	0.1351	0.2083	0.1964	0.2183	0.2006	0.083	0.116	0.040	0.014
27	0.1331	0.1959	0.1928	0.2083	0.1997	0.107	0.073	0.044	0.006
28	0.1277	0.1894	0.1778	0.2075	0.1935	0.220	0.148	0.038	0.013
29	0.1269	0.1761	0.1722	0.1988	0.1863	0.215	0.153	0.056	0.014
30	0.1294	0.1770	0.1748	0.1948	0.1774	0.197	0.145	0.059	0.081
31	0.1298	0.1765	0.1725	0.2054	0.1725	0.331	0.143	0.031	0.092

Continued

Table A.1 – Continued

32	0.1294	0.1690	0.1671	0.1972	0.1719	0.212	0.155	0.049	0.085
33	0.1272	0.1666	0.1627	0.1904	0.1655	0.248	0.174	0.057	0.139
34	0.1263	0.1660	0.1545	0.1949	0.1642	0.216	0.267	0.027	0.129
35	0.1249	0.1608	0.1426	0.1882	0.1627	0.047	0.471	0.033	0.105

---

## A.2 Chapter 6

### A.2.1 Directed network analysis in Parkinson's Disease patients: High resolution networks

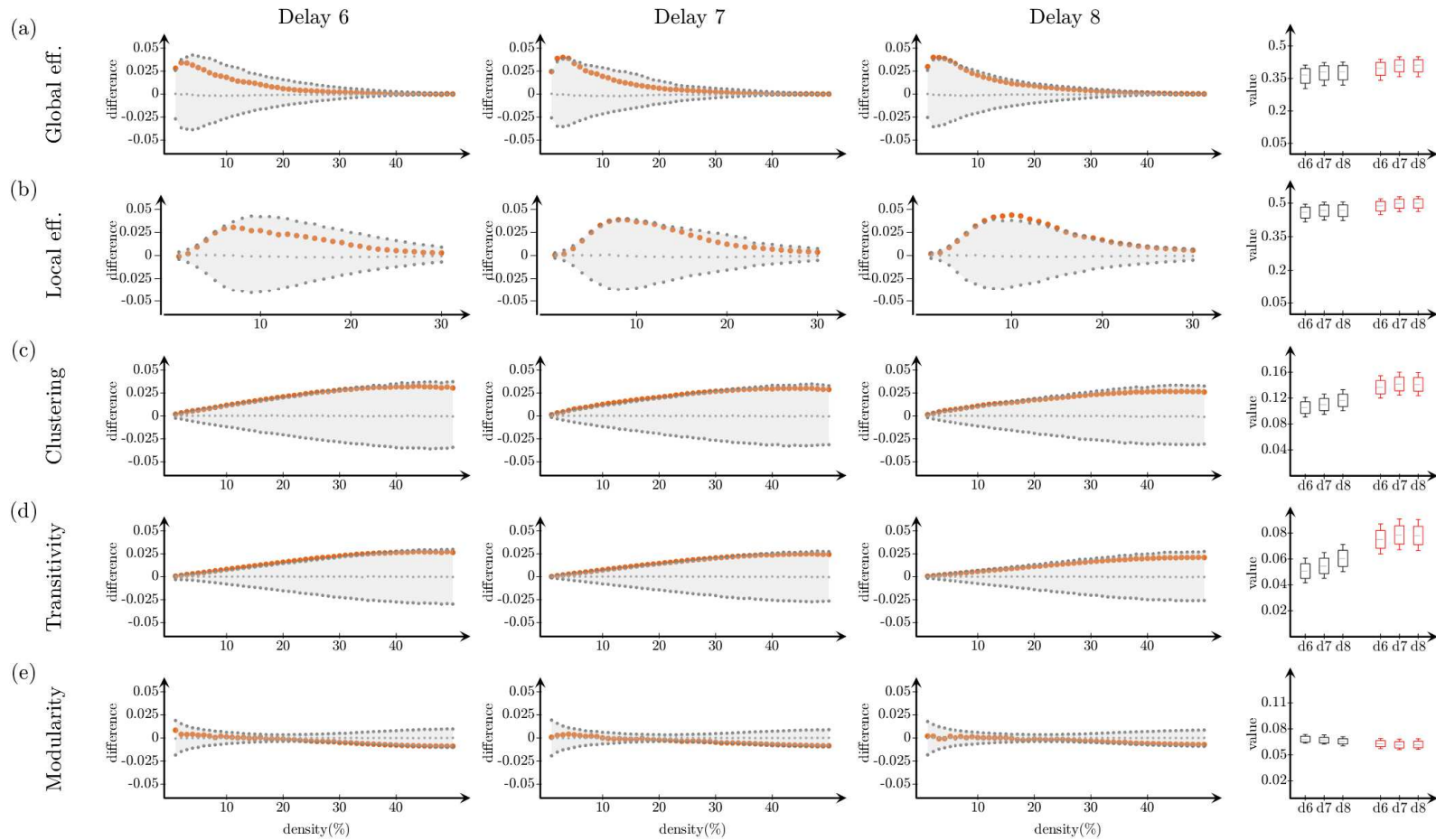


Figure A.1: Changes in global network measures as a function of network density. PD-CN group is compared to healthy controls for high resolution networks. Global efficiency (a), local efficiency (b), clustering coefficient (C), transitivity (D), and modularity (E) are calculated for delays of 6 (leftmost), 7 (left-center) and 8 (right-center). Rightmost: The values of the corresponding measures for PD-CN (red) and controls (black) over a selected range of densities.

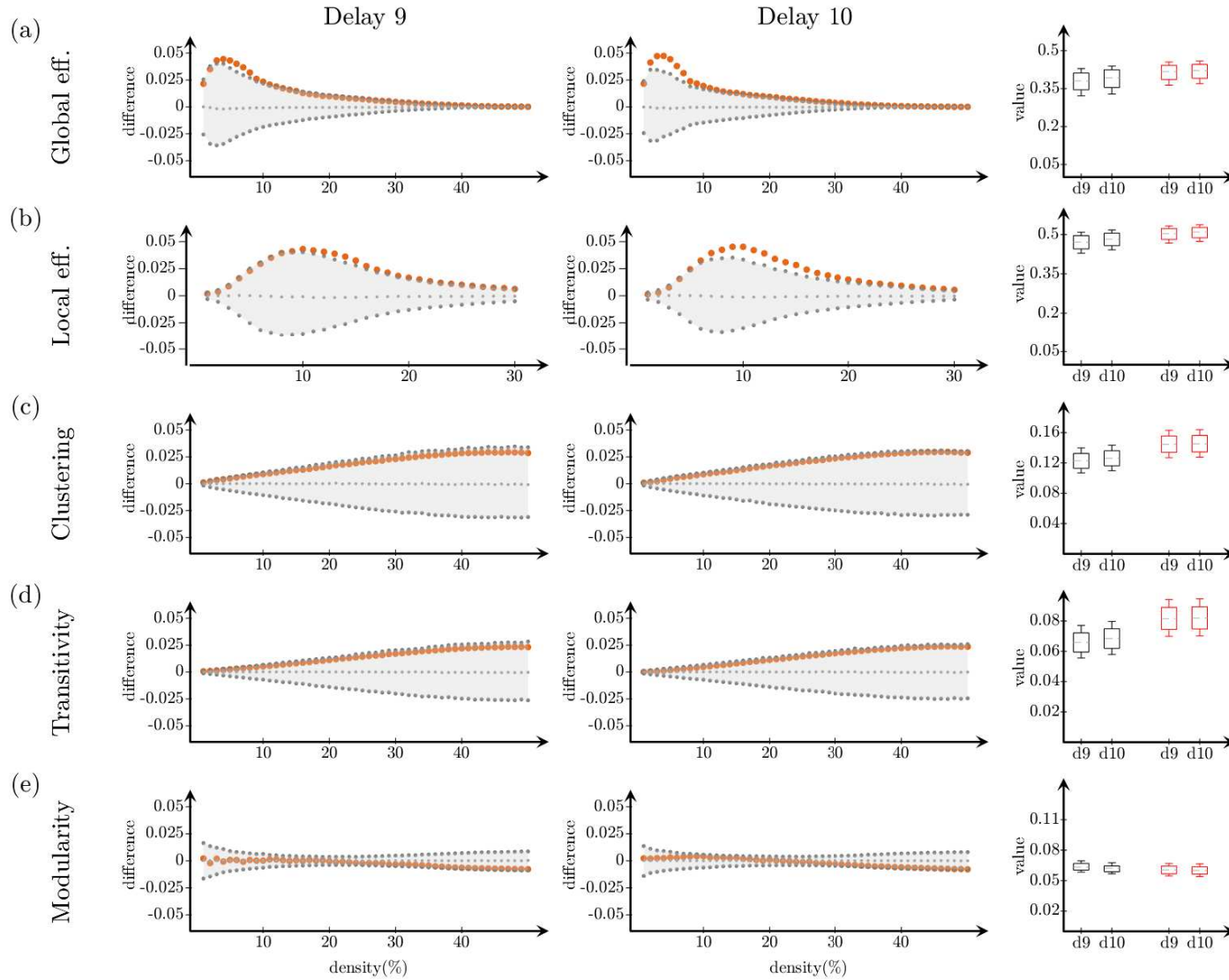


Figure A.2: Changes in global network measures as a function of network density. PD-CN group is compared to healthy controls for high resolution networks. Global efficiency (a), local efficiency (b), clustering coefficient ( $C$ ), transitivity (D), and modularity (E) are calculated for delays of 9 (left) and 10 (center). Right: The values of the corresponding measures for PD-CN (red) and controls (black) over a selected range of densities.

## A.2.2 Correlation of global measures with UPDRS: Delay

7

Table A.2: Correlation between global measures and UPDRS for low resolution networks. P-values for the correlation analysis between each global measures calculated in this analysis and UPDRS scores of the corresponding patients. The global measures were calculated based on the low resolution parcellation scheme. The p-values were considered significant at the level  $p < 0.05$ .

Low resolution analysis - Delay 7 - UPDRS					
Density (%)	Global eff.	Local eff.	Clustering	Transitivity	Modularity
1	0.015	0.332	0.135	0.009	0.390
2	0.000	0.032	0.000	0.000	0.371
3	0.000	0.026	0.000	0.001	0.725
4	0.002	0.016	0.000	0.001	0.352
5	0.004	0.002	0.001	0.001	0.763
6	0.007	0.001	0.000	0.002	0.647
7	0.010	0.000	0.001	0.002	0.492
8	0.009	0.000	0.001	0.002	0.852
9	0.018	0.000	0.002	0.003	0.806
10	0.026	0.000	0.001	0.002	0.853
11	0.035	0.001	0.002	0.003	0.682
12	0.037	0.001	0.002	0.002	0.666
13	0.048	0.002	0.002	0.003	0.654
14	0.051	0.003	0.003	0.003	0.372
15	0.056	0.004	0.003	0.002	0.308
16	0.071	0.008	0.004	0.003	0.237
17	0.086	0.013	0.004	0.003	0.544
18	0.098	0.019	0.005	0.003	0.517
19	0.102	0.029	0.005	0.003	0.204
20	0.107	0.043	0.004	0.003	0.017
21	0.120	0.060	0.005	0.004	0.008

Continued



Table A.2 – Continued

22	0.132	0.081	0.005	0.004	0.002
23	0.149	0.112	0.006	0.004	0.003
24	0.139	0.117	0.006	0.004	0.001
25	0.121	0.141	0.008	0.005	0.002
26	0.113	0.140	0.007	0.005	0.001
27	0.101	0.149	0.007	0.005	0.002
28	0.102	0.154	0.007	0.005	0.000
29	0.094	0.160	0.008	0.005	0.000
30	0.092	0.152	0.008	0.005	0.001
31	0.097	0.160	0.008	0.005	0.002
32	0.096	0.162	0.009	0.006	0.002
33	0.098	0.155	0.009	0.006	0.002
34	0.089	0.147	0.010	0.006	0.004
35	0.108	0.156	0.011	0.007	0.002
36	0.111	0.149	0.011	0.007	0.007
37	0.116	0.152	0.012	0.007	0.004
38	0.118	0.146	0.012	0.007	0.005
39	0.117	0.136	0.011	0.007	0.006
40	0.125	0.134	0.012	0.008	0.007
41	0.143	0.143	0.012	0.008	0.007
42	0.162	0.162	0.012	0.008	0.009
43	0.161	0.153	0.012	0.007	0.009
44	0.198	0.182	0.012	0.008	0.009
45	0.228	0.210	0.012	0.008	0.011
46	0.231	0.214	0.011	0.007	0.009
47	0.247	0.234	0.012	0.007	0.010
48	0.356	0.343	0.013	0.008	0.010
49	0.343	0.334	0.013	0.008	0.011
50	0.400	0.399	0.013	0.008	0.010

---

Table A.3: Correlation between global measures and UPDRS for high resolution networks. P-values for the correlation analysis between each global measures calculated in this analysis and UPDRS scores of the corresponding patients. The global measures were calculated based on the high resolution parcellation scheme. The p-values were considered significant at the level  $p < 0.05$ .

<b>High resolution analysis - Delay 7 - UPDRS</b>					
Density (%)	Global eff.	Local eff.	Clustering	Transitivity	Modularity
1	< 0.001	0.092	< 0.001	< 0.001	0.851
2	< 0.001	0.007	< 0.001	< 0.001	0.970
3	0.003	< 0.001	< 0.001	< 0.001	0.794
4	0.006	< 0.001	< 0.001	< 0.001	0.682
5	0.011	< 0.001	< 0.001	< 0.001	0.749
6	0.016	< 0.001	0.002	< 0.001	0.325
7	0.022	< 0.001	0.003	< 0.001	0.417
8	0.028	< 0.001	0.003	< 0.001	0.363
9	0.029	0.003	0.003	< 0.001	0.161
10	0.033	0.005	0.003	< 0.001	0.130
11	0.039	0.009	0.004	< 0.001	0.280
12	0.036	0.013	0.003	< 0.001	0.129
13	0.042	0.018	0.004	0.002	0.105
14	0.046	0.023	0.004	0.002	0.074
15	0.045	0.030	0.004	0.002	0.071
16	0.052	0.037	0.004	0.002	0.024
17	0.048	0.042	0.004	0.002	0.006
18	0.041	0.047	0.004	0.002	0.007
19	0.038	0.051	0.004	0.002	0.006
20	0.040	0.058	0.004	0.002	0.003
21	0.043	0.063	0.004	0.002	< 0.001
22	0.049	0.066	0.004	0.002	< 0.001
23	0.038	0.031	0.004	0.002	< 0.001

Continued

Table A.3 – Continued

24	0.046	0.035	0.005	0.002	< 0.001
25	0.058	0.041	0.005	0.002	< 0.001
26	0.083	0.054	0.005	0.002	< 0.001
27	0.087	0.055	0.005	0.002	< 0.001
28	0.127	0.082	0.005	0.002	< 0.001
29	0.153	0.101	0.005	0.003	< 0.001
30	0.163	0.113	0.005	0.002	< 0.001
31	0.218	0.218	0.005	0.003	< 0.001
32	0.252	0.252	0.005	0.003	< 0.001
33	0.313	0.313	0.005	0.003	< 0.001
34	0.341	0.341	0.006	0.003	0.002
35	0.394	0.394	0.006	0.003	0.002
36	0.458	0.458	0.006	0.003	0.003
37	0.500	0.500	0.006	0.003	0.003
38	0.492	0.492	0.006	0.003	0.004
39	0.660	0.660	0.007	0.004	0.004
40	0.635	0.635	0.006	0.003	0.004
41	0.679	0.679	0.007	0.004	0.004
42	0.713	0.713	0.007	0.004	0.004
43	0.704	0.704	0.007	0.004	0.005
44	0.651	0.651	0.007	0.004	0.005
45	0.840	0.840	0.008	0.004	0.005
46	0.557	0.557	0.007	0.004	0.005
47	0.955	0.955	0.008	0.005	0.005
48	0.708	0.708	0.008	0.005	0.006
49	0.319	0.319	0.008	0.005	0.006
50	0.875	0.875	0.008	0.005	0.006

---

### A.2.3 Longitudinal analysis of Parkinson’s Disease patients

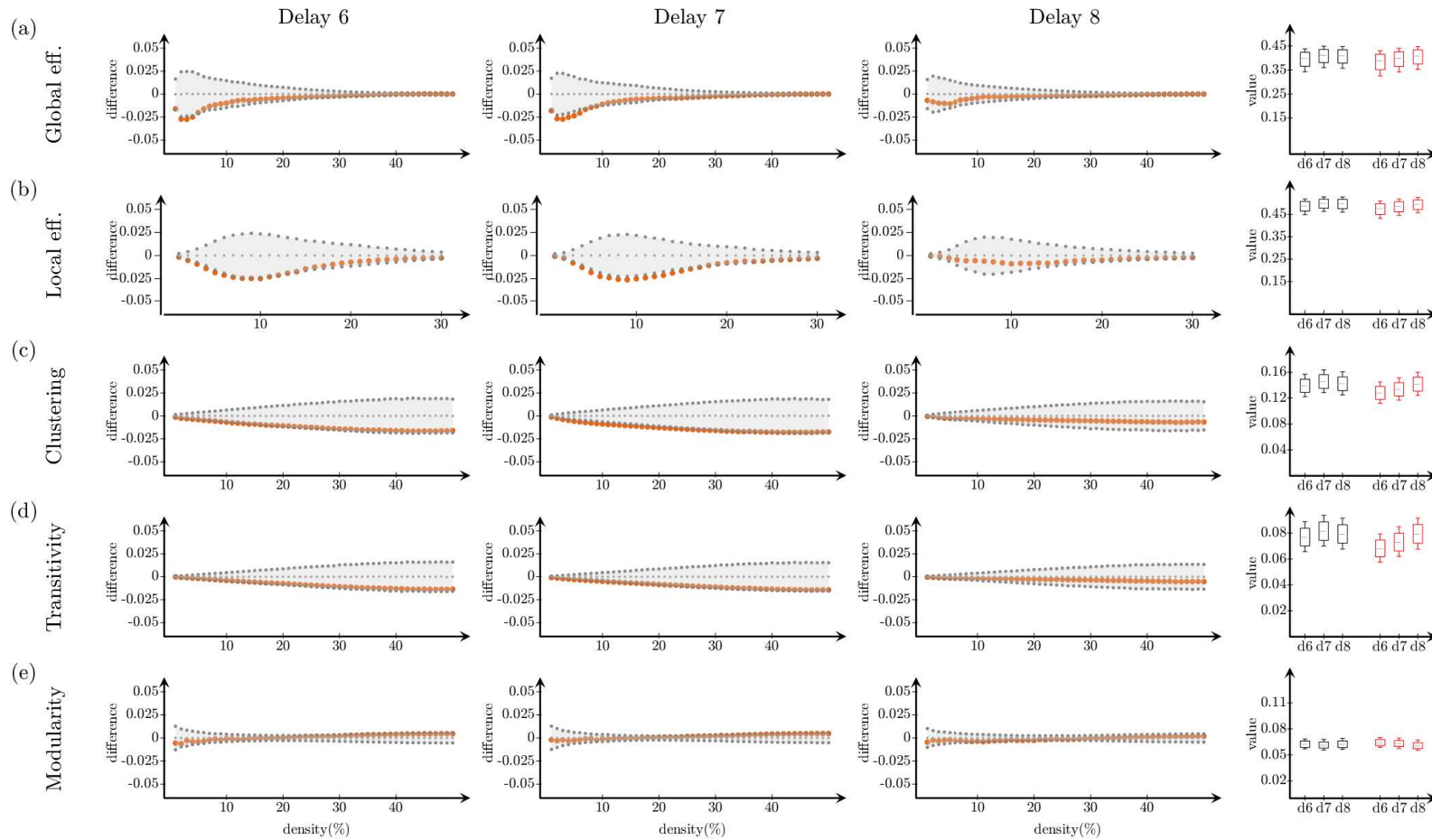


Figure A.3: Changes in global network measures as a function of network density for longitudinal data. The baseline and longitudinal networks are compared for the PD-CN subgroup for high resolution networks. Global efficiency (a), local efficiency (b), clustering coefficient (C), transitivity (D), and modularity (E) are calculated for delays of 9 (left) and 10 (center). Right: The values of the corresponding measures for baseline (red) and longitudinal (black) data over a selected range of densities. These results were calculated based on the high resolution parcellation scheme.

#### A.2.4 Directed network analysis in Alzheimer's Disease patients: Delays 4-6

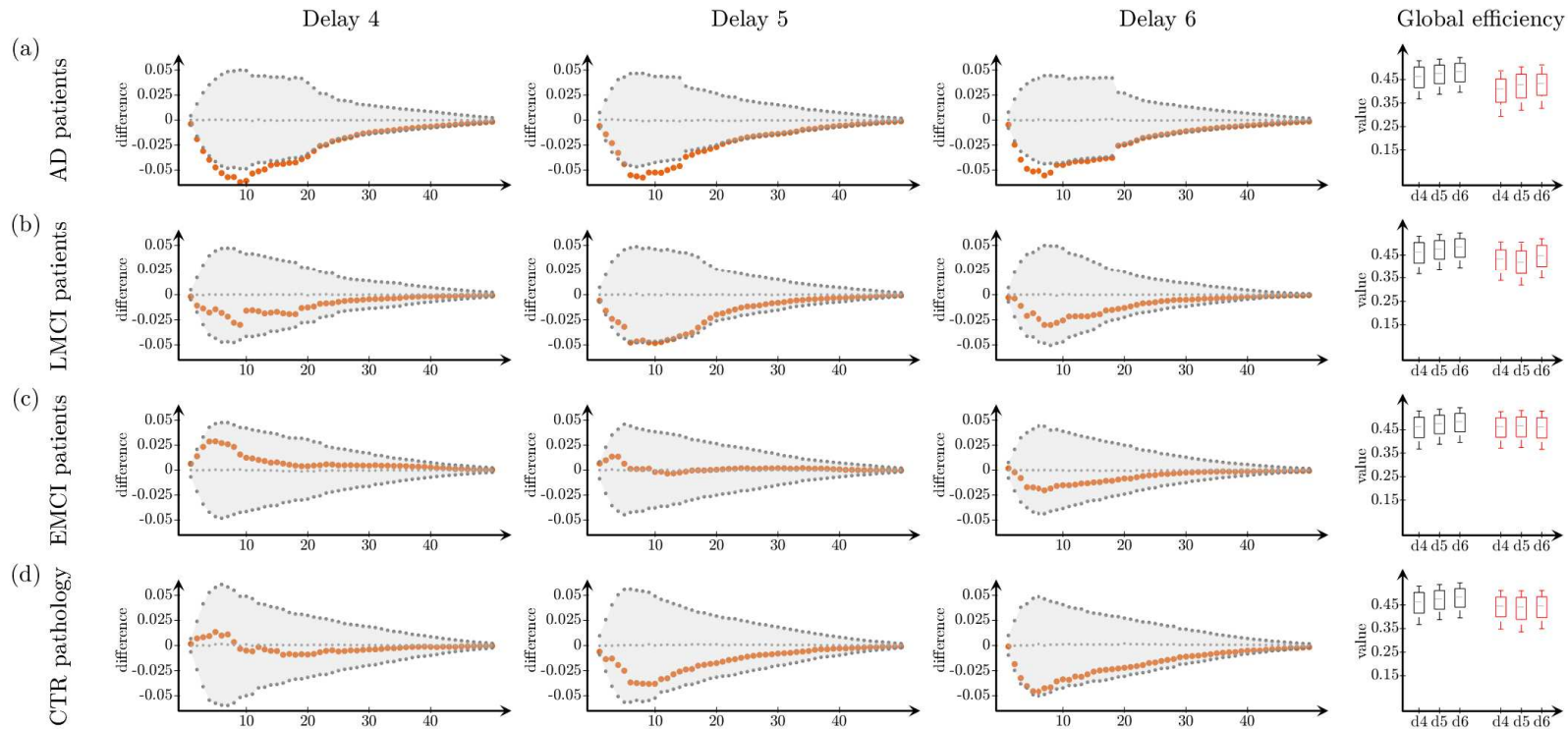


Figure A.4: Changes in global efficiency as a function of network density for delays 4-6. CTR – A0 group is compared to CTR – A1 (a), eMCI (b), lMCI(C) and AD (D) patients for delays of 4 (leftmost), 5 (left-center) and 6 (right-center). Rightmost: The values of the global efficiency for the corresponding groups (controls shown in black).

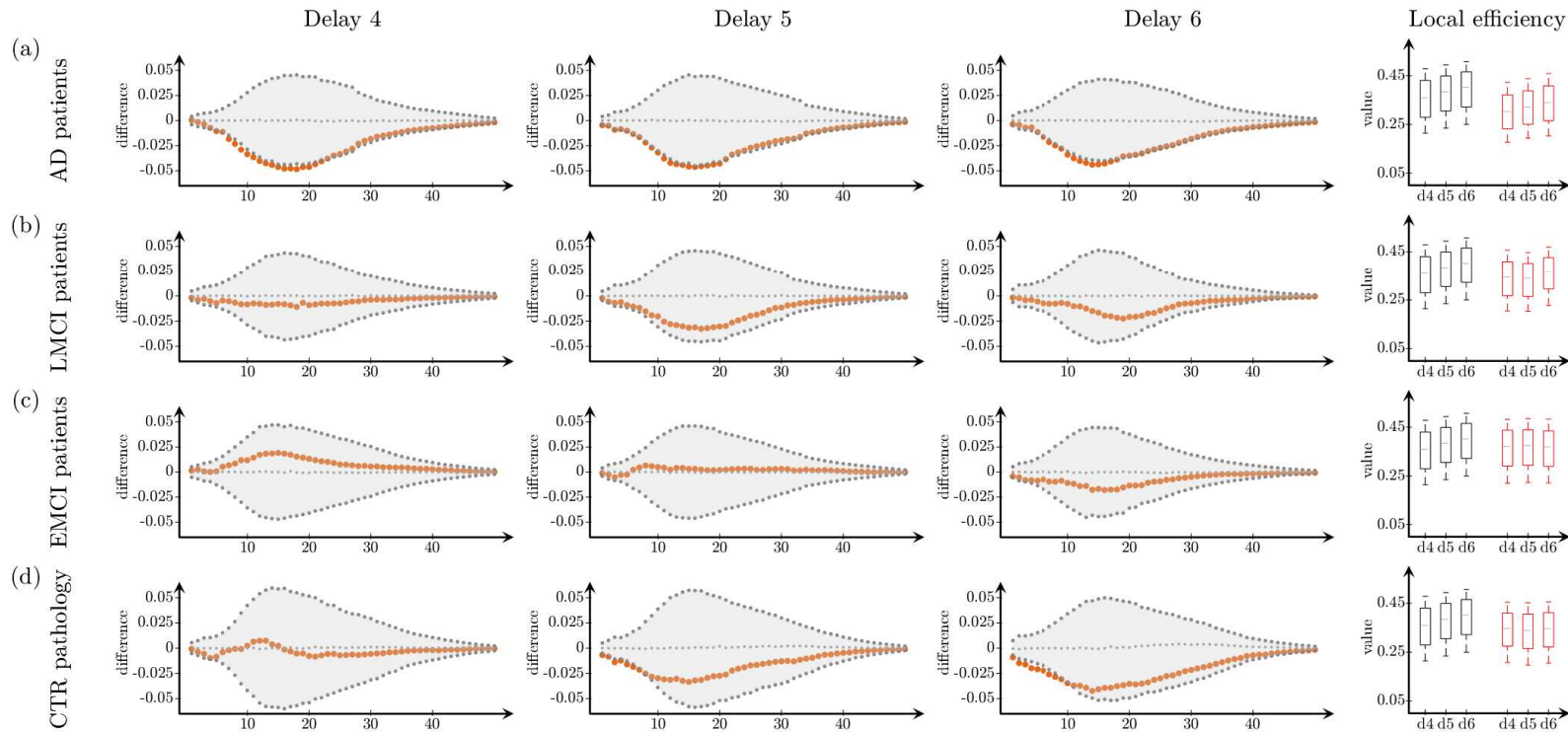


Figure A.5: Changes in local efficiency as a function of network density for delays 4-6. CTR – A0 group is compared to CTR – A1 (a), eMCI (b), lMCI (c) and AD (d) patients for delays of 4 (leftmost), 5 (left-center) and 6 (right-center). Rightmost: The values of the local efficiency for the corresponding groups (controls shown in black).

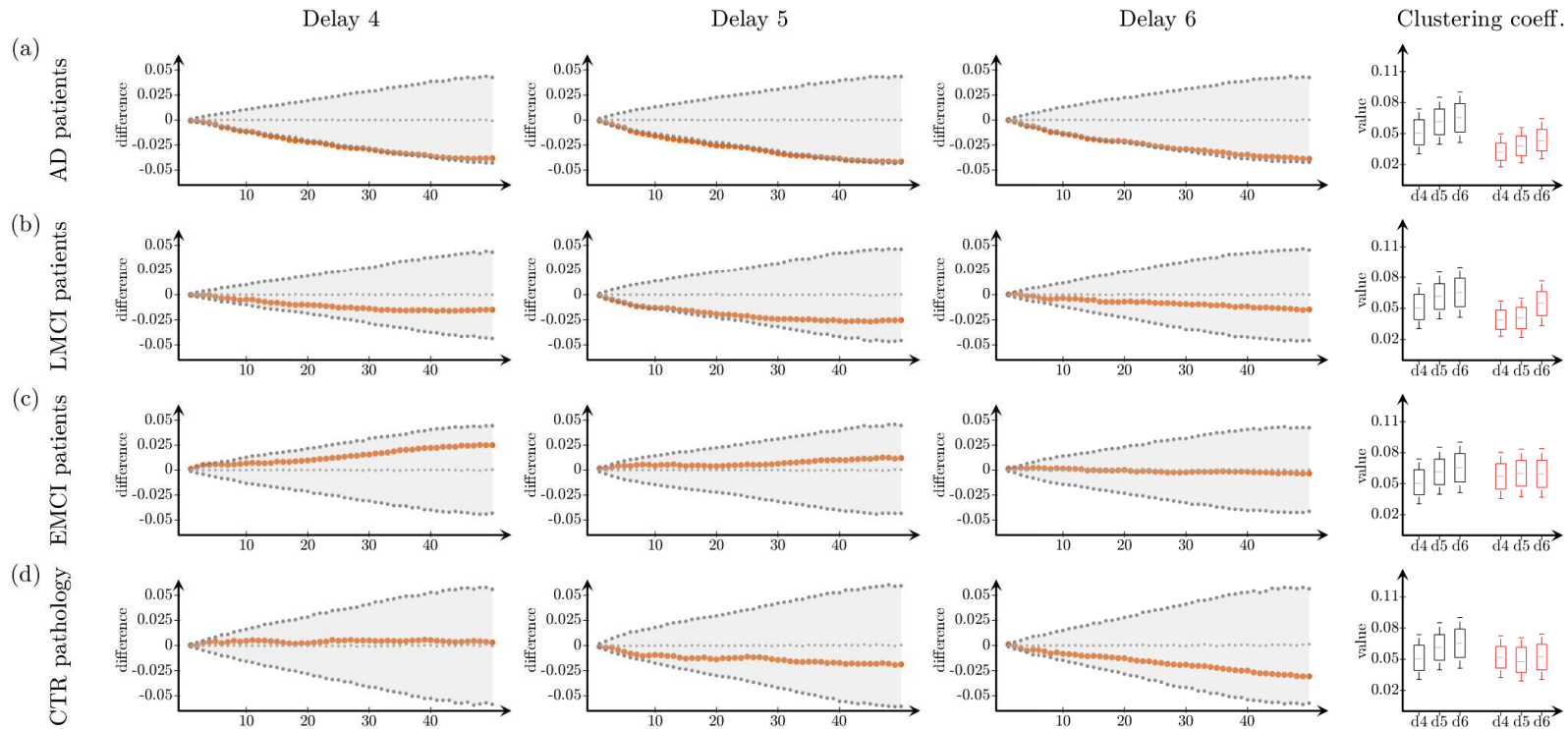


Figure A.6: Changes in clustering coefficient as a function of network density for delays 4-6. CTR – A0 group is compared to CTR – A1 (a), eMCI (b), lMCI(C) and AD (D) patients for delays of 4 (leftmost), 5 (left-center) and 6 (right-center). Rightmost: The values of the clustering coefficient for the corresponding groups (controls shown in black).



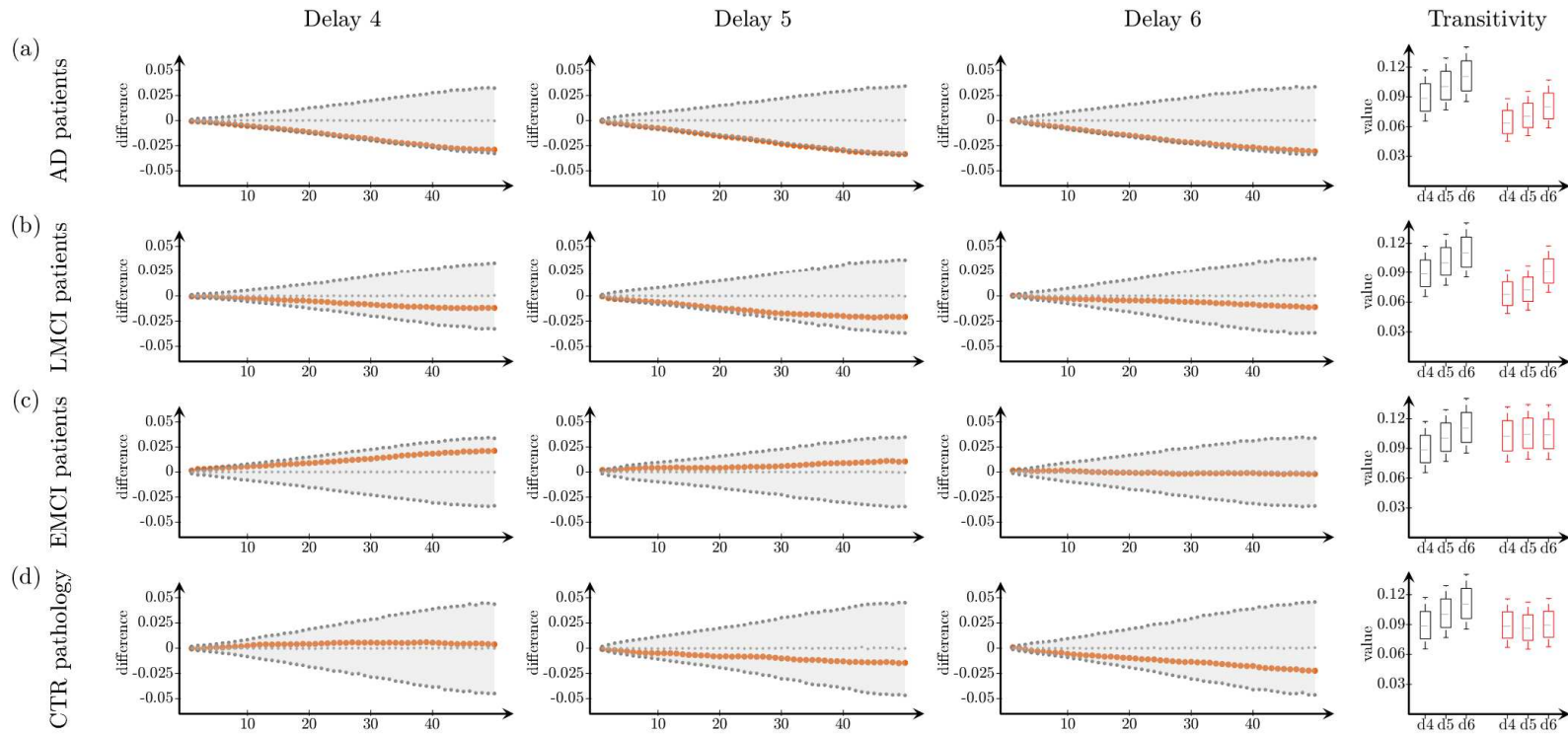


Figure A.7: Changes in transitivity as a function of network density for delays 4-6. CTR – A0 group is compared to CTR – A1 (a), eMCI (b), lMCI (c) and AD (d) patients for delays of 4 (leftmost), 5 (left-center) and 6 (right-center). Rightmost: The values of the transitivity for the corresponding groups (controls shown in black).

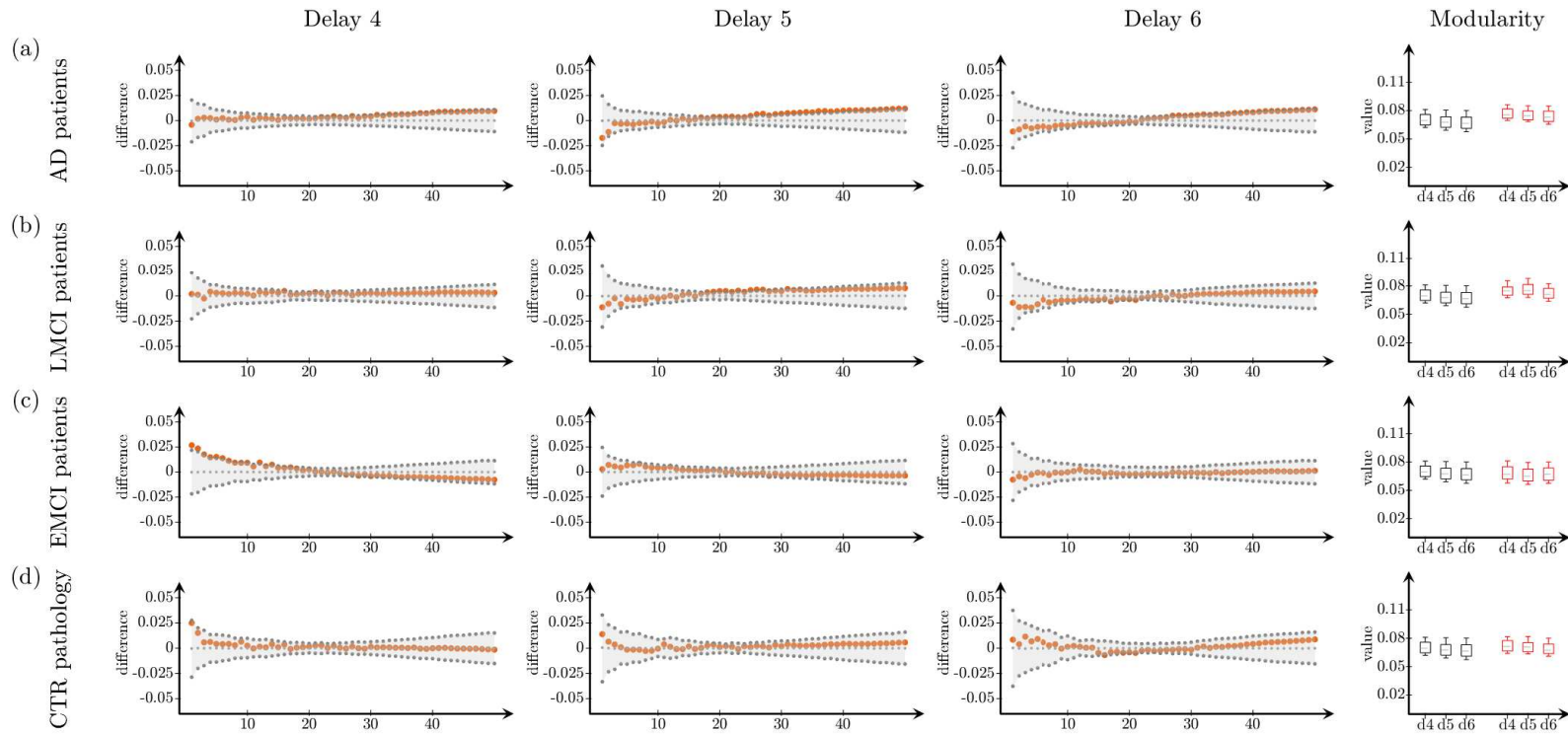


Figure A.8: Changes in modularity as a function of network density for delays 4-6. CTR – A0 group is compared to CTR – A1 (a), eMCI (b), lMCI (c) and AD (d) patients for delays of 4 (leftmost), 5 (left-center) and 6 (right-center). Rightmost: The values of the modularity for the corresponding groups (controls shown in black).

# Appendix B

## Publications

RESEARCH ARTICLE

# BRAPH: A graph theory software for the analysis of brain connectivity

Mite Mijalkov<sup>1</sup>, Ehsan Kakaei<sup>1</sup>, Joana B. Pereira<sup>2</sup>, Eric Westman<sup>2</sup>, Giovanni Volpe<sup>1,3\*</sup>, for the Alzheimer's Disease Neuroimaging Initiative

**1** UNAM—National Nanotechnology Research Center & Department of Physics, Bilkent University, Ankara, Turkey, **2** Department of Neurobiology, Care Sciences and Society, Karolinska Institutet, Stockholm, Sweden, **3** Department of Physics, Goteborg University, Goteborg, Sweden

\* [giovanni.volpe@physics.gu.se](mailto:giovanni.volpe@physics.gu.se)



**OPEN ACCESS**

**Citation:** Mijalkov M, Kakaei E, Pereira JB, Westman E, Volpe G, for the Alzheimer's Disease Neuroimaging Initiative (2017) BRAPH: A graph theory software for the analysis of brain connectivity. PLoS ONE 12(8): e0178798. <https://doi.org/10.1371/journal.pone.0178798>

**Editor:** Satoru Hayasaka, University of Texas at Austin, UNITED STATES

**Received:** February 8, 2017

**Accepted:** May 18, 2017

**Published:** August 1, 2017

**Copyright:** © 2017 Mijalkov et al. This is an open access article distributed under the terms of the [Creative Commons Attribution License](https://creativecommons.org/licenses/by/4.0/), which permits unrestricted use, distribution, and reproduction in any medium, provided the original author and source are credited.

**Data Availability Statement:** MRI Data used in preparation of this article were obtained from the Alzheimer's Disease Neuroimaging Initiative (ADNI) database ([adni.loni.usc.edu](http://adni.loni.usc.edu)) and the Parkinson's Progression Markers Initiative (PPMI) (<http://www.ppmi-info.org/>). Since we do not own the ADNI or PPMI data used in this study, we do not have permission to redistribute these data ourselves, as is stated in the data use agreements from ADNI ([http://adni.loni.usc.edu/wp-content/uploads/how\\_to\\_apply/ADNI\\_Data\\_Use\\_Agreement.pdf](http://adni.loni.usc.edu/wp-content/uploads/how_to_apply/ADNI_Data_Use_Agreement.pdf)) and PPMI (<https://ida.loni.usc.edu/collaboration/>)

## Abstract

The brain is a large-scale complex network whose workings rely on the interaction between its various regions. In the past few years, the organization of the human brain network has been studied extensively using concepts from graph theory, where the brain is represented as a set of nodes connected by edges. This representation of the brain as a connectome can be used to assess important measures that reflect its topological architecture. We have developed a freeware MatLab-based software (BRAPH—BRain Analysis using graPH theory) for connectivity analysis of brain networks derived from structural magnetic resonance imaging (MRI), functional MRI (fMRI), positron emission tomography (PET) and electroencephalogram (EEG) data. BRAPH allows building connectivity matrices, calculating global and local network measures, performing non-parametric permutations for group comparisons, assessing the modules in the network, and comparing the results to random networks. By contrast to other toolboxes, it allows performing longitudinal comparisons of the same patients across different points in time. Furthermore, even though a user-friendly interface is provided, the architecture of the program is modular (object-oriented) so that it can be easily expanded and customized. To demonstrate the abilities of BRAPH, we performed structural and functional graph theory analyses in two separate studies. In the first study, using MRI data, we assessed the differences in global and nodal network topology in healthy controls, patients with amnesic mild cognitive impairment, and patients with Alzheimer's disease. In the second study, using resting-state fMRI data, we compared healthy controls and Parkinson's patients with mild cognitive impairment.

## Introduction

Graph theory studies the properties and behavior of networks, which are systems consisting of a set of elements (nodes) linked by connections or interactions (edges). Many systems found in Nature, ranging from social interactions to metabolic networks and transportation systems, can be modeled within this framework, pointing to a set of underlying similarities among these very diverse systems. The human brain can also be modeled as a network (the *human connectome*) [1], where brain regions are the *nodes* and the connections between them are the

[access/appLicense.jsp](http://access/appLicense.jsp)). However, the data can be obtained through procedures and under conditions as described on the ADNI (<http://adni.loni.usc.edu/data-samples/access-data/>) and PPMI (<http://www.ppmi-info.org/access-data-specimens/download-data/>) websites.

**Funding:** Data used in the preparation of this article were obtained from the Alzheimer's Disease Neuroimaging Initiative (ADNI) and the Parkinson's Progression Markers Initiative (PPMI). Data collection and sharing of ADNI was funded by the National Institutes of Health Grant U01 AG024904 and Department of Defense award number W81XWH-12-2-0012. ADNI is funded by the National Institute on Aging, the National Institute of Biomedical Imaging and Bioengineering, and through generous contributions from the following: Alzheimer's Association; Alzheimer's Drug Discovery Foundation; BioClinica, Inc.; Biogen Idec Inc.; Bristol-Myers Squibb Company; Eisai Inc.; Elan Pharmaceuticals, Inc.; Eli Lilly and Company; F. Hoffmann-La Roche Ltd and its affiliated company Genentech, Inc.; GE Healthcare; Innogenetics, N.V.; IXICO Ltd.; Janssen Alzheimer Immunotherapy Research & Development, LLC.; Johnson & Johnson Pharmaceutical Research & Development LLC.; Medpace, Inc.; Merck & Co., Inc.; Meso Scale Diagnostics, LLC.; NeuroRx Research; Novartis Pharmaceuticals Corporation; Pfizer Inc.; Piramal Imaging; Servier; Synarc Inc.; and Takeda Pharmaceutical Company. The Canadian Institutes of Health Research is providing funds to support ADNI clinical sites in Canada. Private sector contributions are facilitated by the Foundation for the National Institutes of Health ([www.fnih.org](http://www.fnih.org)). The grantee organization is the Northern California Institute for Research and Education, and the study is coordinated by the Alzheimer's Disease Cooperative Study at the University of California, San Diego. ADNI data are disseminated by the Laboratory for Neuro Imaging at the University of California, Los Angeles. PPMI—a public-private partnership—is funded by the Michael J. Fox Foundation for Parkinson's Research and funding partners, including Abbott, Avid Radiopharmaceuticals, Biogen Idec, Bristol-Myers Squibb, Covance, Elan, GE Healthcare, Genentech, GSK-GlaxoSmithKline, Lilly, Merck, MSD-Meso Scale Discovery, Pfizer, Roche, UCB ([www.ppmi-info.org/fundingpartners](http://www.ppmi-info.org/fundingpartners)). For up-to-date information on the PPMI database visit [www.ppmi-info.org](http://www.ppmi-info.org). We would also like to thank the Swedish Foundation for Strategic Research (SSF) grant number 4-3193/2014, the Strategic Research Programme in Neuroscience at Karolinska Institutet (StratNeuro), Hjärtfonden grant number FO2015-0173, Vetenskapsrådet grant number

*edges*. The human brain is thus an ideal candidate for graph theoretical analysis. The nodes can be defined as the brain regions underlying electrodes or using an anatomical, functional or histological parcellation scheme. The edges are obtained as measures of association between the brain regions, such as connection probabilities (diffusion tensor imaging, DTI), inter-regional correlations in cortical thickness (magnetic resonance imaging, MRI) and electrophysiological signals (electroencephalography, EEG; magnetoencephalography, MEG) or statistical dependencies in time series (functional MRI, fMRI) and blood flow (arterial spin labeling, ASL).

After compiling all pairwise associations between the nodes into a *connectivity matrix* (or *brain graph*), several network properties can be calculated in order to characterize the global and local organization of the connectome. For instance, the *small-worldness* can be used to assess the balance between short-distance and long-distance connectivity [2], while the *modularity* defines how well the network can be divided into *subnetworks* (or *modules*) [3,4], which generally correspond to well-known brain systems such as the default-mode or fronto-parietal networks [5,6]. These network properties and many others can be used to reveal fundamental aspects of normal brain organization and highlight important aspects of underlying brain pathology in diseases such as Alzheimer's disease (AD) [7], Parkinson's disease [8], epilepsy [9,10,11], schizophrenia [12,13], multiple sclerosis [14] and autism [15].

Several toolboxes have been developed to study brain connectivity, including the Brain Connectivity Toolbox [16], eConnectome [17], GAT [18], CONN [19], BrainNet Viewer [20], GraphVar [21] and GRETNA [22]. In addition, with the emergence of time-varying brain networks as a powerful method to characterize mental illnesses [23,24], several toolboxes that allow the calculation of dynamic functional connectivity measures have also been developed [25,26]. While all of them made important contributions by providing new options to build, characterize and visualize brain network topology, they require some programming experience, or deal only with some aspects of the analysis, or are coded in such a way that their adaptation is hard to achieve. Hence, a reliable, streamlined, user-friendly, fast, and scalable software that deals with all aspects of network organization is still lacking.

In this article, we present BRAPH—BRain Analysis using graph theory (<http://www.brAPH.org/>), a software package to perform graph theory analysis of the brain connectome. BRAPH is the first object-oriented open-source software written in MatLab for graph theoretical analysis with a graphical user interface (GUI). In contrast to previous toolboxes, BRAPH takes advantage of the object-oriented programming paradigm to provide a clear modular structure that makes it easy to maintain and modify existing code, since new objects can be added without the need for an extensive knowledge of the underlying implementation. From the clinical point of view, BRAPH presents the following strengths: (a) it allows comparing the regional mean values between groups using permutation testing to get a first impression of the data and group differences before the actual network analysis; (b) it visualizes individual connectivity matrices and individual network measures, which is crucial to detect potential outliers, a major confound in neuroimaging studies; (c) it carries out longitudinal graph theory analyses that provide an important insight into topological network changes over time; (d) it assesses modular structure using different algorithms and allows performing subnetwork analyses within the defined modules, which is important for studies testing hypotheses within a particular structural or functional brain network; (e) it provides utilities for multi-modal graph theory analysis by integrating information from different neuroimaging modalities, which is arguably the next challenge in imaging connectomics; for example, the user can compare structural (MRI) and functional (fMRI) data in BRAPH by defining the networks derived from both modalities with the same atlas. From the user point of view, BRAPH is the only fully vertically integrated software that allows carrying out all the steps of a graph theory analysis, from importing the neuroimaging data to saving the final results and the analysis parameters in a

2016-02282 2017-2020, and Birgitta och Sten Westerberg for additional financial support. We would also like to thank TÜBİTAK 2215 Graduate Programme for their support.

**Competing interests:** While commercial funding was obtained by the ADNI and PPMI initiatives, the authors have not directly received commercial funding. This does not alter our adherence to PLOS ONE policies on sharing data and materials.

single file. Importantly, this is not only practical but also increases the reliability and reproducibility of the results, which is an increasingly important issue within the research community. In addition, BRAPH offers a comprehensive manual, continuous release of new utilities, and a support forum, all of which can be accessed at <http://www.brAPH.org/>. Finally, BRAPH offers online videos that provide a step-by-step guide on how to perform graph theory analyses, allowing the users a simple and quick start for their brain connectivity studies.

Below we describe in detail the different options that BRAPH offers for graph theory analyses when it comes to building connectivity matrices, applying threshold strategies, performing weighted or binary network analyses and computing random networks. Our software has already been successfully applied in previous graph theory studies [27,28] but to further demonstrate its abilities, in this article we assess network topology on structural MRI data from patients with amnesic mild cognitive impairment (MCI) and AD, and on fMRI data from PD patients with MCI.

## Materials and methods

### Overview of BRAPH

BRAPH is a complete software package that allows carrying out all the steps of a graph theoretical analysis, visualize the results and generate high-quality publication-ready images. It can obtain undirected binary and weighted brain connectivity graphs starting from data acquired using various neuroimaging modalities, including MRI, fMRI, EEG, and positron emission tomography (PET). BRAPH can also assess the modular structure of the brain graph, employing various algorithms and extracting modules for further analysis. To test for significant differences between groups, BRAPH carries out non-parametric permutation tests and allows correcting the results for multiple comparisons using false discovery rate (FDR) [29]. It also provides options to normalize the network measures by random graphs as well as to carry out longitudinal graph theory analyses, the statistical significance of which is reported by non-parametric permutation tests.

As shown in Fig 1, the software consists of three independent layers connected by software interfaces: Graph, Data Structures and Graphical User Interfaces (GUIs). The Graph package includes the fundamental functions to perform a graph theory analysis and calculating the global and nodal measures. The Data Structures package provides the core functionalities of the software and allows defining the brain atlas, the cohort of subjects, and the type of graph analysis; importantly, all these functionalities can be accessed by command-line and can therefore be scripted by advanced users. Finally, the GUIs package provides a streamlined way to carry out graph theory analyses based on a series of GUIs for users without a computational background: (a) the *GUI Brain Atlas* allows selecting and editing the brain atlas; (b) the *GUI Cohort* allows defining the cohort of subjects by uploading the relevant data; (c) the *GUI Graph Analysis* allows building the connectivity matrices by selecting the type of graph (*weighted, binary*, see also Fig 2) and thresholding method (*threshold, density*) as well as calculating topological measures and visualizing the results. For the *GUI Cohort* and *GUI Graph Analysis*, four options can be selected (MRI, fMRI, PET, EEG) depending on the nature of the analysis. Fig 3 shows an overview of these different steps. Thanks to this three-layered structure, BRAPH can be easily expanded and customized to address any needs, e.g., by implementing new graph measures or new approaches for building brain graphs.

### Defining the nodes

The first step of a graph theory analysis consists of defining the nodes, which generally correspond to the regions included in a brain atlas. This atlas should contain the names and labels

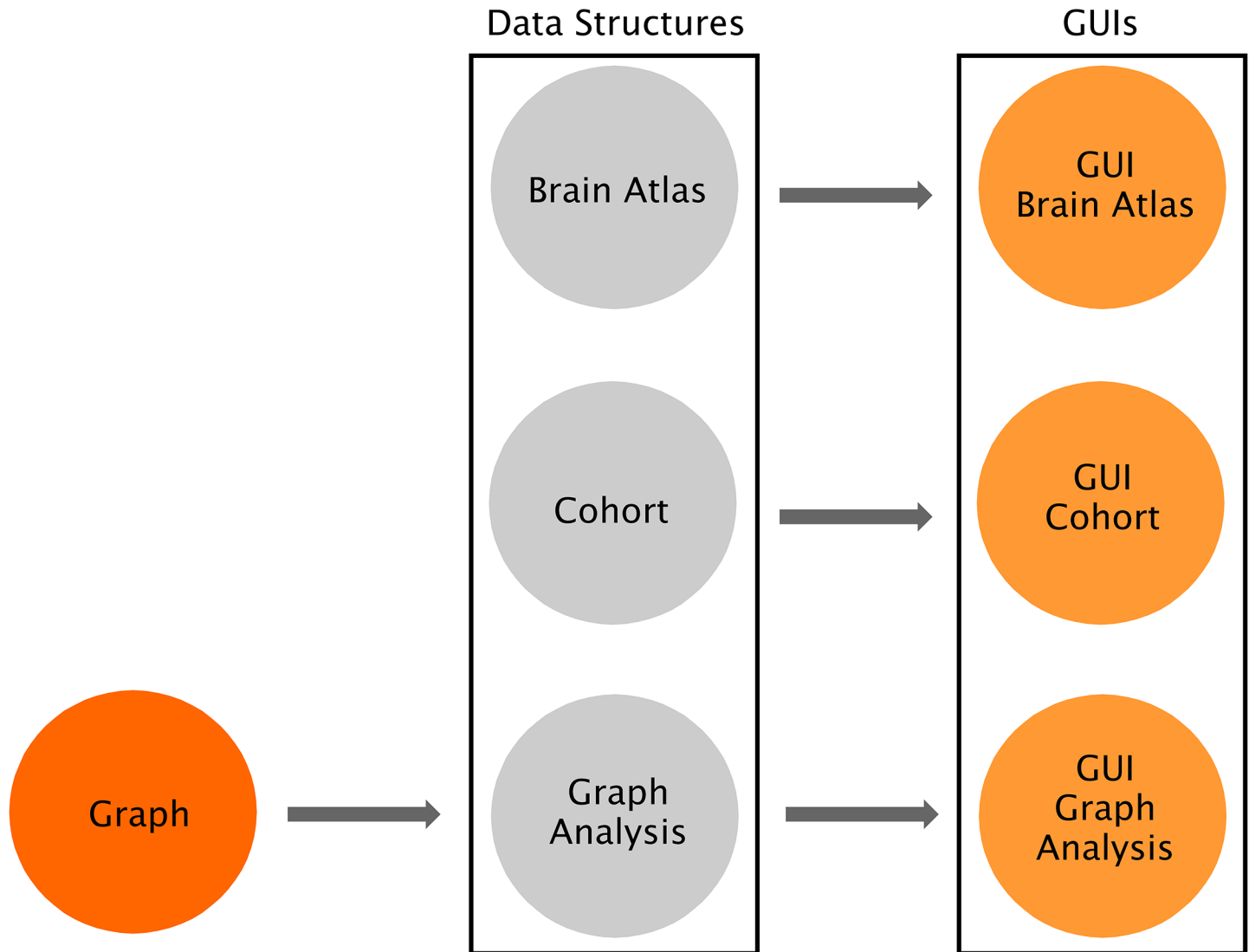


**Fig 1. Overview of BRAPH software architecture.** BRAPH consists of three layers, from left to right: *Graph*, *Data Structures* and *Graphical User Interfaces* (GUIs). These layers are connected by unidirectional software interfaces (arrows). *Graph* contains the functions to perform graph analyses. In *Data Structures*, *Brain Atlas* allows defining the nodes of the network, *Cohort* allows defining the subjects to be studied and dividing them into groups, and *Graph Analysis* permits building the connectivity matrices and calculating network measures; each of these is implemented in an object, whose functionalities can be called by command line. For each of these objects, a GUI is provided (i.e. *GUI Brain Atlas*, *GUI Cohort* and *GUI Graph Analysis*). Thanks to this architecture BRAPH can be very easily maintained, expanded and customized.

<https://doi.org/10.1371/journal.pone.0178798.g001>

of the brain regions as well as their spatial coordinates ( $x, y, z$ ) in order to project them onto a 3D surface and create a visual representation of the brain graph. In the case of the analysis of structural networks (e.g. obtained from structural MRI data or  $T_1$ -weighted images), the nodes are usually defined using an anatomical parcellation scheme that divides the brain into regions using the brain sulci and gyri as anatomical landmarks. Examples of anatomical atlases are the automated anatomical labeling (AAL) [30], Desikan [31] or Destrieux [32] atlases. BRAPH already provides these atlases ready for upload on the *GUI Brain Atlas* interface. In the case of the analysis of functional networks (e.g. obtained from fMRI data), the atlas may be defined using an anatomical parcellation scheme, a meta-analysis, or a clustering-based method of spatially coherent and homogenous regions. Examples of functional atlases are the Dosenbach

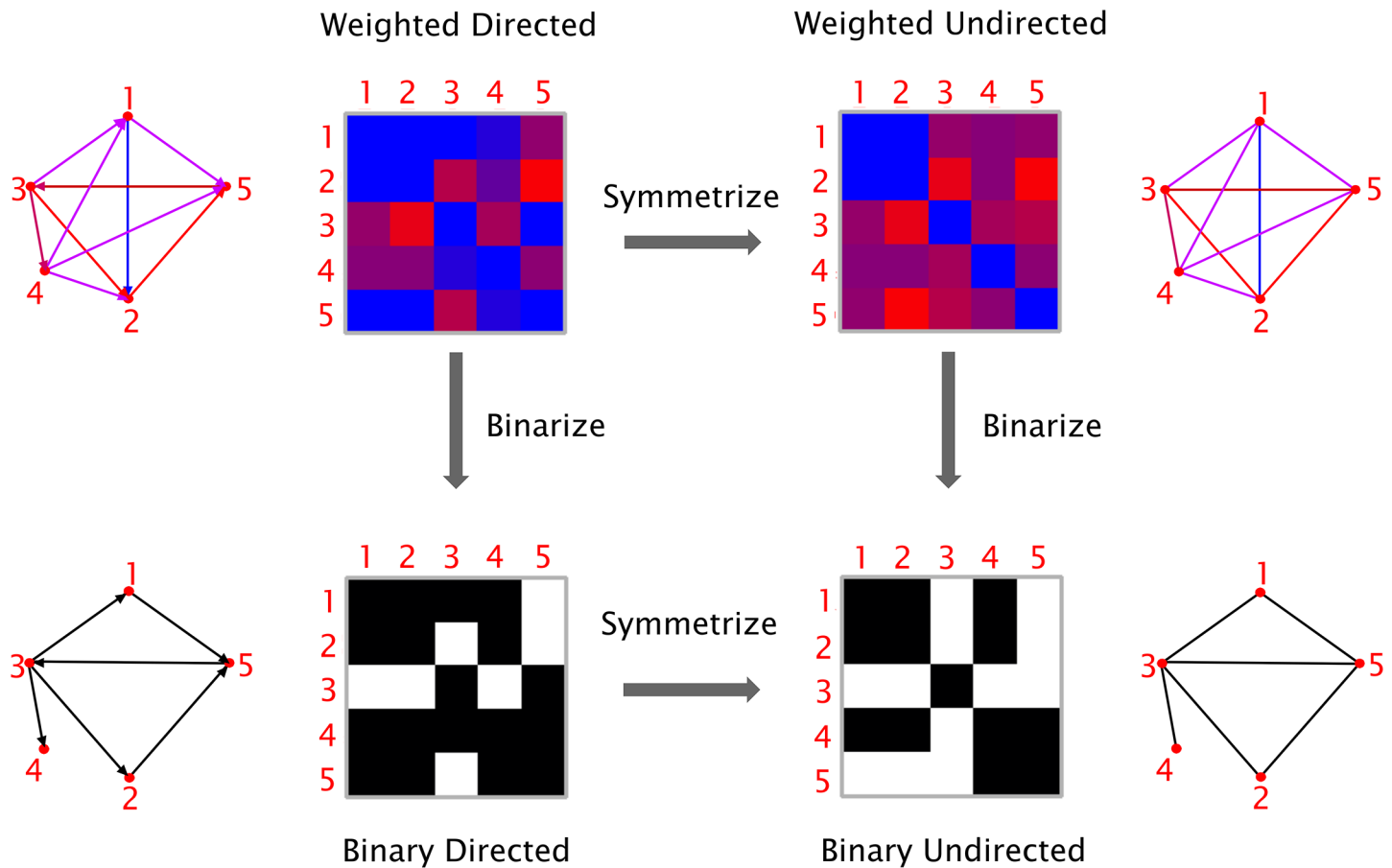


**Fig 2. Types of graphs.** Graphs can be classified based on their edge weights (*weighted* or *binary*) and directionality (*directed* or *undirected*). It is possible to transform a directed graph into an undirected one by symmetrization (i.e. by removing the information about the edge directions), and a weighted graph into a binary one by thresholding (i.e. by assigning a value of 1 to the edges above a given threshold and 0 to those below threshold).

<https://doi.org/10.1371/journal.pone.0178798.g002>

[33], the Power [34] and the Craddock [35] atlases, all of which are also provided by BRAPH. The user may also upload a different atlas from an external file (in.xml,.txt or.xls format) or create an entirely new one in the GUI. The resulting atlas can be saved as a.atlas file (see manual and website for an example of a.atlas file).

After the atlas has been created or uploaded into the software, the user should then upload the subject data into the *GUI Cohort* interface. This data may consist, for example, of cortical thickness, surface area or volume measures in structural MRI; regional time-series in resting-state fMRI; glucose metabolism or blood flow in PET and ASL; and electrophysiological signals in EEG or MEG. These regional values can be obtained using the Statistical Parametric Mapping (SPM; <http://www.fil.ion.ucl.ac.uk/spm/>), FMRI Software Library (FSL; <https://fsl.fmrib.ox.ac.uk/fsl/fslwiki>), FreeSurfer (<https://surfer.nmr.mgh.harvard.edu/>) or any other image pre-processing software. In addition, they may be corrected for the effects of nuisance variables such as age, gender or scanner site by means, for example, of linear regression (in this case the residual values should substitute the raw values in the network analysis) [36].

### Defining the edges

Once the nodes of the network have been defined, the edges representing the relationship between them need to be computed. In BRAPH, the edges are calculated in *GUI Graph*



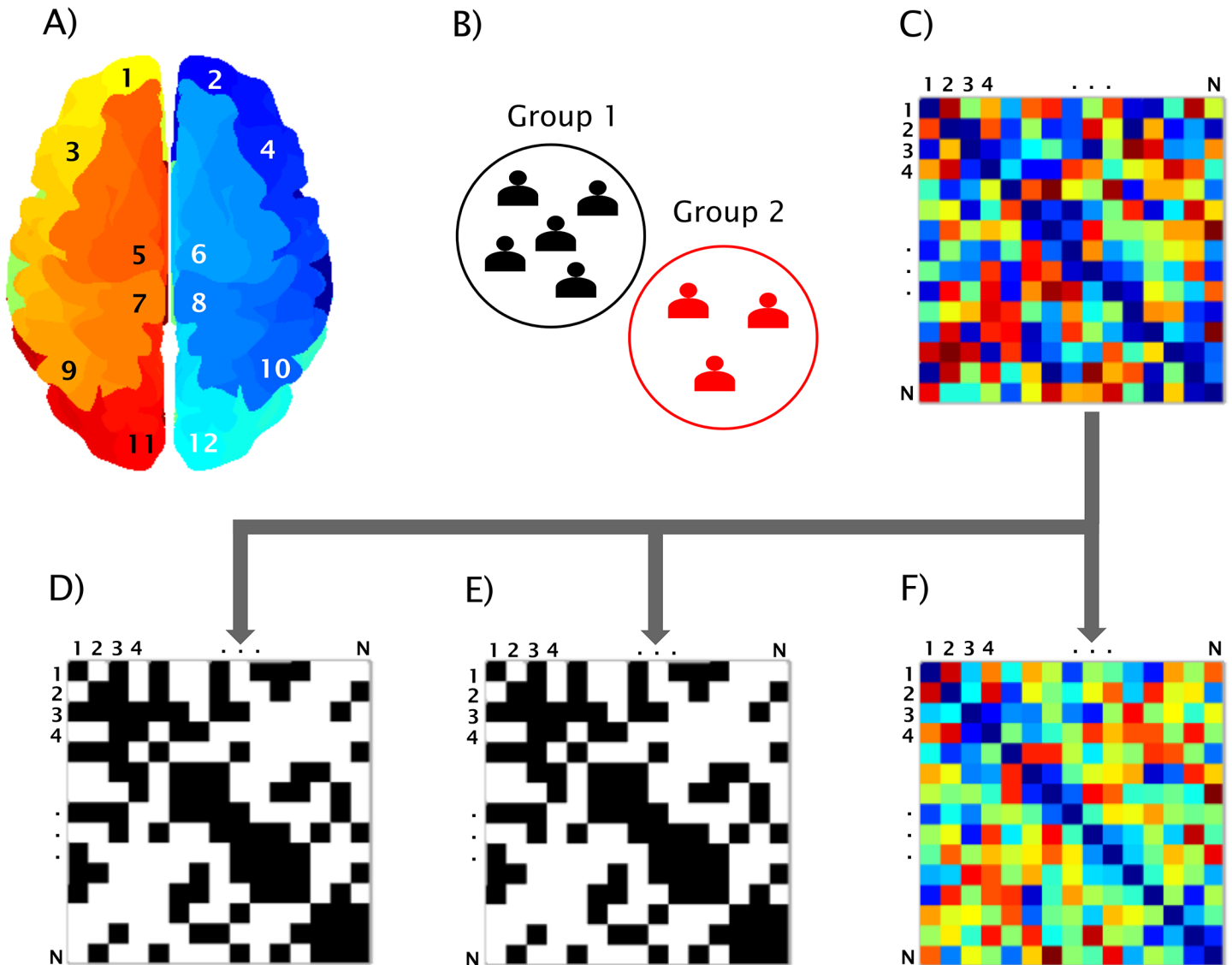


**Fig 3. BRAPH workflow.** Workflow for a graph theory analysis in BRAPH and relative graphical user interfaces (GUIs). A) The brain regions are defined in the *GUI Brain Atlas*. B) The data of the subjects are imported in the *GUI Cohort* and the user can define groups and edit their age, gender and other relevant data. C) The connectivity matrix is calculated in the *GUI Graph Analysis* after selecting the parameters defining the type of correlation, how to deal with negative correlation coefficients, and which type of graph to analyze: D) binary undirected graphs at a fixed density (*GUI Graph Analysis BUD*); E) binary undirected graphs at a fixed threshold (*GUI Graph Analysis BUT*); F) weighted undirected graphs (*GUI Graph Analysis WU*).

<https://doi.org/10.1371/journal.pone.0178798.g003>

*Analysis* as the statistical correlation between the values of all pairs of brain regions for an individual or for a group of subjects, depending on the neuroimaging technique. Different types of parametric and non-parametric correlations may be selected for this purpose: Pearson, Spearman, Kendall rank correlation coefficients, or (Pearson or Spearman) partial correlation coefficients. Note that all self-connections are eliminated from the analysis by setting the diagonal entries in the connectivity matrix to zero. In addition, the user can also choose whether to retain the negative correlation coefficients, substitute them with their absolute value, replace them by zero, or transform the values using an s-transform.

## Network construction

To minimize the computation time, the graph measures can be calculated using optimized algorithms based on linear algebra. Therefore, a graph is more conveniently represented as a connectivity matrix, where the rows/columns denote the nodes and the matrix elements represent the edges between the nodes. Each row of the connectivity matrix represents the edges that are going out from a node; for example, row  $j$  represents the edges that are going out from node  $j$ . Each column of the matrix represents the nodes that arrive to a node; for example, column  $k$  represents the edges that are arriving to node  $k$ . Thus, the element  $(j, k)$  represents the edge that goes from node  $j$  to node  $k$ . The specific order of the nodes in the matrix does not affect the calculation of the graph theory measures, but only the graphical representation of the connectivity matrix. As illustrated in Fig 2, based on the nature of the edges' weight and directionality, four types of graphs can be defined. *Weighted directed* (WD) graphs have edges associated with a real number, indicating the strength of the connection, and are directed (i.e., node  $j$  can be connected to node  $k$  without node  $k$  being connected to node  $j$ ). The edges in the *weighted undirected* (WU) graphs are associated with a real number indicating the strength of the connection and are undirected (i.e., if node  $j$  is connected to node  $k$ , then node  $k$  is also connected to node  $j$ ), resulting in a symmetric connectivity matrix. *Binary directed* (BD) graphs have directed edges, which can either be 0 or 1, indicating the absence or presence of a connection. The edges in a *binary undirected* (BU) network can also be either 0 or 1 and they have no directionality. In order to transform a directed graph into an undirected graph, the connectivity matrix needs to be symmetrized. In BRAPH, the connectivity matrix can be symmetrized via command line by: (a) taking the sum between the matrix itself and its transpose; (b) taking the difference between the previous two; (c) comparing the matrix to its transpose and selecting either the smaller or the larger value for each entry. We remark that, even though the directed measures are not currently used in the analyses performed by BRAPH, they are already available in the *Graph* package and ready to be used in future versions of the software.

To transform a weighted graph into a binary one, BRAPH assigns a value of 1 to the edges above a given threshold and 0 to those below it. There are two ways of applying a threshold: (a) by selecting a correlation coefficient as the cut-off value below which all connections are excluded from the analysis (*binary undirected threshold* (BUT) interfaces); or (b) by fixing the fraction of edges (i.e., a specific density) that will be connected (*binary undirected density* (BUD) interfaces). The choice between these two options becomes significant when comparing different groups of subjects, as it may lead to different results; currently the density approach is more often employed in the literature, because it permits analyzing differences in network architecture while controlling for the different number of edges across individuals or groups. Additionally, BRAPH can be straightforwardly extended to include any alternative approach to determine the threshold, such as using a threshold-dependent cost function [37], maintaining the degree for each graph [38], keeping the ratio of strongest edges fixed [39], or using a heuristic approach based on the Dijkstra's algorithm [40]; all these approaches can be implemented by creating new objects analogous to *MRIGraphAnalysisBUT* or *MRIGraphAnalysisBUD*, and adapting the already existing methods in BRAPH.

For MRI or static PET data, a single connectivity matrix is calculated for each group of subjects; therefore, the graph theory measures reflect the group's properties. For fMRI data and other neuroimaging sequences that provide a measure of brain function over time, an individual connectivity matrix is calculated for each subject; therefore, the graph theory measures reflect the characteristics of each subject, which can then be averaged within a particular group.

## Network analysis

BRAPH allows calculating both global and nodal network measures, on weighted or binary networks, using different thresholds or densities. To test for significant differences between groups (cross-sectional analysis) or two different points across time (longitudinal analysis), BRAPH performs non-parametric permutation tests, reporting one-tailed and two-tailed p-values based on 95% confidence intervals. The tests are performed by first randomly permuting the subjects from both groups and then calculating the differences in the graph measures between the new randomized groups. By repeating this procedure multiple (typically 1000 or 10000) times, a distribution of between-group differences is obtained. The p-values are then calculated as the fraction of the difference distribution values that exceeded the difference value between the actual groups. The same procedure is employed for the analysis of the longitudinal data with the difference that only the data corresponding to the same subject at different time points are permuted in order to prevent a group from containing the subject's data from two data points.

The network measures can also be compared with the corresponding measures calculated on random graphs with the same degree or weight distribution. These can be used, for example, to normalize weighted network measures. The needed random graphs are generated using the algorithms provided in the Brain Connectivity Toolbox [16].

Regarding nodal network measures, the permutation tests are carried out for each brain region, assessing simultaneously multiple null hypotheses, which consequently increases the risk of finding false positives. BRAPH deals with this issue by providing the adjusted p-values that should be considered to correct the results for multiple comparisons with false discovery rate (FDR) using the Benjamini-Hochberg procedure [29].

## Graph theory measures

BRAPH can calculate several graph theory measures that assess the topology of the whole brain network as well as of its regions. Here, we explain briefly some of the most relevant ones; for a complete list with formulas and details, please refer to the BRAPH manual and website. The code we used to calculate the graph measures was adapted from the Brain Connectivity Toolbox (<http://www.brain-connectivity-toolbox.net/>) [16], which is regarded as the most important reference in the field since it provided the seminal groundwork for the use of graph theory by neuroimaging researchers.

The simplest, yet most fundamental, measure that can be assessed in a graph is the *degree*, which is the number of connections a node has with the rest of the network. The degree distribution in the brain follows an exponentially bound power law [41] meaning that similarly connected areas tend to communicate with each other [42]. In weighted graphs, BRAPH allows the user to calculate the nodal *strength* as well as nodal degree: the nodal strength is given by the sum of the weights of all connections linked to the node; and the nodal degree is the total number of the node's connections (thus assuming each edge has weight 1, making it analogous to the case of binary graphs).

Another important measure is the *shortest path length*, which is the shortest distance between two nodes. In a binary graph, distance is measured as the minimum number of edges that need to be crossed to go from one node to the other. In a weighted graph, the length of an edge is a function of its weight; typically, the edge length is inversely proportional to the edge weight because a high weight implies a stronger connection. The average of the shortest path lengths between one node and all other nodes is the *characteristic path length* [2]. One can also define two related measures of centrality: the *closeness centrality*, which is the inverse of the shortest path length, and the *betweenness centrality*, which is the fraction of all shortest paths

in the network that pass through a given node [16]. These and other measures can be used to assess whether a node is a brain hub [43], regulating most of the information flow within the network.

The closer the nodes are to each other, the shorter is the path length and the more efficient is the transfer of information between them. Therefore, one can define the *global efficiency* of a node as the inverse of the shortest path from that node to any other node in the network [44]. To assess the communication efficiency between a node and its immediate neighbors, the *local efficiency* can be calculated. Both global and local efficiency measures can be averaged over all nodes to describe global properties of the brain network [44].

The *clustering coefficient* is a measure that assesses the presence of cliques or clusters in a graph [2]. For each node, this can be calculated as the fraction of the node's neighbors that are also neighbors of each other. For the whole network, the nodal clustering coefficients of all nodes can be averaged into the mean clustering coefficient. A closely related measure to the clustering is the *transitivity*, which is defined as the ratio of paths that transverse two edges to the number of triangles. If a node is connected to another node, which in turn is connected to a third one, the transitivity reflects the probability that the first node is connected to the third.

The *small-worldness* is given by the ratio between the characteristic path length and mean clustering coefficient (normalized by the corresponding values calculated on random graphs) [2]; this is an important organizational property that describes an optimal network architecture. Compared to a random graph, a small-world network is characterized by similarly short paths but a significantly higher clustering coefficient.

A network can also be divided into separate communities corresponding to anatomical proximity or to a specific function shared by a group of nodes. The extent to which a network can be divided into these communities or modules can be calculated using the *modularity*, which maximizes the number of edges within communities and minimizes the number of edges between different communities [45]. The *within-module z-score* quantifies how well a node is connected with other nodes from the same module, while the *participation coefficient* assesses if a node has many connections with nodes from different modules. If a node has a high within-module degree, it is considered a provincial hub; if it has a high participation coefficient, it is considered a connector hub.

## Subjects

To demonstrate the abilities of BRAPH, we performed structural and functional graph theory analyses in two separate studies. In the first study, we assessed the differences in global and nodal network topology in healthy controls, patients with amnesic MCI, and patients with AD (see Table 1) from the Alzheimer's Disease Neuroimaging Initiative (ADNI) database ([adni.loni.usc.edu](http://adni.loni.usc.edu)). The ADNI was launched in 2003 as a public-private partnership, led by Principal Investigator Michael W. Weiner, MD. The primary goal of ADNI has been to test whether serial MRI, PET, other biological markers, and clinical and neuropsychological assessment can be combined to measure the progression of MCI and early AD. All participants were scanned on a 1.5 Tesla MRI system using a sagittal 3D T<sub>1</sub>-weighted MPRAGE sequence: repetition time (TR) = 9–13 ms; echo time (TE) = 3.0–4.1 ms; inversion time (IT) = 1000 ms; flip angle (FA) = 8°; voxel size = 1.1×1.1×1.2 mm<sup>3</sup>.

In the second study, we carried out a graph theory analysis on the resting-state fMRI data of healthy controls, PD patients that were cognitively normal and PD patients with MCI (see Table 2) from the Parkinson's Progression Markers Initiative (PPMI) (2011) [46] ([www.ppmi-info.org/data](http://www.ppmi-info.org/data); accessed in November, 2015), an international, multicenter study launched in 2010 to identify PD progression biomarkers. PD patients were classified as having MCI

**Table 1. Characteristics of the structural MRI sample.**

	CTR (n = 210)	MCI (n = 377)	AD (n = 181)	F or $\chi^2$ (p value)
Age (y)	76.1(5.0)	74.5(7.5)	75.6 (7.0)	0.017
Sex (M/F)	110/100	243/134	97/84	0.005
Education (y)	16.0(2.9)	15.7(3.0)	14.8(3.2)	<0.001
MMSE	29.1(0.9)	27.0(1.8)	23.2(2.0)	<0.001

Means are followed by standard deviations. Differences in age, years of education, and MMSE scores were assessed using an analysis of variance (ANOVA). Differences in gender were assessed using a  $\chi^2$  test. CTR, controls; MCI, mild cognitive impairment; AD, Alzheimer’s disease; MMSE, mini-mental state examination.

<https://doi.org/10.1371/journal.pone.0178798.t001>

(PD-MCI) if they scored 1.5 standard deviations below the scaled mean scores on any two cognitive tests, following previously published procedures for PD-MCI diagnosis in the PPMI cohort [47]. Patients that did not fulfill criteria for MCI were classified as cognitively normal (PD-CN). All PD patients and controls were scanned on a 3 Tesla Siemens scanner (Erlangen, Germany). Resting-state functional images were acquired using an echo-planar imaging sequence (repetition time = 2400 ms; echo time = 25 ms; flip angle = 80°; matrix = 68×68; voxel size = 3.25×3.25×3.25 mm<sup>3</sup>). The scan lasted 8 minutes and 29 seconds and included 210 volumes.

Each participating site in ADNI and PPMI received approval from an ethical standards committee before study initiation and obtained written informed consent from all participants.

### Network construction and analysis

To assess structural network topology in controls, amnesic MCI patients, and AD patients from ADNI, the T<sub>1</sub>-weighted images of these subjects were preprocessed using FreeSurfer (version 5.3), as published elsewhere [28]. The cortical thickness and subcortical volumes of 82 regions were extracted and included as nodes in the network analysis. The edges between these regions were computed as Pearson correlations, setting the negative correlations to zero, and the network analyses were carried out on the binary undirected graphs, while controlling for the number of connections, across a range of densities from 5% to 25%, in steps of 0.5%.

To assess functional network topology in PD-CN patients, PD-MCI patients and a group of elderly controls from PPMI, fMRI images were preprocessed using SPM8 (<http://www.fil.ion>.

**Table 2. Characteristics of the fMRI sample.**

	CTR (n = 15)	PD-CN (n = 69)	PD-MCI (n = 15)	CTR vs PD-CN (p value)	CTR vs PD-MCI (p value)	PD-CN vs PD-MCI (p value)
Age (y)	66.4(9.1)	61.0(10.4)	63.5(8.2)	0.066	0.372	0.378
Sex (M/F)	13/2	46/23	11/4	0.125	0.361	0.616
Education (y)	16.5(2.3)	15.3(2.9)	14.2(3.1)	0.112	0.024	0.204
UPDRS-III	-	18.2(9.1)	21.8(8.9)	-	-	0.161
HY stage	-	1.7(0.5)	1.8(0.4)	-	-	0.297
MoCA	27.9(1.6)	27.6(1.9)	24.0(3.7)	0.615	0.001	<0.001
Disease duration (y)	-	1.2(0.9)	2.4(1.5)	-	-	<0.001

Means are followed by standard deviations. Differences in age, years of education, and MoCA scores were assessed using Student’s T test. Differences in gender were assessed using a  $\chi^2$  test. CTR, controls; PD-CN, Parkinson’s disease cognitively normal; PD-MCI, Parkinson’s disease with mild cognitive impairment; UPDRS-III, Unified Parkinson’s disease rating scale–Part III; HY stage, Hoehn and Yahr stage; MoCA, Montreal cognitive assessment scale.

<https://doi.org/10.1371/journal.pone.0178798.t002>

[ucl.ac.uk/spm](http://ucl.ac.uk/spm)) using the following steps: removal of first five volumes, slice-timing correction, realignment, normalization to the Montreal Neurological Institute (MNI) template (voxel size  $3 \times 3 \times 3 \text{ mm}^3$ ), temporal filtering (0.01–0.08 Hz), regression of white matter, cerebrospinal fluid signals and six head motion parameters. The regional time-series of the 200 brain regions included in the Craddock atlas [35] were extracted from each subject. To compute the relationship between these regions, we used Pearson correlations and performed the network analyses on the weighted undirected graphs.

In both studies, non-parametric permutation tests with 10000 permutations were carried out to assess differences between groups, which were considered significant for a two-tailed test of the null hypothesis at  $p < 0.05$ . In addition, to adjust the nodal network results for multiple comparisons, an FDR procedure was applied to control for the number of regions that were tested at  $q < 0.05$ .

## Results

### Structural network topology in amnesic MCI and AD

The structural correlation matrices and brain graphs of patients and controls can be found in Fig 4. All groups showed strong correlations between bilaterally homologous regions.

Regarding global network topology (Fig 5), we found increases in the characteristic path length and local efficiency in MCI and AD patients compared to controls at several network densities. The transitivity and modularity showed the most widespread topological changes: the transitivity was decreased and the modularity was increased in MCI and AD patients across almost all network densities compared to controls. Compared to MCI, AD patients showed increases in the characteristic path length at a few network densities and widespread changes in the transitivity and modularity.

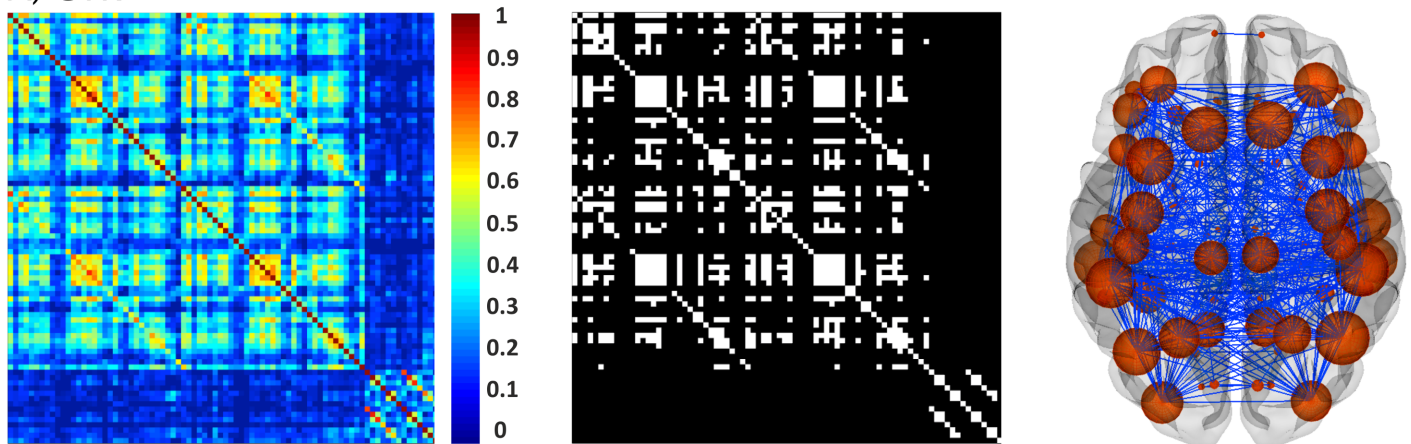
Regarding regional network topology (Fig 6), the nodal degree showed significant increases in the left medial orbitofrontal, right insula, bilateral rostral anterior cingulate and posterior cingulate gyri in addition to decreases in the left middle temporal, right precentral and right inferior parietal gyri in AD patients compared to controls. When compared to MCI, AD patients also presented a higher nodal degree in the left rostral anterior cingulate and isthmus cingulate gyri.

We also compared the nodal local efficiency between groups. This measure showed significant increases in the left transverse temporal gyrus in MCI patients compared to controls. AD patients showed increases in the local efficiency in the bilateral temporal pole and left entorhinal cortex as well as decreases in several regions from the frontal (bilateral superior frontal, left pars triangularis, bilateral pars opercularis, right postcentral gyri), temporal (bilateral inferior temporal gyri, amygdala, hippocampus) and parietal (left inferior parietal, right precuneus) lobes. When the two patient groups were compared to each other, AD patients showed efficiency increases in the right rostral anterior cingulate compared to the MCI group.

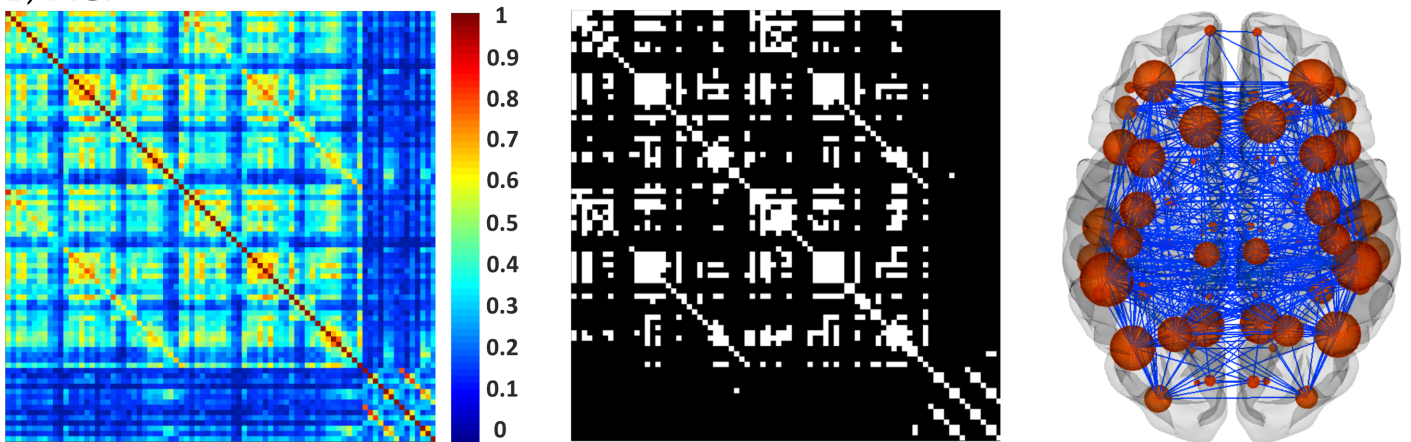
### Functional network topology in PD-MCI

The functional connectivity matrices of controls, PD-CN and PD-MCI patients can be found in Fig 7. The comparison of the weighted average degree showed that both PD-CN and PD-MCI patients presented a lower number of connections compared to controls (PD-MCI = 172.6; PD-CN = 175.2; controls = 183.7), which showed a trend towards significance in the comparison with PD-CN ( $p$ -value = 0.081) and was statistically significant in the comparison with PD-MCI ( $p$ -value = 0.027). Then, we performed a modularity analysis on the weighted graphs of each group to assess the presence of smaller communities of regions (modules). This analysis showed there were five modules in controls, PD-CN and PD-MCI patients, which

A) CTR



B) MCI



C) AD

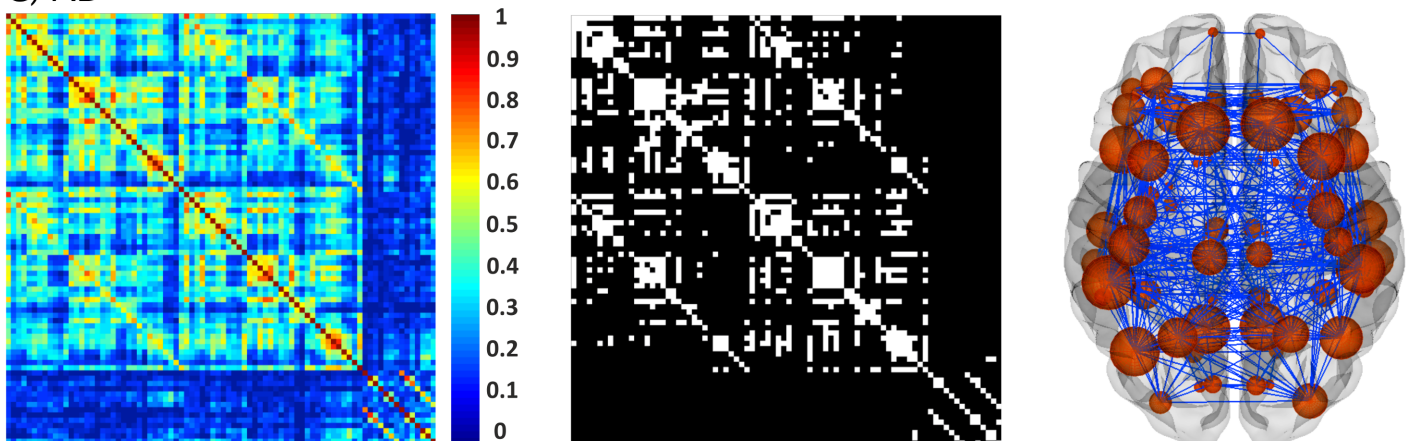


**Fig 4. Structural brain networks in controls, MCI patients, and AD patients.** From left to right: weighted correlation matrices of 82 regions, binary correlation matrices after fixing density at 15%, and corresponding brain graphs from A) controls (CTR), B) patients with amnesic mild cognitive impairment (MCI), and C) Alzheimer's disease (AD) patients.

<https://doi.org/10.1371/journal.pone.0178798.g004>

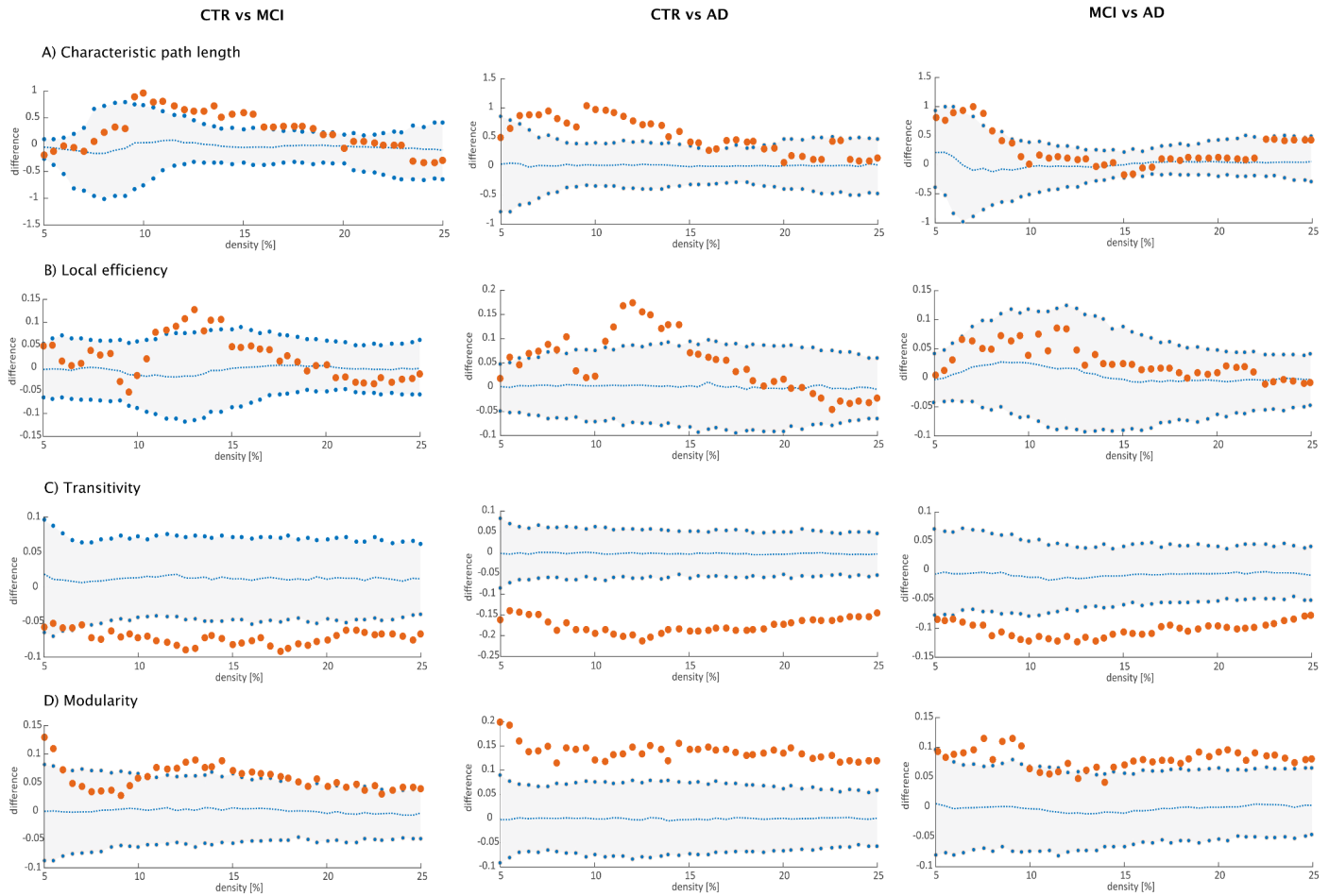


**Fig 5. Differences between groups in global structural topology.** Left: differences between controls (CTR) and Alzheimer’s disease (AD) patients; middle: differences between controls (CTR) and patients with mild cognitive impairment (MCI); right: differences between patients with mild cognitive impairment (MCI) and Alzheimer’s disease (AD) patients for A) characteristic path length, B) local efficiency, C) transitivity and D) modularity. The plots show the lower and upper bounds (blue circles) of the 95% Confidence Intervals (CI) (gray shade) as a function of density. The orange circles show the differences between groups and, when falling outside the CI, indicate that the difference was statistically significant at  $p < 0.05$ . The blue dots in the middle with values around zero indicate the mean values of the difference in global network measures between the randomized groups after permutation tests.

<https://doi.org/10.1371/journal.pone.0178798.g005>

were quite similar in the three groups. Module I included medial frontal areas, the posterior cingulate and bilateral angular gyri, resembling the default-mode network. Module II comprised temporal and cerebellar areas. Module III included several middle, inferior frontal and parietal regions, similarly to the fronto-parietal network usually found in resting-state studies [5,6]. Module IV consisted of most of the visual cortex similarly to the previously reported visual network. Finally, Module V included mainly temporal and inferior frontal areas as well as the insula.

When we assessed the average degree of each module, we observed that PD-CN patients had a lower number of connections compared to controls in Module II, which included temporal and cerebellar areas (PD-CN = 49.02; controls = 51.89;  $p$ -value = 0.020), and Module V consisting of insular, temporal and inferior frontal regions (PD-CN = 28.39; controls = 28.93;  $p$ -value = 0.040). The regions within each of these modules did not show significant differences between controls and PD-CN patients after applying FDR corrections.



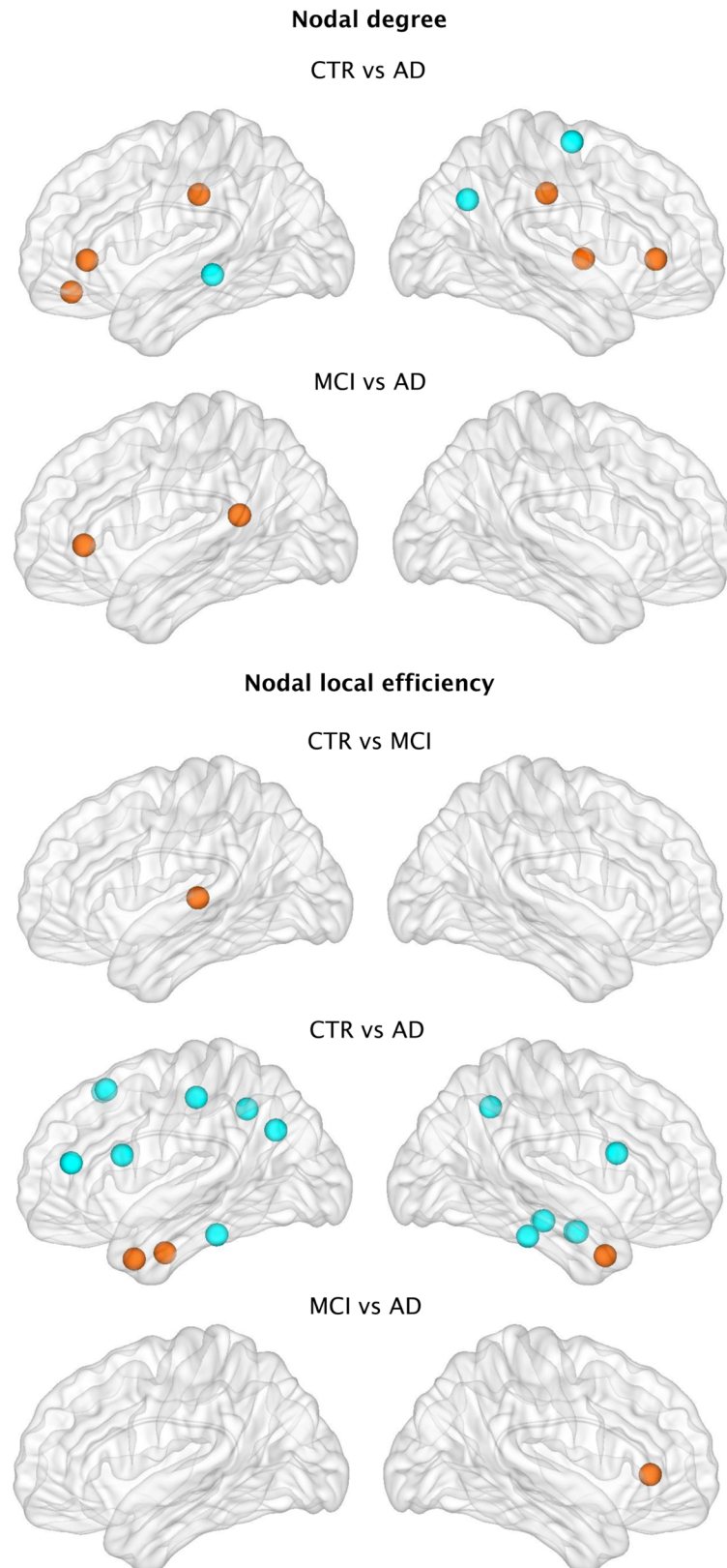
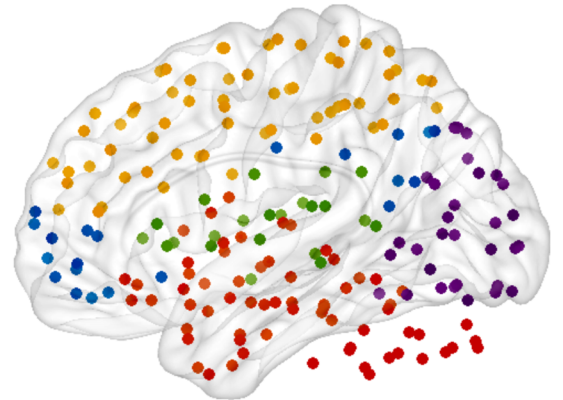
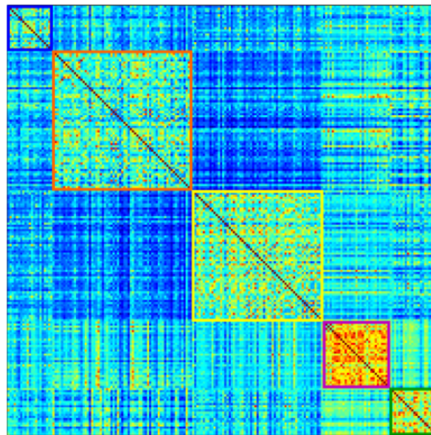


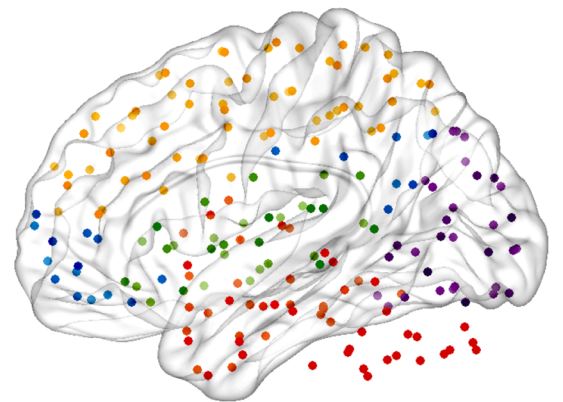
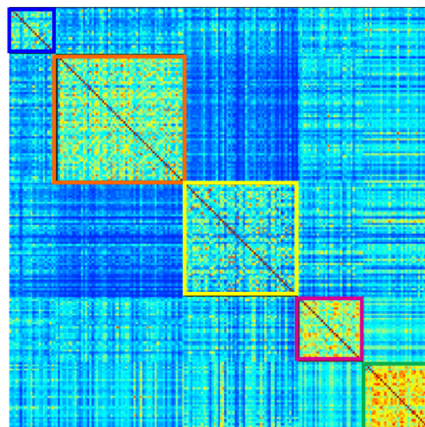
**Fig 6. Differences between groups in nodal structural measures.** Nodes showing significant differences between groups in the nodal degree and nodal local efficiency after FDR corrections. Orange indicates increases in nodal measures, while blue indicates decreases.

<https://doi.org/10.1371/journal.pone.0178798.g006>

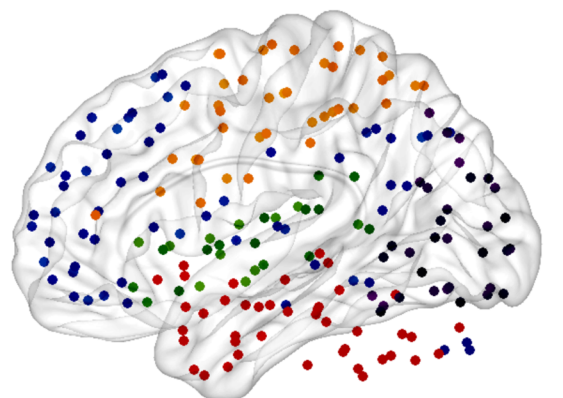
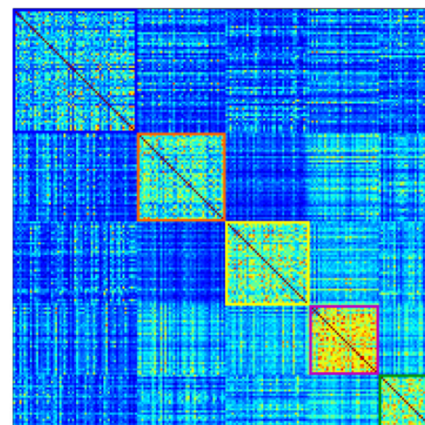
A) CTR



B) PD-CN



C) PD-MCI



● Module I ● Module II ● Module III ● Module IV ● Module V

**Fig 7. Functional brain networks and modules in controls and PD-MCI patients.** Weighted connectivity matrices and modules in A) controls (CTR) and Parkinson's disease patients B) with normal cognition (PD-CN) and C) with mild cognitive impairment (PD-MCI). Five modules were identified in each group.

<https://doi.org/10.1371/journal.pone.0178798.g007>

We also found that, with respect to controls, PD-MCI patients had a lower number of connections in Module III comprising fronto-parietal areas (PD-MCI = 54.87; controls = 57.95;  $p$ -value = 0.002) and Module V involving insular, temporal and inferior frontal areas (PD-MCI = 28.37; controls = 28.93;  $p$ -value = 0.040). Within Module III, the regions showing a significantly lower degree in PD-MCI patients after FDR corrections were the bilateral superior frontal, bilateral superior parietal gyri, precuneus, left middle frontal gyrus, inferior frontal gyrus and left anterior cingulate (Fig 8A). Within Module V, the regions showing a significantly lower degree in PD-MCI patients after FDR corrections were the left insula, right frontal orbital gyrus and bilateral transverse temporal gyri (Fig 8B).

To assess whether the presence of different MCI subtypes influenced the results in the PD-MCI group, we compared the average degree and the nodal degree of Modules III and V between each subtype and controls. In this study, the PD-MCI group consisted of 9 patients with multiple-domain MCI and 6 patients with single-domain MCI (5 amnesic, 1 patient non-amnesic). These two subtypes showed lower average degree in Module III (multiple-domain MCI = 54.6; single-domain MCI = 55.3; controls = 58.0) and Module V (multiple-domain MCI = 28.4; single-domain MCI = 28.3; controls = 28.9) compared to the control group. All the regions within these modules showed a lower nodal degree in the two MCI subtypes compared to controls, except the right transverse temporal gyrus, which had a similar degree in controls and single-domain MCI patients (S1 Table).

## Discussion

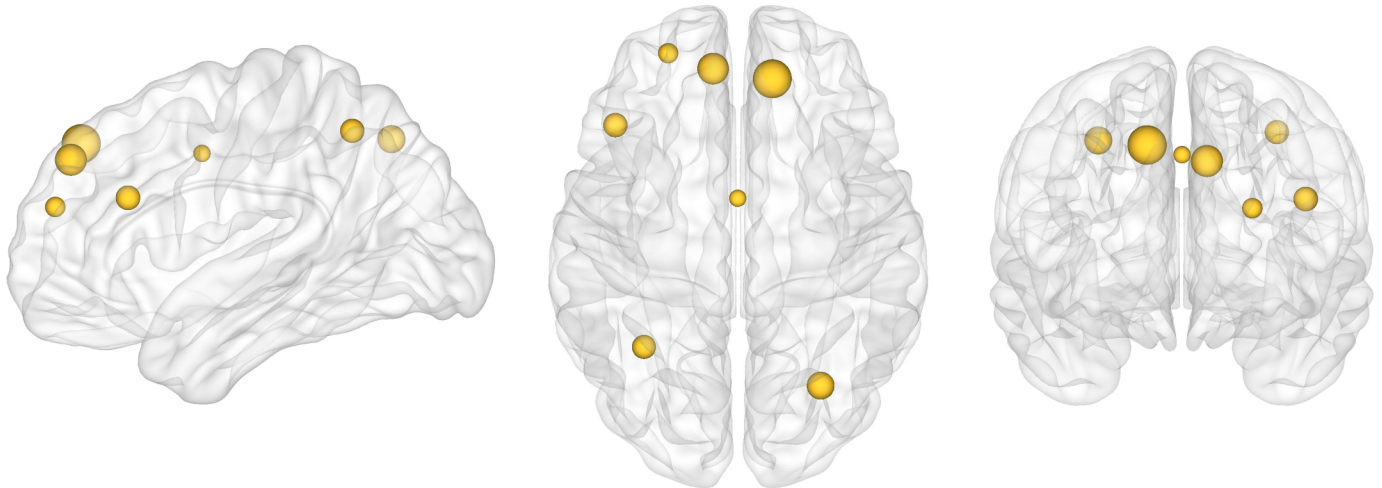
Graph theory has introduced new opportunities for understanding the brain as a complex system of interacting elements. Thanks to this framework, we have come to appreciate that the human brain relies on fundamental aspects of network organization such as a small-world architecture, modular structure and vulnerable hubs. These properties allow our brains to evolve, grow and adapt within an environment presenting increasing cognitive demands, and their disruption accounts for some of the key aspects underlying pathology in neurological diseases. In this report, we present BRAPH, the first object-oriented software for graph theory analysis intended for all researchers, regardless of their scientific background. As modern network science continues to develop at an increasing pace, it is important to have a software that allows modifying existent code in a structured manner so that past knowledge can be easily integrated with new topological analyses and graph theory measures. We are currently working on some of these developments with a particular focus on multimodal analyses and effective connectivity measures. Amongst BRAPH's strengths is the fact that it deals with all the aspects of graph theory analysis, by providing the user with extensive assistance, from the first basic steps such as defining the nodes and edges to producing the final publication-ready figures of the results as well as to archiving the results and relative analysis procedure in a dedicated file. To get an impression on BRAPH's abilities, below we discuss some of the results we obtained in two different studies in patients with amnesic MCI, AD and PD-MCI.

### Large-scale structural networks in amnesic MCI and AD

AD is currently one of the most prevalent neurodegenerative disorders, with a significant impact on society and caregiver burden [48]. Although the devastating impact of this condition has pushed forward a large research effort towards a more accurate diagnosis, the underlying effects of AD on network topology remain poorly understood. There is increasing evidence suggesting that the pathological hallmarks of AD, consisting of amyloid plaques neurofibrillary tangles, could spread in the brain through synapses and neural connections. Hence, the application

### CTR vs PD-MCI

#### Nodal degree: Module III



#### Nodal degree: Module V

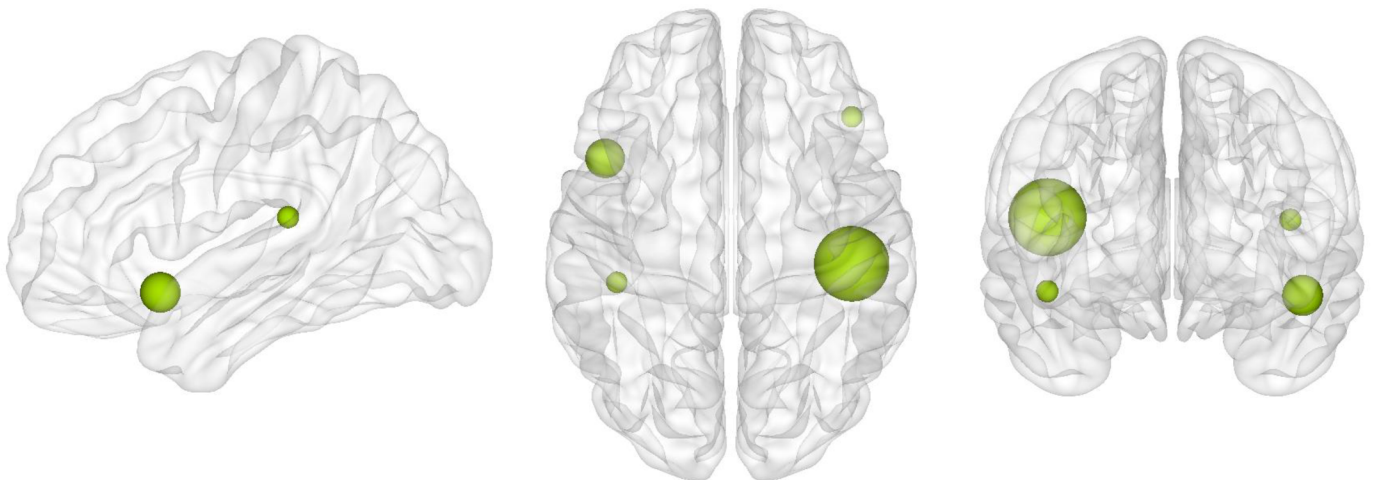


**Fig 8. Differences between groups in the nodal functional degree.** Significant decreases in the nodal degree of regions from Module III or fronto-parietal network in Parkinson's disease patients with mild cognitive impairment (PD-MCI) compared to controls (CTR) after FDR corrections.

<https://doi.org/10.1371/journal.pone.0178798.g008>

of graph theory to the study of brain connectivity could shed light on the mechanisms of disease propagation in AD.

In the current study, we found that AD patients presented an abnormal global network topology as reflected by increases in the path length, local efficiency and modularity, and by decreases of transitivity. These changes indicate that the regions of their networks communicated less efficiently with other brain regions and between different brain modules. In particular, the most widespread changes in network organization were observed for the transitivity and modularity. The decreases in transitivity found in AD suggest that the regions of their network were poorly connected to neighboring areas, whereas the increases in modularity

indicate that their modules had higher within-module connectivity and worse inter-module connectivity. Patients with amnesic MCI, who are potentially on the path to develop AD, also showed similar, albeit less extensive, network changes suggesting that amnesic MCI might be indeed an intermediate stage between healthy aging and dementia. These findings agree with the results obtained in previous studies [7, 28].

The assessment of the nodal degree in AD showed widespread changes in the number of connections of regions that belong to the default-mode network, including the medial orbito-frontal, the anterior cingulate and posterior cingulate gyri, compared to controls or patients with MCI. This network has been strongly associated with AD as its regions coincide with the areas showing amyloid deposition, gray matter atrophy and glucose hypometabolism in these patients [49]. Hence, the changes we found in this study may partially reflect pathological and metabolic abnormalities that usually occur in AD patients.

In contrast to the nodal degree, the nodal local efficiency showed alterations both in MCI and AD patients. Whereas in MCI patients, these changes were confined to a single region in the left temporal lobe, in AD patients the local efficiency was altered across several frontal, temporal and parietal areas, including the hippocampus and amygdala, which are involved in AD pathology [50]. The local efficiency reflects how efficient is the communication between a region and its neighboring areas. Decreases in this measure might indicate a loss of local connections, whereas increases could reflect a compensatory mechanism by which the number of connections between close brain areas increases to compensate for the loss of connections between distant brain areas.

Hence, altogether our findings indicate that graph theory is a useful method to assess abnormalities in brain connectivity and topology in the prodromal and clinical stages of AD.

## Large-scale functional networks in PD

Cognitive impairment is one of the most important non-motor symptoms in PD that greatly affect quality of life. During the course of the disease, most PD patients develop impairment in one or more cognitive domains, for which they receive a diagnosis of MCI. The presence of MCI in PD is associated with an increased risk to progress to dementia [51]. Hence, there is a pressing need to identify the underlying mechanisms of MCI to prevent cognitive decline in PD patients. Using a weighted network approach in BRAPH, we found that PD-MCI patients presented a lower number of connections in the whole brain network compared to controls. This indicates that in general their regions were more disconnected. However, after identifying the modular structure and performing the same analysis within each module, we observed that these effects were mostly driven by a lower degree in the fronto-parietal network and in a network involving temporal and inferior frontal regions in the PD-MCI group. The regions that were most affected in these networks were the superior frontal gyri, superior parietal gyri, precuneus, transverse temporal gyri and insula. All of these regions have been previously shown to display reduced connectivity in PD [8]. In addition, they have also been identified as important brain hubs in previous graph theory studies [43]. Within the graph theory framework, the brain hubs are the most important and central regions of a network as they mediate numerous long-distance connections. This characteristic also suggests they might have higher metabolic costs and a greater vulnerability to oxidative stress [43]. In a previous study [52], it was shown that the pathological brain lesions are concentrated in hub regions of the connectome in several neurodegenerative disorders, including PD, in line with our findings. The analyses that were carried out in the separate single-domain and multiple-domain MCI groups showed that the previous regions had reduced connectivity in both subtypes, suggesting that our results in PD-MCI patients were not driven by a particular subgroup.

In addition to the results found in the PD-MCI group, we also found a reduced number of connections in PD-CN patients in two networks that consisted of temporo-cerebellar areas and temporo-frontal regions. Previous studies using fMRI have found abnormalities in these brain areas in patients with PD [8]. Moreover, the inferior temporal gyri and inferior frontal cortex are amongst the first cortical areas becoming affected by Lewy body pathology in autopsy cases with PD [53] suggesting that they might play a relevant role in the progression of the disease from brainstem structures to cortical brain areas. The fact that both PD-CN and PD-MCI patients showed abnormalities in the same network of inferior temporal and frontal areas provides support to this assumption and suggests that these regions are important to understand disconnectivity in PD regardless of cognitive status.

## BRAPH features

The application of graph theory to the field of imaging connectomics is still in its early beginnings. There are several important challenges that need to be addressed such as whether the nodes and edges are an accurate description of the true underlying brain connectome in all its complexity of billions of neurons and synapses. Although we have limited knowledge on how to address this particular issue, there are several other challenges that can be addressed through the use of BRAPH. For instance, given that the true connectome is a sparse network, it is important to threshold the structural or functional edges, which typically consist of continuous association indices [54]. This thresholding can be carried out using different methods. On the one hand, a threshold can be applied so that only the connections that are below some significance level are included in the analysis. In this way, the weaker connections of the graph are eliminated and considered spurious. This approach will yield different numbers of connections across different individuals or groups. On the other hand, a threshold can be applied such that all networks have the same number of connections through a fixed value of density. In this way, only a percentage of edges are included in the analyses and the graph theory measures are independent of the number of edges [54]. In BRAPH, both thresholding options are available so that the user can easily compare them.

Another important challenge is the choice of a given value of threshold since there is currently no way to establish which is the best value. To solve this issue, BRAPH allows testing a hypothesis across different levels of significance or densities to determine the robustness of the results. Some authors consider choosing a range of thresholds an arbitrary process that produces values that are strongly dependent on this choice. For this reason, we also provide an option for weighted network analysis, which allows assessing both strong and weak connections present in a graph and is not dependent on a particular thresholding scheme.

Another challenge that is beginning to emerge in the scientific community is the realization that different node definitions can lead to different network findings. Currently BRAPH provides six anatomical and functional brain atlases that the user can apply within the same study to assess the consistency of the results against different parcellation schemes. In addition, a new brain atlas can be easily created or uploaded in BRAPH that adjusts to the user needs.

Finally, the last challenge that can be addressed through BRAPH is the normalization of graph theory measures by reference to random networks that have a random organization (with the same degree and/or weight distribution). BRAPH provides various options to perform this normalization.

Several aspects of BRAPH will be expanded in future releases. In particular, while currently BRAPH allows analyzing the complete fMRI time-series (static functional connectivity) by calculating statistical correlations or partial correlations between them since this is the most used method to analyze fMRI data, we are planning to include dynamic functional connectivity

analyses [23–26,55] in future versions of the software. Furthermore, we are also planning to allow the user to define the nodes using various data-driven methods, such as independent component analysis [55,56].

In conclusion, the study of the brain connectome is a growing field that will provide important insights into brain organization in health and disease. Amongst its numerous applications, there is the possibility it might help predicting the pathological spread of disease proteins in neurodegenerative disorders, which are becoming increasingly prevalent in the world's aging population. To address the increasing demands in this growing field we provide BRAPH, the first object-oriented software that will integrate new topological analyses and measures in a structured manner, allowing the users to be updated with the latest developments in graph theory. BRAPH can be found at <https://www.brapph.org> with online videos, a comprehensive manual, a support forum and relevant links. It is free for all researchers and can be used in all operating systems.

## Supporting information

**S1 Table. Nodal degree for regions in Module III and V in PD-MCI subtypes and controls.** Means are followed by standard deviations. CTR, controls; PD-CN, Parkinson's disease cognitively normal; PD-MCI, Parkinson's disease with mild cognitive impairment. (DOCX)

## Acknowledgments

Data used in preparation of this article were obtained from the Alzheimer's disease Neuroimaging Initiative (ADNI) database ([adni.loni.ucla.edu](http://adni.loni.ucla.edu)). As such, the investigators within the ADNI contributed to the design and implementation of ADNI and/or provided data but did not participate in analysis or writing of this report. A complete listing of ADNI investigators can be found at: [https://adni.loni.usc.edu/wp-content/uploads/how\\_to\\_apply/ADNI\\_Acknowledgment\\_List.pdf](https://adni.loni.usc.edu/wp-content/uploads/how_to_apply/ADNI_Acknowledgment_List.pdf).

## Author Contributions

**Conceptualization:** JBP EW GV.

**Data curation:** MM EK JBP.

**Formal analysis:** MM EK JBP.

**Funding acquisition:** JBP EW GV.

**Investigation:** MM EK JBP EW GV.

**Methodology:** MM EK JBP EW GV.

**Project administration:** GV.

**Resources:** JBP EW.

**Software:** MM EK GV.

**Supervision:** JBP EW GV.

**Validation:** MM EK JBP EW GV.

**Visualization:** MM EK JBP GV.

**Writing – original draft:** MM EK JBP.

**Writing – review & editing:** MM EK JBP EW GV.

## References

1. Sporns O. The human connectome: origins and challenges. *Neuroimage* 2013; 80: 53–61. <https://doi.org/10.1016/j.neuroimage.2013.03.023> PMID: 23528922
2. Watts DJ, Strogatz SH. Collective dynamics of ‘small-world’ networks. *Nature* 1998; 393: 440–442. <https://doi.org/10.1038/30918> PMID: 9623998
3. Hagmann P, Cammoun L, Gigandet X, Meuli R, Honey CJ, Wedeen VJ, et al. Mapping the structural core of human cerebral cortex. *PLoS Biol* 2008; 6: e159. <https://doi.org/10.1371/journal.pbio.0060159> PMID: 18597554
4. Meunier D, Stamatakis EA, Tyler LK. Age-related functional reorganization, structural changes, and preserved cognition. *Neurobiol Aging* 2014; 35: 42–54. <https://doi.org/10.1016/j.neurobiolaging.2013.07.003> PMID: 23942392
5. Damoiseaux JS, Rombouts SA, Barkhof F, Scheltens P, Stam CJ, Smith SM, et al. Consistent resting-state networks across healthy subjects. *Proc Natl Acad Sci U S A* 2006; 103: 13848–13853. <https://doi.org/10.1073/pnas.0601417103> PMID: 16945915
6. van den Heuvel MP, Hulshoff Pol HE. Exploring the brain network: a review on resting-state fMRI functional connectivity. *Eur Neuropsychopharmacol* 2010; 20: 519–534. <https://doi.org/10.1016/j.euroneuro.2010.03.008> PMID: 20471808
7. Tijms BM, Wink AM, de Haan W, van der Flier WM, Stam CJ, Scheltens P, et al. Alzheimer’s disease: connecting findings from graph theoretical studies of brain networks. *Neurobiol Aging* 2013; 34: 2023–2036. <https://doi.org/10.1016/j.neurobiolaging.2013.02.020> PMID: 23541878
8. Baggio HC, Segura B, Junque C. Resting-state functional brain networks in Parkinson’s disease. *CNS Neurosci Ther* 2015; 21: 793–801. <https://doi.org/10.1111/cns.12417> PMID: 26224057
9. Liao W, Zhang Z, Pan Z, Mantini D, Ding D, Duan X, et al. Altered functional connectivity and small-world in mesial temporal lobe epilepsy. *PLoS ONE* 2010; 5, e8525. <https://doi.org/10.1371/journal.pone.0008525> PMID: 20072616
10. Zhang Z, Liao W, Chen H, Mantini D, Ding JR, Xu Q, et al. Altered functional–structural coupling of large-scale brain networks in idiopathic generalized epilepsy. *Brain* 2011; 134, 2912–2928. <https://doi.org/10.1093/brain/awr223> PMID: 21975588
11. Ji GJ, Yu Y, Miao HH, Wang ZJ, Tang YL, Liao W. Decreased network efficiency in benign epilepsy with centrotemporal spikes. *Radiology* 2016, 160422.
12. Liu Y, Liang M, Zhou Y, He Y, Hao Y, Song M, et al. Disrupted small-world networks in schizophrenia. *Brain* 2008; 131, 945–961. <https://doi.org/10.1093/brain/awn018> PMID: 18299296
13. Lynall ME, Bassett DS, Kerwin R, McKenna PJ, Kitzbichler M, Muller U, et al. Functional connectivity and brain networks in schizophrenia. *Journal of Neuroscience* 2010; 30, 9477–9487. <https://doi.org/10.1523/JNEUROSCI.0333-10.2010> PMID: 20631176
14. Shu N, Liu Y, Li K, Duan Y, Wang J, Yu C, et al. Diffusion tensor tractography reveals disrupted topological efficiency in white matter structural networks in multiple sclerosis. *Cerebral Cortex* 2011; 21, 2565–2577. <https://doi.org/10.1093/cercor/bhr039> PMID: 21467209
15. Barttfeld P, Wicker B, Cukier S, Navarta S, Lew S, Leiguarda R, et al. State-dependent changes of connectivity patterns and functional brain network topology in autism spectrum disorder. *Neuropsychologia* 2012; 50, 3653–3662. <https://doi.org/10.1016/j.neuropsychologia.2012.09.047> PMID: 23044278
16. Rubinov M, Sporns O. Complex network measures of brain connectivity: uses and interpretations. *Neuroimage* 2010; 52: 1059–1069. <https://doi.org/10.1016/j.neuroimage.2009.10.003> PMID: 19819337
17. He B, Dai Y, Astolfi L, Babiloni F, Yuan H, Yang L. eConnectome: A MATLAB toolbox for mapping and imaging of brain functional connectivity. *J Neurosci Methods* 2011; 195: 261–269. <https://doi.org/10.1016/j.jneumeth.2010.11.015> PMID: 21130115
18. Hosseini SM, Hoefft F, Kesler SR. GAT: a graph-theoretical analysis toolbox for analyzing between-group differences in large-scale structural and functional brain networks. *PLoS One* 2012; 7: e40709. <https://doi.org/10.1371/journal.pone.0040709> PMID: 22808240
19. Whitfield-Gabrieli S, Nieto-Castanon A. Conn: a functional connectivity toolbox for correlated and anticorrelated brain networks. *Brain Connect* 2012; 2: 125–141. <https://doi.org/10.1089/brain.2012.0073> PMID: 22642651



20. Xia M, Wang J, He Y. BrainNet Viewer: a network visualization tool for human brain connectomics. *PLoS One* 2013; 8: e68910. <https://doi.org/10.1371/journal.pone.0068910> PMID: 23861951
21. Kruschwitz JD, List D, Waller L, Rubinov M, Walter H. GraphVar: a user-friendly toolbox for comprehensive graph analyses of functional brain connectivity. *J Neurosci Methods* 2015; 245: 107–115. <https://doi.org/10.1016/j.jneumeth.2015.02.021> PMID: 25725332
22. Wang J, Wang X, Xia M, Liao X, Evans A, He Y. GRETNA: a graph theoretical network analysis toolbox for imaging connectomics. *Front Hum Neurosci* 2015; 9: 386. <https://doi.org/10.3389/fnhum.2015.00386> PMID: 26175682
23. Calhoun VD, Miller R, Pearlson G, Adali T. The chronnectome: time-varying connectivity networks as the next frontier in fMRI data discovery. *Neuron* 2014; 84, 262–274. <https://doi.org/10.1016/j.neuron.2014.10.015> PMID: 25374354
24. Liao W, Zhang Z, Mantini D, Xu Q, Ji GJ, Zhang H, et al. Dynamical intrinsic functional architecture of the brain during absence seizures. *Brain Structure Function* 2014; 219, 2001–2015. <https://doi.org/10.1007/s00429-013-0619-2> PMID: 23913255
25. Liao W, Wu GR, Xu Q, Ji GJ, Zhang Z, Zang YF, et al. DynamicBC: a MATLAB toolbox for dynamic brain connectome analysis. *Brain Connectivity* 2014; 4, 780–790. <https://doi.org/10.1089/brain.2014.0253> PMID: 25083734
26. Cui J, Xu L, Bressler SL, Ding M, Liang H. BSMART: a Matlab/C toolbox for analysis of multichannel neural time series. *Neural Networks* 2008; 21, 1094–1104. <https://doi.org/10.1016/j.neunet.2008.05.007> PMID: 18599267
27. Pereira JB, Aarsland D, Ginestet CE, Lebedev AV, Wahlund LO, Simmons A, et al. Aberrant cerebral network topology and mild cognitive impairment in early Parkinson's disease. *Hum Brain Mapp* 2015; 36: 2980–2995. <https://doi.org/10.1002/hbm.22822> PMID: 25950288
28. Pereira JB, Mijalkov M, Kakaie E, Mecocci P, Vellas B, Tsolaki M, et al. Disrupted Network Topology in Patients with Stable and Progressive Mild Cognitive Impairment and Alzheimer's Disease. *Cereb Cortex* 2016; 26: 3476–3493. <https://doi.org/10.1093/cercor/bhw128> PMID: 27178195
29. Benjamini Y, Hochberg Y. Controlling the false discovery rate: a practical and powerful approach to multiple testing. *J Royal Stat Soc. Series B (Methodological)* 1995; 289–300.
30. Tzourio-Mazoyer N, Landeau B, Papathanassiou D, Crivello F, Etard O, Delcroix N, et al. Automated anatomical labeling of activations in SPM using a macroscopic anatomical parcellation of the MNI MRI single-subject brain. *Neuroimage* 2002; 15: 273–289. <https://doi.org/10.1006/nimg.2001.0978> PMID: 11771995
31. Desikan RS, Segonne F, Fischl B, Quinn BT, Dickerson BC, Blacker D, et al. An automated labeling system for subdividing the human cerebral cortex on MRI scans into gyral based regions of interest. *Neuroimage* 2006; 31: 968–980. <https://doi.org/10.1016/j.neuroimage.2006.01.021> PMID: 16530430
32. Destrieux C, Fischl B, Dale A, Halgren E. Automatic parcellation of human cortical gyri and sulci using standard anatomical nomenclature. *Neuroimage* 2010; 53: 1–15. <https://doi.org/10.1016/j.neuroimage.2010.06.010> PMID: 20547229
33. Dosenbach NU, Visscher KM, Palmer ED, Miezin FM, Wenger KK, Kang HC, et al. A core system for the implementation of task sets. *Neuron* 2006; 50: 799–812. <https://doi.org/10.1016/j.neuron.2006.04.031> PMID: 16731517
34. Power JD, Cohen AL, Nelson SM, Wig GS, Barnes KA, Church JA, et al. Functional network organization of the human brain. *Neuron* 2011; 72: 665–678. <https://doi.org/10.1016/j.neuron.2011.09.006> PMID: 22099467
35. Craddock RC, James GA, Holtzheimer PE, 3rd, Hu XP, Mayberg HS. A whole brain fMRI atlas generated via spatially constrained spectral clustering. *Hum Brain Mapp* 2012; 33: 1914–1928. <https://doi.org/10.1002/hbm.21333> PMID: 21769991
36. Voevodskaya O, Simmons A, Nordenskjold R, Kullberg J, Ahlstrom H, Lind L, et al. The effects of intracranial volume adjustment approaches on multiple regional MRI volumes in healthy aging and Alzheimer's disease. *Front Aging Neurosci* 2014; 6: 264. <https://doi.org/10.3389/fnagi.2014.00264> PMID: 25339897
37. Bassett DS, Bullmore E, Verchinski BA, Mattay VS, Weinberger DR, Meyer-Lindenberg A. Hierarchical organization of human cortical networks in health and schizophrenia. *J Neurosci* 2008; 28, 9239–9248. <https://doi.org/10.1523/JNEUROSCI.1929-08.2008> PMID: 18784304
38. Stam CJ, Jones BF, Nolte G, Breakspear M, Scheltens P. Small-world networks and functional connectivity in Alzheimer's disease. *Cerebral cortex* 2007; 17, 92–99. <https://doi.org/10.1093/cercor/bhj127> PMID: 16452642

39. Rubinov M, Knock SA, Stam CJ, Micheloyannis S, Harris AW, Williams LM, et al. Small-world properties of nonlinear brain activity in schizophrenia. *Hum Brain Mapp* 2009; 30, 403–416. <https://doi.org/10.1002/hbm.20517> PMID: 18072237
40. Dimitriadis SI, Laskaris NA, Tsirka V, Vourkas M, Micheloyannis S, Fotopoulos S. Tracking brain dynamics via time-dependent network analysis. *J Neurosci Methods* 2010; 193, 145–155. <https://doi.org/10.1016/j.jneumeth.2010.08.027> PMID: 20817039
41. Achard S, Salvador R, Whitcher B, Suckling J, Bullmore E. A resilient, low-frequency, small-world human brain functional network with highly connected association cortical hubs. *J Neurosci* 2006; 26: 63–72. <https://doi.org/10.1523/JNEUROSCI.3874-05.2006> PMID: 16399673
42. Barabási AL. *Network science*. Cambridge University Press, 2016.
43. van den Heuvel MP, Sporns O. Network hubs in the human brain. *Trends Cogn Sci* 2013; 17: 683–696. <https://doi.org/10.1016/j.tics.2013.09.012> PMID: 24231140
44. Latora V, Marchiori M. Efficient behavior of small-world networks. *Phys Rev Lett* 2001; 87: 198701. <https://doi.org/10.1103/PhysRevLett.87.198701> PMID: 11690461
45. Girvan M, Newman ME. Community structure in social and biological networks. *Proc Natl Acad Sci U S A* 2002; 99: 7821–7826. <https://doi.org/10.1073/pnas.122653799> PMID: 12060727
46. Parkinson Progression Marker Initiative. The Parkinson Progression Marker Initiative (PPMI). *Prog Neurobiol* 2011; 95: 629–635. <https://doi.org/10.1016/j.pneurobio.2011.09.005> PMID: 21930184
47. Weintraub D, Simuni T, Caspell-Garcia C, Coffey C, Lasch S, Siderowf A, et al. Cognitive performance and neuropsychiatric symptoms in early, untreated Parkinson's disease. *Mov Disord* 2015; 30: 919–927. <https://doi.org/10.1002/mds.26170> PMID: 25737166
48. Winblad B, Amouyel P, Andrieu S, Ballard C, Brayne C, Brodaty H et al. Defeating Alzheimer's disease and other dementias: a priority for European science and society. *Lancet Neurol* 2016; 15: 455–532. [https://doi.org/10.1016/S1474-4422\(16\)00062-4](https://doi.org/10.1016/S1474-4422(16)00062-4) PMID: 26987701
49. Buckner RL, Snyder AZ, Shannon BJ, LaRossa G, Sachs R, Fotenos AF, et al. Molecular, structural, and functional characterization of Alzheimer's disease: evidence for a relationship between default activity, amyloid, and memory. *J Neurosci* 2005; 25: 7709–7717. <https://doi.org/10.1523/JNEUROSCI.2177-05.2005> PMID: 16120771
50. Braak H, Braak E. Neuropathological stageing of Alzheimer-related changes. *Acta Neuropathol* 1991; 82: 239–259. PMID: 1759558
51. Svenningsson P, Westman E, Ballard C, Aarsland D. Cognitive impairment in patients with Parkinson's disease: diagnosis, biomarkers, and treatment. *Lancet Neurol* 2012; 11: 697–707. [https://doi.org/10.1016/S1474-4422\(12\)70152-7](https://doi.org/10.1016/S1474-4422(12)70152-7) PMID: 22814541
52. Crossley NA, Mechelli A, Scott J, Carletti F, Fox PT, McGuire P, et al. The hubs of the human connectome are generally implicated in the anatomy of brain disorders. *Brain* 2014; 137: 2382–2395. <https://doi.org/10.1093/brain/awu132> PMID: 25057133
53. Braak H, Del Tredici K, Rüb U, de Vos RA, Steur EN, Braak E. Staging of brain pathology related to sporadic Parkinson's disease. *Neurobiology of aging*. 2003 Apr 30; 24(2):197–211. PMID: 12498954
54. Fornito A, Zalesky A, Breakspear M. Graph analysis of the human connectome: promise, progress, and pitfalls. *Neuroimage* 2013; 80: 426–444. <https://doi.org/10.1016/j.neuroimage.2013.04.087> PMID: 23643999
55. Yu Q, Erhardt EB, Sui J, Du Y, He H, Hjelm D, et al. Assessing dynamic brain graphs of time-varying connectivity in fMRI data: Application to healthy controls and patients with schizophrenia. *Neuroimage* 2015; 107, 345–355. <https://doi.org/10.1016/j.neuroimage.2014.12.020> PMID: 25514514
56. Smith SM, Miller KL, Salimi-Khorshidi G, Webster M, Beckmann CF, Nichols TE, et al. Network modelling methods for FMRI. *Neuroimage* 2011; 54, 875–891.

## ORIGINAL ARTICLE

# Disrupted Network Topology in Patients with Stable and Progressive Mild Cognitive Impairment and Alzheimer's Disease

Joana B. Pereira<sup>1</sup>, Mite Mijalkov<sup>2</sup>, Ehsan Kakaei<sup>2</sup>, Patricia Mecocci<sup>4</sup>, Bruno Vellas<sup>5</sup>, Magda Tsolaki<sup>6</sup>, Iwona Kłoszewska<sup>7</sup>, Hilka Soininen<sup>8,9</sup>, Christian Spenger<sup>10,11</sup>, Simmon Lovestone<sup>12</sup>, Andrew Simmons<sup>13</sup>, Lars-Olof Wahlund<sup>1</sup>, Giovanni Volpe<sup>2,3</sup> and Eric Westman<sup>1</sup>, AddNeuroMed consortium, for the Alzheimer's Disease Neuroimaging Initiative

<sup>1</sup>Department of Neurobiology, Care Sciences and Society, Karolinska Institutet, Stockholm, Sweden, <sup>2</sup>Department of Physics, Soft Matter Lab, <sup>3</sup>UNAM—National Nanotechnology Research Center, Bilkent University, Ankara, Turkey, <sup>4</sup>Institute of Gerontology and Geriatrics, University of Perugia, Perugia, Italy, <sup>5</sup>INSERM U 558, University of Toulouse, Toulouse, France, <sup>6</sup>Aristotle University of Thessaloniki, Thessaloniki, Greece, <sup>7</sup>Medical University of Lodz, Lodz, Poland, <sup>8</sup>University of Eastern Finland, Joensuu, Finland, <sup>9</sup>University Hospital of Kuopio, Kuopio, Finland, <sup>10</sup>Department of Clinical Science, Intervention and Technology at Karolinska Institutet, Division of Medical Imaging and Technology, Stockholm, Sweden, <sup>11</sup>Department of Radiology, Karolinska University Hospital in Huddinge, Solna, Sweden, <sup>12</sup>King's College London, Institute of Psychiatry, London, UK and <sup>13</sup>NIHR Biomedical Research Centre for Mental Health, London, UK

Address correspondence to Joana B. Pereira, Department of Neurobiology, Care Sciences and Society, Karolinska Institutet, Novum 5th floor, SE-141 86 Stockholm, Sweden. Email: joana.pereira@ki.se

Data used in preparation of this article were obtained from the Alzheimer's Disease Neuroimaging Initiative (ADNI) database (adni.loni.ucla.edu). As such, the investigators within the ADNI contributed to the design and implementation of ADNI and/or provided data but did not participate in analysis or writing of this report. A complete listing of ADNI investigators can be found at: [http://adni.loni.ucla.edu/wp-content/uploads/how\\_to\\_apply/ADNI\\_Acknowledgement\\_List.pdf](http://adni.loni.ucla.edu/wp-content/uploads/how_to_apply/ADNI_Acknowledgement_List.pdf)

## Abstract

Recent findings suggest that Alzheimer's disease (AD) is a disconnection syndrome characterized by abnormalities in large-scale networks. However, the alterations that occur in network topology during the prodromal stages of AD, particularly in patients with stable mild cognitive impairment (MCI) and those that show a slow or faster progression to dementia, are still poorly understood. In this study, we used graph theory to assess the organization of structural MRI networks in stable MCI (sMCI) subjects, late MCI converters (lMCic), early MCI converters (eMCic), and AD patients from 2 large multicenter cohorts: ADNI and AddNeuroMed. Our findings showed an abnormal global network organization in all patient groups, as reflected by an increased path length, reduced transitivity, and increased modularity compared with controls. In addition, lMCic, eMCic, and AD patients showed a decreased path length and mean clustering compared with the sMCI group. At the local level, there were

nodal clustering decreases mostly in AD patients, while the nodal closeness centrality detected abnormalities across all patient groups, showing overlapping changes in the hippocampi and amygdala and nonoverlapping changes in parietal, entorhinal, and orbitofrontal regions. These findings suggest that the prodromal and clinical stages of AD are associated with an abnormal network topology.

**Key words:** closeness centrality, clustering, modularity, structural covariance networks, transitivity

## Introduction

Alzheimer's disease (AD) is a devastating neurodegenerative disorder that slowly deprives individuals of their memories and other essential cognitive functions, including executive, visuospatial abilities and language. There is increasing evidence showing that the progression of these cognitive symptoms occurs in an orderly fashion, which reflects the accumulation of amyloid deposits and the spatial distribution of neurofibrillary tangles (Frisoni et al. 2010). For instance, while memory loss takes place at early disease stages, reflecting the presence of tangles in medial temporal regions (Scahill et al. 2002; Thal et al. 2002; Thompson et al. 2004); aphasia and apraxia typically occur at later stages, reflecting the spread of tangles and plaques into neocortical areas (Braak et al. 2006; McDonald et al. 2009). This incremental spread of pathology between interconnected brain regions suggests that AD might be a disconnection syndrome characterized by abnormalities in brain networks (Pievani et al. 2011).

Graph theory has become a very useful tool in neuroimaging to assess the relationship between different brain regions and their organization into large-scale networks (Filippi et al. 2013). Using this method, previous studies have shown that healthy individuals have an efficient network topology, combining a high level of integration between distant brain regions (short path length) and a good local communication between neighboring areas (high clustering). This small-world configuration (Humphries et al. 2006) is thought to be specially suited for cognitive processing (Bassett and Bullmore 2006) and has been shown in previous functional MRI, structural MRI, electroencephalogram, and diffusion tensor imaging (DTI) studies (Achard and Bullmore 2007; Ferri et al. 2007; Bassett et al. 2008; Iturria-Medina et al. 2008; Gong et al. 2009). The combination of high efficiency and clustering in a small-world architecture is an attractive principle of brain network organization as it could deliver both segregated and integrated information processing (Bullmore and Sporns 2012). For instance, visual processing is a segregated process that would benefit from the clusters of connections between regions that are topologically close, whereas executive processing is an integrated process that would benefit from the long paths that allow transferring information across the whole network (Bullmore and Sporns 2012). In addition, it has been shown that regions showing high clustering tend to be very well connected to areas with the same functional specialization (Sporns and Betzel 2016). In line with this, several studies have shown that the brain is organized into communities or modules of interconnected regions (Hagmann et al. 2008; Meunier et al. 2009), which may correspond to large-scale brain systems such as the executive control, the dorsal attention, and the default-mode network. This network property is commonly referred to as modularity and has been shown in healthy individuals by previous studies (Chen et al. 2008; He et al. 2009).

Graph theory can be applied to different neuroimaging modalities to assess brain networks in vivo in AD, including DTI, structural, and functional MRI (for reviews, see Tijms, Moller,

et al. 2013; Tijms, Wink, et al. 2013; Dai and He 2014) as well as positron emission tomography (PET) (Sanabria-Diaz et al. 2013; Sepulcre et al. 2013; Yao et al. 2015). Using structural MRI, a few studies have shown that AD patients present changes in global network organization compared with healthy controls (Dai and He 2014; Phillips et al. 2015); however, there is surprisingly little agreement about the nature of these changes: while some studies showed an increased path length and clustering in the networks of AD patients, others found decreases or no changes at all (Li et al. 2012; Dai and He 2014). Regarding network configuration, some studies using structural MRI have found a preserved small-world organization in AD patients, while others found random or regular network topologies (Dai and He 2014). This inconsistency between studies could be due to the inclusion of small samples of patients with heterogeneous clinical characteristics. Despite this interest in assessing brain connectivity in AD, to date no studies have assessed modularity in the structural MRI networks of AD patients.

Amnesic mild cognitive impairment (MCI) is a transition state between normal aging and AD with a high risk of progression to dementia (Petersen et al. 1999). Although MCI has been associated with reduced white matter integrity and abnormal functional connectivity (Medina et al. 2006; Zhang et al. 2007; Petrella et al. 2011; Binnewijzend et al. 2012), it is not clear whether these patients also present altered brain network topology: Yao et al. (2010) found no differences in the path length or clustering between MCI patients and controls, while Phillips et al. (2015) found differences that varied according to the network construction method. There is increasing evidence showing that MCI patients progress to AD at a rate of approximately 15% per year (Grundman et al. 2004). The assessment of network organization in stable MCI patients and those who show a slow or faster progression to dementia is important as it could provide important clues into which network changes mark the transition to AD and improve our understanding on the effects of disease progression on brain networks.

The aim of the current study was to establish the nature of structural abnormalities in the organization of brain networks in stable MCI (sMCI) subjects, patients who show a slow progression to dementia (late MCI converters, lMCIc), patients who show a fast progression to dementia (early MCI converters, eMCIc), and AD patients using graph theory. To achieve this goal, we assessed over 1000 patients and controls from 2 large multicenter cohorts: the Alzheimer's Disease Neuroimaging Initiative (ADNI) and the AddNeuroMed study. We calculated various global and local network measures, including the characteristic path length, the mean clustering coefficient, the small-worldness, the nodal clustering, and the nodal closeness centrality. In addition, in contrast to previous studies, we calculated for the first time the transitivity and modularity in the structural MRI networks of MCI and AD patients. These graph theory measures reflect how well a region is connected to its neighbouring areas and within brain modules, providing important information on the network's ability for specialized processing to occur within densely interconnected groups of brain regions (Rubinov and Sporns 2010). We

hypothesized that global network measures would show abnormalities across all patient groups, with IMCIc, eMCIc, and AD patients showing more severe network changes compared with controls than sMCI patients. In addition, based on previous evidence showing that the sequence of brain abnormalities between regions of the default-mode network is reminiscent of the spread of tangle pathology in AD (Buckner et al. 2005, 2009), we hypothesized that patients would show changes in local network measures in the regions of this network.

## Methods

### Subjects

Data used in the preparation of this article were obtained from the ADNI database ([adni.loni.usc.edu](http://adni.loni.usc.edu)) and the AddNeuroMed study. In total, 1008 subjects were included, consisting of 301 controls, 425 MCI, and 282 AD patients. Regarding MCI patients, 87 converted to AD after 1 year (eMCIc), 71 converted to AD after 3 years (IMCIc), and 110 remained stable after 3 years (sMCI). In addition, 157 MCI patients remained stable after 1 year but had no additional follow-ups after that period. We classified these subjects as sMCI-1y and compared them with the other groups in a supplementary analysis. Eight subjects were excluded from the previous groups due to uncertain diagnosis.

The ADNI was launched in 2003 as a public-private partnership, led by Principal Investigator Michael W. Weiner, MD. The primary goal of ADNI has been to test whether serial magnetic resonance imaging (MRI), PET, other biological markers, and clinical and neuropsychological assessment can be combined to measure the progression of MCI and early AD. In the ADNI cohort, the inclusion criteria for the control group were Mini-Mental State Examination (MMSE) scores between 24 and 30, a Clinical Dementia Rating-Sum of Boxes (CDR-SB) score of 0, and lack of depression, MCI, or dementia. Inclusion criteria for the MCI group followed the Peterson criteria (Peterson et al. 1999) for amnesic MCI. AD participants met the National Institute for Neurological and Communicative Disorders and Stroke-Alzheimer's Disease and Related Disorder Association (NINDS/ADRD) criteria for probable AD, had a MMSE score between 18 and 26, and a CDR-SB of 0.5–1.0. Exclusion criteria comprised history of structural brain lesions or head trauma, significant neurological disease other than incipient AD, and the use of psychotropic medications that could affect memory. For up-to-date information about the ADNI study, see [www.adni-info.org](http://www.adni-info.org).

AddNeuroMed is an Integrated Project funded by the European Union Sixth Framework program (Lovestone et al. 2007, 2009). AddNeuroMed aims to develop and validate novel surrogate markers of disease and treatment, based upon *in vitro* and *in vivo* models in animals and humans in AD. The neuroimaging part of AddNeuroMed uses MRI and magnetic resonance spectroscopy (MRS) to establish imaging markers for early diagnosis and detection of disease and efficacy of disease modifying therapy in man, as well as translational imaging biomarkers in animal models of AD. Human data were collected from 6 different sites across Europe: University of Kuopio (Finland), University of Perugia (Italy), Aristotle University of Thessaloniki (Greece), King's College London (United Kingdom), University of Lodz (Poland), and University of Toulouse (France) (Lovestone et al. 2009; Simmons et al. 2009, 2011). The inclusion criteria for the control group were Mini-Mental State Examination (MMSE) scores between 24 and 30, a CDR score of 0, 65 years, or above, and lack of depression, dementia, other neurological diseases, unstable systematic illnesses, or organ failure. The inclusion criteria for

MCI patients were similar to the control group except for the CDR score of 0.5 and report of memory problems by the patient or informant. AD patients met the NINDS/ADRD and DSM-IV criteria for probable AD, had a MMSE score between 12 and 28, had 65 years or above, and did not have significant neurological or psychiatric illnesses other than AD, unstable systematic illnesses, or organ failure.

### MRI Acquisition

Data acquisition for the AddNeuroMed study was designed to be compatible with ADNI (Jack et al. 2008; Simmons et al. 2009, 2011). In particular, all participants, both from ADNI and AddNeuroMed, were scanned on a 1.5 Tesla MRI system using a sagittal 3D  $T_1$ -weighted MPRAGE sequence: repetition time (TR) = 9–13 ms; echo time (TE) = 3.0–4.1 ms; inversion time (IT) = 1000 ms; flip angle (FA) = 8°; voxel size =  $1.1 \times 1.1 \times 1.2$  mm<sup>3</sup>. Images from ADNI were acquired in 58 sites, while images from AddNeuroMed were acquired in 5 sites or centers. We have combined these 2 cohorts in several previous studies (Spulber et al. 2013; Falahati et al. 2016), showing that they present similar patterns of atrophy and predictive power in discriminating patients with AD or MCI from controls (Westman et al. 2011).

### Image Preprocessing

All  $T_1$ -weighted images were preprocessed using the FreeSurfer software, version 5.1. Briefly, preprocessing included: correction of motion artifacts and spatial distortions due to gradient nonlinearity and B1 field inhomogeneity; removal of nonbrain tissue using a hybrid watershed/surface deformation procedure (Segonne et al. 2004); automated transformation into the Talairach standard space; intensity normalization (Sled et al. 1998); tessellation of the gray/white matter boundary; automated topology correction (Segonne et al. 2007); and surface deformation following intensity gradients to optimally place the gray/white and gray/CSF borders at the location where the greatest shift in intensity defines the transition to the other tissue class (Fischl and Dale 2000). Once the cortical models were complete, registration to a spherical atlas took place, which utilizes individual cortical folding patterns to match cortical geometry across subjects (Fischl et al. 1999). This was followed by parcellation of the cerebral cortex into 68 cortical regions using the atlas by Desikan et al. (2006) (Fig. 1). In addition to these 68 regions, 7 subcortical structures were also included: hippocampus, amygdala, thalamus, caudate, putamen, accumbens, and pallidum (Fig. 1). All data was preprocessed through the HiveDB database system (Muehlboeck et al. 2014). We excluded 8 subjects that were outliers in cortical thickness and subcortical volume measures.

### Network Construction and Analysis

For every cortical region, a linear regression was performed to control for the effects of age, gender, and education (He et al. 2007). The same procedure was carried out for subcortical regions including intracranial volume as an additional covariate. To ensure that our results were not influenced by the fact that subjects were scanned at different centers, we included scanning site as an additional covariate in a supplementary analysis.

The residuals of these regressions were used to substitute the raw values and build the structural covariance networks. In these networks, every node corresponded to a brain region and the edges represented the correlations between them (He et al. 2007). In this study, both cortical thicknesses and subcortical volumes were used to build the structural networks due to

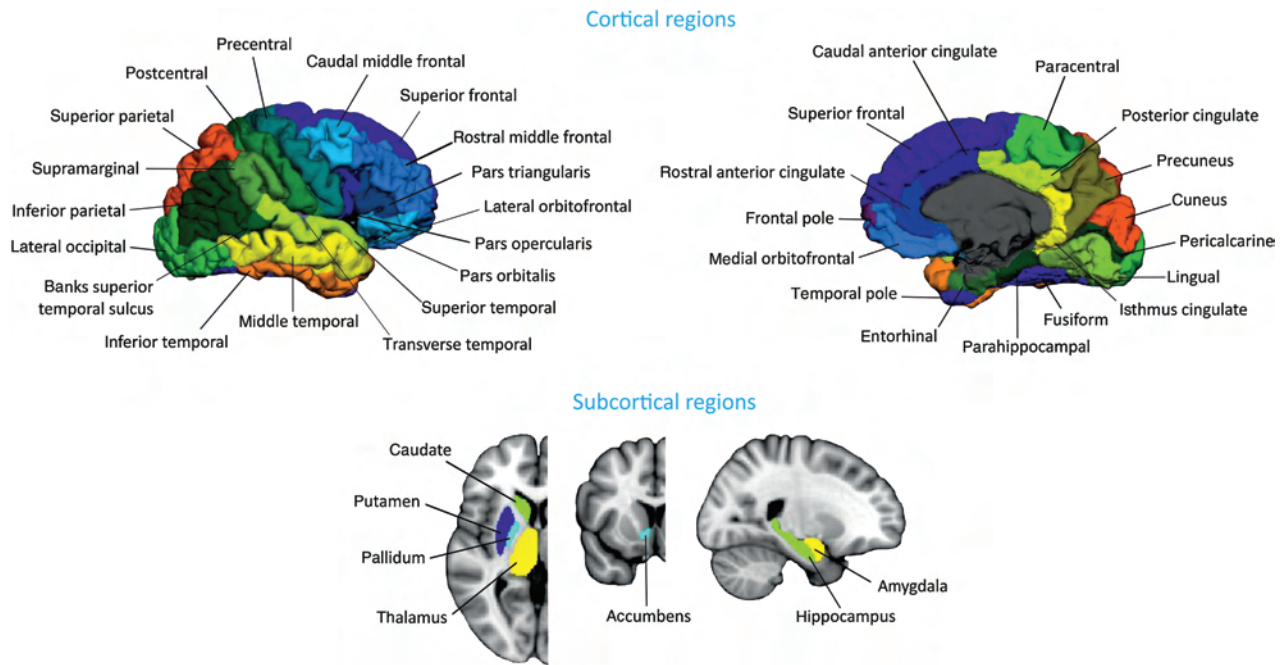


**Figure 1.** Brain regions used in network construction and analysis. The cortical thickness and subcortical volumes were extracted from these regions for every subject.

previous evidence showing the involvement of cortical and subcortical regions in MCI and AD and similarly to previous graph theory studies (Hosseini et al. 2013; Pereira et al. 2015).

For every group, we built an  $82 \times 82$  association matrix, where each entry was defined as the Pearson correlation coefficient between corrected anatomical measures of every pair of regions across participants (Fig. 2). For each association matrix, a binary matrix was computed, where the correlation coefficient was considered 1 if it was above a threshold and 0 if it was below (He et al. 2007). Since thresholding association matrices of different groups may yield networks with a different number of nodes and edges, we thresholded the association matrices at a range of network densities  $D$  ( $D_{\min} = 5\%$  to  $D_{\max} = 35\%$ , in steps of 1%) and compared the network topologies across that range. For densities below 5%, the number of edges was inferior to the number of nodes, corresponding to a widely disconnected network. For  $D$  above 35%, the networks became similar to random graphs and showed a small-world index close to 1. All self-connections and negative correlations were excluded from the analyses.

To detect differences between groups in global network topology, we calculated the characteristic path length, the mean clustering coefficient, the transitivity, the modularity, and the small-worldness. The characteristic path length is the average shortest path length between all pairs of nodes in the network and indicates how easy it is (on average) to reach a node from any other node in the network (Watts and Strogatz 1998); this measure was calculated only within connected components of the network as implemented in the formulas by Rubinov and Sporns (2010). The clustering coefficient is the average over the whole network of the fraction of a node's neighbors that are also neighbors of each other; it reflects how well the nodes are connected to nearby regions forming clusters (Watts and Strogatz 1998). The transitivity is similar to the clustering coefficient but, instead of being normalized individually by every node, it is normalized by the whole network and is not influenced by nodes with a low degree (Newman 2003). The modularity describes the extent to which a network can be divided into modules or

communities of regions with a large number of within-modules connections and a minimal number of between-module connections (Newman 2006). The small-worldness is a measure of how much a network is locally interconnected compared with a random network but still retaining global connectivity between distant brain regions (Watts and Strogatz 1998; Humphries et al. 2006).

To assess differences between groups in regional network topology, we calculated the nodal clustering and the closeness centrality. We selected these 2 nodal network measures, because they are sensitive to different aspects of network topology and remain largely unexplored in MCI and AD. Specifically, the nodal clustering is a measure of segregation, which reflects the ability for specialized information processing to occur within groups of brain regions, while the closeness centrality is a measure of interaction that reflects the ability to combine information from distributed brain areas (Rubinov and Sporns 2010). The nodal clustering is calculated as the mean clustering coefficient but only for a given node. The closeness centrality is the inverse of the average shortest path length from 1 node to all other nodes in the network. To compare the roles of the nodes in each module and their differences between groups, we also calculated the within-module degree and participation coefficient. The within-module degree measures the connectivity of the node within the module compared with the other nodes in the same module. The participation coefficient expresses how strongly a node is connected to other modules and tends to 1 if a node has a homogeneous connection distribution with all the modules and 0 if it does not have any intermodule connections (Guimera and Amaral 2005; Guimera et al. 2005).

The formulas that were used to calculate the global and nodal graph theory measures are provided by Rubinov and Sporns (2010). We used BrainNet Viewer (<http://www.nitrc.org/projects/bnv/>) for network visualization (Xia et al. 2013).

### Comparison of Network Measures Between Groups

We tested the statistical significance of the differences between groups using nonparametric permutation tests with 1000

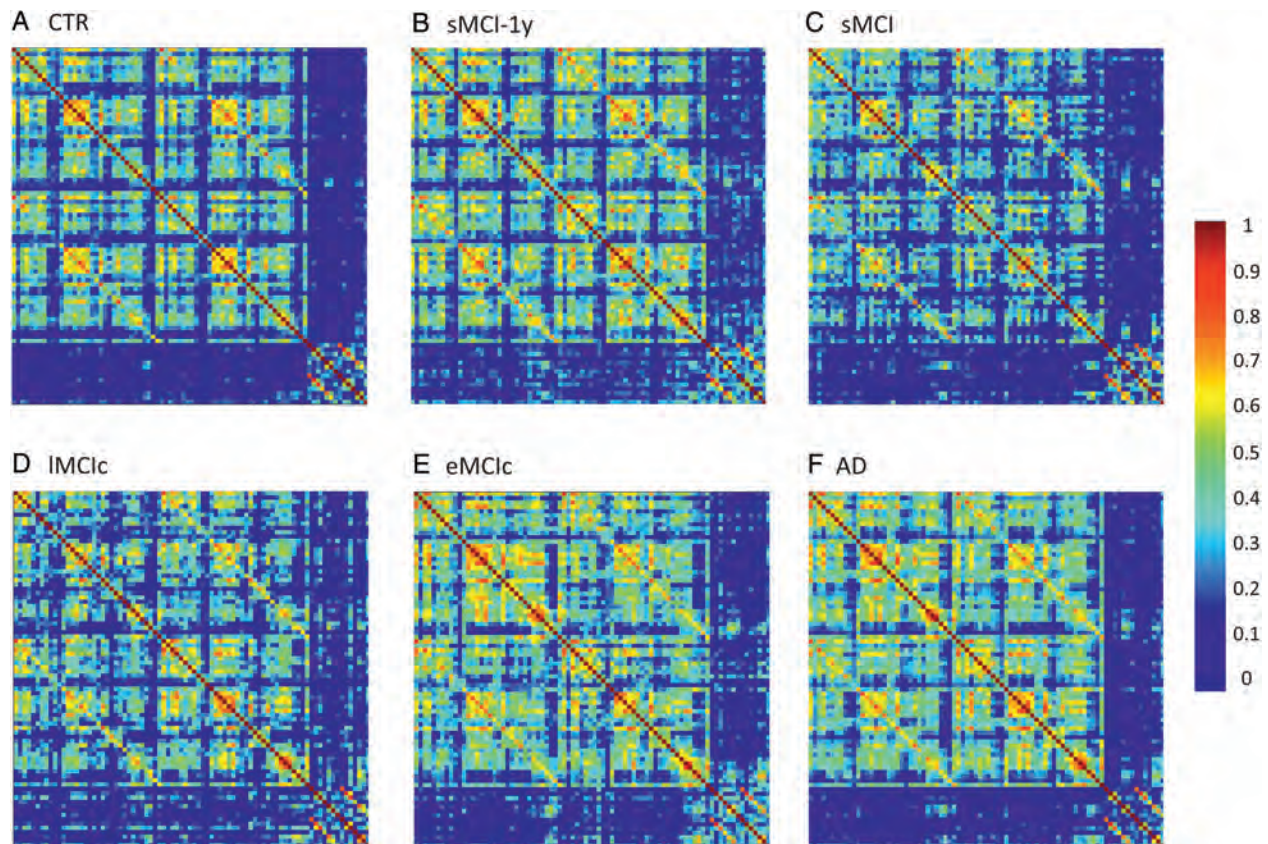


**Figure 2.** Structural correlation matrices for (A) controls (CTR), (B) patients with stable mild cognitive impairment after 1 year (sMCI-1y), (C) patients with sMCI (after 3 years), (D) IMCic, (E) eMCic, and (F) AD patients. In these matrices, the first rows and columns correspond to the correlations between cortical regions, while the last ones correspond to the correlations between subcortical areas. The color bar indicates the strength of the correlation coefficients: warmer colors represent stronger correlations, while colder colors represent weaker correlations.

permutations (Bassett et al. 2008; He et al. 2008). In each permutation, the corrected anatomical values of every subject were randomly reassigned to one of a pair of groups with the same number of subjects as in the original groups. Then, an association matrix was built for each pair of randomized groups, and the binary matrices were calculated at a range of network densities. The network measures were calculated at each density, and the differences between the new randomized groups were computed. This randomization procedure was repeated 1000 times for every density value, and the 95% confidence intervals (CI) of each distribution were used as critical values for a 2-tailed test of the null hypothesis at  $P < 0.05$ . To correct the nodal network results for multiple comparisons, we used a false discovery rate (FDR) procedure (Genovese et al. 2002) at a  $q$  value of 0.05.

## Results

The characteristics of the sample can be found in Table 1. There were significant differences in gender and years of education between the groups ( $P < 0.001$ ). For this reason, the cortical thickness and subcortical measures were corrected by these variables in the current study. As expected, all patient groups showed lower MMSE scores ( $P < 0.001$ ) and higher CDR scores ( $P < 0.001$ ) compared with controls. In addition, IMCic, eMCic, and AD patients showed lower MMSE scores compared with sMCI patients ( $P < 0.05$ ). AD patients showed worse MMSE scores compared with sMCI, IMCic, eMCic patients ( $P < 0.05$ ), and sMCI-1y patients had lower MMSE scores compared with sMCI patients ( $P < 0.05$ ).

## Global Network Analysis

The weighted correlation matrices for each group are presented in Figure 2. We observed that the correlation patterns of all groups showed strong correlations between bilaterally homologous regions.

In general, with progressively higher values of network density ( $D$ ), the characteristic path length and modularity decreased, the mean clustering coefficient and transitivity increased, and a small-world topology was observed across all groups (Fig. 3).

Our statistical analyses showed significant increases in the characteristic path length in the sMCI, IMCic, eMCic, and AD groups compared with controls at several network densities ( $P$  range, 0.043–0.001) (Fig. 4). The clustering coefficient also showed significant changes, being decreased across different densities in IMCic, eMCic, and AD ( $P$  range, 0.043–0.001) but not in sMCI patients, compared with controls. The transitivity and modularity showed the greatest differences between patients and controls: the transitivity was significantly decreased ( $P$  range, 0.049–0.001) and the modularity was significantly increased ( $P$  range, 0.049–0.001) in patients at most network densities (Fig. 4). We also found significant decreases in the small-worldness in the patient groups compared with controls ( $P$  range, 0.040–0.010); however, these differences were only observed at a few network thresholds (Fig. 4).

When we compared the different patient groups, we observed that IMCic, eMCic, and AD patients had a decreased characteristic path length ( $P$  range, 0.048–0.001) and clustering coefficient

Table 1 Characteristics of the sample

	CTR (n = 301)	sMCI-1y (n = 157)	sMCI (n = 110)	LMCic (n = 71)	eMCic (n = 87)	AD (n = 282)	F or $\chi^2$ (P value)
Age	75.1 (5.7)	75.0 (6.5)	74.7 (7.5)	74.8 (7.0)	74.1 (6.7)	75.6 (7.0)	0.9 (0.475)
Gender (m/f) <sup>a,b,c,d,e</sup>	156/145	88/69	74/36	43/28	54/33	130/152	19.2 (0.002)
Education (y) <sup>f,a,g,h,i,j,k,l,c,m,d,e</sup>	14.2 (4.4)	11.8 (5.2)	15.7 (3.0)	16.1 (3.0)	13.9 (4.2)	12.2 (4.9)	21.2 (<0.001)
MMSE <sup>f,a,g,n,h,i,b,o,l,c,d,e</sup>	29.1 (1.1)	27.0 (1.6)	27.6 (1.7)	26.7 (1.7)	26.6 (1.8)	22.4 (3.5)	272.8 (<0.001)
CDR <sup>f,a,g,n,h,b,c,d,e</sup>	0	0.5	0.5	0.5	0.5	0.9 (0.4)	880.2 (<0.001)

Note: Means are followed by standard deviations. Differences in age, years of education, and MMSE scores were assessed using an analysis of variance (ANOVA). Differences in CDR scores were assessed using a Kruskal–Wallis test and differences in gender were assessed using a  $\chi^2$  test. CTR, controls; sMCI, stable mild cognitive impairment after 1 year (sMCI-1y) or 3 years (sMCI); LMCic, late mild cognitive impairment converters; eMCic, early mild cognitive impairment converters; AD, Alzheimer's disease; MMSE, mini-mental state examination; CDR, clinical dementia rating scale.

<sup>a</sup>Significant differences between CTR and sMCI patients ( $P < 0.05$ ).

<sup>b</sup>Significant differences between sMCI-1y and AD patients ( $P < 0.05$ ).

<sup>c</sup>Significant differences between sMCI and AD patients ( $P < 0.05$ ).

<sup>d</sup>Significant differences between LMCic and AD patients ( $P < 0.05$ ).

<sup>e</sup>Significant differences between eMCic and AD patients ( $P < 0.05$ ).

<sup>f</sup>Significant differences between CTR and sMCI-1y patients ( $P < 0.05$ ).

<sup>g</sup>Significant differences between CTR and LMCic patients ( $P < 0.05$ ).

<sup>h</sup>Significant differences between CTR and AD patients ( $P < 0.05$ ).

<sup>i</sup>Significant differences between sMCI-1y and sMCI patients ( $P < 0.05$ ).

<sup>j</sup>Significant differences between sMCI-1y and LMCic patients ( $P < 0.05$ ).

<sup>k</sup>Significant differences between sMCI-1y and eMCic patients ( $P < 0.05$ ).

<sup>l</sup>Significant differences between sMCI and eMCic patients ( $P < 0.05$ ).

<sup>m</sup>Significant differences between LMCic and eMCic patients ( $P < 0.05$ ).

<sup>n</sup>Significant differences between CTR and eMCic patients ( $P < 0.05$ ).

<sup>o</sup>Significant differences between sMCI and LMCic patients ( $P < 0.05$ ).

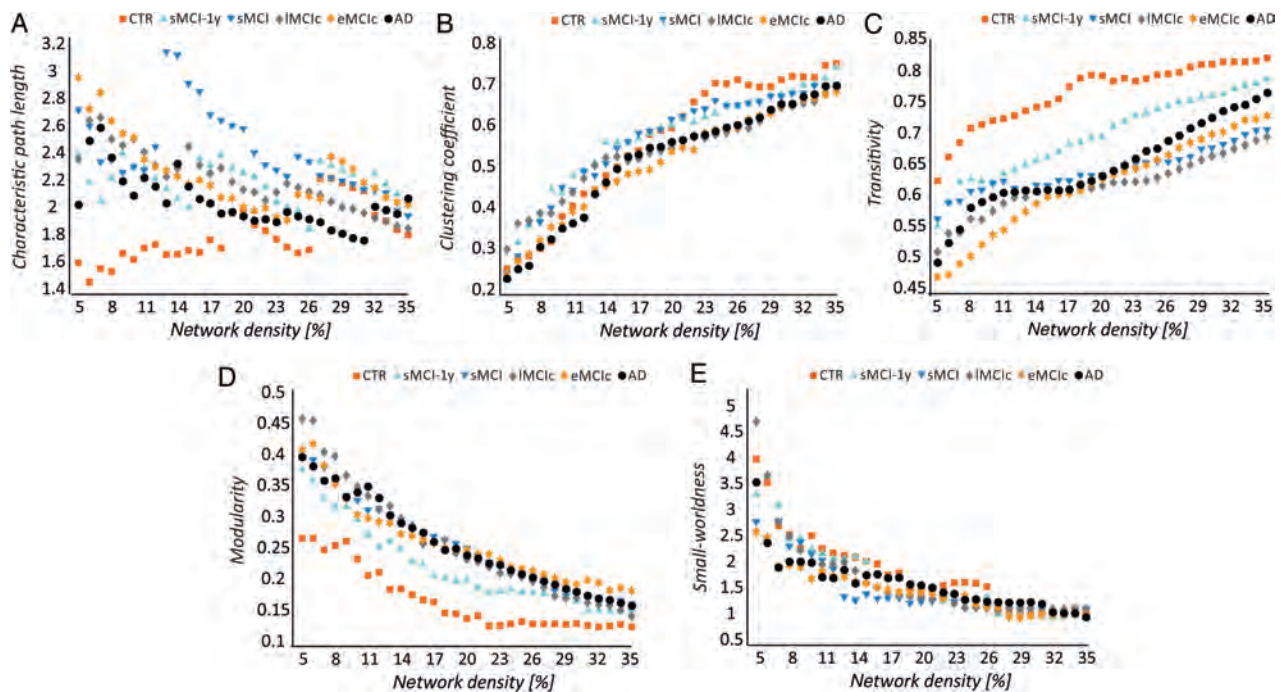


Figure 3. Changes in global network measures as a function of network density. Characteristic path length (A), clustering coefficient (B), transitivity (C), modularity (D), and small-worldness (E) for controls (CTR), patients with stable mild cognitive impairment after 1 year (sMCI-1y), patients with sMCI (after 3 years), LMCic, eMCic, and AD patients.

( $P$  range, 0.042–0.001) compared with sMCI patients (Fig. 5). There were no significant differences in transitivity or modularity between these groups. In addition, there were no differences in global network topology between LMCic, eMCic, and AD patients.

The global network comparisons carried out in the sMCI-1y group can be found in [Supplementary Figure 1](#). These patients showed evidence of larger paths ( $P$  range, 0.045–0.004) and

changes in the clustering ( $P$  range, 0.044–0.018) at a few network thresholds, but no changes in the transitivity or modularity compared with controls, in contrast to the other MCI groups. They also showed higher clustering compared with eMCic ( $P$  range, 0.046–0.018) and AD patients ( $P$  range, 0.043–0.016) and higher transitivity ( $P$  range, 0.048–0.019) compared with AD patients at several densities. The modularity and small-worldness did not



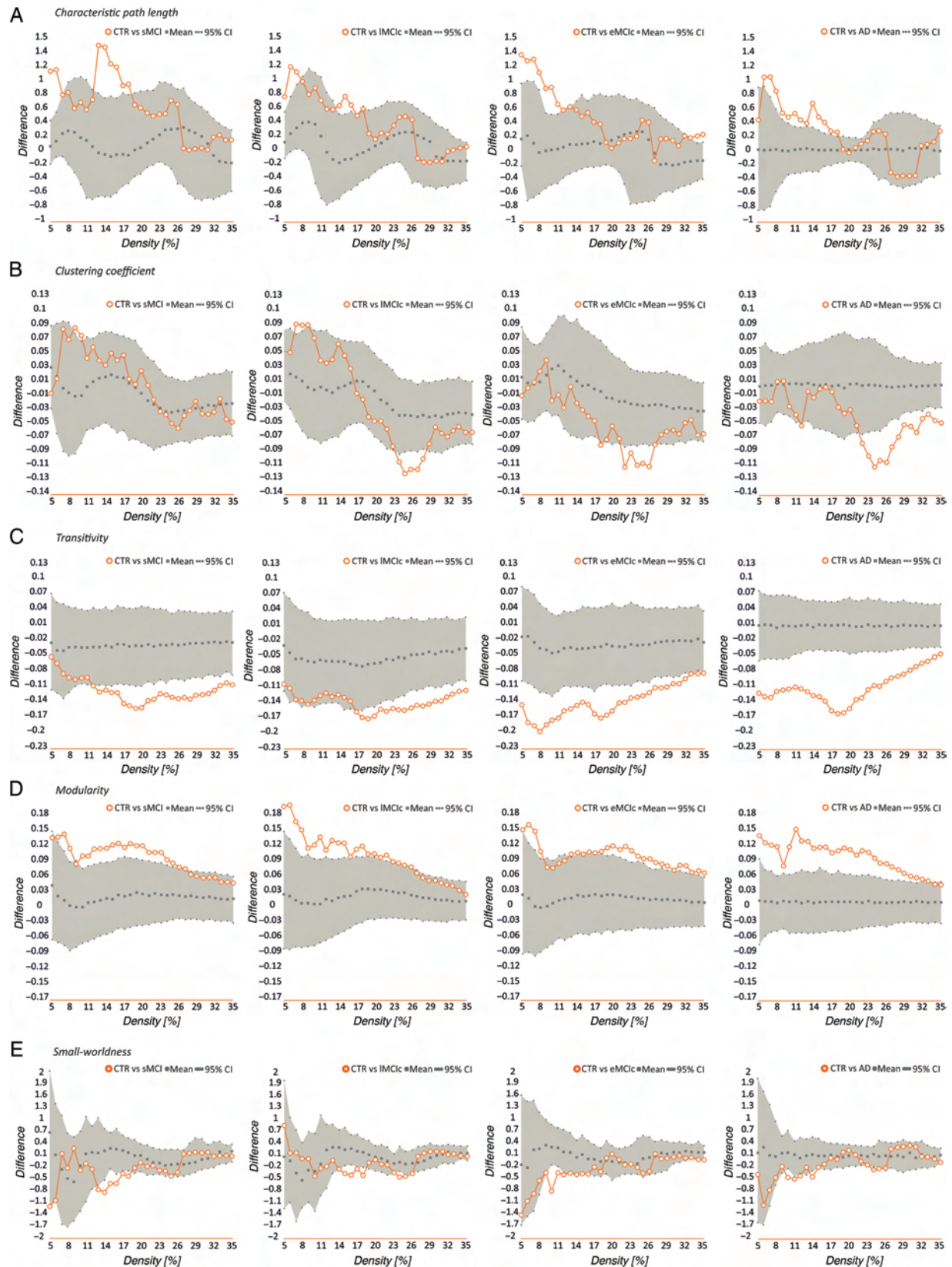


**Figure 4.** Differences between controls, sMCI, IMCI, eMCI, and AD patients in global network measures. Plots showing the differences between controls (CTR) and sMCI patients; CTR and IMCI; CTR and eMCI; CTR and AD patients in the characteristic path length (A), clustering coefficient (B), transitivity (C), modularity (D), and small-worldness (E). The plots show the upper and lower bounds of the 95% confidence intervals (CI) (in gray) and the differences in the network measures between groups (in orange circles) as a function of network density. If these differences fall outside the CIs, there is a statistical significant difference at  $P < 0.05$ .

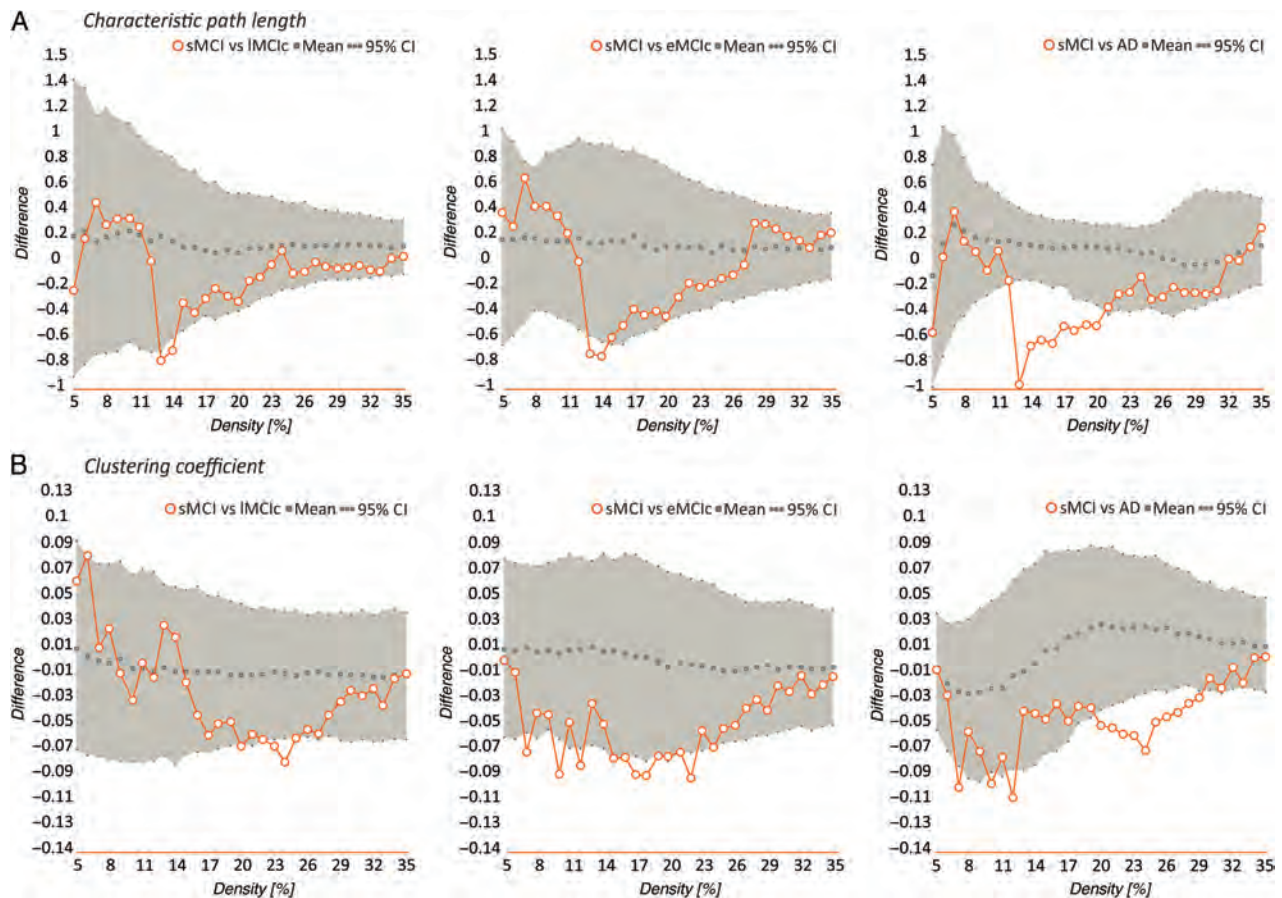


**Figure 5.** Differences between sMCI, lMCic, eMCic, and AD patients in global network measures. Plots showing the differences between sMCI and lMCic patients; sMCI and eMCic patients; sMCI and AD patients in the characteristic path length (A) and clustering coefficient (B). The plots show the upper and lower bounds of the 95% confidence intervals (CI) (in gray) and the differences in the network measures between groups (in orange circles) as a function of network density. If these differences fall outside the CIs, there is a statistical significant difference at  $P < 0.05$ .

show significant changes in sMCI-1y compared with the other patient groups.

To assess whether our results were influenced by different scanning centers, we repeated the analyses comparing controls to the patient groups after including the centers as an additional covariate. These analyses showed similar differences in the characteristic path length, mean clustering, transitivity, and modularity between patients and controls, suggesting that the differences in scanning sites did not influence our results (see [Supplementary Table 1](#)).

### Nodal Network Analysis

We identified several changes in nodal network measures between groups. In summary, the nodal clustering was decreased in patients compared with controls and showed widespread changes only in the AD group. The nodal closeness centrality was decreased in the bilateral hippocampi and amygdala across all patient groups and showed increases in medial parietal, medial temporal, and limbic regions that varied according to the patient group. Below, we describe these changes in greater detail.

After correcting for multiple comparisons ( $FDR, q < 0.05$ ), we observed that sMCI patients showed clustering decreases in the left superior frontal gyrus, while eMCic patients showed

decreases in the right postcentral gyrus compared with controls. In AD patients, the nodal clustering decreases involved several regions: the bilateral precuneus, superior frontal gyri, lateral orbitofrontal gyri, middle temporal gyri, inferior temporal gyri, fusiform, hippocampi, and amygdala; the left pars triangularis gyrus, postcentral gyrus; and the right caudal middle frontal gyrus, pars opercularis gyrus, and lateral occipital gyrus (Fig. 6 and Table 2). AD patients also showed significant clustering decreases in the left postcentral gyrus compared with sMCI patients ( $FDR, q < 0.05$ ).

Regarding the closeness centrality, in addition to the significant decreases found in the hippocampi and amygdala in sMCI, lMCic, eMCI, and AD patients compared with controls, there were additional decreases in the right pericalcarine gyrus in sMCI and lMCic patients; the right accumbens in eMCic patients. The increases in closeness centrality were observed in the left posterior cingulate in sMCI patients; the left pallidum, right insula, right temporal pole, right entorhinal in lMCic patients; the left posterior cingulate, right lateral orbitofrontal gyrus, bilateral insula, bilateral entorhinal in AD patients (Fig. 7 and Table 3).

There were also significant differences in closeness centrality between the patient groups, mostly in temporal, occipital, and subcortical regions (for further details, see Table 3).

In Table 4, we present a summary of the most relevant global and nodal network results found in the current study.

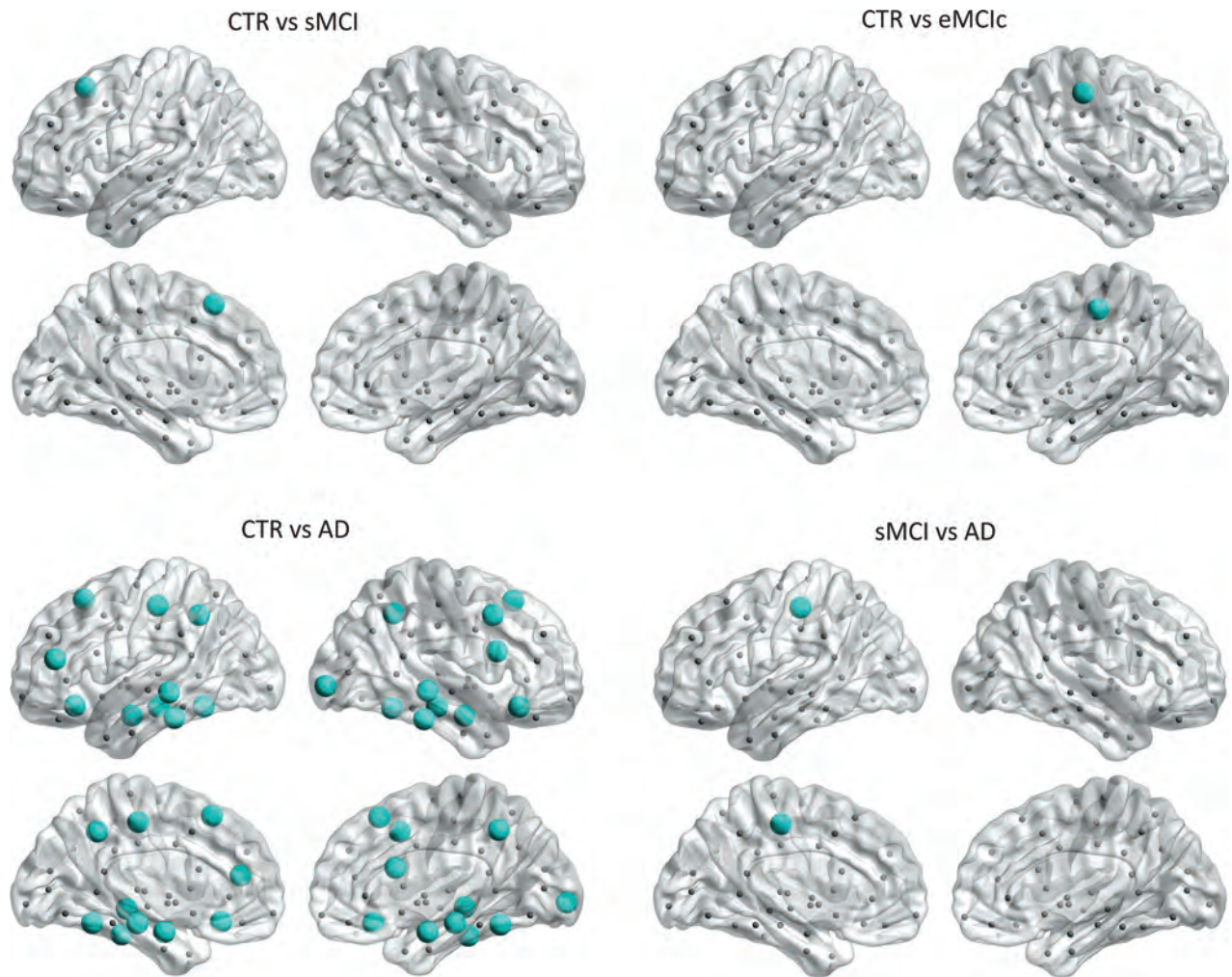


**Figure 6.** Significant decreases in the nodal clustering coefficient in sMCI, eMCIc, and AD patients. CTR, controls; sMCI, stable MCI; eMCIc, early MCI converters, AD, Alzheimer's disease. The regions showing clustering decreases in patients are listed in Table 2.

### Brain Modules

We identified 4 modules in controls; 3 modules in sMCI, lMCIc, and eMCIc patients; and 5 modules in AD patients (Fig. 8). For a full list of the regions belonging to each module, see Table 5.

Briefly, in controls, Module I included the superior frontal gyri, posterior cingulate, and supramarginal gyri, which are part of the default-mode network. Module II included the entorhinal gyri and subcortical regions. Module III was the largest, including several lateral frontal, parietal, and occipital regions. Module IV included the parahippocampal gyri.

In sMCI, lMCIc, and eMCIc patients, the modules were similar to those in controls. However, Module I did not include the superior frontal, lateral parietal, or posterior parietal regions and Module II included additional areas in the patient groups. In AD patients, Module II lost several regions that formed 2 new modules, which were not present in the other groups: one composed of the caudate, putamen, accumbens, and pallidum (Module IV) and the other composed of the bilateral thalami (Module V).

To assess differences between groups in the previous modules, we measured the within-module degree and participation coefficient. We found significant increases in the within-module degree and decreases in the participation coefficient in AD patients compared with controls, after FDR corrections (Table 6).

The within-module degree increases were observed in the left postcentral, left superior parietal, right pars opercularis gyri, and right insula, which were part of Module I and Module III. The participation coefficient decreases were observed in the left pars orbitalis and bilateral cuneus, which were part of Module III. Although they did not survive correction for multiple comparisons, lMCIc and eMCIc patients also showed within-module degree increases and participation coefficient decreases in some of these regions, compared with controls (Table 6).

### Discussion

This study is the largest to date to assess network topology in MCI patients that remain stable, show a slow or fast progression to dementia as well as AD patients. Our findings revealed an abnormal organization in the networks of all patient groups as reflected by an increased path length, reduced transitivity, and increased modularity, compared with controls. The clustering coefficient showed a different pattern, being decreased in lMCIc, eMCIc, and AD but not in sMCI patients. Altogether, these findings suggest that the prodromal and clinical stages of AD are associated with a reduced ability to integrate information across distributed brain regions and an altered communication between neighboring areas and modules.

**Table 2** Significant differences in the nodal clustering coefficient between groups (FDR-corrected)

Region	CTR	sMCI	P value
Lh Superior frontal G	0.83	0.50	0.002
Rh Postcentral	CTR 0.94	eMCIC 0.56	0.001
Lh Superior frontal G	CTR 0.83	AD 0.57	0.001
Lh Lateral orbitofrontal G	0.81	0.51	0.001
Lh Pars triangularis G	0.90	0.65	0.001
Lh Postcentral G	0.96	0.68	0.001
Lh Precuneus	0.78	0.58	0.001
Lh Middle temporal G	0.78	0.62	0.017
Lh Inferior temporal G	0.94	0.64	0.002
Lh Fusiform	0.79	0.56	0.004
Lh Hippocampus	1	0.33	0.001
Lh Amygdala	1	0.33	0.001
Rh Superior frontal G	0.78	0.52	0.001
Rh Caudal middle frontal G	0.92	0.77	0.009
Rh Lateral orbitofrontal G	0.71	0.45	0.003
Rh Pars opercularis G	0.96	0.62	0.001
Rh Precuneus	0.80	0.62	0.017
Rh Lateral occipital G	0.74	0.60	0.007
Rh Middle temporal G	0.81	0.61	0.016
Rh Inferior temporal G	0.90	0.66	0.003
Rh Fusiform	0.84	0.53	0.001
Rh Hippocampus	1	0.33	0.001
Rh Amygdala	1	0.33	0.001
Lh Postcentral	sMCI 0.95	AD 0.68	0.001

Note: CTR, controls; sMCI, stable mild cognitive impairment; lMCIC, late mild cognitive impairment converters; eMCIC, early mild cognitive impairment converters; AD, Alzheimer's disease; Lh, left hemisphere; Rh, right hemisphere; G, gyrus.

In the current study, we found a larger path length across all patient groups compared with controls, indicating an abnormal global network organization. Previous evidence suggests that a short path length ensures rapid information transmission across remote brain regions that are thought to be the basis of cognitive functioning (Sporns and Zwi 2004). The path length increases found in our study show that the distance between any 2 regions was greater in the patient's networks, making the communication between them less efficient. This finding is in line with those of previous graph theory studies in AD, which found an increased path length in the structural and functional networks of these patients (He et al. 2008; Lo et al. 2010; Sanz-Arigita et al. 2010; Yao et al. 2010; Shu et al. 2012). In one of these studies using DTI to build individual white matter networks, the path length increases were associated with worse MMSE performance (Shu et al. 2012), suggesting that this measure might indeed be a marker of cognitive dysfunction in AD.

Our analyses also showed decreases in the mean clustering coefficient in lMCIC, eMCIC, and AD patients relative to controls, indicating that there were fewer connections between neighboring areas in their networks. This result is in line with some (Tijms, Moller, et al. 2013; Tijms, Wink, et al. 2013) but not all previous studies (He et al. 2008; Yao et al. 2010), suggesting that differences in methodology, sample sizes, and patient characteristics might lead to different network findings. In a previous study, Li et al. (2012) found that MCI converters presented

longitudinal decreases of the clustering coefficient suggesting that reductions in this network measure are associated with conversion to dementia in AD.

Furthermore, our study is the first to assess transitivity and modularity in the structural networks of MCI and AD patients. We found that these measures identified greater abnormalities in the networks of all patient groups compared with the path length or clustering, reaching significance across most network densities. Similarly to the clustering coefficient, the transitivity is a measure that reflects how well a region is integrated within its local cluster. However, in contrast to the clustering, the transitivity is less influenced by nodes with fewer connections (Rubinov and Sporns 2010), being a superior measure in networks with poorly connected nodes. Hence, we recommend the use of this measure in future studies assessing structural networks in amnesic MCI and AD as it offers greater sensitivity to the effects of the disease. The modularity is a more sophisticated measure that describes the existence of communities of regions within the network (Newman 2004). This network measure increases when brain regions are well connected within their module but are poorly connected with regions belonging to other modules. In the current study, we found significant modularity increases in sMCI, lMCIC, eMCIC, and AD patients compared with controls, indicating higher intramodule connectivity and lower connectivity between modules. This finding indicates that there is a worse communication between modules in patients, suggesting that their whole-brain networks were fragmented into a few large, isolated components. The within-module degree increases and participation coefficient decreases we found in frontal, parietal, and occipital regions in the patient groups compared with controls further confirm that the modules were well connected within themselves but not between each other in patients. In a previous fMRI study, significant modularity increases were also found in patients with Parkinson's disease with mild cognitive impairment, who have a higher risk of developing dementia (Baggio et al. 2014). These increases in modularity can be interpreted as an abnormal process by which the connections between brain areas belonging to a certain module increase, leaving the other modules relatively isolated. In that study, the abnormal modularity increases were associated with worse memory and visuospatial performance in Parkinson's patients, confirming they were pathological and related to greater clinical decline (Baggio et al. 2014). In our study, we also observed that, despite having similar modules to controls, the regions belonging to each module changed across the patient groups, with AD patients showing 2 modules that were not present in the other groups. Hence, our findings suggest that there is a reorganization of the modules in sMCI, lMCIC, eMCIC, and AD patients. Similarly to previous studies assessing modularity in structural MRI networks (Chen et al. 2008, 2011; Wu et al. 2012), we did not find an exact correspondence between the brain modules and previously reported resting-state fMRI networks (Greicius et al. 2004).

In addition to global network changes, we also observed alterations in the topology of specific brain regions. We found there were decreases in the nodal clustering of several areas in AD patients compared with controls, indicating worse local communication between neighboring areas. Some of these areas belonged to the default-mode network and included the precuneus and superior frontal gyri (Greicius et al. 2004), in line with our initial hypothesis and with previous studies showing pathological changes within this network in AD (Buckner et al. 2005, 2009; Li et al. 2013). In addition, we also observed clustering decreases in other frontal and temporal regions in AD patients, suggesting that the regional clustering changes were quite widespread, in

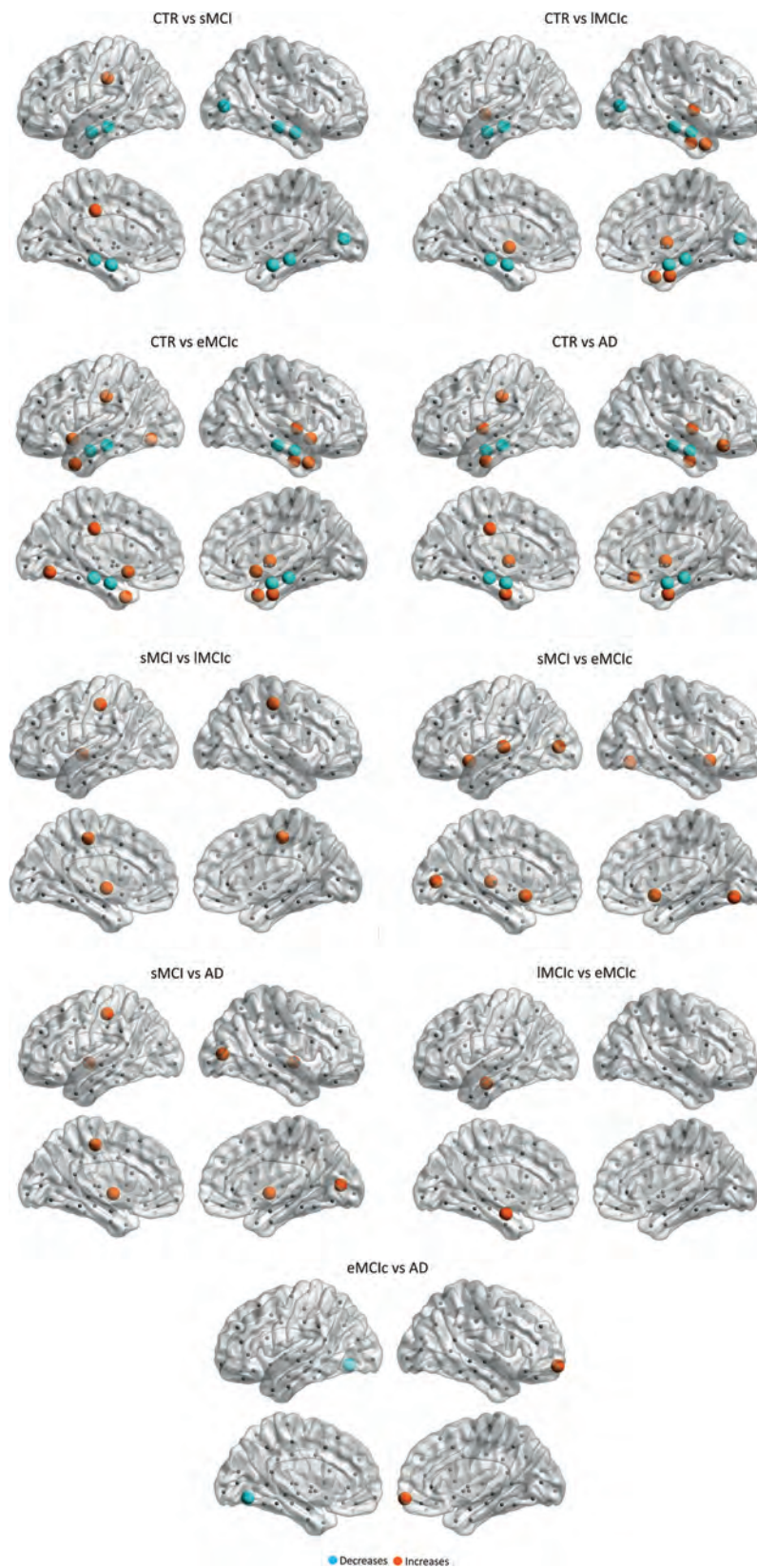


**Figure 7.** Significant differences in the closeness centrality between controls and sMCI, IMCic, eMCic, and AD patients. CTR, controls; sMCI, stable mild cognitive impairment; IMCic, late MCI converters; eMCic, early MCI converters; AD, Alzheimer's disease. The regions showing significant closeness centrality decreases are colored in blue, while the regions showing closeness centrality increases in patients are colored in orange. These regions are listed in Table 3.

**Table 3** Significant differences in the nodal closeness centrality between groups (FDR-corrected)

Region	CTR	sMCI	P value
Lh Posterior cingulate	0.30	0.48	0.001
Lh Hippocampus	1	0.29	0.001
Lh Amygdala	1	0.34	0.001
Rh Pericalcarine	0.38	0.28	0.001
Rh Hippocampus	1	0.38	0.001
Rh Amygdala	1	0.33	0.001
	CTR	lMCiC	
Lh Pallidum	0.39	1	0.001
Lh Hippocampus	1	0.39	0.001
Lh Amygdala	1	0.34	0.001
Rh Insula	0.28	0.53	0.001
Rh Pericalcarine	0.38	0.30	0.001
Rh Temporal pole	0.29	0.46	0.001
Rh Entorhinal	0.22	0.45	0.001
Rh Hippocampus	1	0.44	0.001
Rh Amygdala	1	0.33	0.001
	CTR	eMCiC	
Lh Posterior cingulate	0.30	0.54	0.001
Lh Lingual G	0.43	0.56	0.001
Lh Temporal pole	0.39	0.49	0.001
Lh Hippocampus	1	0.26	0.001
Lh Amygdala	1	0.35	0.001
Lh Accumbens	0.36	1	0.001
Rh Insula	0.28	0.49	0.001
Rh Temporal pole	0.29	0.45	0.001
Rh Entorhinal	0.22	0.46	0.001
Rh Hippocampus	1	0.32	0.001
Rh Amygdala	1	0.32	0.001
Rh Accumbens	0.54	1	0.001
	CTR	AD	
Lh Insula	0.38	0.51	0.001
Lh Posterior cingulate	0.30	0.55	0.001
Lh Entorhinal	0.29	0.44	0.001
Lh Hippocampus	1	0.31	0.001
Lh Amygdala	1	0.31	0.001
Rh Lateral orbitofrontal G	0.47	0.58	0.006
Rh Insula	0.28	0.53	0.001
Rh Entorhinal	0.22	0.44	0.001
Rh Hippocampus	1	0.31	0.001
Rh Amygdala	1	0.31	0.001
	sMCI	lMCiC	
Lh Postcentral G	0.41	0.58	0.005
Lh Pallidum	0.21	1	0.001
Rh Postcentral	0.41	0.61	0.001
	sMCI	eMCiC	
Lh Pericalcarine	0.26	0.41	0.001
Lh Transverse temporal G	0.40	0.54	0.001
Lh Accumbens	0.21	1	0.001
Rh Lingual G	0.32	0.50	0.001
Rh Accumbens	0.21	1	0.001
	sMCI	AD	
Lh Postcentral G	0.41	0.60	0.001
Lh Pallidum	0.21	1	0.001
Rh Pericalcarine	0.28	0.37	0.001
Rh Pallidum	0.21	1	0.001
	lMCiC	eMCiC	
Lh Accumbens	0.30	1	0.001
	eMCiC	AD	
Lh Lingual	0.55	0.43	0.001
Rh Frontal pole	0.34	0.45	0.001

Note: CTR, controls; sMCI, stable mild cognitive impairment; lMCiC, late mild cognitive impairment converters; eMCiC, early mild cognitive impairment converters; AD, Alzheimer's disease; Lh, left hemisphere; Rh, right hemisphere; G, gyrus.

line with evidence showing extended brain atrophy at advanced stages of AD (Lehmann et al. 2011). The MCI patient groups only showed clustering decreases in a few frontal and parietal regions, in contrast with the widespread changes observed in AD patients.

The nodal closeness centrality showed both increases and decreases in sMCI, lMCiC, eMCiC, and AD patients compared with controls. The decreases were mainly observed in the bilateral hippocampi and amygdala across all patient groups, indicating a loss of number of connections between these structures and other regions of the network. This could be related to white matter integrity loss or disruption of white matter fibers connecting these brain areas, which has been previously observed in MCI and AD patients in DTI studies (for a review, see Chua et al. 2008). The increases of closeness centrality were mainly observed in the posterior cingulate, temporal pole, entorhinal cortex, insula, and orbitofrontal regions. The closeness centrality is a measure of interaction between regions; the fact that it is increased in regions showing pathological changes in AD (Braak and Braak 1991; Thal et al. 2002; Frisoni et al. 2010) could be related to shared mechanisms in neurodegeneration (Zhu et al. 2012). Within the graph theory framework, 2 regions might correlate with each other not only if they are structurally or functionally connected but also if they become atrophied at the same rate (Alexander-Bloch et al. 2013). Thus, since medial temporal, medial parietal, and limbic regions show atrophy since early stages of AD, it seems natural that they might strongly interact with other regions in the network that become atrophied with disease progression.

In the current study, we also compared global and local network topology between the patient groups. We observed that sMCI patients had a larger path length and reduced nodal closeness centrality in several regions compared with the other patients, indicating that they presented greater abnormalities in the communication or interaction between distant brain areas. Previous evidence suggests that the initial pathological changes occurring in AD do not target regions that are close to each other but rather distant brain areas (Zhou et al. 2012), which are often connected by long and poorly myelinated axons. Hence, it is possible that these changes are more prominent in sMCI patients, which are potentially at earlier stages of AD. In contrast to the path length, the clustering coefficient was reduced in lMCiC, eMCiC, and AD patients compared with sMCI patients, suggesting that the loss of connections between neighboring areas reflects better the changes occurring in patients that are on the path to develop AD or already have dementia.

In the past few years, there has been increasing evidence showing that there is substantial heterogeneity among MCI patients. For instance, many MCI subjects remain stable for several years, while others show a fast progression to dementia and some can even fully reverse to normal cognition (Koepsell and Monsell 2012). Moreover, there are several non-AD pathologies that may produce amnesic MCI such as frontotemporal dementia (Yaffe et al. 2006), vascular dementia (Zanetti et al. 2006), and hippocampal sclerosis (Dickson et al. 1994). In the current study, we observed heterogeneity in the network topology abnormalities between the MCI groups. Specifically, sMCI-1y patients showed evidence of increased clustering and almost no changes in the transitivity and modularity compared with controls (see Supplementary Fig. 1), in contrast to the other MCI patients. It is possible that the sMCI-1y group included a mixture of subjects who remained stable, converted to dementia after a few years, had a non-AD related disorder or simply did not have any neurodegenerative disease (the cognitive deficits they presented were due to a transient medical condition). This heterogeneity might

Table 4 Summary of the most relevant global and nodal network results

Measures	CTR vs. sMCI	CTR vs. lMCic	CTR vs. eMCic	CTR vs. AD	sMCI vs. lMCic	sMCI vs. eMCic	sMCI vs. AD
Characteristic path length	↑	↑	↑	↑	↓	↓	↓
Clustering coefficient	—	↓	↓	↓	↓	↓	↓
Transitivity	↓	↓	↓	↓	—	—	—
Modularity	↑	↑	↑	↑	—	—	—
Small-worldness	↓	↓	↓	↓	—	—	—
Nodal clustering	↓	—	↓	↓	—	—	↓
	1 region		1 region	21 regions			1 region
Nodal closeness centrality	↓	↓	↓	↓	—	—	—
	5 regions	5 regions	4 regions	4 regions			
	↑	↑	↑	↑	↑	↑	↑
	1 region	4 regions	8 regions	6 regions	3 regions	5 regions	4 regions

Note: Compared with controls, all patient groups showed an increased path length and modularity as well as changes in the nodal closeness centrality. The mean clustering coefficient was decreased only in lMCic, eMCic, and AD groups, while the nodal clustering showed the most prominent changes in AD patients by being decreased in a total of 21 regions compared with controls. Compared with sMCI patients, the other patient groups showed a decreased path length, mean clustering coefficient, and increased closeness centrality. There were also nodal clustering decreases in 1 region in AD patients compared with sMCI patients.

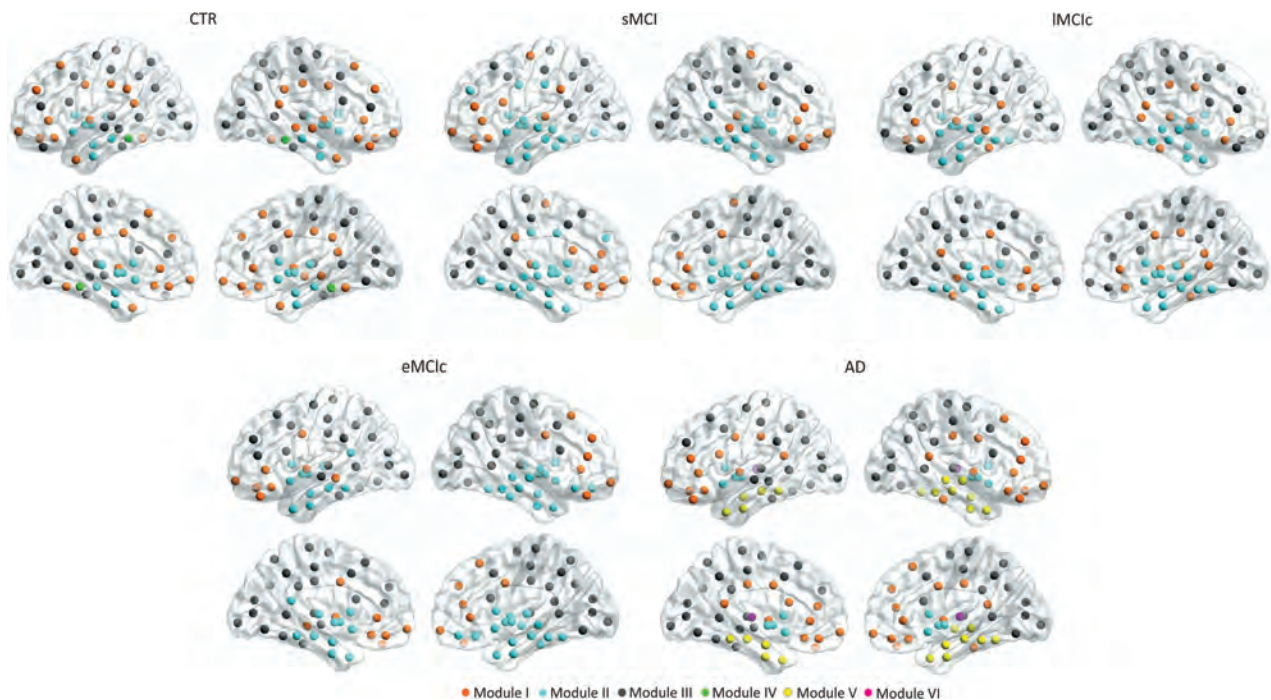


Figure 8. Brain modules in controls and sMCI, lMCic, eMCic, and AD patients. CTR, controls; sMCI, stable mild cognitive impairment; lMCic, late MCI converters; eMCic, early MCI converters; AD, Alzheimer's disease. Four modules were identified in the networks of CTR; 3 modules were identified in sMCI, lMCic, and eMCic patients; 5 modules were identified in the networks of AD patients. For each group, the left and right lateral (top) and medial (bottom) brain views are shown.

account for the lack of changes in the transitivity and modularity in sMCI-1y, in contrast to the other groups that were more homogeneous. Studies assessing network topology in MCI subjects should consider their results with respect to this important heterogeneity.

Although brain networks are sparse, current neuroimaging analyses build network representations that are continuous association matrices (Fornito et al. 2013). For this reason, many studies apply a threshold to these matrices in an attempt to retain the true brain connections and remove the potentially spurious ones. One way of applying a threshold is to retain the connections that overcome a level of significance. However, this approach will result in different groups of subjects having

different numbers of edges or connections. In the current study, we applied a threshold to the connectivity matrices of each group by retaining the most significant connections, while ensuring an equal number of connections across groups. Although this step would ideally consist of applying a single threshold to the connectivity matrices of different groups, there is currently no absolute way of determining which threshold is best (Fornito et al. 2013). For this reason, we decided to test for group differences across a range of densities, similarly to previous studies (He et al. 2008; Yao et al. 2010). Since it does not make sense to compute topological measures in networks that have a random configuration, in the current study we defined the higher bound of this range using the small-world index,

Table 5 Brain modules in controls, sMCI, lMCiC, eMCiC, and AD patients

Hemisphere	Brain region	Modules CTR	Modules sMCI	Modules lMCiC	Modules eMCiC	Modules AD
Left	Superiorfrontal	I	III	III	III	III
Left	Frontalpole	I	I	III	I	I
Left	Rostralmiddlefrontal	I	II	III	III	III
Left	Caudalmiddlefrontal	III	III	III	III	III
Left	Parsorbitalis	III	I	III	I	I
Left	Lateralorbitofrontal	I	I	I	I	I
Left	Parstriangularis	III	I	III	III	I
Left	Parsopercularis	III	I	III	III	I
Left	Medialorbitofrontal	I	I	I	I	I
Left	Rostralanteriorcingulate	I	I	I	I	I
Left	Caudalanteriorcingulate	I	II	I	I	I
Left	Insula	I	II	I	I	I
Left	Precentral	III	I	III	III	III
Left	Postcentral	III	III	III	III	III
Left	Supramarginal	I	I	III	III	III
Left	Superiorparietal	III	III	III	III	III
Left	Inferiorparietal	III	III	III	III	III
Left	Paracentral	III	III	III	III	III
Left	Posteriorcingulate	I	II	III	III	I
Left	Isthmuscingulate	I	II	I	III	I
Left	Precuneus	III	III	III	III	III
Left	Cuneus	III	III	III	III	III
Left	Pericalcarine	III	III	III	III	III
Left	Lingual	III	III	III	III	III
Left	Lateraloccipital	III	III	III	III	III
Left	Transversetemporal	III	I	III	III	III
Left	Bankssts	III	III	III	III	III
Left	Superiortemporal	III	II	II	III	III
Left	Middletemporal	III	II	I	I	III
Left	Inferiortemporal	III	II	I	III	III
Left	Temporalpole	I	II	II	II	V
Left	Entorhinal	II	II	II	II	V
Left	Parahippocampal	IV	II	II	II	V
Left	Fusiform	I	II	II	III	III
Left	Thalamus	II	II	II	II	VI
Left	Caudate	II	II	II	II	II
Left	Putamen	II	II	II	II	II
Left	Pallidum	II	II	II	II	II
Left	Hippocampus	II	II	II	II	V
Left	Amygdala	II	II	II	II	V
Left	Accumbens	II	II	II	II	II
Right	Superiorfrontal	I	III	III	I	I
Right	Frontalpole	I	I	III	I	I
Right	rostralmiddlefrontal	I	III	III	I	I
Right	Caudalmiddlefrontal	III	III	III	III	III
Right	Parsorbitalis	I	I	III	I	I
Right	Lateralorbitofrontal	I	I	I	II	I
Right	Parstriangularis	III	I	III	I	I
Right	Parsopercularis	III	III	III	III	III
Right	Medialorbitofrontal	I	I	III	II	I
Right	Rostralanteriorcingulate	I	I	I	I	I
Right	Caudalanteriorcingulate	I	I	I	I	I
Right	Insula	I	II	I	II	I
Right	Precentral	III	I	III	III	III
Right	Postcentral	III	III	III	III	III
Right	Supramarginal	I	III	III	III	III
Right	Superiorparietal	III	III	III	III	III
Right	Inferiorparietal	III	III	III	III	III
Right	Paracentral	III	III	III	III	III
Right	Posteriorcingulate	I	III	I	III	I
Right	Isthmuscingulate	I	III	I	II	I
Right	Precuneus	III	III	III	III	III

Continued



Table 5 Continued

Hemisphere	Brain region	Modules CTR	Modules sMCI	Modules lMCiC	Modules eMCiC	Modules AD
Right	Cuneus	III	III	III	III	III
Right	Pericalcarine	III	III	III	III	III
Right	Lingual	III	III	III	III	III
Right	Lateraloccipital	III	III	III	III	III
Right	Transversetemporal	III	I	I	III	III
Right	Bankssts	III	III	I	III	III
Right	Superiortemporal	I	II	II	II	V
Right	Middletemporal	I	I	II	II	V
Right	Inferiortemporal	III	II	I	II	I
Right	Temporalpole	I	II	II	II	V
Right	Entorhinal	II	II	II	II	V
Right	Parahippocampal	IV	II	II	II	V
Right	Fusiform	I	II	II	II	V
Right	Thalamus	II	II	II	II	VI
Right	Caudate	II	II	II	II	II
Right	Putamen	II	II	II	II	II
Right	Pallidum	II	II	II	II	II
Right	Hippocampus	II	II	II	II	V
Right	Amygdala	II	II	II	II	V
Right	Accumbens	II	II	II	II	II

Note: CTR, controls; sMCI, stable mild cognitive impairment; lMCiC, late mild cognitive impairment converters; eMCiC, early mild cognitive impairment converters; AD, Alzheimer's disease.

Table 6 Differences in the within-module degree and participation coefficient between groups

Within-module degree	CTR	lMCiC	P value
Region			
Rh Pars opercularis G	-3.29	0.53	0.002
Within-module degree			
Region			
Lh Postcentral G	-0.35	1.22	0.004
Lh Superior Parietal G	-0.35	0.99	0.017
Within-module degree			
Region			
Lh Postcentral G	-1.12	0.70	0.001
Lh Superior Parietal G	-1.12	0.89	0.002
Lh Superior Temporal G	0.39	1.86	0.003
Rh Pars Opercularis G	-2.81	0.42	0.001
Participation coefficient			
Region			
Lh Lateral Occipital G	0.66	0.23	0.004
Rh Postcentral G	0.66	0.24	0.008
Rh Lateral Occipital G	0.66	0.32	0.001

Note: CTR, controls; sMCI, stable mild cognitive impairment; lMCiC, late mild cognitive impairment converters; eMCiC, early mild cognitive impairment converters; AD, Alzheimer's disease; Lh, left hemisphere; Rh, right hemisphere; G, gyrus. Differences between controls and AD patients survived corrections for multiple comparisons with FDR, while the other differences between groups were significant at an uncorrected level ( $P < 0.05$ ).

which indicates whether the networks are meaningfully organized. Our results showed that there were significant differences between groups at different densities, suggesting they were consistent.

We would like to highlight that the present study has some limitations. First, despite providing useful information, the

analysis of structural covariance networks does not allow correlation analyses to be performed with clinical measures since there are no individual networks but only a network per group. Nevertheless, Tijms et al. (2012, 2016), Tijms, Moller, et al. (2013), and Tijms, Wink, et al. (2013) have overcome this limitation by providing a method that can create single-subject structural networks using structural MRI; this method could be considered in future graph theory studies assessing structural networks in large cohorts of AD and MCI patients. Secondly, we had limited longitudinal data regarding the clinical diagnosis of patients of only up to 3 years. Hence, it is possible that many of the individuals included in the sMCI group converted to dementia shortly after this period.

In conclusion, our study is the largest to date to assess structural network topology in stable MCI, progressive MCI, and AD by including 1008 patients and controls from 2 large multicenter cohorts. Our findings show, for the first time, that the transitivity and modularity are important graph theory measures that offer greater sensitivity to MCI and AD compared with the path length and clustering coefficient, which have been used more frequently in graph theory studies in AD. In addition, in contrast to previous studies, we provide a detailed description of nodal network changes in sMCI, lMCiC, eMCiC, and AD patients. Specifically, we show that while the nodal clustering showed widespread changes in AD patients, the closeness centrality detected alterations in several regions in all groups, showing overlapping changes in the hippocampi and amygdala and nonoverlapping changes in medial parietal and limbic areas in sMCI, lMCiC, eMCiC, and AD patients. These results offer an important glimpse into how AD progresses across different brain regions and ultimately leads to changes in global network organization.

## Supplementary Material

Supplementary material can be found at: <http://www.cercor.oxfordjournals.org/>.

## Funding

This study was supported by InnoMed, (Innovative Medicines in Europe) an Integrated Project funded by the European Union of the Sixth Framework program priority FP6-2004-LIFESCIHEALTH-5, Life Sciences, Genomics and Biotechnology for Health. Data collection and sharing for this project was funded by the Alzheimer's Disease Neuroimaging Initiative (ADNI) (National Institutes of Health Grant U01 AG024904) and DOD ADNI (Department of Defense award number W81XWH-12-2-0012). ADNI is funded by the National Institute on Aging, the National Institute of Biomedical Imaging and Bioengineering, and through generous contributions from the following: Alzheimer's Association; Alzheimer's Drug Discovery Foundation; BioClinica, Inc.; Biogen Idec Inc.; Bristol-Myers Squibb Company; Eisai Inc.; Elan Pharmaceuticals, Inc.; Eli Lilly and Company; F. Hoffmann-La Roche Ltd and its affiliated company Genentech, Inc.; GE Healthcare; Innogenetics, N.V.; IXICO Ltd.; Janssen Alzheimer Immunotherapy Research & Development, LLC.; Johnson & Johnson Pharmaceutical Research & Development LLC.; Medpace, Inc.; Merck & Co., Inc.; Meso Scale Diagnostics, LLC.; NeuroRx Research; Novartis Pharmaceuticals Corporation; Pfizer Inc.; Piramal Imaging; Servier; Synarc Inc.; and Takeda Pharmaceutical Company. The Canadian Institutes of Health Research is providing funds to support ADNI clinical sites in Canada. Private sector contributions are facilitated by the Foundation for the National Institutes of Health ([www.fnih.org](http://www.fnih.org)). The grantee organization is the Northern California Institute for Research and Education, and the study is coordinated by the Alzheimer's Disease Cooperative Study at the University of California, San Diego. ADNI data are disseminated by the Laboratory for Neuro Imaging at the University of California, Los Angeles. We would also like to thank the Swedish Foundation for Strategic Research (SSF), the Strategic Research Programme in Neuroscience at Karolinska Institutet (StratNeuro), Hjärfonden, and Birgitta och Sten Westerberg for additional financial support. J.B.P. was funded by a Marie Curie fellowship for postdoctoral researchers (grant No. FP7-PEOPLE-2012-IEF-328758). Funding to pay the Open Access publication charges for this article was provided by the Swedish Foundation for Strategic Research (SSF).

## Notes

*Conflict of Interest:* None declared.

## References

- Achard S, Bullmore E. 2007. Efficiency and cost of economical brain functional networks. *PLoS Comput Biol.* 3(2):e17.
- Alexander-Bloch A, Giedd JN, Bullmore E. 2013. Imaging structural co-variance between human brain regions. *Nat Rev Neurosci.* 14(5):322–336.
- Baggio HC, Sala-Llonch R, Segura B, Marti MJ, Valldeoriola F, Compta Y, Tolosa E, Junque C. 2014. Functional brain networks and cognitive deficits in Parkinson's disease. *Hum Brain Mapp.* 35(9):4620–4634.
- Bassett DS, Bullmore E. 2006. Small-world brain networks. *Neuroscientist.* 12(6):512–523.
- Bassett DS, Bullmore E, Verchinski BA, Mattay VS, Weinberger DR, Meyer-Lindenberg A. 2008. Hierarchical organization of human cortical networks in health and schizophrenia. *J Neurosci.* 28(37):9239–9248.
- Binnewijzend MA, Schoonheim MM, Sanz-Arigitia E, Wink AM, van der Flier WM, Tolboom N, Adriaanse SM, Damoiseaux JS, Scheltens P, van Berckel BN, et al. 2012. Resting-state fMRI changes in Alzheimer's disease and mild cognitive impairment. *Neurobiol Aging.* 33(9):2018–2028.
- Braak H, Alafuzoff I, Arzberger T, Kretschmar H, Del Tredici K. 2006. Staging of Alzheimer disease-associated neurofibrillary pathology using paraffin sections and immunocytochemistry. *Acta Neuropathol.* 112(4):389–404.
- Braak H, Braak E. 1991. Neuropathological stageing of Alzheimer-related changes. *Acta Neuropathol.* 82(4):239–259.
- Buckner RL, Sepulcre J, Talukdar T, Krienen FM, Liu H, Hedden T, Andrews-Hanna JR, Sperling RA, Johnson KA. 2009. Cortical hubs revealed by intrinsic functional connectivity: mapping, assessment of stability, and relation to Alzheimer's disease. *J Neurosci.* 29(6):1860–1873.
- Buckner RL, Snyder AZ, Shannon BJ, LaRossa G, Sachs R, Fotenos AF, Sheline YI, Klunk WE, Mathis CA, Morris JC, et al. 2005. Molecular, structural, and functional characterization of Alzheimer's disease: evidence for a relationship between default activity, amyloid, and memory. *J Neurosci.* 25(34):7709–7717.
- Bullmore E, Sporns O. 2012. The economy of brain network organization. *Nat Rev Neurosci.* 13(5):336–349.
- Chen ZJ, He Y, Rosa-Neto P, Germann J, Evans AC. 2008. Revealing modular architecture of human brain structural networks by using cortical thickness from MRI. *Cereb Cortex.* 18(10):2374–2381.
- Chen ZJ, He Y, Rosa-Neto P, Gong G, Evans AC. 2011. Age-related alterations in the modular organization of structural cortical network by using cortical thickness from MRI. *Neuroimage.* 56(1):235–245.
- Chua TC, Wen W, Slavin MJ, Sachdev PS. 2008. Diffusion tensor imaging in mild cognitive impairment and Alzheimer's disease: a review. *Curr Opin Neurol.* 21(1):83–92.
- Dai Z, He Y. 2014. Disrupted structural and functional brain connectomes in mild cognitive impairment and Alzheimer's disease. *Neurosci Bull.* 30(2):217–232.
- Desikan RS, Segonne F, Fischl B, Quinn BT, Dickerson BC, Blacker D, Buckner RL, Dale AM, Maguire RP, Hyman BT, et al. 2006. An automated labeling system for subdividing the human cerebral cortex on MRI scans into gyral based regions of interest. *Neuroimage.* 31(3):968–980.
- Dickson DW, Davies P, Bevona C, Van Hoesven KH, Factor SM, Grober E, Aronson MK, Crystal HA. 1994. Hippocampal sclerosis: a common pathological feature of dementia in very old ( $\geq 80$  years of age) humans. *Acta Neuropathol.* 88:212–221.
- Falahati F, Ferreira D, Soinen H, Mecocci P, Vellas B, Tsolaki M, Kłoszewska I, Lovestone S, Eriksdotter M, Wahlund LO, et al. 2016. The effect of age correction on multivariate classification in Alzheimer's disease, with a focus on the characteristics of incorrectly and correctly classified subjects. *Brain Topogr.* 29:296–307.
- Ferri R, Rundo F, Bruni O, Terzano MG, Stam CJ. 2007. Small-world network organization of functional connectivity of EEG slow-wave activity during sleep. *Clin Neurophysiol.* 118:449–456.
- Filippi M, van den Heuvel MP, Fornito A, He Y, Hulshoff Pol HE, Agosta F, Comi G, Rocca MA. 2013. Assessment of system dysfunction in the brain through MRI-based connectomics. *Lancet Neurol.* 12(12):1189–1199.
- Fischl B, Dale AM. 2000. Measuring the thickness of the human cerebral cortex from magnetic resonance images. *PNAS.* 97(20):11050–11055.
- Fischl B, Sereno MI, Dale AM. 1999. Cortical surface-based analysis. II: inflation, flattening, and a surface-based coordinate system. *Neuroimage.* 9(2):195–207.

- Fornito A, Zalesky A, Breakspear M. 2013. Graph analysis of the human connectome: promise, progress, and pitfalls. *Neuroimage*. 80:426–444.
- Frisoni GB, Fox NC, Jack CR Jr, Scheltens P, Thompson PM. 2010. The clinical use of structural MRI in Alzheimer disease. *Nat Rev Neurol*. 6(2):67–77.
- Genovese CR, Lazar NA, Nichols T. 2002. Thresholding of statistical maps in functional neuroimaging using the false discovery rate. *Neuroimage*. 15(4):870–878.
- Gong G, He Y, Concha L, Lebel C, Gross DW, Evans AC, Beaulieu C. 2009. Mapping anatomical connectivity patterns of human cerebral cortex using in vivo diffusion tensor imaging tractography. *Cereb Cortex*. 19:524–536.
- Greicius MD, Srivastava G, Reiss AL, Menon V. 2004. Default-mode network activity distinguishes Alzheimer's disease from healthy aging: evidence from functional MRI. *PNAS*. 101(13):4637–4642.
- Grundman M, Petersen RC, Ferris SH, Thomas RG, Aisen PS, Bennett DA, Foster NL, Jack CR Jr, Galasko DR, Doody R, et al. 2004. Mild cognitive impairment can be distinguished from Alzheimer disease and normal aging for clinical trials. *Arch Neurol*. 61(1):59–66.
- Guimera R, Amaral LA. 2005. Cartography of complex networks: modules and universal roles. *J Stat Mech*. (P02001):P02001-1–P02001-13.
- Guimera R, Mossa S, Turtschi A, Amaral LA. 2005. The worldwide air transportation network: Anomalous centrality, community structure, and cities' global roles. *PNAS*. 102(22):7794–7799.
- Hagmann P, Cammoun L, Gigandet X, Meuli R, Honey CJ, Wedeen VJ, Sporns O. 2008. Mapping the structural core of human cerebral cortex. *PLoS Biol*. 6:e159.
- He Y, Chen ZJ, Evans AC. 2007. Small-world anatomical networks in the human brain revealed by cortical thickness from MRI. *Cereb Cortex*. 17(10):2407–2419.
- He Y, Chen Z, Evans A. 2008. Structural insights into aberrant topological patterns of large-scale cortical networks in Alzheimer's disease. *J Neurosci*. 28(18):4756–4766.
- He Y, Wang J, Wang L, Chen ZJ, Yan C, Yang H, Tang H, Zhu C, Gong Q, Zang Y, et al. 2009. Uncovering intrinsic modular organization of spontaneous brain activity in humans. *PLoS ONE*. 4:e5226.
- Hosseini SM, Black JM, Soriano T, Bugescu N, Martinez R, Raman MM, Kesler SR, Hoef F. 2013. Topological properties of large-scale structural brain networks in children with familial risk for reading difficulties. *Neuroimage*. 71:260–274.
- Humphries MD, Gurney K, Prescott TJ. 2006. The brainstem reticular formation is a small-world, not scale-free, network. *Proc Royal Soc B Biol Sci*. 273:503–511.
- Iturria-Medina Y, Sotero RC, Canales-Rodriguez EJ, Aleman-Gomez Y, Melie-Garcia L. 2008. Studying the human brain anatomical network via diffusion-weighted MRI and graph theory. *Neuroimage*. 40:1064–1076.
- Jack CR Jr, Bernstein MA, Fox NC, Thompson P, Alexander G, Harvey D, Borowski B, Britson PJ, Whitwell J, Ward C, et al. 2008. The Alzheimer's disease neuroimaging initiative (ADNI): MRI methods. *J Magn Reson Imaging*. 27:685–691.
- Koepsell TD, Monsell SE. 2012. Reversion from mild cognitive impairment to normal or near-normal cognition Risk factors and prognosis. *Neurology*. 79(15):1591–1598.
- Lehmann M, Crutch SJ, Ridgway GR, Ridha BH, Barnes J, Warrington EK, Rossor MN, Fox NC. 2011. Cortical thickness and voxel-based morphometry in posterior cortical atrophy and typical Alzheimer's disease. *Neurobiol Aging*. 32(8):1466–1476.
- Li X, Li TQ, Andreasen N, Wiberg MK, Westman E, Wahlund LO. 2013. Ratio of A $\beta$ 42/P-tau181p in CSF is associated with aberrant default mode network in AD. *Sci Reports*. 3(1339):1–5.
- Li Y, Wang Y, Wu G, Shi F, Zhou L, Lin W, Shen D; Alzheimer's Disease Neuroimaging Initiative. 2012. Discriminant analysis of longitudinal cortical thickness changes in Alzheimer's disease using dynamic and network features. *Neurobiol Aging*. 33(2):427.e15–427.e30.
- Lo CY, Wang PN, Chou KH, Wang J, He Y, Lin CP. 2010. Diffusion tensor tractography reveals abnormal topological organization in structural cortical networks in Alzheimer's disease. *J Neurosci*. 30(50):16876–16885.
- Lovestone S, Francis P, Kloszewska I, Mecocci P, Simmons A, Soininen H, Spenger C, Tsolaki M, Vellas B, Wahlund LO, et al. 2009. AddNeuroMed—the European collaboration for the discovery of novel biomarkers for Alzheimer's disease. *Ann NY Acad Sci*. 1180:36–46.
- Lovestone S, Francis P, Strandgaard K. 2007. Biomarkers for disease modification trials—the innovative medicines initiative and AddNeuroMed. *J Nutrition Health Aging*. 11(4):359–361.
- McDonald CR, McEvoy LK, Gharapetian L, Fennema-Notestine C, Hagler DJ Jr, Holland D, Koyama A, Brewer JB, Dale AM; Alzheimer's Disease Neuroimaging Initiative. 2009. Regional rates of neocortical atrophy from normal aging to early Alzheimer disease. *Neurology*. 73(6):457–465.
- Medina D, DeToledo-Morrell L, Urresta F, Gabrieli JD, Moseley M, Fleischman D, Bennett DA, Leurgans S, Turner DA, Stebbins GT. 2006. White matter changes in mild cognitive impairment and AD: A diffusion tensor imaging study. *Neurobiol Aging*. 27(5):663–672.
- Meunier D, Achard S, Morcom A, Bullmore E. 2009. Age-related changes in modular organization of human brain functional networks. *Neuroimage*. 44:715–723.
- Muehlboeck JS, Westman E, Simmons A. 2014. TheHiveDB image data management and analysis framework. *Front Neuroinformatics*. 7:49.
- Newman MEJ. 2003. The structure and function of complex networks. *SIAM Rev*. 45:167–256.
- Newman MEJ. 2004. Fast algorithm for detecting community structure in networks. *Phys Rev E*. 69:066133.
- Newman ME. 2006. Modularity and community structure in networks. *PNAS*. 103(23):8577–8582.
- Pievani M, de Haan W, Wu T, Seeley WW, Frisoni GB. 2011. Functional network disruption in the degenerative dementias. *Lancet Neurol*. 10(9):829–843.
- Pereira JB, Aarsland D, Ginestet CE, Lebedev AV, Wahlund LO, Simmons A, Volpe G, Westman E. 2015. Aberrant cerebral network topology and mild cognitive impairment in early Parkinson's disease. *Hum Brain Mapp*. 36(8):2980–2995.
- Petersen RC, Smith GE, Waring SC, Ivnik RJ, Tangalos EG, Kokmen E. 1999. Mild cognitive impairment: clinical characterization and outcome. *Arch Neurol*. 56(3):303–308.
- Petrella JR, Sheldon FC, Prince SE, Calhoun VD, Doraiswamy PM. 2011. Default mode network connectivity in stable vs progressive mild cognitive impairment. *Neurology*. 76(6):511–517.
- Phillips DJ, McGlaughlin A, Ruth D, Jager LR, Soldan A; Alzheimer's Disease Neuroimaging Initiative. 2015. Graph theoretic analysis of structural connectivity across the spectrum of Alzheimer's disease: the importance of graph creation methods. *NeuroImage Clin*. 7:377–390.
- Rubinov M, Sporns O. 2010. Complex network measures of brain connectivity: uses and interpretations. *Neuroimage*. 52(3):1059–1069.

- Sanabria-Diaz G, Martinez-Montes E, Melie-Garcia L; Alzheimer's Disease Neuroimaging Initiative. 2013. Glucose metabolism during resting state reveals abnormal brain networks organization in the Alzheimer's disease and mild cognitive impairment. *PLoS ONE*. 8(7):e68860.
- Sanz-Arigita EJ, Schoonheim MM, Damoiseaux JS, Rombouts SA, Maris E, Barkhof F, Scheltens P, Stam CJ. 2010. Loss of 'small-world' networks in Alzheimer's disease: graph analysis of fMRI resting-state functional connectivity. *PLoS one*. 5(11): e13788, 1–14.
- Scahill RI, Schott JM, Stevens JM, Rossor MN, Fox NC. 2002. Mapping the evolution of regional atrophy in Alzheimer's disease: unbiased analysis of fluid-registered serial MRI. *PNAS*. 99(7):4703–4707.
- Segonne F, Dale AM, Busa E, Glessner M, Salat D, Hahn HK, Fischl B. 2004. A hybrid approach to the skull stripping problem in MRI. *Neuroimage*. 22(3):1060–1075.
- Segonne F, Pacheco J, Fischl B. 2007. Geometrically accurate topology-correction of cortical surfaces using nonseparating loops. *IEEE Trans Med Imaging*. 26(4):518–529.
- Sepulcre J, Sabuncu MR, Becker A, Sperling R, Johnson KA. 2013. In vivo characterization of the early states of the amyloid-beta network. *Brain*. 136(Pt 7):2239–2252.
- Shu N, Liang Y, Li H, Zhang J, Li X, Wang L, He Y, Wang Y, Zhang Z. 2012. Disrupted topological organization in white matter structural networks in amnesic mild cognitive impairment: relationship to subtype. *Radiology*. 265(2):518–527.
- Simmons A, Westman E, Muehlboeck S, Mecocci P, Vellas B, Tsolaki M, Kloszewska I, Wahlund LO, Soininen H, Lovestone S, et al. 2011. The AddNeuroMed framework for multi-centre MRI assessment of Alzheimer's disease: experience from the first 24 months. *Int J Ger Psychiatry*. 26(1):75–82.
- Simmons A, Westman E, Muehlboeck S, Mecocci P, Vellas B, Tsolaki M, Kloszewska I, Wahlund LO, Soininen H, Lovestone S, et al. 2009. MRI measures of Alzheimer's disease and the AddNeuroMed study. *Ann NY Acad Sci*. 1180:47–55.
- Sled JG, Zijdenbos AP, Evans AC. 1998. A nonparametric method for automatic correction of intensity nonuniformity in MRI data. *IEEE Trans Med Imaging*. 17(1):87–97.
- Sporns O, Betzel RF. 2016. Modular brain networks. *Ann Rev Psychol*. 67:613–640.
- Sporns O, Zwi JD. 2004. The small world of the cerebral cortex. *Neuroinformatics*. 2(2):145–162.
- Spulber G, Simmons A, Muehlboeck JS, Mecocci P, Vellas B, Tsolaki M, Kloszewska I, Soininen H, Spenger C, Lovestone S, et al. 2013. An MRI-based index to measure the severity of Alzheimer's disease-like structural pattern in subjects with mild cognitive impairment. *J Intern Med*. 273:396–409.
- Thal DR, Rub U, Orantes M, Braak H. 2002. Phases of A beta-deposition in the human brain and its relevance for the development of AD. *Neurology*. 58(12):1791–1800.
- Thompson PM, Hayashi KM, De Zubicaray GI, Janke AL, Rose SE, Semple J, Hong MS, Herman DH, Gravano D, Doddrell DM, et al. 2004. Mapping hippocampal and ventricular change in Alzheimer disease. *Neuroimage*. 22(4):1754–1766.
- Tijms BM, ten Kate M, Wink AM, Visser PJ, Ecury M, Clerigue M, Estanga A, Sebastian MG, Izaguirre A, Villanua J, Lage PM. 2016. Gray matter network disruptions and amyloid beta in cognitively normal adults. *Neurobiol Aging*. 37:154–160.
- Tijms BM, Moller C, Vrenken H, Wink AM, de Haan W, van der Flier WM, Stam CJ, Scheltens P, Barkhof F. 2013. Single-subject grey matter graphs in Alzheimer's disease. *PLoS ONE*. 8(3): e58921.
- Tijms BM, Series P, Willshaw DJ, Lawrie SM. 2012. Similarity-based extraction of individual networks from gray matter MRI scans. *Cereb Cortex (New York, NY)*. 22(7): 1530–1541.
- Tijms BM, Wink AM, de Haan W, van der Flier WM, Stam CJ, Scheltens P, Barkhof F. 2013. Alzheimer's disease: connecting findings from graph theoretical studies of brain networks. *Neurobiol Aging*. 34(8):2023–2036.
- Watts DJ, Strogatz SH. 1998. Collective dynamics of 'small-world' networks. *Nature*. 393(6684):440–442.
- Westman E, Simmons A, Muehlboeck JS, Mecocci P, Vellas B, Tsolaki M, Kloszewska I, Soininen H, Weiner MW, Lovestone S, et al. 2011. AddNeuroMed and ADNI: similar patterns of Alzheimer's atrophy and automated MRI classification accuracy in Europe and North America. *Neuroimage*. 58(3):818–828.
- Wu K, Taki Y, Sato K, Kinomura S, Goto R, Okada K, Kawashima R, He Y, Evans AC, Fukuda H. 2012. Age-related changes in topological organization of structural brain networks in healthy individuals. *Hum Brain Mapp*. 33(3):552–568.
- Xia M, Wang J, He Y. 2013. BrainNet viewer: a network visualization tool for human brain connectomics. *PLoS ONE*. 8(7):e68910.
- Yaffe K, Petersen RC, Lindquist K, Kramer J, Miller B. 2006. Subtype of mild cognitive impairment and progression to dementia and death. *Dem Ger Cog Disord*. 22(4):312–319.
- Yao Z, Hu B, Zheng J, Zheng W, Chen X, Gao X, Xie Y, Fang L; Alzheimer's Disease Neuroimaging Initiative. 2015. A FDG-PET study of metabolic networks in apolipoprotein e epsilon4 allele carriers. *PLoS ONE*. 10(7):e0132300.
- Yao Z, Zhang Y, Lin L, Zhou Y, Xu C, Jiang T; Alzheimer's Disease Neuroimaging Initiative. 2010. Abnormal cortical networks in mild cognitive impairment and Alzheimer's disease. *PLoS Comp Biol*. 6(11):e1001006.
- Zanetti M, Ballabio C, Abbate C, Cutaia C, Vergani C, Bergamaschini L. 2006. Mild cognitive impairment subtypes and vascular dementia in community-dwelling elderly people: a 3-year follow-up study. *J Am Geriatr Soc*. 54:580–586.
- Zhang Y, Schuff N, Jahng GH, Bayne W, Mori S, Schad L, Mueller S, Du AT, Kramer JH, Yaffe K, et al. 2007. Diffusion tensor imaging of cingulum fibers in mild cognitive impairment and Alzheimer disease. *Neurology*. 68(1):13–19.
- Zhou J, Gennatas ED, Kramer JH, Miller BL, Seeley WW. 2012. Predicting regional neurodegeneration from the healthy brain functional connectome. *Neuron*. 73(6):1216–1227.
- Zhu W, Wen W, He Y, Xia A, Anstey KJ, Sachdev P. 2012. Changing topological patterns in normal aging using large-scale structural networks. *Neurobiol Aging*. 33(5):899–913.